Bacterial morphology analysis by cryo-soft X-ray tomography and cryo-(scanning) transmission electron microscopy

Antoine Cossa

THESE DE DOCTORAT

NNT : 2022UPASF091

Bacterial morphology analysis by cryo-soft X-ray tomography and cryo-(scanning) transmission electron microscopy

Analyse de la morphologie bactérienne par cryo-tomographie à rayons-X mous et cryo-microscopie électronique en transmission (à balayage)

Thèse de doctorat de l'université Paris-Saclay et de la Universidad Autónoma de Madrid

École doctorale n° 571, Sciences Chimiques : Molécules, Matériaux, Instrumentation et Biosystèmes (2MIB)
Spécialité de doctorat : Physique
Graduate School : Chimie. Référent : Faculté des Sciences d'Orsay
UAM doctoral program of Molecular Biosciences

Thèse préparée dans les unités de recherche **Laboratoire Léon Brillouin (Université Paris-Saclay, CEA, CNRS)**, **Centre d'Imagerie Multimodale (Université Paris-Saclay, Institut Curie, CNRS, Inserm)** et **Biocomputing Unit (CNB-CSIC)**, sous la direction de **Véronique ARLUISON**, Maître de conférences, la co-direction de **José María CARAZO**, Professeur, le co-encadrement de **Sylvain TREPOUT**, Ingénieur de recherche.

Thèse soutenue à Paris-Saclay, le 16 décembre 2022, par

Antoine COSSA

Composition du Jury

Membres du jury avec voix délibérative

Amélie LEFORESTIER Directrice de recherche, Laboratoire de Physique des Solides (SOBIO, Orsay)	Présidente
Vincent RAUSSENS Professeur, Université Libre de Bruxelles (SFMB, Bruxelles, Belgique)	Rapporteur & Examinateur
Jean-Marc VICTOR Directeur de recherche, Sorbonne Université (LPTMC, CNRS, Paris)	Rapporteur & Examinateur
Raúl GUANTES Professeur associé, Université Autonome de Madrid (Department of Condensed Matter Physics, Madrid, Espagne)	Examinateur

université PARIS-SACLAY

ÉCOLE DOCTORALE
Sciences Chimiques : Molécules, Matériaux, Instrumentation et Biosystèmes (2MIB)

Titre : Analyse de la morphologie bactérienne par cryo-tomographie à rayons-X mous et cryo-microscopie electronique en transmission (à balayage)

Mots clés : Cryo-SXT, Cryo-STEM, Imagerie haute resolution, Imagerie bacterienne, Biophysique, Microbiologie

Résumé : Chez les bactéries, l'ADN n'est pas séparé du reste de la cellule par une membrane, contrairement aux eucaryotes qui possèdent un noyau. Cet ADN a donc besoin d'être à la fois protégé tout en restant accessible pour permettre l'expression génétique. Cette structuration de l'ADN se fait via des protéines appelées NAPs (pour "Nucleoid Associated Protein"). Parmi ces NAPs, on trouve la protéine Hfq. Hfq est un facteur pléiotrope impliqué dans la physiologie bactérienne. Sa fonction la plus connue est de réguler des processus ARNs dépendants. Cependant, sa capacité à former une structure amyloïde lui permet d'interagir avec l'ADN, de former des ponts entre des parties éloignées de l'ADN et ainsi de le compacter fortement. Si cette propriété a pu être démontrée *in vitro*, les analyses *in cellulo* manquaient.

Ce travail de thèse met en lumière les effets directs et indirects d'Hfq sur la l'état de compaction du nucléoïde. Ainsi les complexes ou les cellules ont pu être observés à l'aide de techniques de cryo-microscopie électronique en transmission (à balayage) (cryo-(S)TEM) et de cryo-tomographie à rayons-X mous (cryo-SXT). Cette dernière, est une technique d'imagerie tri-dimensionnelle qui permet de quantifier le volume et la densité du nucléoïde bactérien. Ce projet de thèse a permis de caractériser l'impact d'Hfq sur la structure de l'ADN et la morphologie bactérienne, ce qui permettra de tester *in cellulo* l'effet de nouveaux antibiotiques qui pourront être développés en lien avec cette propriété dans le futur.

Title: Bacterial morphology analysis by cryo-soft X-ray tomography and cryo-(scanning) transmission electron microscopy

Keywords: Cryo-SXT, Cryo-STEM, High-resolution imaging, Bacterial imaging, Biophysics, Microbiology

Abstract: In bacteria, DNA is not separated in the cell by a membrane, converse to eukaryotes, which have a nucleus. Therefore, DNA must be protected, while remaining accessible to allow for gene expression. The DNA structuring is achieved via proteins called NAPs (standing for "Nucleoid Associated Protein"). Among these NAPs, the Hfq protein is found. Hfq is a pleiotropic factor involved in bacterial physiology. Its best-known function is to regulate RNA-dependent processes. However, its ability to form an amyloid structure allows it to interact with DNA, to form bridges between distant parts of DNA and thus to compact it strongly. If this property was demonstrated *in vitro*, analyses were lacking *in cellulo*.

This PhD work highlights the direct and indirect effects of Hfq on the compaction of the nucleoid. The complexes or the cells were observed using cryo-(scanning) transmission electron microscopy (cryo-(S)TEM) and cryo-soft X-ray tomography (cryo-SXT) techniques. The latter is a three-dimensional imaging technique that permits to quantify the volume and density of the bacterial nucleoid. This PhD project made possible to characterize the impact of Hfq on the structure of DNA and bacterial morphology, which will make it possible to test *in cellulo* the effects of new antibiotics, which could be developed in connection with this property in the future.

Dedicated to my mother and my grandparents.

Acknowledgments

Je souhaiterais tout d'abord témoigner toute ma gratitude envers Véronique Arluison, ma directrice de thèse, pour m'avoir accepté comme étudiant et permis de réaliser cette thèse tout en me soutenant jusqu'au bout de celle-ci. Je remercie également José María Carazo d'avoir accepté d'assurer la codirection de ma thèse et Carlos Óscar Sánchez Sorzano pour son aide. Je remercie Sylvain Trépout d'avoir initié cette thèse.

Je remercie ensuite mes rapporteurs, Vincent Raussens et Jean-Marc Victor, d'avoir accepté d'évaluer mon travail de thèse et pour le temps qu'ils consacreront à sa lecture. Je tiens également à remercier les membres de mon jury de thèse, Amélie Leforestier et Raúl Guantes d'avoir accepté d'évaluer ce travail. Je remercie Eva Pereiro pour sa participation en tant que membre invité.

Je remercie l'Institut Curie d'avoir financé une année de ma thèse, ainsi que l'ADI IDEX Paris-Saclay pour avoir financé les deux années restantes et me permettre ainsi de mener à bien ce projet de recherche.

Je remercie les membres du Multimodal Imaging Center de l'Institut Curie, Cédric Messaoudi, Christine Walczak, Marie-Noëlle Soler, Ting-Di Wu, Jean-Luc Guerquin-Kern, Sandrine Bourgeois, Amandine Verguet, Ptissam Bergam, Jean-Michel Lenz, et tout particulièrement Frédéric Coquelle pour son temps, ses conseils et son assistance auprès de l'Institut Curie et l'Université. Et bien évidemment Laetitia Besse pour tous les bons moments que nous avons partagés et toutes nos discussions.

Je remercie aussi les membres du LLB au CEA Saclay pour leur accueil chaleureux, et particulièrement Eric Eliot.

Je remercie l'ensemble des membres de la Biocomputing Unit du CNB-CSIC de Madrid, pour leur accueil bien que la pandémie ait limité nos échanges à de la visio. Je remercie particulièrement Blanca pour son aide sur le plan administratif.

Je souhaite également remercier toutes les personnes avec qui j'ai pu collaborer durant ma thèse. Evidemment Eva Pereiro pour nos nombreux échanges, ses précieux conseils, sa positivité et son aide. Merci également à Frank, Ana, Federico, Teresa, Marcos, et Eric Le Cam. Merci à Sergio Marco pour sa bienveillance.

Je remercie également l'ensemble des personnes qui se sont spontanément proposées pour relire ma thèse. Merci également à Richard Sinden pour sa relecture attentive.

Je remercie mes amis, pour tous les moments passés ensemble durant ces trois dernières années et leur soutien à toute épreuve, ainsi que toutes les belles rencontres que j'ai pu faire. Je tiens particulièrement à remercier mes compagnons du 15bis qui m'ont aidé à traverser cette étrange période du 1er confinement, Juju et Kanok pour nos sorties escalade, Chloé, Arthur et Laura, Luca.

Anthony et Camille, ces six mois de stages à partager le même bureau avec vous ont été une véritable bouffée d'air frais. Je suis heureux que nos chemins aient pu se croiser.

Thomas, merci pour ton soutien, nos discussions de tout et de rien, les expos, la photographie.

Guillaume, je te remercie pour ton soutien et tes précieux conseils.

Anne et Lucie, merci pour tout, tous nos moments, nos débriefs du dimanche… Merci d'avoir été là et de m'avoir soutenu tout au long de ce périple.

Je souhaite enfin remercier ma famille, et notamment ma mère, mes grands-parents et ma petite sœur, pour m'avoir permis d'aller au bout de mes études, pour avoir toujours cru en moi et pour leur soutien sans faille.

List of figures

List of abbreviations

2D	Two dimensional
3D	Three dimensional
Å	Angstrom
AB	Antibiotic
ADF	Annular Dark Field
AFM	Atomic Force Microscopy
BF	Bright Field
CD	Circular Dichroism
CS	Compressed Sensing
CTR	C-terminal region
ddH2O	Double-distilled water
DF	Dark Field
DNA	Deoxyribonucleic Acid
dsDNA	double-stranded DNA
E. coli	*Escherichia coli*
EHEC	Enterohaemorrhagic E. coli
EMSA	Electrophoretic Mobility Shift Assay
FEG	Field Emission Gun
FoV	Field of View
FP	Fluorescent Protein
FTIR	Fourier-Transform Infrared Spectroscopy
HADF	High-angle Annular Dark Field
LBT	Lanthanide Binding Tag
LSm	Sm-like
mRNA	messenger RNA
NAP	Nucleoid Associated Protein
NTR	N-terminal region
pm	Picometer
RBS	Ribosome-binding site
RNA	Ribonucleic Acid

SANS	Small-Angle Neutron Scattering
SAXS	Small-Angle X-ray Scattering
SNR	Signal to Noise Ratio
SPA	Single Particle Analysis
sRNA	small non-coding RNA
ssDNA	single-stranded DNA
STED	Stimulated Emission Depleted microscopy
STEM	Scanning Transmission Electron Microscopy
STET	Scanning Transmission Electron Tomography
STORM	Stochastic Optical Reconstruction Microscopy
TEM	Transmission Electron Microscopy
TET	Transmission Electron Tomography
VLM	Visible Light Microscopy
WHO	World Health Organisation
WT	Wild Type
ZP	Zone Plate

Table of contents

Résumé synthétique

Les antibiotiques sont des molécules qui ciblent et tuent spécifiquement les cellules bactériennes. Cette action antibactérienne utilise généralement quatre mécanismes principaux, l'inhibition des enzymes impliquées dans la biosynthèse de la paroi cellulaire (le peptidoglycane), la rupture de la membrane, la traduction des protéines ou le métabolisme et la réparation de l'ADN (Peleg and Hooper 2010). Les principales familles d'antibiotiques utilisant ces mécanismes sont *(i)* les β-lactames et glycopeptides, *(ii)* les polymyxines, *(iii)* les aminoglycosides, les macrolides et la tétracycline, et *(iv)* les quinolones.

Cependant, les bactéries sont très efficaces pour acquérir des résistances aux antibiotiques, en particulier sous la pression de sélection trouvée dans les hôpitaux (Peleg and Hooper 2010). Si l'émergence de souches résistantes est un phénomène naturel (le microbiote intestinal par exemple possède des gènes de résistance aux antibiotiques), la mauvaise utilisation des antibiotiques accélère ce processus de multirésistance ; les gènes de résistance aux antibiotiques proviennent ainsi d'autres bactéries et l'acquisition de la résistance repose souvent sur le phénomène du transfert génétique, où les plasmides en particulier jouent un rôle central (Bennett 2008).

Actuellement, la problématique de la résistance aux antibactériens est donc particulièrement critique en raison de l'absence de développements de nouvelles classes d'antibiotiques et ceci depuis une trentaine d'années (Fig. I) (Shore and Coukell 2016). Beaucoup d'efforts ont été déployés pendant cette période pour modifier et améliorer les antibiotiques préexistants. Cependant, le principal problème avec cette approche est le développement rapide de nouvelles résistances, qui n'exigent généralement pas ou peu de modification des mécanismes de résistance déjà existants. Par conséquent, la recherche de nouvelles cibles d'antibiotiques dans les cellules bactériennes est de la plus haute importance. C'est en ce sens que de nouvelles approches ont été expérimentées au cours de la dernière décennie. Par exemple, certains groupes ont essayé de bloquer l'assemblage de la machinerie de division bactérienne (ce que l'on appelle le divisome).

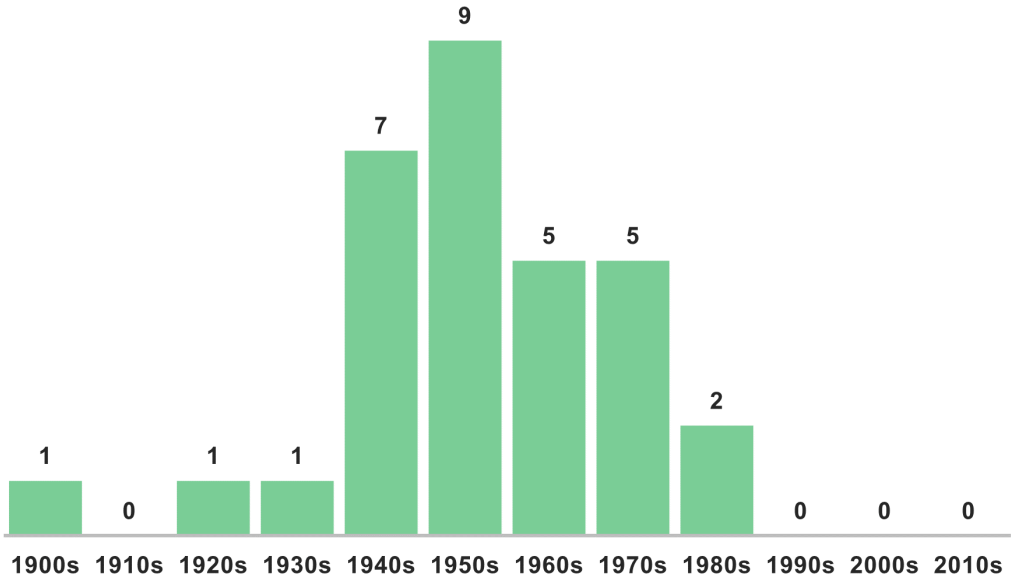

Fig. I. Développement de nouveaux antibiotiques depuis le début du 20ème siècle (Shore and Coukell 2016). (Listée comme Figure. 2 dans la liste des figures du texte principal)

Notre objectif pendant mon projet de thèse visait à étudier les amyloïdes bactériens pour, dans le futur, développer de nouveaux antimicrobiens (Zhou et al. 2012). Ces structures, appelées amyloïdes fonctionnels, aident à maintenir l'état physiologique normal de la cellule bactérienne (Otzen and Riek 2019). Ils sont dits fonctionnels par opposition aux amyloïdes pathologiques, plus connus et plus étudiés car impliqués dans de nombreuses pathologies humaines, telles que les maladies neurodégénératives d'Alzheimer ou de Parkinson (Agrawal and Skelton 2019; El-Agnaf et al. 2004). Dans ce dernier cas le mauvais repliement est associé à la conversion de peptides ou de protéines spécifiques depuis leur état fonctionnel soluble en agrégats fibrillaires. Au cours de cette agrégation, les protéines monomériques subissent des réarrangements structuraux conduisant à l'assemblage de feuillets β en une structure quaternaire dite « cross-β ». Cette conformation est l'empreinte des structures amyloïdes (Bonar, Cohen, and Skinner 1969; Eisenberg and Sawaya 2017). Par rapport aux amyloïdes dits « pathogènes », les amyloïdes dits « fonctionnels » ont la propriété d'apporter des fonctions bénéfiques à la cellule, mais ils gardent la conformation décrite ci-dessus.

Mes travaux, dans le cadre de ce projet de thèse, portent plus particulièrement sur une protéine bactérienne appelée Hfq présentant une région amyloïde (Brennan and Link 2007; Vogel and Luisi 2011). Les bactéries sont des organismes unicellulaires qui s'adaptent constamment aux changements environnementaux (Kavita, de Mets, and Gottesman 2018).

Cette adaptation est particulièrement critique lorsque des bactéries colonisent un hôte, notamment des bactéries pathogènes qui doivent adapter leur métabolisme en fonction des conditions de croissance rencontrées chez un hôte. Les bactéries doivent donc être capables de changer rapidement leur expression génétique tout en communiquant entre elles. Bien que la façon dont les bactéries s'adaptent aussi rapidement à leur environnement ne soit pas encore totalement mise à jour, il a été possible de montrer que les bactéries utilisent à cette fin la protéine Hfq et de petits ARN régulateurs dits non codants. Le terme « non codant » sous-entend qui ne code pas pour une protéine, mais contribue à l'expression génétique ou plus généralement à la vie cellulaire. Ces deux partenaires permettent des changements rapides de la machinerie d'expression génétique bactérienne, conduisant à l'adaptation des bactéries, par exemple en réponse à une carence en fer qui est fréquente lors de l'infection d'un hôte (Massé and Gottesman 2002).

Outre son interaction avec les ARNs, il a pu être prouvé que Hfq interagit aussi avec l'ADN et que la région amyloïde de Hfq contribue fortement à cette propriété *in vitro*. Cette structuration sous forme amyloïde est retrouvée dans la région C-terminale (CTR) de la protéine, région qui représente en séquence environ 1/3 de la protéine totale.

Mes travaux visent initialement à mieux comprendre le rôle de Hfq et de son domaine CTR dans la compaction de l'ADN *in vivo* grâce à différentes approches d'imagerie *in cellulo*. Notamment, ils visent à caractériser le phénotype de cellules bactériennes, soit totalement dépourvues de Hfq, ou bien uniquement dépourvues de la région CTR de Hfq, pour comparer ces phénotypes à celui de cellules de référence exprimant normalement Hfq. Dans ce but les techniques de cryo-microscopie électronique (cryo-(S)TEM) et cryo-tomographie aux rayons-X mous (cryo-SXT) ont été utilisées (Cossa, Cren, et al. 2022; Cossa, Wien, et al. 2022; Cossa, Trépout, et al. 2022). Ces analyses nous ont permis de prouver l'effet de Hfq sur la structuration de l'ADN *in cellulo*. En outre pendant ma thèse j'ai eu l'occasion de découvrir les techniques d'imageries moléculaires permettant de caractériser les complexes Hfq:ADN *in vitro*. J'ai pu utiliser les techniques de cryo-microscopie électronique cryo-TEM et de microscopie électronique après coloration positive (Kubiak et al. 2022).

Les principaux résultats de ma thèse sont donc les suivants : *(i)* j'ai contribué à caractériser en imagerie moléculaire la façon dont le CTR de Hfq interagit avec l'ADN double brin et permet sa compaction. Des modèles 3D basés sur des expériences de cryo-TEM sont en construction et viendront compléter une analyse par diffusion de neutrons aux petits angles (DNPA) déjà

réalisée. Même si ce travail n'est pas complètement terminé il devrait déboucher sur une nouvelle publication en 2023 ; *(ii)* nous avons aussi montré que Hfq et plus particulièrement son CTR interagit avec l'ADN simple brin. La principale conclusion de cette partie de mon travail est que le CTR change la conformation et aligne l'ADN simple brin, ce qui entraîne des conséquences importantes sur l'expression génétique ; *(iii)* le résultat majeur de ma thèse a consisté à analyser l'effet de Hfq et de son CTR *in cellulo*. Nous avons pu prouver que Hfq permet la compaction de l'ADN directement, mais aussi indirectement en utilisant des régulations utilisant des ARNs non codants ; *(iv)* j'ai pu évaluer les perspectives d'une acquisition parcimonieuse en cryo-STEM, permettant ainsi une réduction des radiations appliquées à l'échantillon par le faisceau d'électrons, pour l'analyse d'échantillons épais et applicable à l'étude des bactéries. Un des développements envisagés est celui de l'imagerie corrélative cryo-SXT/cryo-STEM. Cet aspect que j'aurais dû développer pendant ma thèse, notamment durant mon séjour en Espagne, n'a malheureusement pas été possible due à la pandémie de SARS-CoV-2 ; *(v)* enfin pendant ma thèse j'ai aussi montré qu'une étiquette protéique appelée LBT fixant des ions lanthanides pourrait être utilisée pour l'imagerie corrélative alliant cryo-SXT, cryo-(S)TEM et fluorescence X. Les premiers tests sur ce développement sont très prometteurs, et j'espère que notre groupe pourra développer ce nouvel outil dans le futur.

En résumé, les analyses *in cellulo* effectuées pendant ma thèse ont permis de faire significativement progresser l'analyse des bactéries Gram négatives par la méthode de cryo-SXT permettant l'analyse de cellules cryo-préservées (Cossa, Trépout, et al. 2022). Cette approche, qui pourra à terme être utilisée en imagerie corrélative avec de la microscopie électronique, permet de visualiser la bactérie à haute résolution au niveau de son nucléoïde contenant l'ADN (par cryo-SXT) et de la visualisation simultanée des membranes (en cryo-(S)TEM), le but étant d'imager exactement les mêmes bactéries en utilisant ces deux méthodes. Par la suite, l'objectif de notre groupe sera de développer des composés qui pourront inhiber ou interférer avec l'autoassemblage de Hfq et bloquer son interaction avec l'ADN (Malabirade, Jiang, et al. 2017; Turbant et al. 2022). Récemment, il a pu être montré que certains composés connus pour empêcher l'autoassemblage des amyloïdes formés lors de pathologies neurodégénératives sont capables d'affecter la fibrillation de Hfq et la survie de la bactérie (Partouche et al. 2018; Turbant, Hamoui, et al. 2021; Turbant, Partouche, et al. 2021). Nous pensons que cette approche pourrait aider à développer une nouvelle classe d'antibiotiques visant à bloquer les régulations permises par Hfq, avec des conséquences connexes sur la

physiologie bactérienne. Les méthodes d'analyses *in cellulo* que j'ai contribuées à développer seront donc extrêmement utiles pour évaluer l'effet des inhibiteurs *in cellulo*.

Chapter I. General introduction

1.1. Gram negative bacteria, antibiotics and global health

Bacteria are unicellular organisms that must constantly adapt to changes in their environment. Recently, bacteria have become a growing interest for human health with the emergence of new roles, mainly as "gut microbiota", i.e., bacteria (but also some eukaryotes) that colonise the gastrointestinal tract and who evolved over years with their host for a beneficial relationship (W.-L. Wang et al. 2015). These roles include host protection against pathogens, modulation of immunity, or regulation of some metabolic processes. Nevertheless, the same bacteria, for instance *Escherichia coli*, can either be beneficial or pathogenic for its host. Indeed, a microbiotal bacterium can become pathogenic if its growth-rate raises and if it begins to outcompete other cells on the surface or the mucosa where it lives. Precisely, commensal bacteria are normally restricted to certain regions of the host (skin, buccal and nasal mucosae, gastrointestinal tract…); but under specific conditions they can invade organs (Ribet and Cossart 2015). This is also the case for some bacteria who change the expression of some virulence factors that favours the host colonization (Ribet and Cossart 2015). This is very problematic as bacteria are at least as abundant as eucaryotic cells in the human body (ranging from ~ 3.10^{13} to 10^{14} bacteria compared to 10^{13} human cells) (Sender, Fuchs, and Milo 2016). Thus, only one pathogenic bacterium will give many pathogens in a short time, taking into account their fast exponential division in the host (~ 1-2 hour) (Myhrvold et al. 2015).

To kill pathogenic bacteria, antibacterial compounds have been developed. The first antibiotic (AB), Penicillin, was discovered in 1928 by Alexander Fleming and then used in 1941 to treat patients.

Currently, about 15 families of antibiotics are used. Antibacterial action generally falls within four mechanisms, which are the inhibition of enzymes involved in cell-wall biosynthesis (peptidoglycan, a layer of a polymer of sugars and amino acids), or the disruption of the bacterial cell membrane, protein synthesis or DNA metabolism and repair (Figure 1) (Peleg and Hooper 2010). The main families of ABs using these mechanisms are (i) β-lactams and

glycopeptides, (ii) polymyxins (not frequently used because they are neuro- and nephrotoxic), (iii) aminoglycosides, macrolides and tetracyclines, and (iv) quinolones, respectively.

Nevertheless, AB resistance is one of the challenges we are facing in the 21st century. Recent statistics indicate that Gram-negative bacteria (i.e., surrounded by two membranes and thin layer of peptidoglycan) are responsible for more than 30% of hospital-acquired infections (Peleg and Hooper 2010). While urinary infections are the most common, bloodstream and respiratory infections are the most fatal. Gram *(-)* bacteria predominate in hospital-acquired pneumonia (*Pseudomonas aeruginosa*, *Acinetobacter baumanni)*, infection of the bloodstream (*Escherichia coli*, *Klebsiella* species, *P. aeruginosa*) or the urinary tract (*E. coli*). Bacteria and in particular Enterobacterales such as *E. coli* are very efficient in acquiring resistance to ABs, especially under selection pressure found in hospitals where AB are of current use. If the emergence of resistance is a natural phenomenon (natural flora naturally possess resistance genes), the misuse of ABs accelerates this process. Indeed, AB-resistance genes originate from other bacteria and acquisition of resistance relies on the phenomenon of gene transfer, where plasmids in particular serve a central role (Bennett 2008).

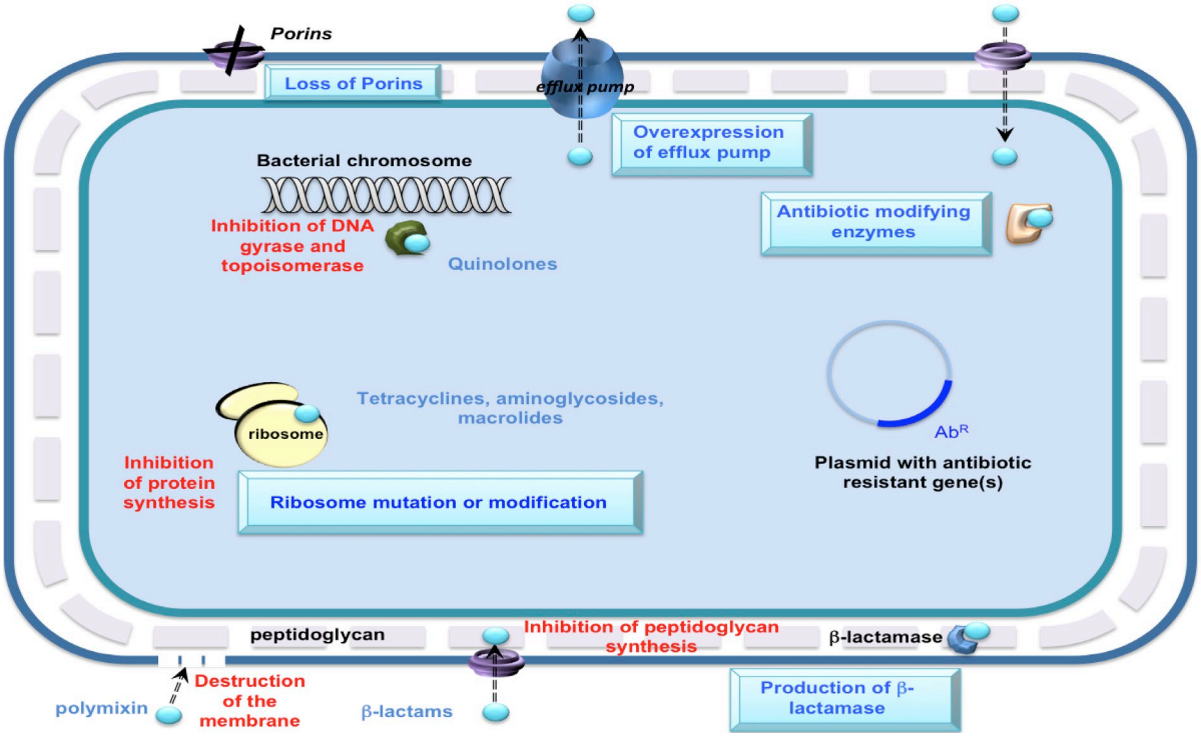

Figure 1. ABs actions and mechanisms of resistance in Gram (-) bacteria. Main mechanisms of resistance include the loss of porins, which reduces the entrance of drug inside the cell; presence of β-lactamases in the periplasmic space, which degrades the β-lactam; in increased expression of the efflux pump, which exports the drug outside the bacterium; ribosomal mutations or modifications, which stop

the inhibition of protein synthesis; AB-modifying enzymes or target site mutations, which make the AB incapable of interacting with its target. Resistance genes are often brought by plasmids.

Mechanisms of AB resistance in bacteria may vary and include AB detoxification, target protection or stoppage of AB accumulation. Bacteria can for instance develop mechanisms of resistance relying on the loss of porins, which reduces the entrance of AB inside the cell, or in ribosomal mutations, which prevent the AB from inhibiting bacterial protein synthesis (Figure 1). Another well-known example of resistance consists in the production of β-lactamases by bacteria. β-lactamases are naturally present in some Gram *(-)* bacteria and degrade the β-lactam ring found in ABs such as Penicillin or Carbapenem. Indeed, Gram *(-)* bacteria have an envelope formed by two membranes sandwiching peptidoglycan that maintains the shape and the integrity of the cell. β-lactam-based ABs interfere with the synthesis of peptidoglycan, so that the architecture of the bacterial cell is lost (Figure 1). Since mammalian cells lack peptidoglycan, this class of ABs targets specifically bacteria, with no significant effects for the host. For this reason, β-lactam is the most used group of ABs. Nevertheless, due to the nature of their envelope, Gram-negative bacteria are less susceptible to these ABs than those that do not contain a second membrane covering the peptidoglycan layer (i.e., Gram-positive bacteria). In addition, the easy acquisition of resistance by Gram *(-)* bacteria to this class of AB poses important therapeutic challenges.

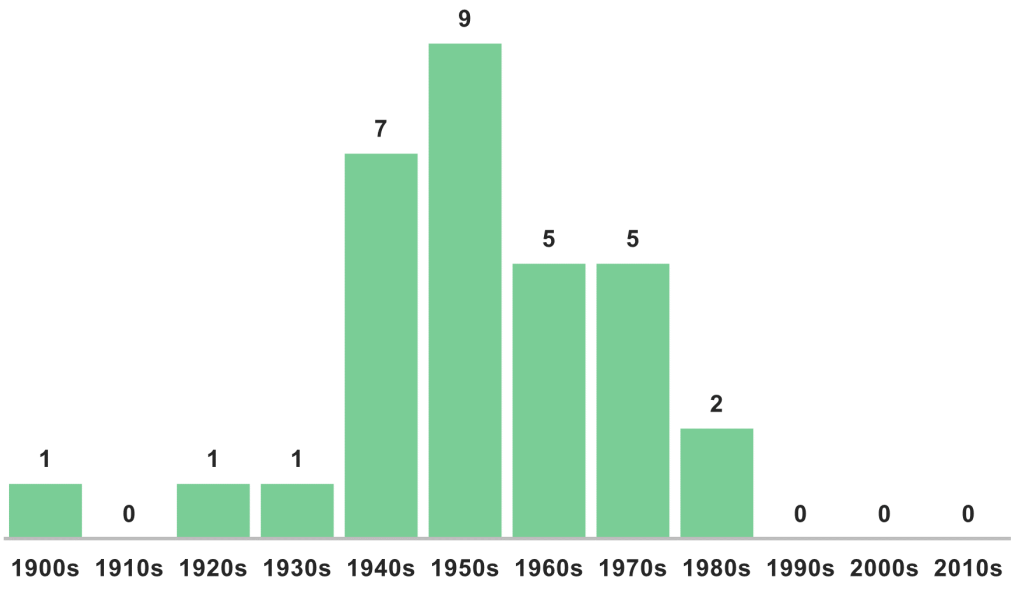

Figure 2. New antibiotic development since the beginning of the 20th century. (Shore and Coukell 2016)

Currently, the question of antibacterial resistance is particularly problematic due to the absence of new family of antibiotic development for about thirty years (Figure 2) (Shore and Coukell 2016). Much effort has been done since 1990 to modify and improve existing ABs. However, the main problem with this approach is the development of new resistances, which usually requires little or no modification of existing mechanisms. Therefore, the search for novel antibiotic targets in bacterial cells is of utmost importance. In this way, new approaches have been tried during the last decade, for instance, blocking the assembly of the essential bacterial division machinery (divisome) (Söderström and Daley 2017).

Another research direction aims at exploring potential targets within proteins involved in the regulation of the genetic expression. This includes proteins that allow bacteria to adapt to their environment in case of the host infection, for instance virulence factors whose expression is switched on by the passage from outside to the host environment (Poole 2012). Only this adaptation allows the infection and for this goal, bacteria can use two main ways:

- Regulation at the transcriptional level. Nucleoid-associated proteins (NAP) are involved in the maintenance of bacterial chromosomal architecture and have a role in the regulation of genes (Dorman 2009; Dorman et al. 2020). NAPs affect the expression of a large number of genes, most coding for housekeeping-proteins, but also for proteins involved in response to environmental changes induced during host colonisation (Hołówka and Zakrzewska-Czerwińska 2020). One of the best illustrations of this is the H-NS NAP (Badaut et al. 2002; Dame, Wyman, and Goosen 2000; Fang and Rimsky 2008; van der Maarel et al. 2016), involved in the control of virulence when bacteria must adapt to new growth conditions, such as salmonella in the gastrointestinal tract (Harrison et al. 1994; Schechter et al. 2003).

- Regulation at the post-transcriptional level (Porcheron and Dozois 2015). One of the most promising approaches in this direction consists of blocking noncoding RNA-based regulation. About 30,000 sequences of ncRNA from different species have been identified and among them, those from bacteria are on average 100 nucleotides long, hence their name of small RNA (sRNA) (S. Gottesman and Storz 2011). The sRNA often functions by base pairing within regions around the translation initiation signal (Ribosome Binding Site RBS and/or AUG initiation codon) of the associated messenger RNA (mRNA) target, and therefore acts on both mRNA translation and stability (Aiba 2007). *In vivo*, a protein called Hfq is required for sRNA-regulation as it promotes annealing of the regulatory sRNA to its cognate mRNA (Arluison et al. 2007; Vogel and Luisi 2011). Due to the diversity of their mRNA targets, sRNA

and Hfq are thus involved in important bacterial cell processes, including virulence, quorum sensing or pathogenicity (Bardill, Zhao, and Hammer 2011; Chao and Vogel 2010; Sittka et al. 2007).

1.2. *Escherichia coli* as a model of Gram-negative bacterium

Escherichia coli is a Gram *(-)* and rod-shaped bacterium, which is typically around 1-2 µm long and 0.5 µm wide. Most strains of *E. coli* are non-pathogenic and present in the human and animals. But some strains such as enterohaemorrhagic *E. coli* (EHEC) are pathogenic and cause severe infections and haemorrhagic diarrhoea. These strains outbreaks can originate from faecal contaminations, raw milk products, dirty vegetables, raw or undercooked meat. They represent a global sanitary problem and can lead to a haemolytic uraemic syndrome (HUS) characterized by acute renal failure and low platelet counts.

Furthermore, *E. coli* is frequently used as a model organism as it grows fast, making it a model organism for molecular genetics (Blount 2015). In addition, numerous molecular tools are available to perform genetic manipulations. These tools include plasmids and specific bacteriophages. Note that non-pathogenic and pathogenic *E. coli* strains display variation in their genomes: similarity between the genomes of *E. coli* K-12 strain (a laboratory non-pathogenic strain) and O157:H7 pathogenic *E. coli* is only around 40% (Abe et al. 2008; Schneider et al. 2002).

Previous contributions to fight Gram *(-)* bacterial infections and in particular *E. coli* infections focussed on Hfq and sRNA-based regulation, with the objective to block the adaptation of bacterium to their environment (El-Mowafi et al. 2014). In my PhD project, we intended to pinpoint another property of the protein. Indeed, Hfq, which belongs to the nucleoid associated protein (NAP) family association to DNA has also been observed *in vitro* and *in vivo* (Azam et al. 1999; Cech et al. 2016; Diestra et al. 2009; Geinguenaud et al. 2011). Our group demonstrated that Hfq has significant DNA-compacting properties (Jiang et al. 2015; Malabirade, Jiang, et al. 2017; Malabirade et al. 2018), resulting in consequences for fundamental cellular processes such as transcription and replication (Cech et al. 2014; Le Derout et al. 2010). Furthermore, Hfq interacts with the RNA polymerase (Sukhodolets and Garges 2003), influences transcription termination (Rabhi et al. 2011) and controls the expression of bacterial transcription σ factors, such as σ^S (Arluison et al. 2007; Battesti,

Majdalani, and Gottesman 2011; Hwang, Arluison, and Hohng 2011). Thus, Hfq appears to be capable of affecting a variety of DNA-related mechanisms (Figure 3) (Cech et al. 2016; Malabirade et al. 2018; Mandin and Guillier 2013).

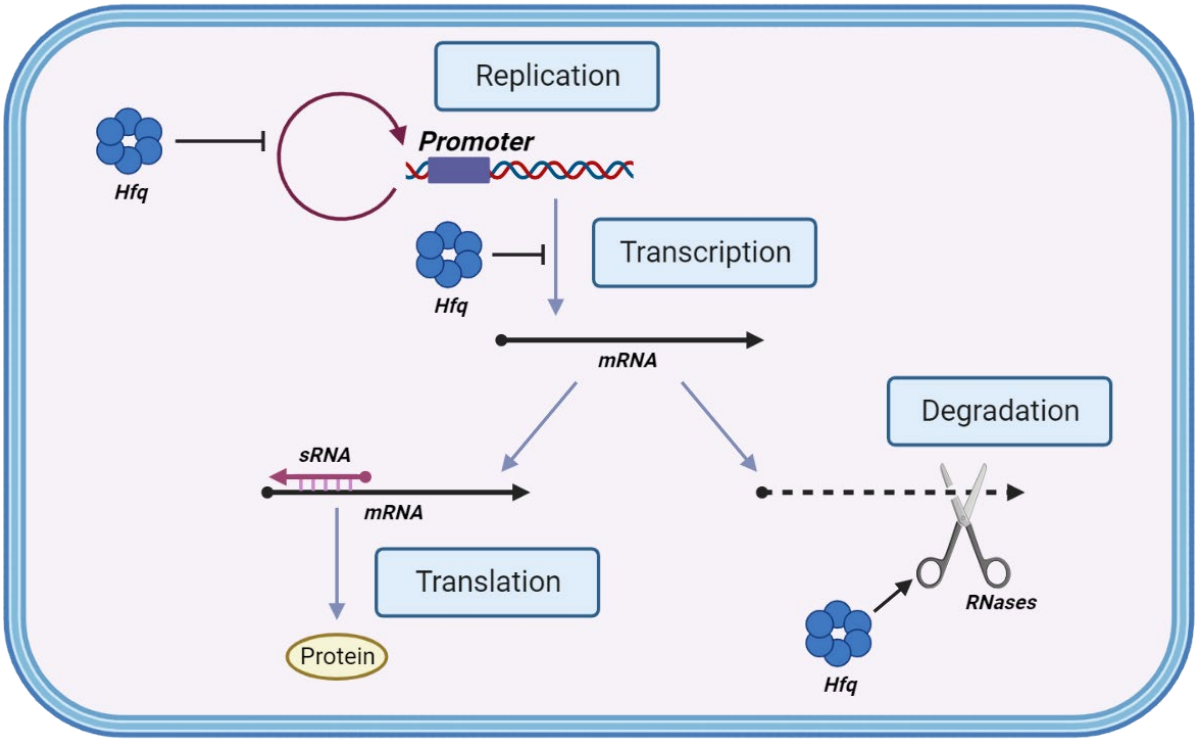

Figure 3. Network of Hfq-dependent regulations. Hfq regulates genetic expression at the transcriptional and post-transcriptional levels in response to several stresses encountered during host infection; Furthermore, it also influences bacterial replication and thus cell division. Positive and negative regulation are indicated by arrows and horizontal bars.

1.3. The Hfq protein

Hfq was first described in 1968 as an *E. coli* host factor required for the bacteriophage Qβ RNA replication (Franze de Fernandez, Eoyang, and August 1968; de Fernandez, Hayward, and August 1972). Later it was shown to be present in about 2/3 of bacterial species with a pleiotropic function (Sun, Zhulin, and Wartell 2002). Deletion or disruption of the *hfq* gene is not lethal for the bacteria (the protein is not essential) but results in many phenotypes (H.-C. T. Tsui, Leung, and Winkler 1994; H. C. Tsui, Feng, and Winkler 1997). Briefly, these phenotypes include decreased growth rate, impairing of bacterial cell ability to respond against environmental changes, loss of virulence, increases its UV sensitivity, more elongated cells... Most of these effects are due to Hfq implication in RNA transactions (see below).

The best characterized role of Hfq in Gram *(-)* bacteria is to play a general role in RNA metabolism. Indeed, Hfq facilitates the pairing of regulatory small non-coding RNA (sRNA) with target messenger RNA (mRNA), usually around the mRNA Ribosome Binding Site (RBS) and/or AUG translation initiation codon (Hwang, Arluison, and Hohng 2011; Kavita, de Mets, and Gottesman 2018; Zhang et al. 2003). This allows a regulation at the post-transcriptional level, usually in a negative way (Storz, Opdyke, and Zhang 2004) (Figure 4). This post-transcriptional modulation of gene expression can affect bacterial adaptation to changing environments.

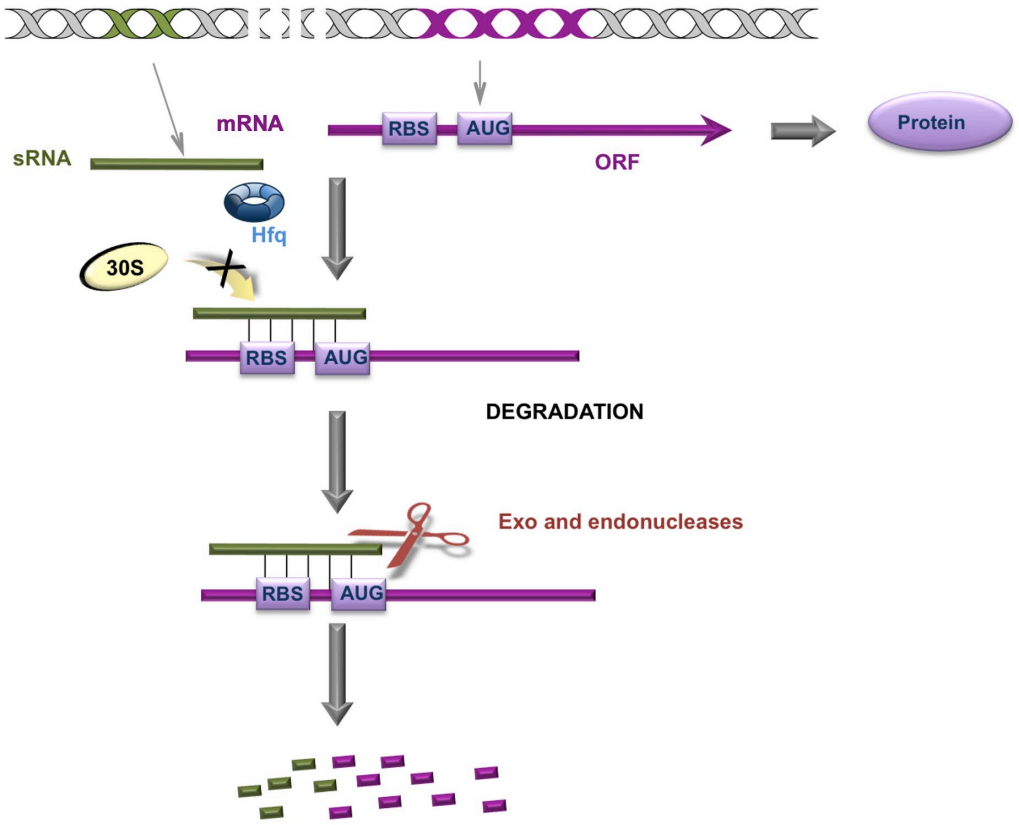

Figure 4. Post-transcriptional regulation by Hfq and sRNA. Hfq facilitates the pairing of sRNA with target mRNA(s), usually around the ribosome binding site (RBS). This allows Hfq to control gene expression at the post-transcriptional level, usually acting as a negative regulator. In addition, Hfq can regulate gene expression by changing RNA stability.

While it is present in both Gram *(+)* and Gram *(-)* bacteria, Hfq role in Gram *(+)* bacteria remains unclear (Bohn, Rigoulay, and Bouloc 2007; Bouloc and Repoila 2016; Rochat et al. 2012). In *Bacillus subtilis*, Hfq is not essential for sRNA-dependent regulation, but it binds and stabilizes a few sRNAs (Christopoulou and Granneman 2022). The importance of

Staphylococcus aureus Hfq is also unclear with conflicting findings; it seems however that the deletion of Hfq had almost no effect in most *S. aureus* strains (Christopoulou and Granneman 2022). Although Hfq is found in many Gram *(+)* bacteria, it does not seem to function in the same way as in Gram *(-)* on gene expression (Christopoulou and Granneman 2022).

In *Escherichia coli*, Hfq is an abundant protein (approximately 50 000 copies per cell), comparable to ribosome concentration (Azam et al. 1999). Usually found in the cytoplasm, the protein may be localized near the internal membrane, where it is associated with other proteins involved in the degradation of RNA (e.g., RNAses) (Diestra et al. 2009; Taghbalout, Yang, and Arluison 2014). It is also associated with chromosomal DNA (Diestra et al. 2009). This structure of the bacterial circular chromosome with proteins in a compacted form is called nucleoid (not to be confused with the nucleus of eukaryotic cells, the nucleoid is not surrounded by a membrane).

1.3.1. Structurally, Hfq belongs to the Sm/LSm family

At the structural level, the *E. coli* Hfq is a protein composed of 6 monomers of 102 amino acid (11.2 kDa) residues, which lacks its N-terminal methionine. It forms a homo-hexamer of 66 kDa with a toroidal shape (Brennan and Link 2007; Schumacher et al. 2002; Vogel and Luisi 2011). Hfq belongs to the family of Sm proteins that possess a particular fold, consisting of a curved five-stranded β sheet, preceded by an α helix (Figure 4).

The proteins of the Sm/Sm-like (LSm) protein family are found across living organisms, from bacteria to eucaryotes including archaea. Sm-like proteins all have in common their toroidal structure composed of six or seven monomers. Though bacterial members of this family are homo-hexamers, eucaryotic and archaeal members are mostly homo- or heteroheptamers (Wilusz and Wilusz 2005; 2013; Youkharibache et al. 2019). This characteristic Sm-fold is found in the N-terminal region of *E. coli* Hfq (~66 amino acid residues) (Sauter, Basquin, and Suck 2003).

Sequence comparisons of Sm/LSm proteins showed that the Sm motif is comprised of two conserved regions called Sm1 and Sm2. Sm1 and Sm2 are separated by a region varying in length. Strands β1, β2 and β3 are part of the Sm1 motif, whereas the Sm2 corresponds to β4 and β5 strands. Note that the Sm2 amino acid sequence conserved in archaeal and eukaryotic proteins does not appear clearly in Hfq. In Sm/LSm, the monomers assemble to form a ring using β4 and β5 strands of two consecutive monomers, giving a long β sheet that is continuous

all along the ring. The homo-hexamer thus forms a very stable structure, resistant to denaturation by temperature (the protein is thermostable) and denaturing agents (such as SDS during SDS-PAGE). This applies to Hfq and thermostability indeed simplifies its purification as the protein can be heated at 95°C for 5 minutes in an extract and remains active and in solution.

1.3.2. Structural description of Hfq N-terminal region (NTR)

The sequence of Hfq shown below (Figure 5) indicates the N-terminal region (NTR) of Hfq where we can recognize the Sm-fold (α-helix in red followed by five β-sheets in blue), followed by its C-terminal region (CTR) in orange, which will be further discussed in 1.3.3).

Figure 5. Protein sequence of Hfq and corresponding secondary structure. With the α-helix in red, β-sheets in blue, and the Hfq-CTR in orange.

As for Sm proteins, the NTR monomer is composed of an α-helix at the N-terminal extremity followed by a five-bent antiparallel β-sheet. The interaction between the β-sheets of each monomer permits their auto-assembly into a homohexameric quaternary structure *via* polar interactions (Brennan and Link 2007; Vogel and Luisi 2011). Precisely one monomer interacts with a second one *via* the assembly of the β4 strand of one monomer with the β5 strand of another monomer, so that β-sheets continue over the entire ring (Figure 6).

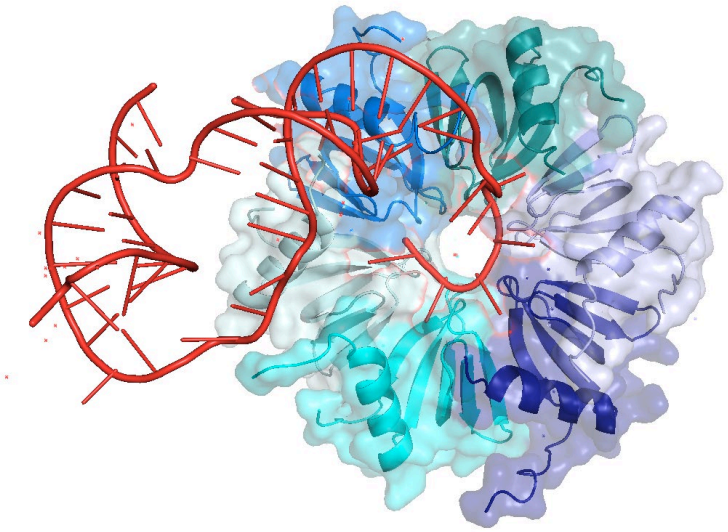

Figure 6. Hfq three-dimensional structure, complexed to an sRNA (PDB ID: 4V2S). In blue, the N-terminal end of Hfq folded into a hexamer, in complex with a non-coding RNA (RydC, in red). This complex then has the ability to bind to a messenger RNA (Dimastrogiovanni et al. 2014).

Functionally, the structure of the Hfq-NTR can be distinguished into two sides, the proximal face which exposes the α-helix and the distal face on the other side. The distal face, the proximal face and the edge of the toroid are all involved in binding of RNA with different specificities (Dimastrogiovanni et al. 2014; Link, Valentin-Hansen, and Brennan 2009; Schumacher et al. 2002). Uridine-containing sequences bind to the proximal face, while A-rich tract binds to the distal face. Usually, sRNAs have a higher affinity for the proximal face while mRNAs preferentially bind the distal face (Dimastrogiovanni et al. 2014). The edge (also called rim) contains basic patches with positively-charged Arginines, which contribute to binding the negatively-charged RNA.

1.3.3. Hfq C-terminal region (CTR)

In addition to its N-terminal region, the *E. coli* protein also possesses a C-terminal region (CTR, about 38 amino acids, see Figure 5).

Structurally, this CTR has been described as intrinsically disordered for twenty years (Vogel and Luisi 2011). Due to its flexibility, the CTR is not present (genetically removed for overexpression) or not observed (present but not resolved) in all the crystal structures obtained for Hfq until now (Dimastrogiovanni et al. 2014; Link, Valentin-Hansen, and Brennan 2009;

Nikulin et al. 2005; Orans et al. 2020; Sauer 2013; Sauter, Basquin, and Suck 2003; Schumacher et al. 2002). In addition, attempts to get a solid-state (ss)NMR structure have been made but were not successful due to the difficulty to label the CTR part that is unstable when expressed alone in the bacteria (Véronique Arluison & Birgit Habenstein, unpublished result). Nevertheless, our group demonstrated in 2005 that it self-assembles as long fibres (Fortas et al. 2015). These fibres were detected both *in vitro* and *in vivo* (Fortas et al. 2015; Partouche et al. 2019; Taghbalout, Yang, and Arluison 2014).

Precisely, the Hfq-CTR forms an amyloid assembly (Fortas et al. 2015), i.e., fibres involving the formation of intermolecular β-sheets (Figure 7), as those found in neurodegenerative pathologies such as Alzheimer or Parkinson (Eisenberg and Sawaya 2017; Fitzpatrick et al. 2013). Such a structure is called a cross-β motif and is formed from the superposition of successive β-sheet layers (Bonar, Cohen, and Skinner 1969; Fitzpatrick et al. 2013). Unlike the amyloids found in the eukaryotic cell, the assembly formed by Hfq allows the proper functioning of the bacterial cell and is referred as a "functional amyloid" (Otzen and Riek 2019). The term functional is used in opposition to "toxic" amyloids, commonly found in neurodegenerative diseases (Chiti and Dobson 2017).

The formation of amyloid fibres formed by Hfq-CTR and its structure was analysed by different biophysical methods (Marcoleta et al. 2019) (Figure 7). First, amyloids are mainly structured as fibres and can therefore be analysed by molecular imaging, electron microscopy (Figure 7D) or atomic force microscopy (AFM, Figure 7C) (Partouche et al. 2018). Amyloids can also be identified using specific dyes such as Thioflavin T (ThT) (Fortas et al. 2015; Partouche et al. 2018). Furthermore, as the fibre consists of an assembly of β-sheets, it is possible to analyse it by circular dichroism or infrared spectroscopies (Malabirade et al. 2018). Circular dichroism (CD) studies the absorption of a molecule, more specifically that of peptide bonds, in the ultraviolet region. An amyloid β-sheet is characterised in CD by a negative spectral band around 218 nm (200 nm if non-amyloid) (Figure 7A) (Turbant, Partouche, et al. 2021). In Fourier Transform Infrared spectroscopy (FTIR), the absorption peak at 1618 cm^{-1} characterises amyloids compared with conventional β-sheets (Figure 7B) (Fortas et al. 2015). Indeed, the latter, less stable, absorb at a greater wavenumber (Ruysschaert and Raussens 2018; Waeytens et al. 2021). These two methods therefore make it possible to monitor the kinetics of fibres formation over time. Note that FTIR spectroscopy and AFM imaging were combined to image isolated Hfq-CTR fibres, using a technique called nanoIR (Waeytens et al. 2021). The β-sheets in the fibres are spaced on average by 4.7 to 4.8 Å and follow each other in large

numbers along an axis (the fibre can be several µm long). This also allows their study by X-ray diffraction (Figure 7E) (Matsuo and Peters 2022). Note that recently a crystal structure of *E. coli* Hfq containing the CTR region has been obtained, that confirms the presence of an amyloid β-sheet stacking (Ben Luisi, Cambridge, personal communication). Nevertheless, the amyloid 3D structure cannot be resolved.

It has been possible to determine that only 11 amino acids out of 101 of Hfq are involved in the formation of the amyloid (see sequence below underlined) (Malabirade, Morgado-Brajones, et al. 2017). Note that the experimental assembly kinetics *in vitro* are very long (several days for bacteria that divide every 20 minutes) (Fortas et al. 2015).

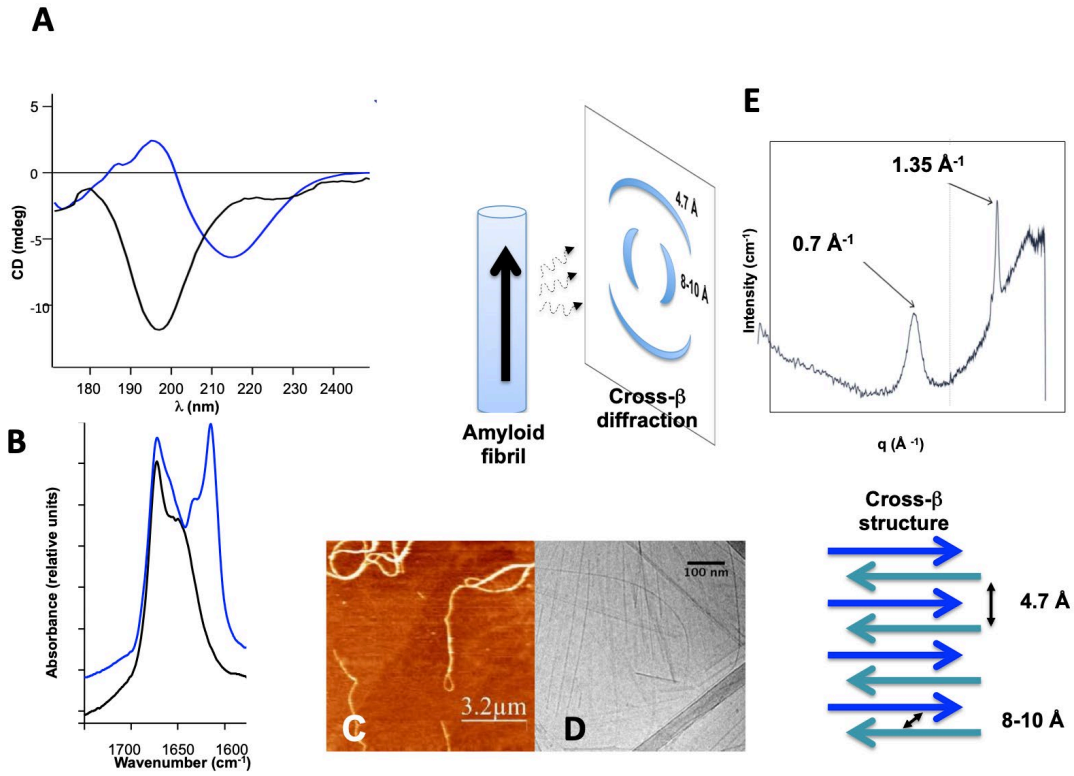

Figure 7. Different methods for the analysis of amyloid structures (adapted from (Marcoleta et al., 2019)). A. Circular Dichroism; B. infrared FTIR spectroscopy. C. AFM; D. TEM, E. X-ray diffraction.

The Hfq-CTR region has a very particular sequence with the presence of Histidine repetition (HH, in yellow), but also with several Aspartates D and Glutamates E (in cyan): SRPVSHHSNNAGGGTSSNYHHGSSAQNTSAQQDSEETE. This is particularly intriguing as Hfq naturally binds to Ni^{2+} ion without the need of His-tag (Milojevic et al. 2013). We thus

suspect that these amino acid residues may be involved in divalent metallic ions binding, which could influence amyloid folding and assembly. This has already been reported for other amyloids (López-Laguna et al. 2020; Srivastava et al. 2019).

It should however be emphasised that Hfq is not a standard amyloid, which generally have neutral charge, are hydrophobic, and have a strong propensity to form β-sheets. According to Biopython (https://biopython.org/docs/1.76/api/Bio.SeqUtils.ProtParam.html), Hfq-CTR has rather a negative charge at pH 7, a hydrophobicity of -1.58 (thus CTR is hydrophilic) and a low propensity to form β-sheets (score of 0.16 on a scale from 0 to 1) (Mehdi Munim, CEA, personal communication).

1.4. Hfq sRNA-based regulations

As explained above, Hfq acts as a regulator of protein expression at the post-transcriptional level through facilitated pairing between non-coding sRNAs with their target mRNA. Hfq uses multiple RNA binding faces (proximal, distal, rim) to perform sRNA/mRNAs annealing and the sRNA and mRNA must bind to different surfaces of Hfq (Kavita, de Mets, and Gottesman 2018).

Usually, this regulation acts negatively and the sRNA:mRNA interaction most often results in stop of the translation and the degradation of the mRNA together with the sRNA. This is mainly achieved by ribonuclease E (RNase E), the major *E. coli* endonuclease (Mackie 2013). This is indeed favoured as RNAse E physically interact with Hfq (Ikeda et al. 2011). The assembly of RNase E and Hfq leads to mRNA-sRNA hybrid rapid degradation. Note that conversely, Hfq protects sRNAs from the attack of ribonucleases when they are not associated with an mRNA (Susan Gottesman 2004).

RNAse E is also located in close proximity of the membrane, together with other RNAses (endo- or exonucleases) in *E. coli* (Khemici et al. 2008; Taghbalout, Yang, and Arluison 2014). The compartmentalization of RNAses in bacteria may control their accessibility to substrates, avoid a premature degradation just after transcription and ensures concerted degradation and synthesis of mRNA (Carpousis et al. 2022). As Hfq interacts with RNAse E, this interaction could explain that a part of Hfq is located close to the inner membrane. Nevertheless, it was later demonstrated that Hfq membrane location seems independent of its interaction with RNAse E (Taghbalout, Yang, and Arluison 2014). Note that

Hfq-RNase E complex coexists in a mutually exclusive manner with the large RNase E-based complex called degradosome (Ait-Bara and Carpousis 2015; Vogel and Luisi 2011).

In some cases, the interaction between sRNA and mRNA may also promote translation by freeing an occupied or inaccessible RBS or AUG. For instance, this is the case for DsrA/*rpoS* regulation (Majdalani et al. 1998; 2004), allowing the expression of σ^S sigma factor that is not expressed during normal condition of growth. In this case, the *rpoS* mRNA RBS is sequestered in a stem. Under stress conditions a small RNA (Dsra) is transcribed. This small RNA anneals to *rpoS* mRNA, changes its conformation and allows σ^S factor translation (Figure 8).

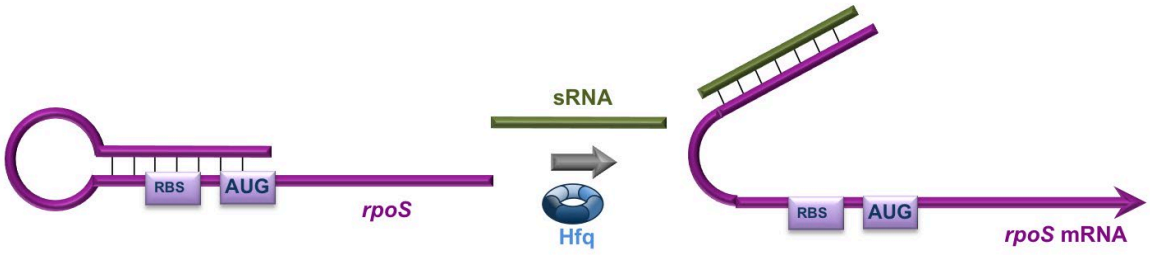

Figure 8. Post-transcriptional regulation of *rpoS* mRNA by Hfq and a sRNA. Hfq facilitates the pairing of sRNA with target mRNA(s); the ribosome binding site (RBS) is no longer sequestered, allowing *rpoS* mRNA translation to produce σ^S sigma factor.

The role of Hfq-CTR in RNA annealing activity of Hfq is controversial: some studies reported that it is dispensable for this function while others found it is needed (Olsen et al. 2010; Sonnleitner et al. 2004; Turbant, Wu, et al. 2021; Večerek et al. 2008). An argument for a probable function for the CTR domain is that in many bacteria it has maintained during evolution, suggesting that the CTR confers benefits to bacterial cells. One current model postulates that the NTR ring promotes annealing in order to anneal a sRNA and its complementary mRNA, forming a duplex that is then released (Santiago-Frangos and Woodson 2018). Recent studies have implicated the acidic part of *E. coli* Hfq-CTR in promoting the release of dsRNA after pairing (Santiago-Frangos et al. 2017)

Finally, it is now known that sRNAs also compete for Hfq binding and that an active cycling is needed, especially as RNAs rarely dissociate on their own (Fender et al. 2010). Indeed, hundreds of sRNAs require Hfq, that is thus limiting even the protein is abundant. The

way sRNAs compete for a Hfq is complex and not completely understood. Hfq-CTR region was proposed to influence the speed of this process (Santiago-Frangos et al. 2016).

1.5. Hfq physically interacts with membranes

As indicated above, a part of Hfq (that we estimate around 50%) is located in close proximity of the inner membrane (Arluison and Taghbalout 2015; Diestra et al. 2009). Different hypotheses have been made to explain this location, such as an interaction with a membrane-localized RNase (McQuail, Carpousis, and Wigneshweraraj 2022; Taghbalout and Rothfield 2008). But Hfq interacts with the membrane by its own. Indeed, our group previously demonstrated that Hfq-CTR physically interacts with *E. coli* inner membrane *in vitro* (Malabirade, Morgado-Brajones, et al. 2017; Turbant et al. 2022), without the need of another partner. As for the basis of this interaction, it has been proposed that a post-translational modification could drive it (Obregon, Hoch, and Sukhodolets 2015). But our group demonstrated that a synthetic peptide, devoid of any post-translational modification, also interacts *in vitro* with the membrane (Malabirade, Morgado-Brajones, et al. 2017). This was however not surprising as other amyloid proteins have been shown to interact with membranes (Drolle et al. 2017).

Observations by cryo-transmission electron microscopy (cryo-TEM) showed that the liposomes in contact with fibrils undergo a deformation, which then results into bursting in a multitude of small vesicles in the vicinity of these fibrils (Figure 9, bottom) (Malabirade, Morgado-Brajones, et al. 2017). This shows that Hfq amyloid fibres induce liposome disruption, an effect already reported for other pathogenic amyloids (Di Scala et al. 2016; Milanesi et al. 2012). The immediate consequence of this interaction is the formation of holes in the membrane. However, the effect of the membrane on the amyloid structure was unknown (Malabirade, Morgado-Brajones, et al. 2017; Turbant et al. 2022). In order to understand this mutual interaction, different biophysical approaches have been used. Our group showed that the CTR of Hfq influences membrane integrity and that, conversely, the membrane affects the amyloid assembly of Hfq. For this goal molecular imaging and in particular AFM with supported membranes have been used (Figure 9, top).

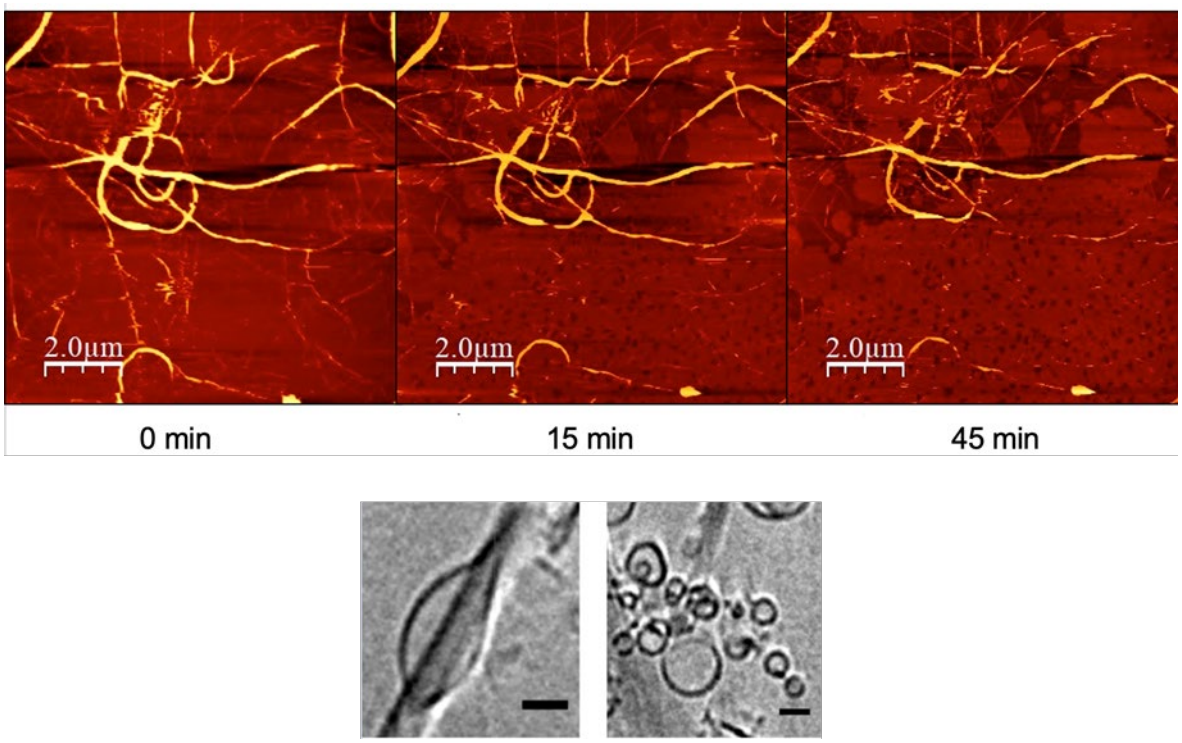

Figure 9. ***AFM (top) and cryo-TEM (bottom) image*** **showing that the bilayer is affected by Hfq CTR amyloid fibrils.** Holes of 1 to 2 nm appear in membrane while fibres dissociate (top) and liposome-fibre contact (bottom) result in liposome burst (scale bar 20 nm) (Malabirade, Jiang, et al. 2017).

Interaction of the CTR fibrils changes the stiffness of lipid bilayers, as previously observed for other amyloids (Bonar, Cohen, and Skinner 1969). In parallel, oriented circular dichroism (OCD) and oriented FTIR spectroscopies indicated that the CTR inserts perpendicular to the membrane when it interacts with it (Turbant et al. 2022) (Figure 10). This results in the formation of holes in the membrane with associated proteins, which could influence the export of bacterial RNAs outside the cell (Malabirade, Morgado-Brajones, et al. 2017). Indeed, Hfq may promote the export of RNA in the periplasm (space between inner and outer membranes). Then outer membrane vesicles (OMVs) may be formed and be secreted together with RNAs. RNA contained in OMVs could allow the bacteria to communicate with other cells using the molecules they contain, which are called “cargoes”.

Recently, our group also observed using the oriented circular dichroism technique, that Hfq-CTR interacts with the outer membrane, but does not appear to be inserted into the OMV membrane. The biological relevance of this analysis is to the possible discovery of a new communication pathway between bacteria or bacteria and host with an important role in pathogenesis and virulence (Kim et al. 2022).

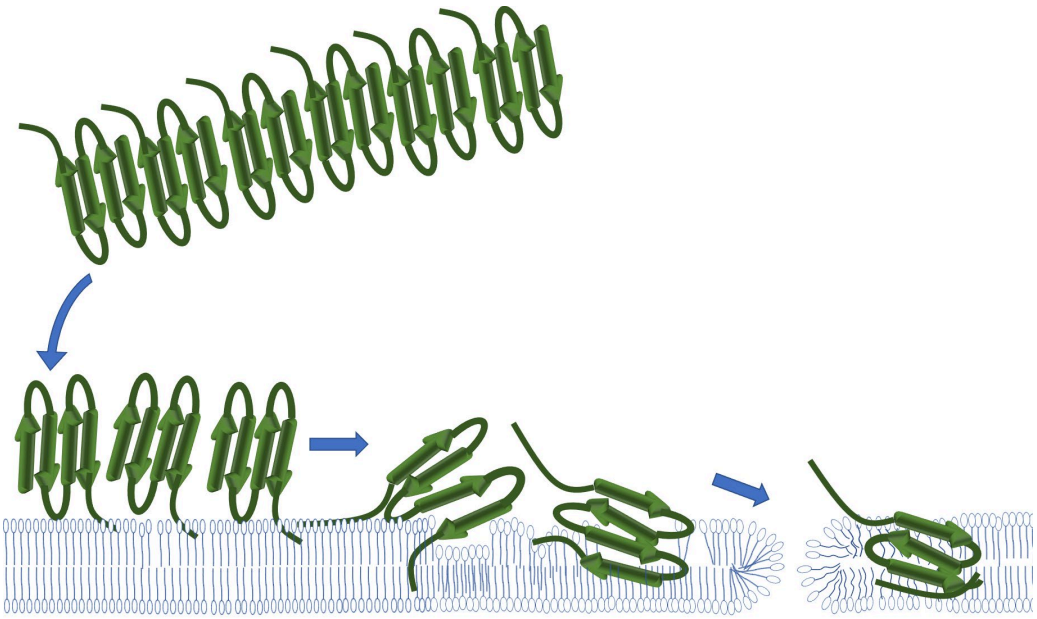

Figure 10. Model of interaction between Hfq CTR amyloid fibrils and bacterial membrane. First, Hfq-CTR fibres interact with the membrane and then depolymerize. Then membrane disruption occurs and holes form. This is accompanied by the peptide insertion perpendicular to the membrane. This occurs with a simultaneous decrease in antiparallel β-sheet content.

1.6. Hfq is a nucleoid associated protein (NAP)

In bacteria, the genome is highly compacted despite the lack of nuclear membrane: the *E. coli* chromosome is 1.5 mm long and must be compacted by a factor 1000 to be stored in a ~1 µm-length cell. This is made possible due to the presence of proteins associated with DNA, which results in a compact structure called the nucleoid. These proteins are called NAP, standing for Nucleoid Associated Proteins (Dorman 2009). Hfq is classed as one of the twelve nucleoid-associated *E. coli* proteins (Azam and Ishihama 1999). Among these NAPs are also found: HU (Histone-like protein from *E. coli* strain U93), H-NS (Heat-stable nucleoid structuring protein), Dps (DNA-binding protein from starved cells), IHF (Integration Host Factor) and Fis (Factor for inversion stimulation protein). For the NAP, several classes of proteins can be distinguished depending on their action on the nucleoid, namely DNA bending (HU, IHF, Fis), DNA stiffening (HU, H-NS), DNA bridging (H-NS, Fis, Hfq), DNA bunching (HU) and DNA wrapping (Fis) (Figure 11) (Verma, Qian, and Adhya 2019).

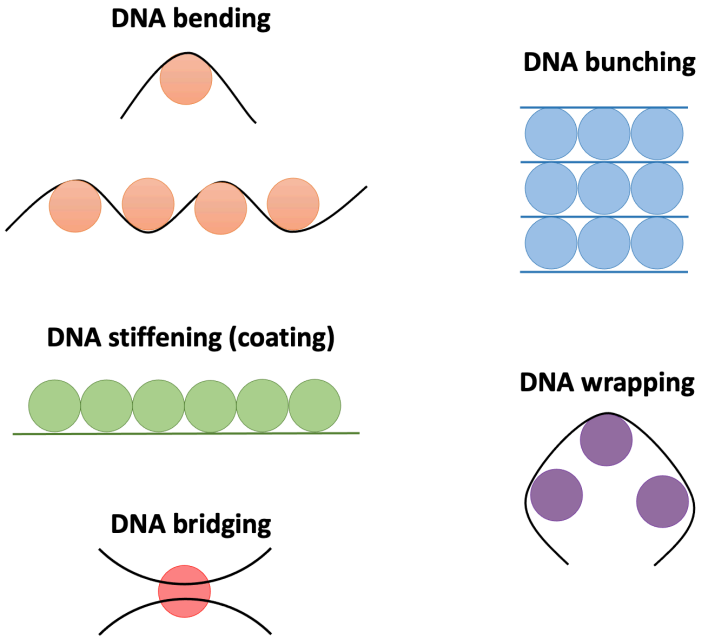

Figure 11. Different types of DNA compaction by NAPs proteins. Adapted from (Verma, Qian, and Adhya 2019).

For DNA binding, we currently know that Hfq uses its proximal face (Orans et al. 2020), even if it had previously been postulated that it may use its distal face (Updegrove et al. 2010). Hfq binds DNA in a non-sequence specific way but has better affinity with curved and A-rich DNAs (Geinguenaud et al. 2011; Updegrove et al. 2010).

Hfq's role in DNA structuring is unclear but it is the third most prevalent protein in the nucleoid during the exponential growth phase (Azam and Ishihama 1999). Moreover, its concentration increases by a factor of two during the stationary phase (Diestra et al. 2009). While other NAPs such as H-NS, HU, Dps or IHF seem to be uniformly distributed in the nucleoid, Hfq seems to have a heterogeneous localization pattern (Azam, Hiraga, and Ishihama 2000). Densely occupied regions have recently been evidenced in the *E. coli* genome and they may contain high concentration of Hfq (Amemiya et al. 2021). As the Hfq average concentration in the nucleoid is about 10-20% of total Hfq (~10-15 µM) (Azam and Ishihama 1999; Diestra et al. 2009), its local concentration could locally reach tens to hundreds of µM.

It must be emphasized that some phenotypic effects due to the lack of Hfq and initially attributed to RNA-based regulation (H.-C. T. Tsui, Leung, and Winkler 1994) may be directly linked to defects in DNA-related processes (Cech et al. 2014; Chen and Gottesman 2017; Gaffke et al. 2021; Haniford and Ellis 2015; Kubiak et al. 2022; Le Derout et al. 2010;

Malabirade et al. 2018; Parekh et al. 2019; H.-C. T. Tsui, Leung, and Winkler 1994). These include DNA supercoiling, more elongated cells, effects on replication efficiency, a change of mutagenesis rate, and a change in transcription.

Recently, our group showed that the NTR is not the only region involved in DNA binding (Orans et al. 2020), and that Hfq CTR also binds to and compacts DNA (Jiang et al. 2015; Malabirade, Jiang, et al. 2017). The high local concentration, in turn, could favour the amyloid self-assembly of Hfq *via* its CTR and contribute to DNA shaping (Milles et al. 2013).

The specific question of Hfq-CTR interaction with DNA is the one we wanted to address *in vitro* and *in cellulo* during my PhD thesis. These points will be discussed below, and imaging technologies used will be described in detail.

1.7. Imaging of Hfq localisation

1.7.1. Fluorescence microcopy

First attempts to image Hfq in the cell have been made using visible light microscopy (VLM). For this goal two main tools were available, either adding a fluorescent protein or detecting endogenous protein (non-fluorescent) by immunolabelling. Both types of labels have advantages and drawbacks.

For the fluorescent tag, a fluorescent protein referred as FP later in the thesis (such as the original Green Fluorescent Protein GFP for *Aequorea victoria*) is added “in phase” with Hfq sequence to make a fusion protein that emits fluorescence in the visible light spectrum. The main advantage of such labelling is that it allows the analysis of Hfq dynamics as cells can be observed without the need of fixation. Nevertheless, even if the chromophore responsible for fluorescence emission is constituted by only 3 amino acids (glycine + tyrosine + serine), the whole protein is needed to observe fluorescence. The consequence is that a large protein of 238 amino acids must be adjoined to Hfq (101 amino acids), which could result in Hfq misfolding and wrong localisation. This is what happened with all FP-tagged proteins constructed previously in the lab, where we observed inclusion bodies. This was the case independently of the FP used (YFP, GFP and RFP have been used) and of the position of the FP (in N-terminus, C-terminus or between N- et C-terminus regions of Hfq). Indeed, we suspect this is even worse in the case of Hfq as it is a hexamer and thus not just only 238 amino acids are added but 6 × 238 amino acids. Note that some analyses described the use of Hfq FP-

labelled protein, but we suspect the foci they observe in most of these studies are due to mis-folding and mis-localisation of a large part of the protein (McQuail, Carpousis, and Wigneshweraraj 2022). Our group also noticed that decreasing growth temperature to 25°C reduces the formation of inclusion bodies.

The second possible way to observe Hfq is immunolabelling. For such an analysis (based on western blot), specific antibodies must be available. This could appear trivial but indeed due to the Flexible/amyloid region of Hfq, having specific antibodies against Hfq is not an easy task and a purification is always needed (Taghbalout, Yang, and Arluison 2014). The advantage of this method is that the endogen protein (without any tag and with normal level of expression) is used, but its main drawback is that it usually requires cell fixation (chemical or cryo). Using such a method was applied to image Hfq localisation. The results obtained confirmed that Hfq is located in the nucleoid (Azam, Hiraga, and Ishihama 2000) and in close proximity to the inner membrane (Arluison and Taghbalout 2015; Fortas et al. 2015; Taghbalout, Yang, and Arluison 2014). Nevertheless, until now only conventional microscopy has been used to localize Hfq. Although it is the fastest, easiest, highest throughput and cheapest method, the major limitation of visible light microscopy (VLM) is the resolution as it is limited to about 200 nm due to diffraction (the resolution is materialized by the minimal distance necessary to resolve two distinct objects).

This limit can, however, be overcome by super-resolution VLM techniques, such as Photo-activated Localization Microscopy (PALM) (Betzig et al. 2006) or Stochastic Optical Reconstruction Microscopy (STORM) (Rust, Bates, and Zhuang 2006). These techniques rely on the stochastic activation of individual fluorophores with photo-activable or photo-switchable properties. The signal of each fluorophore is still subject to the diffraction of light limit. However, because each is activated separately, the centre of mass of the signal can be determined accurately. In the case of Hfq, such analyses have been made but due to the technical difficulty of labelling, in many cases it resulted in the mis-localisation and precipitation of a part of the protein. We however need to indicate that a new labelling method using the red Hfq-mMaple3 tagging (S. Wang et al. 2014) seems promising. It must however be kept in mind as mentioned above and in the publication of Park *et al*, that adding 6 FPs that may complicate analysis of the dynamics of the protein inside the cell (Park et al. 2021).

For this reason, our group intends to develop a smaller tag to allow Hfq imaging without the drawbacks associated with the use of a large FP.

1.7.2. Transmission electron microscopy

The first transmission electron microscope was created and developed by Ernst Ruska and Maxx Knoll in 1931 to circumvent the limitations imposed by light microscopy (Knoll and Ruska 1932). They developed transmission electron microscopy (TEM) based on the use of accelerated electrons instead of photons. TEM exploits the wave-particle duality property of electrons to form images. The theoretical wavelength (λ) of an electron can be determined using the De Broglie relationship, where h is the Planck's constant (6.626×10^{-34} J. Hz^{-1}), m the mass of an electron (3.1×10^{-31} kg), $e = 1.6 \times 10^{-19}$ J (without relativistic adjustments) and V the accelerating voltage, which gives the equation:

$$\lambda = \frac{h}{\sqrt{2meV}} = \frac{12.25 \times 10^{-10}}{\sqrt{V}} \qquad (I.1)$$

Now considering the relativistic effects due to the velocity of electrons reaching about 70% of the speed of light at an accelerating voltage of 200 kV, we obtain the equation:

$$\lambda = \frac{12.25 \times 10^{-10}}{\sqrt{V}} \times \frac{1}{\sqrt{1 + \frac{eV}{2mc^2}}} \qquad (I.2)$$

with c the speed of light equal to ~3.10^8 $m.s^{-1}$. Thus, at an accelerating voltage of 200 kV, electrons have a 2.51 pm wavelength (see Equation I.2). The diffraction limit resolution is given by Abbe can be approximated by:

$$r = \frac{\lambda}{2} \qquad (I.3)$$

This means that the diffraction-limited theoretical attainable resolution with a 200 kV TEM should be approximately of 0.013 Å. Yet the actual achievable resolutions are closer to 1 Å due to the lenses' aberrations of the microscopes.

Image formation

Because electrons are (negatively) charged particles, their trajectory can be influenced by electromagnetic fields. By using copper coils to generate electromagnetic fields, it is possible to deviate their path, acting in the same way as a glass lens would do to photons. This conceptualizes the term of electromagnetic lens which are used to focalize the electron beam in TEM (see Figure 12). Note that unlike in light microscopies, electromagnetic lenses can only be convergent lenses.

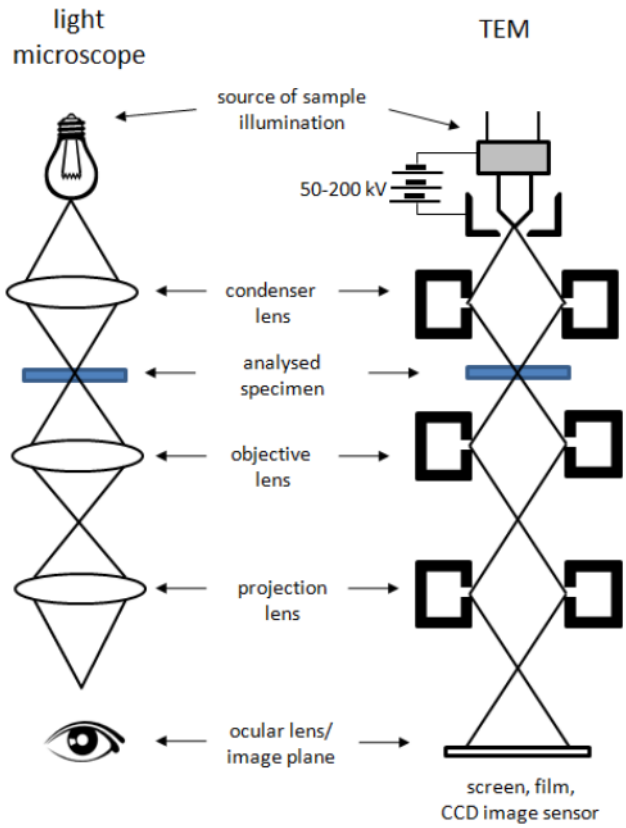

Figure 12. Similarities between a light microscope and a transmission electron microscope from the optical point of view. Schematics of the optic system of a light microscope (Left). Schematics of the optic system of a transmission electron microscope (Right). Adapted from (Płaczek and Kosela 2016).

Contrast formation

Because of the wave-particle duality of electrons inside the microscope, they can be considered both as a group of (negatively) electrically charged particles, and as electromagnetic waves each having a phase and a wavelength.

When passing through the sample, electrons can interact with the sample matter in different ways. Electrons can cross the sample without interaction, in this case they are transmitted and conserve the same energy and phase. If they interact with matter, they can undergo two types of interactions, either elastic or inelastic scattering. Elastic scattering occurs when the electron interacts with an atom's nucleus by passing very close to it. This interaction significantly deviates the electron from its initial trajectory while conserving its energy. On the other hand, inelastic scattering occurs when an electron interacts with the electronic cloud of an atom. In this case, the incident electron can transfer part of its energy to the surrounding

electronic cloud leading to multiple possible outcome such emission of a photon (visible or X-ray), Auger, secondary or back-scattered electron (BSE), and finally inelastic scattering of the incident electron (see Figure 13). This later one is deviated from its original trajectory by only a small angle.

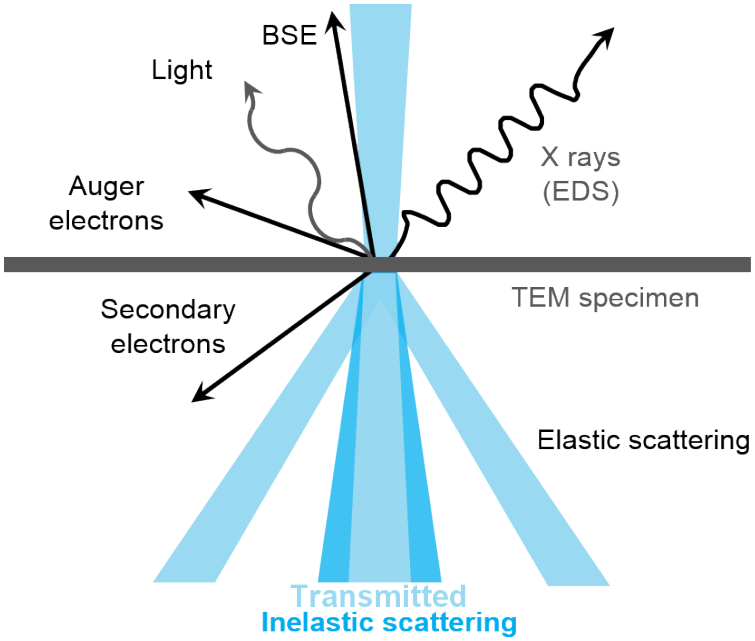

Figure 13. Schematics of the possible outcomes from the interactions of an incident beam of accelerated electrons with a thin specimen. (Adapted from GATAN)

These inelastically scattered electrons can be filtered out by using an in-column or post-column energy filter which acts as a magnetic prism with a small slit at the end thus selecting only zero-loss electrons for example (i.e., transmitted electrons). This permits to increase the signal-to-noise ratio (SNR).

Aberrations

As stated above, the practical attainable resolution of a TEM is limited by imperfections of the electromagnetic lenses. These are divided in three main types which are spherical aberrations (Cs), chromatic aberrations (Cc) and astigmatism. Cs is explained by the fact that electrons are more converged the farther they are from the optical axis. Note that while Cs is the main source of aberrations, recent microscopes can be equipped with Cs correctors.

On the other hand, Cc is caused by the source of electrons which do not generate a purely monochromatic electron beam, meaning that there are small differences in wavelength

between the generated electrons. As Cs, Cc also impacts the convergence of electrons (see Figure 14).

Finally, astigmatism is due to imperfections in the rotational symmetry of the objective lens. It is characterized by a difference of focal length (i.e., magnification) depending on the azimuthal direction. Astigmatism can be corrected inside the microscope.

Other aberrations contribute to the resolution loss, such as the fluctuations in the accelerating voltage, in the electromagnetic lenses, or due to vibrations, parasitic external electromagnetic fields, noise induced by the camera detector (Charged Coupled Device (CCD) or Direct Electron Detector (DED)).

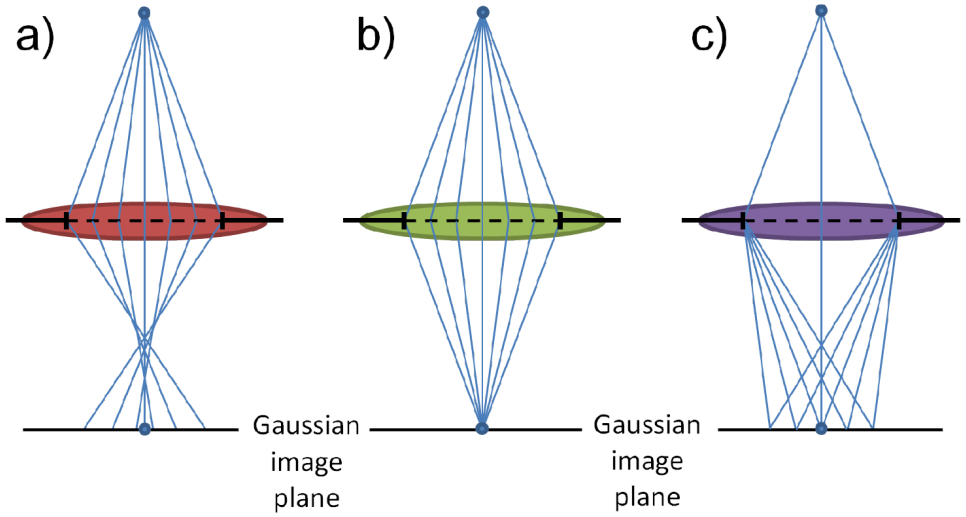

Figure 14. Illustration of lenses aberrations of a point object. a) Spherical aberration. b) Ideal lens. c) Chromatic aberration. (Ke, Bittencourt, and Van Tendeloo 2015)

1.7.3. Tomography

Tomography, in the framework of this thesis, consists of the recovery of the 3D structural information of the sample by acquiring a series of views (2D projections) at incremental tilt-angle.

Then, the set of 2D projections needs to be aligned to a common tilt-axis prior to 3D reconstruction. This is usually done by the addition of gold bead fiducials (i.e., nanoparticles) during sample preparation. These fiducials serve as trackers which can be tracked throughout the tilt-series and are used to align the projections. This alignment process can be done using software such as IMOD etomo (Kremer, Mastronarde, and McIntosh 1996; Mastronarde and

Held 2017) or TomoJ (MessaoudiI et al. 2007; Carlos Oscar Sanchez Sorzano et al. 2009; C.O.S. Sorzano et al. 2020). Note that marker-free alignment is also possible but will not be covered in this thesis.

The three-dimensional (3D) reconstruction of the volume is usually done using either direct methods such as Weighted Back Projection (WBP) or iterative reconstruction methods such as the Algebraic Reconstruction Technique (ART) (Gordon, Bender, and Herman 1970), Simultaneous ART (SART) (Andersen 1984), Simultaneous Iterative Reconstruction Technique (SIRT) (Gilbert 1972). These algorithms are implemented in IMOD, Tomo3D (J. I. Agulleiro and Fernandez 2011; J.-I. Agulleiro and Fernandez 2015), TomoJ, or TomoPy for example (Gürsoy et al. 2014).

However, the main limitations of tomography are that because of the nature of the biological samples and the grids used as support for imaging, there is an increase of the apparent thickness of the sample at high tilt-angle, because of the repeated imaging of the same zone through the acquisition of a tilt-series the radiation dose needs to be sufficiently low to not damage the sample. And finally, because of the grid, the sample cannot be imaged inside the microscope using the full 180° range require to recover the full special information of the volume. This tilt-range that cannot be sampled is causing the missing of part of the information and is commonly called the “missing wedge” (Figure 15A). This missing wedge causes artefacts in the 3D reconstructions and most notably an elongation along the Z-axis.

To counteract this later limitation, it is possible to rotate the grid inside the microscope (with a special device) and acquire a second tilt-series. This will result in the completion of part of the missing wedge, finally resulting in a missing pyramid (Figure 15B).

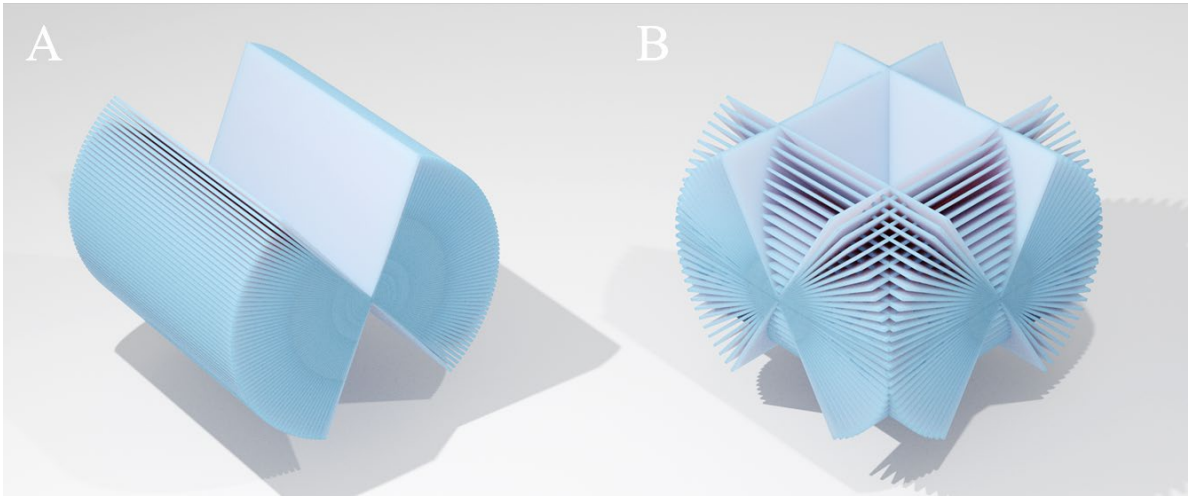

Figure 15. Illustration of the impact of the number of tilt-axes acquisitions on the missing information. A) Single tilt-axis acquisition scheme, leading to two missing wedges along the tilt-axis. B) Dual tilt-axes acquisition scheme, leading to the reduction of the missing wedges into two missing pyramids. Note that in this illustration the total number of tilt-images is constant between A) and B).

1.7.4. Cryo-microscopies & cryo-tomography

Room temperature aqueous samples are generally not suitable for transmission electron microscopy (TEM) or soft X-ray tomography (SXT) because of the high vacuum that these methods require in the microscopes and because of the radiation damage these probes produce. Note that this paradigm may change with some emerging techniques such as “Liquid EM”, Marcello, G. PhD Thesis, University College London, 2021, which are currently under development.

Jacques Dubochet, Joachim Frank and Richard Henderson laid the foundations of cryo-methods and were awarded the Chemistry Nobel prize in 2017 for their pioneering work on high-resolution structure determination of biological macromolecules using cryo-electron microscopy (Nogales 2018).

This method consists in the deposition of the aqueous sample on a cryo-grid (which is usually a copper grid covered with a holey carbon film). The grid is then mounted of a cryo-plunger, the excess of solution is blotted using Whatman filter paper, and the grid finally plunged into liquid ethane at about -174°C (cooled by liquid nitrogen at -196°C). This process results in the vitrification of the sample without ice crystals formation which would otherwise lead to sample deformation and diffraction of the electron beam.

Cryo-preservation methods thus enable the observation of samples in a vitrified close-to-native state without requiring staining or altering the sample with chemical fixation (Lučić, Rigort, and Baumeister 2013). This way it is possible to observe entire bacterial cells using cryo-microscopy techniques such as cryo-transmission electron microscopy (cryo-TEM) or cryo-soft X-ray tomography (cryo-SXT). While cryo-TEM can achieve higher resolutions than cryo-SXT, the former cannot permit the observation of the bacterial nucleoid which is transparent to electrons. On the other hand, using cryo-SXT in the so-called water window energy range (~520 eV) (Figure 16), the oxygen (water) has a very low absorption while carbon-containing (organic) structures have a high absorption (Nave 2018; Wolter 1952). The absorption contrast thus generated makes cryo-SXT a 3D quantitative imaging technique allowing recovery of linear absorption coefficient (LAC) values corresponding to the atomic composition of each voxel. In addition, cryo-SXT enables the observation of thicker samples compared with transmission electron microscopy, at relatively high resolution (30 nm half pitch resolution (Otón et al. 2016)).

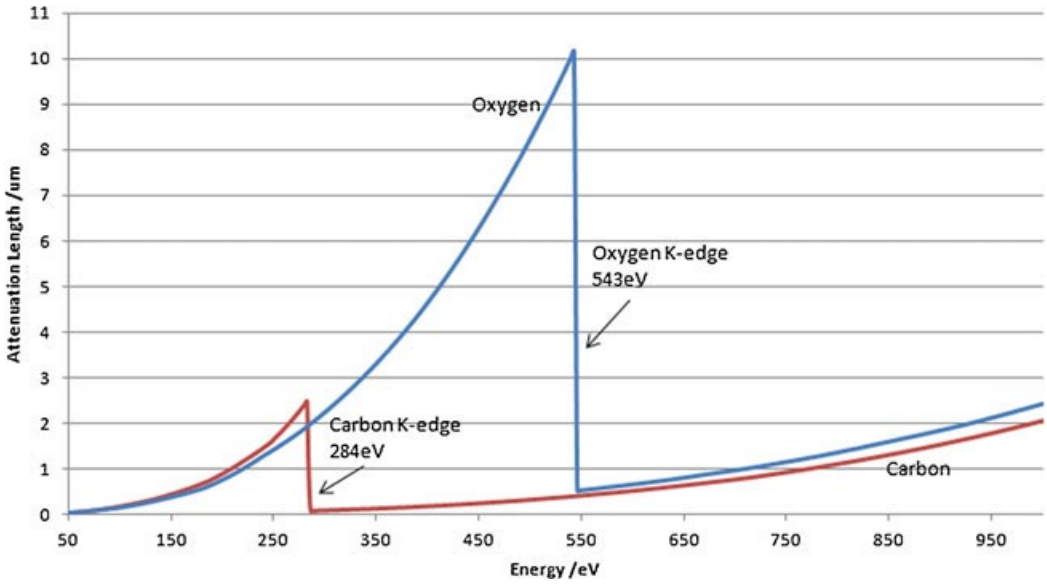

Figure 16. Plot of the water window energy range (284 - 543 eV) showing the k-absorption edges of carbon and oxygen. The plot displays the attenuation length corresponding to the distance (in micrometres) at which the intensity of the beam falls to 1/e (~ 37%) of its value at the surface of the sample (Howells et al. 2007), in function of the incident photons energy (in electron volts). (Carzaniga et al. 2014)

However, the observation of the bacterial nucleoid *in cellulo* remains challenging because of the lack of membrane separating the nucleoid genomic content from the cytoplasm. Because the genomic material is not clearly separated from the rest of the cytoplasm inside the

bacterial cell, it needs to have a high organization for the DNA to be at the same time protected while remaining available for cellular processes such as division and genomic expression.

The details about the use of cryo-TEM methods will be discussed in detail in Chapter II. Nevertheless, it must be indicated here that cryo-TEM main limitation is the thickness of the sample. Indeed, an *E. coli* cell grown in rich media is too thick to be imaged directly. This can however be circumvented by growing the cells in minimal media to make them thinner (Pehau-Arnaudet, Joseleau-Petit, and Arluison 2012) or by using cryo-STEM (see Chapter V). The other drawback of cryo-TEM/SXT is to find an electron-dense tag that does not affect bacteria survival. One such tag has been tested for Hfq, the metallothionein MT tag (Diestra et al. 2009). This tag allowed the localization of Hfq and provided evidence for the first time about its membrane localisation. It also confirmed its presence in the nucleoid. Nevertheless, it must be indicated that this tag use gold ions for labelling that are highly toxic for the cell and result in death if the exposure is too long. This is particularly critical as Hfq expression is highly related to stress and gold toxicity may influence Hfq properties *in vivo*. We thus tried to develop a new tag and this point will be discussed in Chapter VI.

The goal of this dissertation is to have a better understanding of the role of Hfq on DNA compaction *in vivo*, and in general of phenotypes of Hfq-deficient cells using imaging methods to observe Hfq in its native cellular environment.

Chapter II. *In vitro* analysis of the complex between Hfq and double stranded DNA

2.1. Role of Hfq-CTR in DNA compaction

Our group has previously shown that Hfq and in particular Hfq-CTR mediates the bridging of two double stranded DNA molecules (Geinguenaud et al. 2011). Protein-mediated DNA bridging is indeed a ubiquitous mechanism allowing DNA compaction in the cell (Figure 11). Another NAP protein that bridges DNA is for instance H-NS (Dame, Wyman, and Goosen 2000). It has been suggested that first a nucleation on specific sites of DNA occurs, followed by a propagation and spreading on large regions (Lang et al. 2007). We guess the same mechanism applies for Hfq (Vreede and Dame 2012). This may constitute a general mechanism for organizing bacterial DNA (Figure 17). Nevertheless, the way H-NS uses to propagate is different than that of Hfq as it uses a leucine-zipper to self-assemble along the DNA.

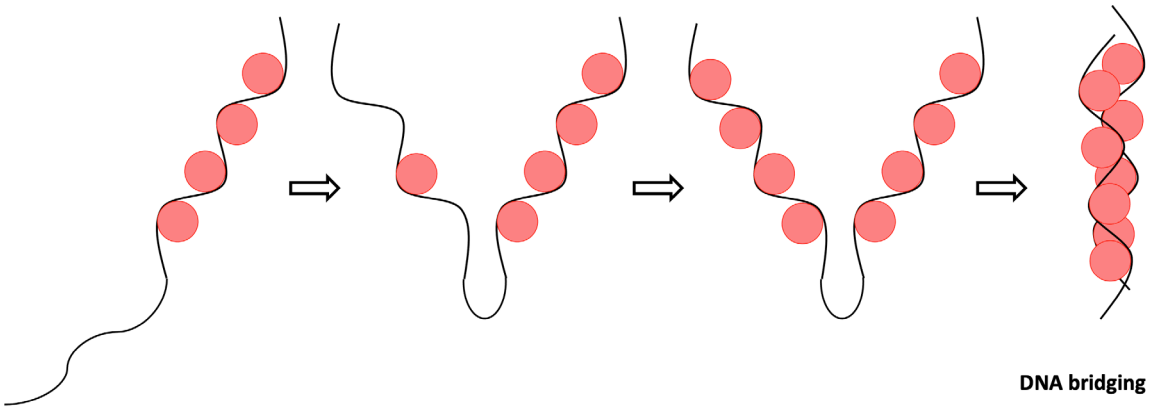

Figure 17. Proposed mechanism of DNA bridging. Initial nucleation of the NAP at high-affinity sites is followed by spreading and condensation of DNA. Spreading and condensation could be concomitant or consecutive. This could induce genetic expression silencing.

Various experimental methodologies have been used to analyse the complex between Hfq or Hfq-CTR with double-stranded DNA (dsDNA). This includes electrophoretic mobility shift assay (EMSA), electron microscopy, atomic force microscopy, circular dichroism (CD) and infrared (FTIR) spectroscopies, isothermal titration calorimetry (ITC), small angle X-ray

and neutrons scattering (SAXS and SANS), and fluorescence microscopy imaging of single DNA molecules confined inside nanofluidic channels (Geinguenaud et al. 2011; Malabirade, Jiang, et al. 2017; Malabirade et al. 2018; Turbant, Hamoui, et al. 2021). All these methods have been used to follow the assembly of the CTR, NTR and full-length of Hfq on DNA and the effect on DNA structure. The results highlight the role of Hfq-CTR in changing the mechanical properties of the double helix and compaction of DNA into a condensed form. The tendency for bridging and compaction of DNA by the CTR is related to its propensity to form an amyloid structure. Furthermore, dsDNA promotes the self-assembly of Hfq-CTR into an amyloid form (Malabirade et al. 2018). All these effects have been analysed *in vitro* and are thus directly due to the assembly of Hfq or its CTR to dsDNA (i.e., not due to an sRNA-based indirect regulation that could happen *in vivo*).

2.2. Indirect effect of Hfq on DNA compaction

In addition to these direct effects, Hfq also regulates genes that may influence DNA structure. Among these genes, we can cite *hns*, encoding the H-NS NAP, and *rpoS* encoding the σ^S sigma factor. This results in an indirect impact on DNA compaction by Hfq during stationary phase as *rpoS* promotes Dps protein production, which compacts DNA during the early stationary phase (Xia et al. 2017). Note that while it inhibits the translation of *hns*, Hfq promotes the translation of *rpoS* mRNA (a *hfq* mutant presents a highly reduced level of expression of σ^S in stationary phase (Muffler, Fischer, and Hengge-Aronis 1996)).

2.3. Hfq-CTR:dsDNA fibres analysis by cryo-electron microscopy

To date, no 3D structure is available for Hfq-CTR complexed with DNA (Vogel and Luisi 2011). Only the structure of a complex between NTR and DNA has been obtained (Orans et al. 2020). This is mainly due to the complexity to get an atomic structure of an amyloid protein, especially when it is a large peptide as for Hfq-CTR (38 amino acid residues here) (Eisenberg and Sawaya 2017). This is even more complicated when the amyloid is complexed to dsDNA. An alternative would be to use the short amyloid region of 11 amino acid residues that forms the amyloid nucleation site (underlined in CTR sequence: RPVSHHSNNAGGGTSSNYHHGS<u>SAQNTSAQQDS</u>EETE), but this peptide does not interact with DNA (Turbant, Hamoui, et al. 2021).

In recent years, cryo-transmission electron microscopy (cryo-TEM) has vastly improved on resolution and observable sample size. With our current analysis we intend to observe the first DNA bridging complex involving an amyloid with numerous perspectives for health, not only for fighting bacterial resistance but also for neurodegenerative diseases. Indeed, other amyloids such as the amyloid-beta peptides related to Alzheimer's disease also bind DNA (Barucker et al. 2014; Camero et al. 2013).

2.4. Cryo-electron microscopy analysis

2.4.1. Principle

Cryo-EM methods have recently become a current approach of choice to analyse amyloid fibres. Indeed, cryo-preservation enables the observation of the sample in a vitrified close-to-native state without requiring staining or altering the sample with chemical fixation (Lučić, Rigort, and Baumeister 2013). Cryo-EM thus implies different steps as *(i)* sample preparation, *(ii)* data acquisition, and *(iii)* single particle analysis (SPA) for structure determination. Central to the analysis is this last step consisting of the processing of raw images to produce 3D structures. Nevertheless, each of these three steps is critical for the final resolution of the determined structures.

2.4.2. *Methods*

The preparation of samples and analysis of amyloid fibres is described in detail in the Publication 1 (Cossa and Trépout 2022).

PUBLICATION 1

"Cryo-Electron Microscopy to Analyze the Structure of Bacterial Amyloids In Vitro."

In *Bacterial Amyloids*, 2538:13–23. Methods in Molecular Biology. Springer US. 2022. https://doi.org/10.1007/978-1-0716-2529-3_2.

Cossa Antoine, and Sylvain Trépout.

Chapter 2

Cryo-electron Microscopy to Analyze the Structure of Bacterial Amyloids In Vitro

Antoine Cossa and Sylvain Trépout

Abstract

Amyloid fibrils are aggregates of proteins or peptides. In humans, they are associated with various pathologies ranging from neurodegenerative diseases such as Alzheimer's and Parkinson's to systemic diseases like type 2 diabetes. In bacteria, amyloids can exert functional roles such as biofilm formation or gene regulation. Up to now, the aggregation mechanism leading to amyloid fibril formation is poorly understood as proteins with different amino acid sequences can fold into similar 3D structures. Understanding the formation of amyloid fibrils constitutes a central challenge for fighting major human health issues such as neurodegenerative diseases and biofilm formation in ports (implantable chambers). Since the dogma linking protein sequence, 3D structure, and function is increasingly disrupted by the growing understanding of the importance of disordered domains in proteins, it is crucial to possess a method capable of building accurate atomic models of amyloids. Aided by the leap forward of cryo-electron microscopy (cryo-EM), which can now routinely achieve sub-nanometric resolutions, it has become the method of choice for studying amyloids. In this chapter, we use the Hfq protein from *Escherichia coli* as an example to present general protocols in cryo-EM to unveil the structure of bacterial amyloids and improve our knowledge of their aggregation mechanism.

Key words Cryo-electron microscopy, Functional amyloid, Hfq, *E. coli*

Abbreviations

CTR	C-terminal region
EM	electron microscopy
RNA	ribonucleic acid

1 Introduction

In the biomedical field, amyloids have been intensively studied because they are infamously responsible for human diseases such as Alzheimer's, Parkinson's, and type 2 diabetes. The literature

Véronique Arluison et al. (eds.), *Bacterial Amyloids: Methods and Protocols*,
Methods in Molecular Biology, vol. 2538, https://doi.org/10.1007/978-1-0716-2529-3_2,

about amyloids associated with neurodegenerative diseases is vast. In bacteriology, some studies have shed light on the potential functional roles of amyloid-like proteins. For example, it has been shown that curli fibrils mediate biofilm formation in *Escherichia coli* [1]. These amyloid-like proteins have also been linked to bacterial pathogenicity and cell adhesion [2, 3], aerial hyphae formation mediated by chaplins in *Streptomyces coelicolor* [4], and responsibility in gene regulation [5]. Moreover, the C-terminal region (CTR) of the small regulatory noncoding RNAs Hfq protein has been demonstrated to form amyloid fibrils in *E. coli* [6].

Amyloids have long been studied to understand how they lead to diseases. Yet, only little is known about the fibril formation mechanism. It is known that amyloids are formed by aggregates of proteins (or peptides) stacked in a cross-β-sheet structure. Nevertheless, independently of the amino acid primary sequence of the protein (or peptide), all amyloids share a similar 3D filamentous structure. Moreover, amyloids contain intrinsically disordered domains [7]. Because of this characteristic, the structure of amyloids cannot be studied using molecular dynamics or sequence-based structure prediction algorithms. In 2015, negative staining electron microscopy (EM) has been used to unveil the structure of RepA-WH1 amyloid filaments at 29 Å resolution [8]. This work is representative of what can be achieved using negative staining EM. At this resolution, the helical pattern of the filament is visible; however, it was not possible to resolve the protein-protein interactions (Fig. 1a). In 2018, X-ray diffraction was used to resolve the structure of the LFKFFK segment from the *S. aureus* PSMα3 virulent peptide at 1.51 Å resolution [9]. Historically, the resolution of X-ray diffraction is superior to that of EM, hence the higher amount of details compared to previous EM works.

At this resolution, the structural information is such that it is possible to visualize which amino acids interact to maintain the cross-β-sheet structure (Fig. 1b). Nevertheless, X-ray diffraction requires that the protein of interest can be crystallized. For amyloids, this crystallization step is rarely possible because of the unfolded domains intrinsic to amyloids. In 2017, cryo-EM has been used to unveil the structure of tau filaments from patient-derived material at 3.4 Å resolution [10]. Using a state-of-the-art model building algorithm, it was possible to accurately fit an 80 amino acid-long atomic model in the cryo-EM maps of the paired helical and the straight filaments (Fig. 1c and d). This 80 amino acid-long sequence corresponds to the core of the tau filament, which structure is highly conserved, as opposed to the loose and unfolded peripheral regions. Several other studies have used high-resolution cryo-EM to unveil the structures of various amyloids [11–14].

Initiated by Dubochet, Frank, and Henderson, cryo-EM enables the study of samples cryo-fixed in a close to native state

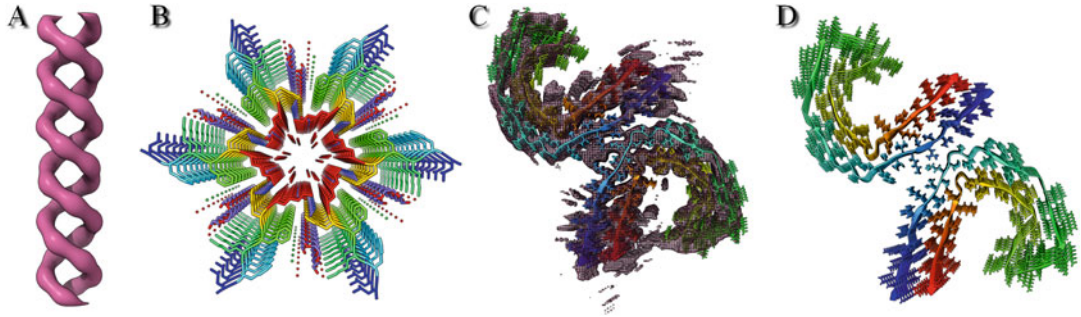

Fig. 1 Examples of amyloid structures with increasing resolution, showing the improvement of the cryo-EM method. (**a**) Negative staining EM map of RepA-WH1 amyloid filaments at 29 Å resolution (EMD-6182) [8]. (**b**) X-ray diffraction structure of the LFKFFK segment from the *S. aureus* PSMα3 virulent peptide at 1.51 Å resolution (PDB 6FHC) [9]. (**c**) Cryo-EM map of tau filaments from patient-derived material at 3.4 Å resolution with atomic model superimposed (EMD-3743 + PDB 5O3T) [10]. (**d**) Atomic model presented in C (PDB 5O3T). EM maps and atomic models have been generated in ChimeraX [24]

[15]. The cryo-EM method has undergone a so-called resolution revolution during the last decade [16]. Advancements in both hardware and software have contributed to a striking improvement of the cryo-EM method, capable now of routinely unveiling protein structures at resolutions better than 3 Å, matching the details provided by X-ray diffraction. These developments allowed for the first time the identification of fibril polymorphisms within the very same sample [13]. Such structural information is crucial to better understand the fibril formation mechanism. This chapter describes the methodology for cryo-EM sample preparation, observation, and characterization of amyloids, using the CTR of the bacterial protein Hfq as a test sample.

2 Materials

In this section, the laboratory setup used for amyloid fiber investigation is described. However, to present more generally the cryo-EM method used for studying amyloid fibers, other commonly used setups are also indicated.

2.1 Amyloid Sample

1. Amyloid proteins can be extracted and purified from tissues or cells [10].
2. Alternatively, shorter amino acid sequences (i.e., amyloid peptides) can be chemically synthesized.

2.2 Cryo-EM Equipment

1. A field emission gun transmission electron microscope with cryo-capabilities, operating at 200 kV (or 300 kV), equipped with an energy filter (in-column or post-column filter), a CCD camera or preferentially a direct electron detector camera (for

sub-nanometric structure determination studies). In our setup, we use a JEOL 2200FS (JEOL Ltd., Tokyo, Japan).

2. A cryo-holder to hold the cryo-grids close to liquid nitrogen temperature (about −175 °C) inside the electron microscope and a cryo-transfer station to mount the cryo-grid on the cryo-holder. In our setup, we use a Gatan 914 cryo-holder (Gatan, Pleasanton, CA, USA).
3. Cryo-EM grids: 200 mesh or 300 mesh R 2/2 or R 1/2 holey carbon copper Quantifoil® grids (Quantifoil Micro Tools). Quantifoil Au grids can also be used in high-resolution studies as they provide more stable support, reducing the electron beam-induced sample drift and improving the collected image quality. Copper grids coated with a continuous carbon layer can also be used during preliminary experiments to verify the sample quality by negative staining.
4. A glow discharger to make cryo-EM grids hydrophilic prior to sample deposition to improve sample adsorption on the grid.
5. A plunge freezer to rapidly cryo-fix the sample in a close to the native state. In our setup, we use a manual plunge freezer. Automatic plunge-freezing systems can also be used if the sample structure is fragile and requires precise humidity and temperature controls.
6. The usual electron microscopy material (precision and anti-capillary tweezers, Whatman filter paper).

2.3 Other Equipment

1. The standard laboratory equipment (micropipettes, Eppendorf tubes, precision balance, parafilm, glass slides, etc.).
2. A powerful workstation preferentially equipped with a CUDA-capable GPU to perform post-acquisition image analysis.

3 Methods

3.1 Amyloid Sample Preparation

The amyloid sample can have various origins. Amyloid proteins can be extracted and purified from tissues or cells. Alternatively, small peptides corresponding to a part of an amyloid protein can be chemically synthesized. In this chapter, we used a 38 amino acids peptide (SRPVSHHSNNAGGGTSSNYHHGSSAQNTSAQQD SEETE) corresponding to the CTR sequence of Hfq. The peptide was chemically synthesized and then reconstituted in deionized ultrapure water at 20 mg/mL [17]. The solution is stored at 4 °C in an Eppendorf tube. The fibril formation can be detected when the aqueous solution becomes viscous. The kinetic of fibril formation depends on several parameters; for more information *see* **Note 1**.

3.2 Grid Preparation

1. Electron microscopy grids are carefully placed with the carbon facing up on a cleaned glass slide using precision tweezers.
2. The glass slide is then placed between the electrodes of the glow-discharge device, the chamber is closed, and the glow-discharge process is started to make the grids hydrophilic (our settings were intensity 25 mA and vacuum 0.39 mBar during 25 s).
3. The electron microscopy grids will stay hydrophilic for about 2 h post glow-discharge if kept in a dry and dust-free environment.

3.3 Sample Screening (Negative Staining)

Negative staining can be used to screen the sample before performing cryo-EM. It is a quick and efficient way to detect the presence of amyloid fibers and to check sample homogeneity. However, negative staining has several limitations and must be used accordingly. For more information, *see* **Note 2**.

1. A 5 μL drop of amyloid solution at 1 mg/mL (i.e., 1/20th dilution of the stock solution) is deposited on the carbon side of the EM grid (e.g., 200 mesh square grid with continuous carbon).
2. After about 1 min of interaction (use longer adsorption times if there is not enough sample on the EM grid after inspection at the electron microscope), the excess of sample is removed by blotting the grid using a Whatman filter paper (a few seconds should suffice to sufficiently dry out the EM grid).
3. Then, heavy atom salts are added to contrast the sample adsorbed on the EM grid. A 5 μL drop of uranyl acetate solution (2% w/w concentration) is deposited on the carbon side of the EM grid. After the 1 min incubation time, the excess of uranyl acetate is blotted out using a Whatman filter paper, and the EM grid is subsequently stored in a dry, dark, dust-free environment until observation at the electron microscope. Since uranyl acetate undergoes decreased availability because of safety matters, other staining solutions have been developed. *See* **Note 3**, for more information.
4. The observation of negatively stained samples is somewhat similar to that of cryo-samples. The reader is then invited to follow the protocol for cryo-sample observation in the next paragraphs.

3.4 Sample Cryo-fixation (Plunge Freezing)

The cryo-fixation method is based on the rapid freezing of a hydrated sample. The cooling rate is such (greater than 10.000 °C/s) that ice crystals cannot form, and the sample is kept close to the native state. The rapid freezing is achieved by quick immersion of the sample in cold liquid ethane (about −175 °C), cooled down by liquid nitrogen (−196 °C). The sample is

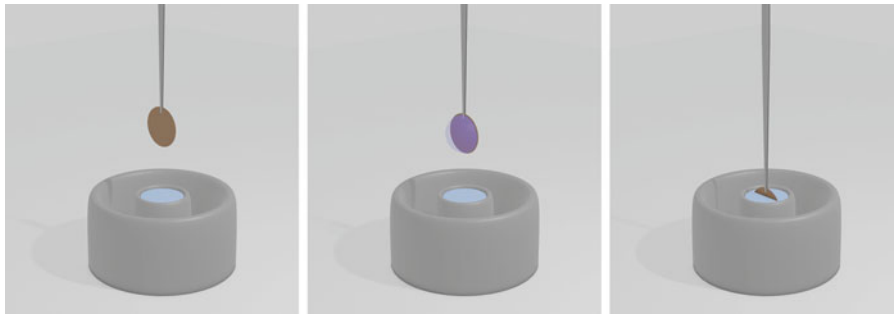

Fig. 2 Schematic of sample cryo-fixation using plunge freezing. From left to right, (i) the cryo-EM grid is mounted on the plunge-freezing device using precision tweezers, (ii) a 5 μL drop of the sample is deposited on the carbon side of cryo-grid, and iii) after blotting the excess of liquid, the cryo-EM grid is subsequently plunged into liquid ethane. Artworks have been generated in Blender (www.blender.org)

contained in thin layers of vitreous ice (about 100–200 nm or less, depending on the sample size), forming in the carbon holes during the plunge-freezing process.

1. The plunge-freezing device is ready for cryo-EM grid preparation.
2. The cryo-EM grid (e.g., Quantifoil R 2/2) is mounted on precision tweezers and attached to the plunge freezer (Fig. 2, left panel). Note that some plunge-freezer devices require specific tweezers.
3. At room temperature, a 5-μL drop of amyloid solution at 1 mg/mL (i.e., 1/20th dilution of the stock solution) is deposited on the carbon side of the cryo-EM grid (Fig. 2, middle panel). In an automated plunge freezer, the temperature can be different from the ambient one if required because of sample fragility.
4. The orientation of the tweezers (drop facing the manipulator or the opposite) is set depending on the blotting direction strategy (front blotting versus back blotting). Note that blotting the drop directly (front blotting) might damage fragile carbon layers, whereas blotting the drop through the grid (back blotting) has the effect of concentrating the sample on the grid.
5. The excess liquid is removed by blotting the grid using a Whatman filter paper, then the plunge-freezer mechanism is subsequently triggered to drop the cryo-EM grid into liquid ethane (Fig. 2, right panel). Blotting conditions (blotting time, blotting direction, humidity, temperature, etc.) might need to be adapted if the sample is not homogeneously distributed at the surface of the cryo-EM grid.

6. After plunge freezing, the grids are inserted in pre-cooled plastic or metallic cryo-boxes stored in liquid nitrogen storage tanks until observation at the electron microscope.

3.5 Cryo-sample Observation at the Electron Microscope

Since amyloid fibrils are thin filaments, they require high magnification settings to be imaged with sufficient details. The electron microscope optics must then be adjusted to enable the highest imaging quality.

1. For side-entry electron microscopes, the cryo-holder must be pumped before introducing the cryo-sample inside the microscope. The double-walled dewar of the cryo-holder must be pumped to achieve a vacuum that will prevent thermal exchanges between the inside of the dewar (which contains the liquid nitrogen) and its exterior.
2. A previously prepared cryo-grid is extracted from the cryo-box and transferred to the cryo-holder using the cryo-transfer station. The transfer station, the cryo-holder, and the precision tweezers must be pre-cooled to prevent any warming of the cryo-grid, ensuring cryo-work conditions. Any warming of the grid would lead to ice devitrification and crystal formation, which would impede the observation of the sample.
3. The cryo-holder is then inserted inside the transmission electron microscope following the conventional insertion procedure.
4. Once the sample is inserted inside the electron microscope, thin ice layers containing isolated amyloid fibrils must be found on the grid. The structure of amyloids will be more easily extracted if fibrils are not aggregated. For this step, magnifications between 1000× and 3000× can be used. Such low magnifications do not introduce electron beam damage to the sample.
5. Individual filaments can be identified on images collected at about 15,000× magnification (Fig. 3a and b). The helical pattern of amyloid filaments can also be distinguished, as shown on images of Hfq CTR amyloid filaments (Fig. 3c, white arrowheads). However, to study the structure of amyloid fibrils at high resolution and allow atomic model building, the magnification must be high enough to reach pixel sizes inferior to 1 Å (depending on the electron microscope and camera setup, this corresponds to magnifications around 100,000× or higher).
6. Other parameters must be set to reach a high resolution. Briefly, the total electron dose per image (or movie) should not exceed 50 $e^{-}/Å^{2}$. Above this value, the sample may suffer important electron beam damages, introducing structure modification of the proteins, which will hamper and deteriorate the

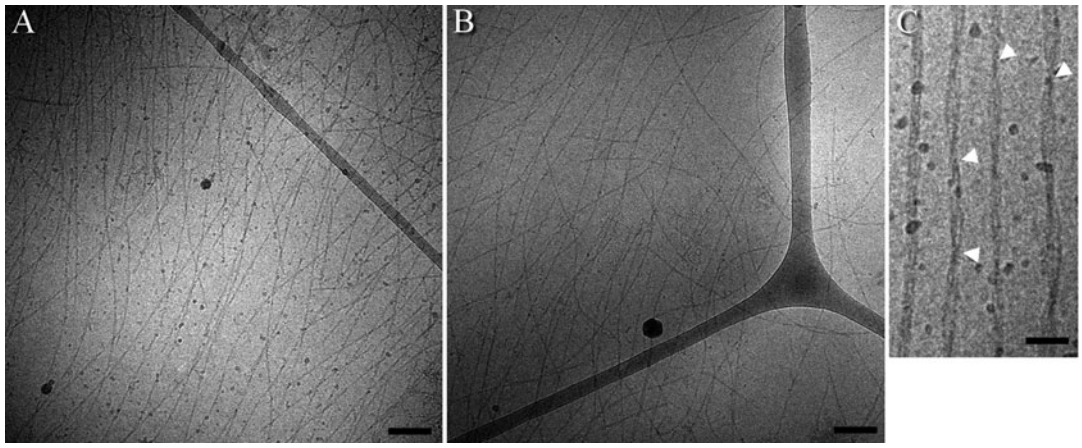

Fig. 3 Observation and characterization of Hfq CTR amyloid filaments. (**a**, **b**) Cryo-images showing the Hfq CTR filaments in vitreous ice. Scale bars represent 150 nm. (**c**) High magnification cryo-EM image showing the helical nature of Hfq CTR filaments. Twists of the filaments are visible (white arrowheads). Scale bar represents 50 nm

final structure resolution. Then, the image series must be collected at several defocus values between 1 and 3 μm to compensate for the information loss at certain frequencies when using a single defocus value. Sharp determination of the defocus value is performed on neighboring carbon areas before collecting the data. For more detailed information about optimum acquisition parameters, refer to the recently published book on single-particle cryo-EM of biological macromolecules [18].

7. After data collection, several image processing steps must be performed before determining an atomic model fitting the cryo-EM map. The detailed description of these processing steps is out of the scope of this chapter. For more information, *see* **Note 4**.

3.6 Correlation with Other Structural Methods

1. Correlative studies have been developed to characterize a sample using two different yet complementary methods. Atomic force microscopy (AFM) is a method used to characterize amyloid fibrils, which was covered by another chapter of this book. Moreover, it has been shown that AFM, AFM-IR, and EM can be correlatively used to study amyloid fibrils' structure and chemical nature [19]. One could also imagine that high-speed AFM [20] and localization AFM [21] could be used to study the dynamics of unfolded peripheral regions of amyloids.
2. As mentioned in the introduction, molecular dynamics often fail to predict the structure of amyloids. Yet, recent deep-learning methods and more particularly AlphaFold [22] and AlphaFold 2 have been developed and could possibly be used in

the future to predict the 3D structure of amyloids [23]. Comparison between cryo-EM-based atomic model and the predicted atomic model would be interesting.

4 Notes

1. The formation of amyloid fibrils starting from monomers depends on several parameters. In the specific case of Hfq CTR, polymerization is performed at 4 °C for a few weeks as the kinetics of fibril formation is slow. Increased temperatures accelerate the process. Also, note that amyloid solution must be present at a relatively high concentration to aggregate and form fibrils. At concentrations below a limit, the pre-formed fibrils may also depolymerize. This property is important and must be taken into account, especially when diluting the sample before cryo-fixation.
2. Negative staining involves sample dehydration and incubation with salt species that can induce aggregation or structural modifications. For these reasons, negative staining cannot be used to determine high-resolution structures. Therefore, high-resolution structural investigations should only be performed in hydrated conditions which are met with cryo-EM. Nevertheless, negative staining can be used to unveil the helical structure of amyloid fibrils (Fig. 1a). Also, note that phosphate buffers must not be used as uranyl ions interact strongly with phosphate ions which could precipitate, leading to grid contamination.
3. Because of safety matters, uranyl acetate can no longer be available from EM product suppliers. Other heavy atom salt solutions can be used, such as gadolinium salts (also known as uranyLess) or solutions based on other lanthanides. These solutions should be tested as they might be a suitable replacement for uranyl acetate.
4. Cryo-EM produces high-resolution images (i.e., down to a few Å), which can be unveiled using successive computation steps. The main steps are briefly described hereinafter. First, the sample drift occurring during image acquisition can be removed to generate still cryo-EM images. Then, the contrast transfer function, which represents how the electron microscope alters the image of a sample (i.e., as compared to a perfect image of the sample), can be modeled and subtracted from the original image. Then, tens or hundreds of thousands of particles (particles represent the object of interest) are extracted from the cryo-EM images, aligned, averaged, and classified. Aligning (translationally and rotationally) and averaging the particles together is performed so that the signal-to-noise

ratio of the average is much higher than that of original particles. Classification is used to discriminate different subpopulations (called classes) among the extracted particles. Classes correspond to different orientations of the particles (a garbage class is also used to discard junk particles). Then, 3D reconstruction is performed using the different classes, generating the cryo-EM map of the protein of interest. Finally, an atomic model is generated and refined to fit the cryo-EM map (Fig. 1c). Detailed information to perform these image processing steps is available in the book on single-particle cryo-EM of biological macromolecules [18].

Acknowledgments

This work was supported by Université Paris-Saclay, CNRS, and CEA. This work is supported by the "ADI 2019" project funded by the IDEX Paris-Saclay, ANR-11-IDEX-0003-02. The authors acknowledge the Multimodal Imaging Centre at Institut Curie for providing access to the electron microscopy facility. The authors are indebted to V. Arluison (University of Paris, France) for many fruitful discussions.

References

1. Chapman MR, Robinson LS, Pinkner JS et al (2002) Role of Escherichia coli curli operons in directing amyloid fiber formation. Science 295: 851–855. https://doi.org/10.1126/science.1067484
2. Gophna U, Oelschlaeger TA, Hacker J, Ron EZ (2002) Role of fibronectin in curli-mediated internalization. FEMS Microbiol Lett 212:55–58. https://doi.org/10.1111/j.1574-6968.2002.tb11244.x
3. Tursi SA, Lee EY, Medeiros NJ et al (2017) Bacterial amyloid curli acts as a carrier for DNA to elicit an autoimmune response via TLR2 and TLR9. PLoS Pathog 13:e1006315. https://doi.org/10.1371/journal.ppat.1006315
4. Claessen D (2003) A novel class of secreted hydrophobic proteins is involved in aerial hyphae formation in Streptomyces coelicolor by forming amyloid-like fibrils. Genes Dev 17: 1714–1726. https://doi.org/10.1101/gad.264303
5. Marcoleta A, Wien F, Arluison V et al (2019) Bacterial amyloids. eLS American Cancer Society, pp 1–9
6. Malabirade A, Morgado-Brajones J, Trépout S et al (2017) Membrane association of the bacterial riboregulator Hfq and functional perspectives. Sci Rep 7:10724. https://doi.org/10.1038/s41598-017-11157-5
7. Dyson HJ, Wright PE (2005) Intrinsically unstructured proteins and their functions. Nat Rev Mol Cell Biol 6:197–208. https://doi.org/10.1038/nrm1589
8. Torreira E, Moreno-del Álamo M, Fuentes-Perez ME et al (2015) Amyloidogenesis of bacterial prionoid RepA-WH1 recapitulates dimer to monomer transitions of RepA in DNA replication initiation. Structure 23:183–189. https://doi.org/10.1016/j.str.2014.11.007
9. Salinas N, Colletier J-P, Moshe A, Landau M (2018) Extreme amyloid polymorphism in Staphylococcus aureus virulent PSMα peptides. Nat Commun 9:3512. https://doi.org/10.1038/s41467-018-05490-0
10. Fitzpatrick AWP, Falcon B, He S et al (2017) Cryo-EM structures of tau filaments from Alzheimer's disease. Nature 547:185–190. https://doi.org/10.1038/nature23002
11. Cao Q, Boyer DR, Sawaya MR et al (2019) Cryo-EM structures of four polymorphic TDP-43 amyloid cores. Nat Struct Mol Biol 26:619–627. https://doi.org/10.1038/s41594-019-0248-4

12. Hervas R, Rau MJ, Park Y et al (2020) Cryo-EM structure of a neuronal functional amyloid implicated in memory persistence in *Drosophila*. Science 367:1230–1234. https://doi.org/10.1126/science.aba3526
13. Röder C, Kupreichyk T, Gremer L et al (2020) Cryo-EM structure of islet amyloid polypeptide fibrils reveals similarities with amyloid-β fibrils. Nat Struct Mol Biol 27:660–667. https://doi.org/10.1038/s41594-020-0442-4
14. Lu J, Cao Q, Hughes MP et al (2020) CryoEM structure of the low-complexity domain of hnRNPA2 and its conversion to pathogenic amyloid. Nat Commun 11:4090. https://doi.org/10.1038/s41467-020-17905-y
15. Nogales E (2018) Profile of Joachim Frank, Richard Henderson, and Jacques Dubochet, 2017 Nobel Laureates in Chemistry. Proc Natl Acad Sci U S A 115:441–444. https://doi.org/10.1073/pnas.1718898114
16. Kühlbrandt W (2014) The resolution revolution. Science 343:1443–1444. https://doi.org/10.1126/science.1251652
17. Fortas E, Piccirilli F, Malabirade A et al (2015) New insight into the structure and function of Hfq C-terminus. Biosci Rep 35:e00190. https://doi.org/10.1042/BSR20140128
18. Glaeser RM, Nogales E, Chiu W (2021) Single-particle Cryo-EM of biological macromolecules. IOP Publishing
19. Partouche D, Mathurin J, Malabirade A et al (2019) Correlative infrared nanospectroscopy and transmission electron microscopy to investigate nanometric amyloid fibrils: prospects and challenges. J Microsc 274:23–31. https://doi.org/10.1111/jmi.12779
20. Ando T, Kodera N, Takai E et al (2001) A high-speed atomic force microscope for studying biological macromolecules. PNAS 98:12468–12472. https://doi.org/10.1073/pnas.211400898
21. Heath GR, Kots E, Robertson JL et al (2021) Localization atomic force microscopy. Nature 594:385–390. https://doi.org/10.1038/s41586-021-03551-x
22. Jumper J, Evans R, Pritzel A et al (2021) Highly accurate protein structure prediction with AlphaFold. Nature 596(7873):583–589. https://doi.org/10.1038/s41586-021-03819-2
23. Pinheiro F, Santos J, Ventura S (2021) AlphaFold and the amyloid landscape. J Mol Biol 433(20):167059. https://doi.org/10.1016/j.jmb.2021.167059
24. Goddard TD, Huang CC, Meng EC et al (2018) UCSF ChimeraX: meeting modern challenges in visualization and analysis. Protein Sci 27:14–25. https://doi.org/10.1002/pro.3235

2.5. Application to the analysis of Hfq-CTR:dsDNA fibres

Sets of double stranded DNA and CTR solutions in water were prepared in our lab. The sequence of the CTR peptide was SRPVSHHSNNAGGGTSSNYHHGSSAQNTSAQQDSEETE (Fortas et al. 2015) while the DNA was a homopolymeric dA:dT sequence (60 base pairs). We determined previously that acidic pH 5 of double-distilled water (ddH2O) is the most suitable to form the complex (Turbant, Hamoui, et al. 2021). The Hfq-CTR:DNA base pair molar ratio used was 1:4, as in previous experiments (El Hamoui et al. 2020; Malabirade et al. 2018). The material was prepared as usual a month before cryo-EM analysis to let it polymerize.

Sample vitrification was first carried out at Institut Curie (Orsay, France). We used copper Quantifoil® coated with holey-carbon film cryo-EM grids. In order for the peptide:DNA complexes to adhere on the grids, these were glow-discharged. We determined the best concentration using the 200 kV JEOL 2200FS transmission electron microscope from Institut Curie. We observed fibres of a few µm-long, as expected. We also observed two sorts of fibres were formed, similar but with different winding (see Figure 18, blue and red arrows).

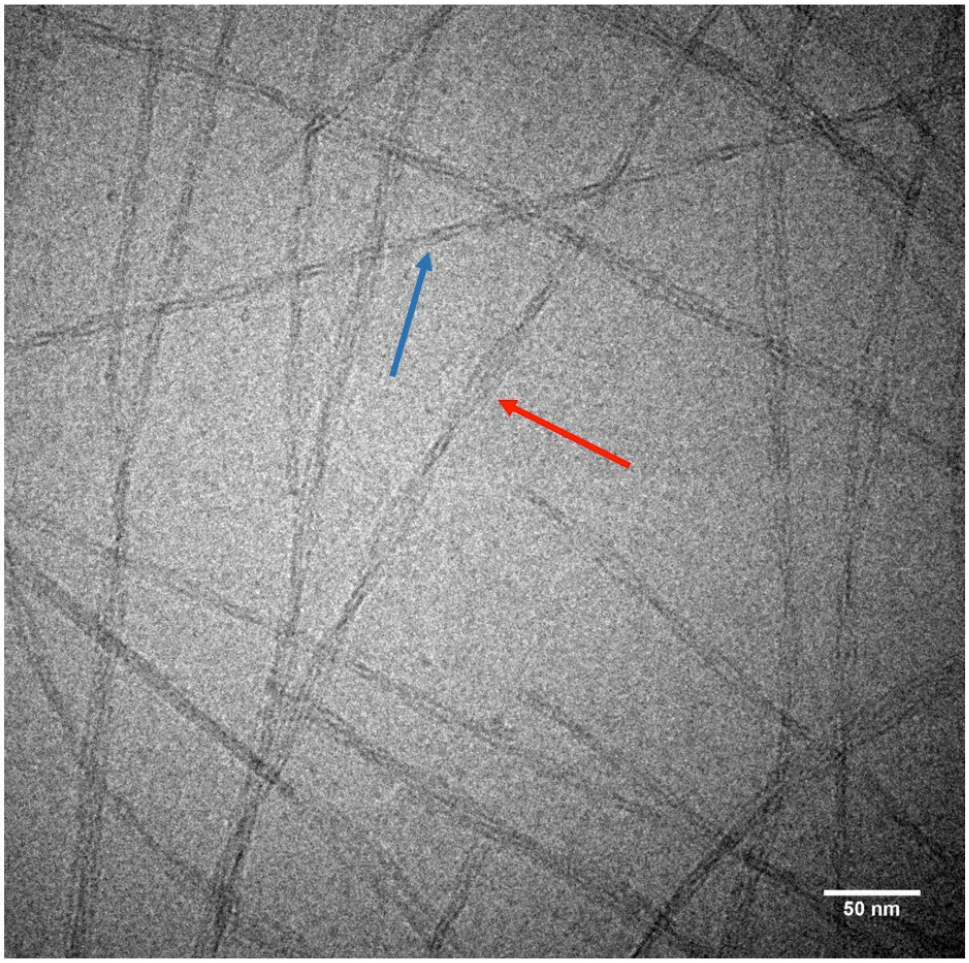

Figure 18. Cryo-transmission electron microscopy observation of the helicoidal structure of Hfq CTR complexed with DNA. Red and blue arrows points to the two observed winding types of fibres.

The resolution of the images we obtained at Institut Curie was not sufficient to perform Single Particle Analysis (SPA) to determine the structure of these fibres. We thus applied for access to the CryoEM facility at the National Centre for Biotechnology (Centro Nacional de Biotecnología of the Spanish National Research Council (CNB-CSIC)) in Madrid (Spain) with an iNEXT-Discovery proposal (PID: 19663) for which I was co-proposer. The proposal was accepted and therefore a set of 1100 movies were acquired on a 200 kV Talos Arctica TEM (Figure 19). We prepared new fresh fibres as described previously.

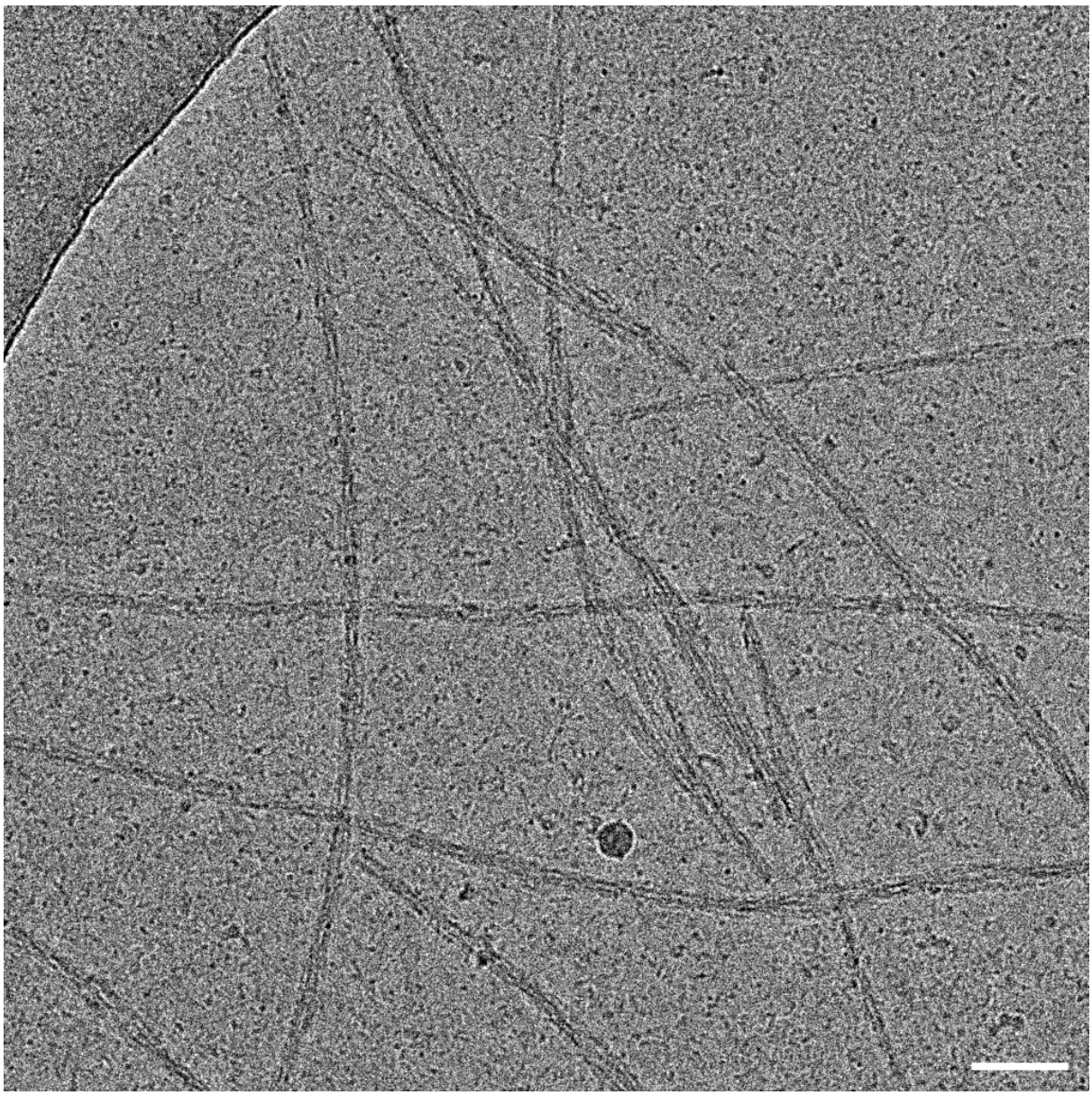

Figure 19. CryoEM image of Hfq-CTR:DNA filaments from the set of 1100 movies acquired through the iNEXT-Discovery proposal (PID: 19663). Original image was binned by a factor 4. Scale bar represents 50 nm.

As in previous experiments, the fibres have a diameter of 5 nm and the pitch of the helix formed is around 100 nm. We similarly observed (at least) two winding types of fibres (see Figure 19). Note that these mean helical parameters have also been confirmed using liquid AFM in collaboration with Dr. M. Velez from the Instituto de Catálisis y Petroleoquímica in Madrid.

Now, the set of movies acquired through the iNEXT project will be subjected to Single Particle Analysis (SPA). This analysis is a part of an Instruct proposal (PID: 23014) that is

currently under evaluation. I intended to participate in this analysis but due to delay we cannot present it in the thesis manuscript. We still hope it can be done by the end of 2022 before the end of my thesis.

The image processing pipeline will proceed as follows: movies acquired by the 200 kV Talos Arctica will be aligned, followed by CTF estimation. One of the most critical parts of the analysis will be the particle picking. Since the dataset will be analysed using Scipion (de la Rosa-Trevín et al. 2016; Strelak et al. 2021; Morena et al. 2022), which contains state-of-the-art picking packages (crYOLO (Wagner et al. 2019)), Topaz (Bepler, Noble, and Berger 2019), Xmipp (de la Rosa-Trevín et al. 2013; C.O.S. Sorzano et al. 2004; Strelak et al. 2021), gautomatch (Kai Zhang, Unpublished),…), several picking strategies will be tested. These include manual picking of fibres (Xmipp), template-based picking (gautomatch) or training deep learning-based pickers (crYOLO, Topaz). The results of the different picking strategies will be combined in a consensus set of coordinates for further evaluation of the dataset quality with 2D classifications. Next, particles will be subjected to 3D classification and 3D refinement in order to identify the two (or more) winding patterns present in the sample, and to reconstruct them at the highest resolution possible. By using SPA, we expect to reveal the DNA-protein topology and to describe the different patterns of winding, complementarily to other approaches.

While SPA will provide useful information on the structure of the fibrils, types of winding and the way that protein and DNA are arranged in space, tomography, and especially subtomogram averaging, will be useful to study the fibrils in their context, either cellular, or in solution. For instance, here we observe that they tend to adopt a specific arrangement as bundles.

Then a second cryoEM acquisition and analysis session, this time for tomography will be made. Though still pending, a proof of was made by acquiring a few tilt-series of the Hfq-CTR:DNA filaments on the 200 kV Talos Arctica. I aligned and reconstructed one of the tilt-series to determine whether the fibres were visible, which is the case as can be seen in Figure 20. However, the fibres are tightly packed, and this might cause reconstruction artefacts which, in turn, could be problematic for tomogram averaging analysis.

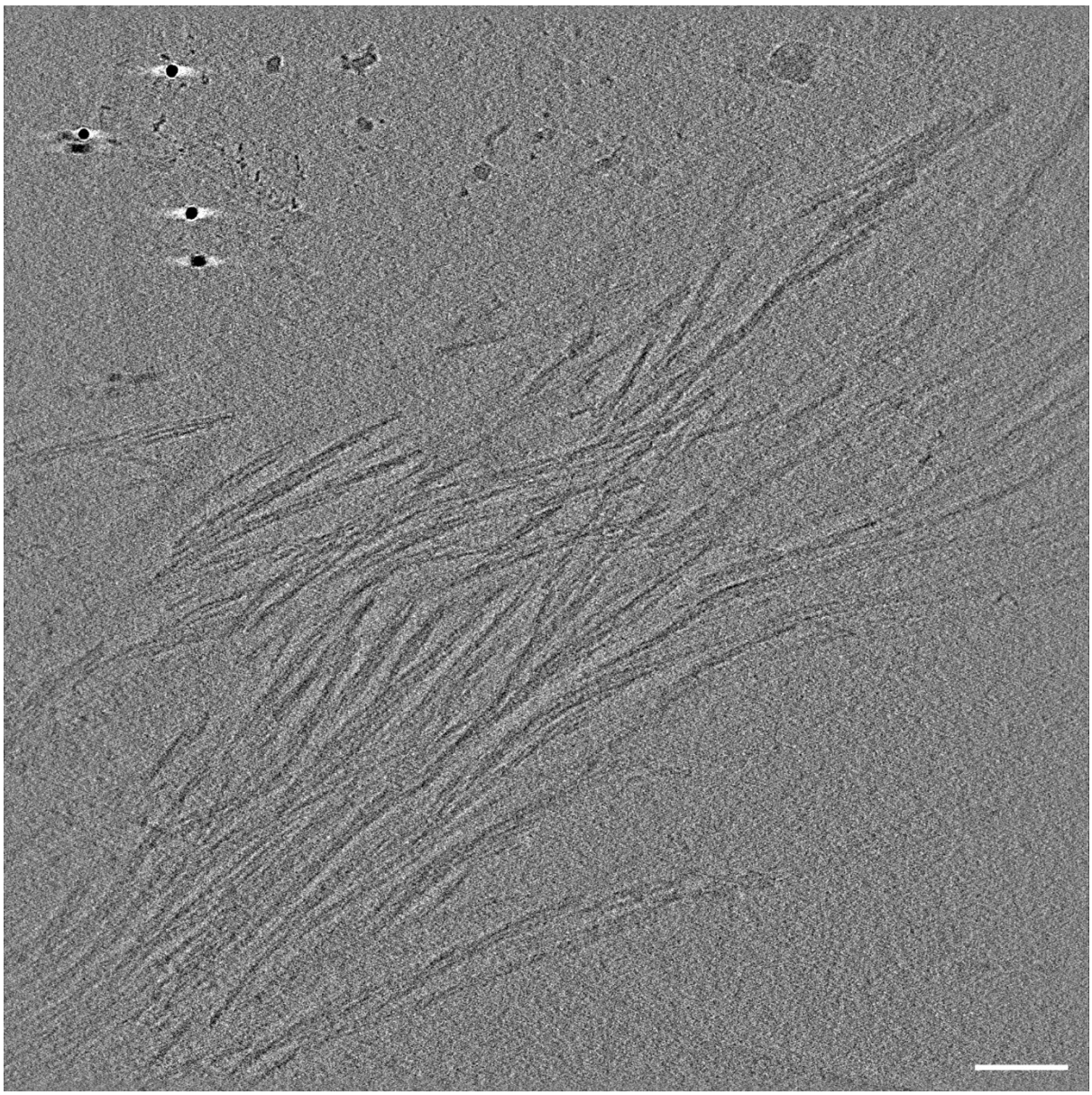

Figure 20. Two-dimensional section of tomographic reconstruction of Hfq amyloid-like fibrils. Scale bar represents 100 nm.

2.6. Conclusion and perspectives of this work

The objective of this part of the work will be to determine at high resolution, the precise structure of the amyloid fibrils and how they interact with DNA. We intend to understand this complex organization and get a 3D structure of the complexes.

Nevertheless, form this analysis alone it will be difficult to discriminate the DNA from the peptide part in the complex by using cryoEM only. For this goal, our group already

performed a Small-Angle Neutron Scattering (SANS) analysis at Institut Laue-Langevin (ILL) in Grenoble (France) on the same complex to determine whether the peptide is located inside the fibre with the DNA wrapping around it, or if oppositely the peptide wraps around DNA. The first case would be comparable to what happens to nucleosomes with histones in eucaryotes (Cutter and Hayes 2015), while the second case would be a new mode of DNA-shaping. For this SANS analysis, the solvent contrast matching method was used (Matsuo et al. 2022). This involves using deuterated or partially deuterated buffers, to allow matching the signal of the DNA conserving the influence of the peptide on it but without observing the peptide (Figure 21A), or oppositely signal from Hfq peptide conserving its influence on the DNA structure without observing the DNA (Figure 21B) (Matsuo et al. 2022). In this way, only the structure of DNA under the influence of the amyloidogenic peptide will be seen or the structure of the amyloidogenic peptide under the influence of the DNA. More precisely, the protein contrast is nullified in ~43% D_2O, whereas the DNA is blanked in ~64% D_2O. The experiment was performed on D22 small-angle neutron scattering diffractometer (https://www.ill.eu/users/instruments/instruments-list/d22/more/d22-manual).

This analysis and the possible models obtained by our collaborators Johan van der Maarel (Singapore) and Tasuhito Matsuo (Japan) are presented on Figure 21. Different models, including hexagonal arrangements are proposed (Figure 21A).

As soon as the first cryoEM 3D complementary maps will be available, SANS and cryoEM models will be confronted. It should thus be possible to accurately determine the Hfq amyloid fibres shape and the conformation of the DNA inside the fibre. This analysis should lead to a new publication in 2023.

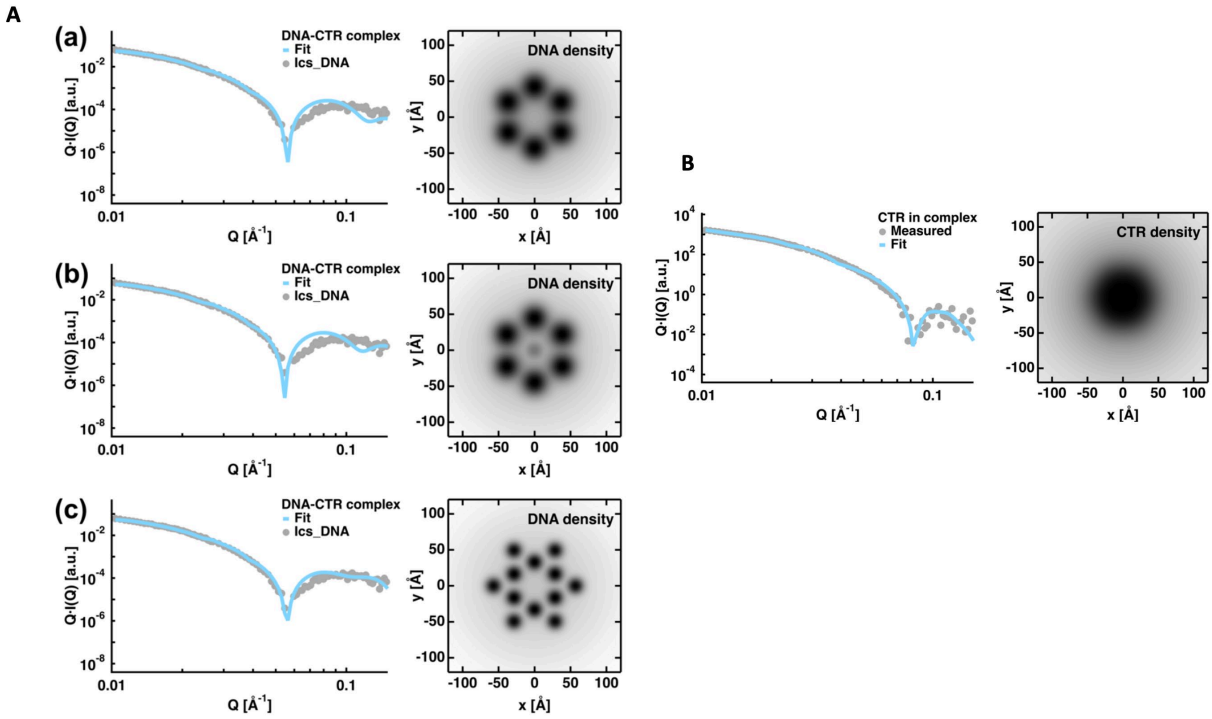

Figure 21. Small-Angle Neutron Scattering (SANS) analysis. A. Comparison of the experimental SANS curves of DNA complexed with CTR with corresponding models. B. Comparison of the experimental SANS curve of Hfq-CTR in the complex. In this analysis only three models are presented in A, all pointing to a peripheric localization of DNA wrapped around the CTR peptide.

Chapter III. Analysis of the complex between Hfq and single stranded DNA

3.1. Importance of single stranded DNA in cells

Although most genetic information is stored in dsDNA, DNA is often unwound into single-stranded DNA (ssDNA). In particular, transient ssDNA regions appear during replication, recombination or repair processes. As ssDNA is more sensitive to degradation and to the formation of secondary structures, which may prevent these biological processes, cells need specialized ssDNA-binding proteins that bind and stabilize ssDNA. We demonstrated that Hfq is one of these proteins.

A combination of experimental methodologies, including spectroscopy and molecular imaging methods, have been used to probe the interactions of Hfq and its amyloid C-terminal region with ssDNA in the Publication 2 (Kubiak et al. 2022). Our analysis revealed that Hfq binds to ssDNA and demonstrated for the first time that it changes the structure of ssDNA, mainly due to its C-terminal amyloid-like domain.

3.2. Methods

In this Publication 2, I mainly participated in two sorts of analyses, Synchrotron Radiation Circular Dichroism (SRCD) spectroscopy at SOLEIL Synchrotron with Frank Wien, and positive staining TEM imaging at Institut Gustave Roussy (IGR) with Eric Le Cam.

3.2.1. Circular dichroism spectroscopy

During my PhD I had the opportunity to participate to Circular Dichroism (CD) spectra acquisition. Concretely, synchrotron radiation CD called SRCD. CD is a technique where the light is polarized, precisely circularly polarised as a right wave and left wave. In the presence of a light absorbing molecule, one of the two polarised lights will be absorbed more than the other (Figure 22). This induces a difference in absorbance called ΔA. This phenomenon

happens in biological molecules because of their chirality. In our case the difference of absorption of light in the ultraviolet (UV) region is due to the presence of the peptide bond for the CTR and bases bound to the ribose (that gives the chirality) for ssDNA. CD can be acquired on a standard circular dichroism spectrophotometer, but the use of synchrotron radiation (SR) has many advantages. First the higher photon flux makes it possible to increase the signal-to-noise ratio and to use less sample materials. But the main advantage of SRCD is to attain regions of higher energies than in a conventional circular dichroism setup, thus reaching wavelengths of 168 nm for aqueous samples. This is particularly important for analysing the amyloid-type structure of Hfq-CTR and that of DNA as both have a significant signal in this region of UV.

Circular dichroism experiments were performed at the DISCO beamline at SOLEIL synchrotron. The samples are deposited between CaF_2 windows, which allows lower UV wavelengths than quartz. A temperature control system is incorporated in the equipment. To analyse these interactions, the experiments were conducted with optical path-length of few µm. Only 2.5 µl is necessary per measurement. We mixed prior to measurement peptide with DNA and also acquire, as controls, peptide and DNA alone.

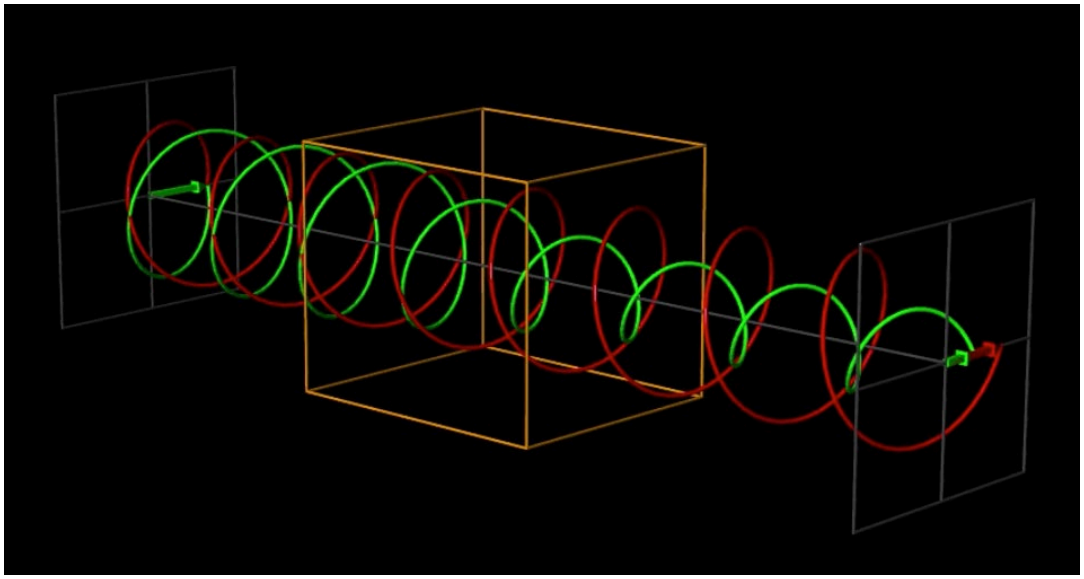

Figure 22. Principle of circular dichroism. A chiral chromophore in an asymmetric medium absorbs right and left circularly polarized light differently. This results in a difference in absorbance $\Delta A = Al - Ar = (\varepsilon l - \varepsilon r)Cl = \Delta\varepsilon Cl$. https://emanim.szialab.org/index.html

3.2.2. Positive staining of DNA for dark-field transmission electron microscopy imaging

In dark-field mode, the unscattered transmitted electron beam (see Figure 13, in 1.7.2) is excluded from the image formation process resulting in an image of white DNA molecules against a dark background. For the off-axis dark-field mode, the high-angle elastic scattered electrons were mainly selected. Eric Le Cam's group has been specifically developing this type of positive staining suitable for DNA and DNA-protein complexes observation.

The difference between positive staining and negative staining is that all but the DNA is stained in the later (Figure 23). Indeed, negative staining consists of making the surface hydrophilic (due to charges). An electron-dense dye, such as Uranyl acetate, is added. The proteins (or other macromolecules) are seen by the differential staining between the background and the sample. The observation is in bright-field mode (all the electrons are selected).

Conversely, positive staining consists of staining only the sample, and then imaging is done in dark-field mode thus obtaining a dark background (certain types of electrons are selected in the microscope adjustment mode (Annular diaphragm, tilted beam, or selection of electrons according to the loss of energy spectrum (EELS)). The white colour here corresponds to an obstacle to the path of the electrons. To make positive colouring, it is necessary to be able to positively functionalize the surface, which is achieved with primary amines (amylamine) with a home-made system at Institut Gustave Roussy lab. The critical point with positive staining is to control the adsorption of the DNA and its spreading on the surface. This allows a precise study of the flexibility variations along the DNA and the measurement of local curvatures.

Experimentally, the first step is the preparation of the carbon-coated grids. Electron microscopy 600 mesh grids are covered with a carbon film (between 2-4 nm thick) which will permit to support and ensure an even spreading of the sample on the grid. If the carbon film is thin enough, it will increase contrast (by enhancing phase shift). To do so, a carbon thread is evaporated on a mica sheet by using a vacuum evaporator at about 100 nm of distance from the source of carbon at a pressure of 10^{-4} Pa. The mica sheet is then plunged into ddH2O to gently separate the carbon film from it. The thin carbon film is then deposited onto the grids and dried in a dust-free environment.

Then, the second step is the activation of the carbon-coated grids. Grids are deposited on a glass slide coated with Parafilm and placed inside the glow discharger. At 1 kPa vacuum, a small amount of amylamine (few µL) is introduced up to about 2 kPa. Ionization is performed over 30 s by switching on the tension (400 V). A faint violet glow discharge light should be visible around the plates. Grids prepared in this manner keep their DNA binding efficiency for about 1 day.

Next, DNA or the complex are then spread on the grid. We deposited 5 µL on the carbon-coated grid for about 1 min. Starting from stock solutions, molecules are diluted in water or with buffer containing various amounts of monovalent (ranging from 50 to 200 mM) and/or divalent (ranging from 2 to 5 mM) ions. The concentration of ions depends on the property of the structures to be observed. Grids are then stained with aqueous 2% (w/v) uranyl acetate, dried with filter paper, and observed in the electron microscope. Images are acquired with a CCD (charge coupled device) camera.

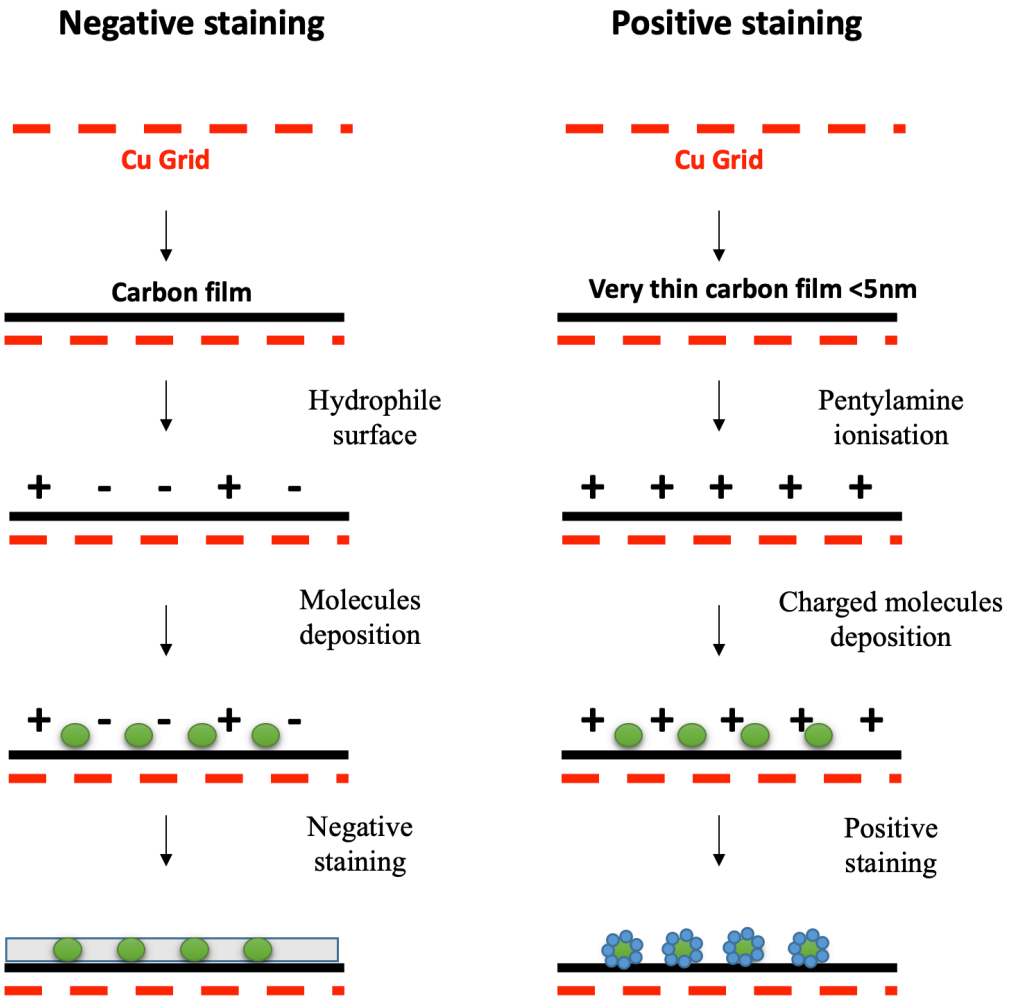

Figure 23. Comparison of positive and negative staining for TEM analysis. The difference between positive and negative staining is that the DNA that is coloured and not the supporting carbon (adapted from (Benureau et al. 2020)).

PUBLICATION 2

"Amyloid-like Hfq Interaction with Single-Stranded DNA: Involvement in Recombination and Replication in *Escherichia Coli*."

In *QRB Discovery*, 3: e15. 2022. https://doi.org/10.1017/qrd.2022.15.

Kubiak Krzysztof, Frank Wien, Indresh Yadav, Nykola C. Jones, Søren Vrønning Hoffmann, Eric Le Cam, Antoine Cossa, Frederic Geinguenaud, Johan R. C. van der Maarel, Grzegorz Węgrzyn, & Véronique Arluison.

QRB Discovery

www.cambridge.org/qrd

Amyloid-like Hfq interaction with single-stranded DNA: involvement in recombination and replication in *Escherichia coli*

Krzysztof Kubiak[1,2], Frank Wien[3], Indresh Yadav[4], Nykola C. Jones[5], Søren Vrønning Hoffmann[5], Eric Le Cam[6], Antoine Cossa[2,7], Frederic Geinguenaud[8], Johan R. C. van der Maarel[4], Grzegorz Węgrzyn[1]* and Véronique Arluison[2,9]*

[1]Department of Molecular Biology, University of Gdansk, Wita Stwosza 59, 80-308 Gdansk, Poland; [2]Laboratoire Léon Brillouin, Université Paris Saclay, CEA, LLB, 91191 Gif-sur-Yvette, France; [3]DISCO Beamline, Synchrotron SOLEIL, 91192 Gif-sur-Yvette, France; [4]Department of Physics, National University of Singapore, Singapore 117542, Singapore; [5]ISA, Department of Physics and Astronomy, Aarhus University, 8000 Aarhus C, Denmark; [6]UMR9019-CNRS, Genome Integrity and Cancer, Université Paris-Saclay, Gustave Roussy, F-94805 Villejuif Cedex, France; [7]Institut Curie, PSL University, Université Paris-Saclay, UMS2016, Inserm US43, Multimodal Imaging Centre, 91400 Orsay, France; [8]Plateforme CNanoMat and Inserm, U1148, Laboratory for Vascular Translational Science, UFR SMBH, Université Paris 13, Sorbonne Paris Cité, F-93017, Bobigny, France and [9]Université Paris Cité, UFR SDV, 75006 Paris, France

Research Article

Cite this article: Kubiak K, Wien F, Yadav I, Jones NC, Vrønning Hoffmann S, Le Cam E, Cossa A, Geinguenaud F, van der Maarel JRC, Węgrzyn G, Arluison V (2022). Amyloid-like Hfq interaction with single-stranded DNA: involvement in recombination and replication in *Escherichia coli*. *QRB Discovery*, **3**: e15, 1–10
https://doi.org/10.1017/qrd.2022.15

Received: 29 June 2022
Revised: 16 August 2022
Accepted: 29 August 2022

Key words:
bacterial amyloid; Hfq; non-coding RNA; nucleoid associated protein; single-stranded DNA-binding protein; Sm-like protein

Author for correspondence:
*Véronique Arluison,
E-mail: veronique.arluison@u-paris.fr;
Grzegorz Węgrzyn,
E-mail: grzegorz.wegrzyn@biol.ug.edu.pl

Abstract

Interactions between proteins and single-stranded DNA (ssDNA) are crucial for many fundamental biological processes, including DNA replication and genetic recombination. Thus, understanding detailed mechanisms of these interactions is necessary to uncover regulatory rules occurring in all living cells. The RNA-binding Hfq is a pleiotropic bacterial regulator that mediates many aspects of nucleic acid metabolism. The protein notably mediates mRNA stability and translation efficiency by using stress-related small regulatory RNA as cofactors. In addition, Hfq helps to compact double-stranded DNA. In this paper, we focused on the action of Hfq on ssDNA. A combination of experimental methodologies, including spectroscopy and molecular imaging, has been used to probe the interactions of Hfq and its amyloid C-terminal region with ssDNA. Our analysis revealed that Hfq binds to ssDNA. Moreover, we demonstrate for the first time that Hfq drastically changes the structure and helical parameters of ssDNA, mainly due to its C-terminal amyloid-like domain. The formation of the nucleoprotein complexes between Hfq and ssDNA unveils important implications for DNA replication and recombination.

Introduction

Although most genetic information is stored in double-stranded (dsDNA), genetic expression requires unwinding of DNA into single-stranded DNA (ssDNA). In particular, transient portions of ssDNA appear during replication, recombination or repair processes; ssDNA is more sensitive to nuclease degradation and this leads to the formation of secondary structures, which prevent previously cited processes. To solve these problems, cells need specialised ssDNA-binding proteins (SSB) that bind and stabilise ssDNA structures. These proteins usually do not share significant sequence similarity, but all contain a DNA-binding oligonucleotide binding OB fold (Su *et al.*, 2014), consisting of a five-stranded curved β sheet capped by a helix. This specific fold is responsible not only for ssDNA binding but also often for the self-assembly of oligomeric SSB. In bacterial cells, ssDNA fragments also play crucial roles, including nucleoid and phage DNA replication or genetic recombination (Molan and Zgur Bertok, 2022).

In bacterial chromosome replication, ssDNA regions are necessary for initiating the process of DNA synthesis by melting the double helix, recruiting the multiprotein machinery and allowing formation of primers and replication forks (Zawilak-Pawlik *et al.*, 2017). Therefore, proteins interacting with ssDNA and/or stabilising such DNA fragments, like the single-stranded DNA-binding protein, play important roles in facilitating the formation of nucleoprotein complexes at replication forks and maintaining their functions (Oakley, 2019). Bacterial proteins that interact with such DNA structures particularly affect replication of viruses, including bacteriophages, having genomes composed of ssDNA (Shulman and Davidson, 2017). The transition from ss to dsDNA is a crucial step in propagation of such viruses; thus, proteins interacting with ssDNA can significantly modulate the viral replication processes.

Another process in which ssDNA is crucial is homologous recombination. DNA strand displacement and replacement occurring in this process require the formation of complexes

including ssDNA and specific proteins (Piazza and Heyer, 2019), and the influence of ssDNA-interacting proteins may be important in modulating recombination efficiency. The function of the bacteriophage λRed-recombination system may serve as an example of such an ssDNA-dependent process (Sharan *et al.,* 2009). In summary, proteins interacting with ssDNA may influence various biological processes, and thus, one should consider that any ssDNA-binding protein might modulate chromosomal and viral replication, as well as genetic recombination.

In this work, we focused our attention on the ssDNA-binding property of the *Escherichia coli* Hfq protein. Hfq is an abundant protein that flexibly binds nucleic acids (NA) (Rajkowitsch and Schroeder, 2007; Vogel and Luisi, 2011). Structurally, the amino-terminal region of Hfq (NTR, 65 residues) shares homologies with the Sm family of protein (Wilusz and Wilusz, 2013) adopting the OB-like fold. Hfq-NTR is comprised of five β-strands and another Sm-proteins assembles into a cyclic oligomer to form the functional unit (Brennan and Link, 2007). Although the mechanism by which Hfq binds NA is not completely clear, it is now established that its NTR binds RNA and DNA. Uridine-rich RNA is bound to one face of the torus called the proximal face, while the A-rich sequences bind to the opposite distal face; dsDNA is also bound on the proximal face of the ring (Supplementary Fig. S1) (Link *et al.,* 2009; Orans *et al.,* 2020).

In addition to the well-characterised Sm domain, the Hfq protein also possesses a C-terminal region (CTR, 40 residues) located at the periphery of the torus (Arluison *et al.,* 2004). Although no atomic 3D structure is known for the CTR, it has been shown to self-assemble into an amyloid structure (Fortas *et al.,* 2015). Recently, it has been suggested that the CTR collaborates with the different RNA binding faces of Hfq, with important outcomes for some RNAs (Kavita *et al.,* 2022).

Functionally, Hfq controls a large number of bacterial functions. Among them, most are related to RNAs. Hfq was first identified as a host factor for a RNA bacteriophage but later found to play a general role in RNA metabolism (Vogel and Luisi, 2011). In particular, it facilitates the pairing of small non-coding RNA (sRNA) with target mRNA, allowing gene regulation at the post-transcriptional level. Indeed, Hfq allows a tight and fast regulation of gene expression and triggers stress-relief pathways (Gottesman, 2019).

Interestingly, Hfq also binds to DNA (Cech *et al.,* 2016) and some of the phenotypic effects appearing due to the lack of Hfq may be linked to defects in DNA-related processes. Hfq binds both linear and circular dsDNA (Takada *et al.,* 1997) and a significant amount of the protein is found in the nucleoid (~20%) (Diestra *et al.,* 2009). Hfq binding results in the condensation of DNA through protein–protein interactions. This activity, consisting of the mediation of NA interactions and referred to as bridging, is observed for other nucleoid-associated proteins (NAPs) to form loops (Rajkowitsch and Schroeder, 2007; Wiggins *et al.,* 2009).

The compaction of DNA by Hfq *in vitro* is mainly due to its CTR (Malabirade *et al.,* 2017a). Thus, Hfq probably plays a critical role in the architecture of the chromosome, even if this has not been established formally. If Hfq does not affect DNA supercoiling and transcription directly (Malabirade *et al.,* 2018), it possibly regulates them indirectly, for instance by regulating the expression of a transcriptional regulator (Majdalani *et al.,* 1998).

The work reported here further explores a newly discovered property of Hfq, its ability to bind ssDNA and to drastically change ssDNA structure by promoting its alignment. Effects of Hfq on DNA transactions in which ssDNA regions are crucial have been assessed.

Methods

Details of methods can be found online as Supplementary Material.

Protein expression and purification

Wild-type (WT) and truncated Hfq forms of *E. coli* Hfq were purified as described previously (Taghbalout *et al.,* 2014; Malabirade *et al.,* 2017b). CTR peptide was chemically synthesised. This part of the protein cannot be purified from bacteria as it is unstable when translated alone (Taghbalout *et al.,* 2014). We determined that the pH ~ 5 used was the most appropriate to form the complex with DNA. Although pH 5 seems to be far from physiological conditions, it is still relevant as Gram-negative bacteria can acidify their cytosol when adapting to the vacuoles of the host macrophage, and many virulent genes belong to the Hfq regulon in these bacterial species (Kenney, 2019).

Fluorescence anisotropy measurements

Fluorescence anisotropy measurements were collected as described previously (Geinguenaud *et al.,* 2011).

Optical microscopy of ssDNA-Hfq/CTR/NTR complexes

DNA in the single-stranded form was prepared by alkali-induced denaturation of double-stranded λ-DNA (Basak *et al.,* 2019). Then, Hfq (29.8 μM) was added to the solution with concentration of one hexamer-Hfq per 200 bases. A similar procedure was used to make the ssDNA with Hfq-CTR and Hfq-NTR. However, the molar concentration of CTR used was six times higher than Hfq, that is, 6 CTR for 200 bases of DNA. For fluorescence imaging, 1 h before imaging, ssDNA was stained with YOYO-1 at a concentration of one YOYO-1 dye per four bases.

Synchrotron radiation circular and linear dichroism

Complex between dA_{59} and Hfq-CTR was prepared as described previously (El Hamoui *et al.,* 2020). Synchrotron radiation circular dichroism (SRCD) measurements were carried out at DISCO/SOLEIL Synchrotron (proposal 20200007). Samples were loaded into a CaF_2 circular cell (24 μm path length). Due to the origin of absorption, spectra of mixed samples could not be standardised to Δε and spectra are presented in mdeg maintaining the same molar ratios for all presented samples. Synchrotron radiation linear dichroism (SRLD) measurements were carried out in the same cell by collecting triplicates every 90° from 0 to 270°. For the data acquisition, the modulator phase was set to λ× 0.608 doubling the lock-in amplifier frequency in order to measure only LD absorption.

Couette flow SRLD

Couette flow SRLD measurements were performed at the AU-CD beamline on the ASTRID2 Synchrotron (proposal ISA-21-102), as detailed in Wien *et al.* (2019). Due to the much larger path length of the Couette flow cell used for SRLD measurements (0.5 mm) compared to the path length used for SRCD measurements

https://doi.org/10.1017/qrd.2022.15 Published online by Cambridge University Press

(0.024 mm), the complex between CTR and the dA_{59} had a very strong LD signal under flow conditions; the samples were diluted (1/36) compared to the concentrations used for SRCD.

Fourier transform infrared spectroscopy

For Fourier transform infrared (FTIR) analysis, the same solutions used for SRCD analysis were lyophilised and re-dissolved in D_2O (5 µL). FTIR measurements were performed as detailed in Geinguenaud *et al.* (2011).

Transmission electron microscopy imaging

3.65 nM circular ssDNA molecules extracted from ΦX174 virions was incubated with 100 nM CTR in Tris–HCl 10 mM pH 7.5 EDTA 1 mM for 10 min at 20 °C. 5 µl was then deposited onto positively functionalised grids covered with a thin carbon film (Beloin *et al.,* 2003). Grids were washed with aqueous 2% (w/v) uranyl acetate, dried and observed in annular darkfield mode using a Zeiss 902 EM. Veletta CCD camera is controlled by iTEM software (Olympus Soft Imaging).

E. coli strains and bacteriophages

E. coli WT strain MG1655 (Jensen, 1993) was used as the *hfq*$^+$ positive control. Its Δ*hfq* and ΔCTR derivatives were constructed as described in Gaffke *et al.* (2021). Quantification of Hfq and its CTR-truncated form was by Western blotting and confirmed by dot blotting. For propagation of bacteriophage M13, *hfq*$^+$, Δ*hfq* and ΔCTR derivatives of *E. coli* strain Hfr3000 (Bachmann, 1972) were constructed by P1 transduction. Bacteriophages M13 (Salivar *et al.,* 1964), λ*cI857S7*(am) (Goldberg and Howe, 1969), called λ*S*(am) in this work, and λ*b519imm21susP* (Wegrzyn *et al.,* 1995), called λ*P* (am) in this work, were used. *E. coli* strain TAP90 (Patterson and Dean, 1987) was used for propagation and titration of phages λ*cI857S7*(am) and λ*b519imm21susP*.

Bacteriophage M13 development and efficiency of phage λ recombination

Development of phage M13 phage and λ recombination efficiency were tested according to the previously described method (Mosberg *et al.,* 2010).

Results

Hfq binds, coats and spreads ssDNA

The potential of Hfq to bind to ssDNA was investigated. We chose $(dA)_n$ sequences because Hfq has the highest affinity for A-rich sequences (Folichon *et al.,* 2003; Geinguenaud *et al.,* 2011). Indeed, A-tracts are over-represented and distributed throughout the *E. coli* genome in phased A-repetitions (~ 12 nucleotides), organised in approximately 100 nucleotides-long clusters (Tolstorukov *et al.,* 2005). Titrations of dA_7, dA_{20} and dA_{59} with Hfq gave K_d values of 3.5 ± 0.2 µM, 183 ± 8 nM and 166 ± 16 nM, respectively (Supplementary Fig. S2). A weaker affinity was measured for the CTR and dA_{59}, about 4.2 ± 0.3 µM, thus suggesting that Hfq can bind dA_{59} using both its NTR and CTR regions, as previously observed for longer dsDNA (Jiang *et al.,* 2015).

The coating of ssDNA by Hfq and its truncated forms was then tested. For this purpose, different approaches have been used. First DNA in its single-stranded form was prepared by alkali-induced denaturation of λ dsDNA. The ssDNA molecules were subsequently complexed with the protein following a buffer exchange according to the method previously reported (Basak *et al.,* 2019). Prior to imaging using fluorescence microscopy, the complexes were stained with YOYO-1 dye. The fluorescence intensity is relatively weak, because for ssDNA the dye is side-bound and cannot intercalate. Two different types of experiments have been done: stretched on a surface combed and confined in a nanochannel. First, the coated molecules were analysed on a flat surface (Allemand *et al.,* 1997). The images are shown in Fig. 1*a*; the corresponding measured average stretches are also presented. As shown, the results are almost identical for Hfq, CTR or NTR. The ssDNA molecules are combed to a similar length of 25 ± 2 µm (0.52 nm/base), irrespective of the protein or its truncated forms. This confirms that both the NTR and CTR bind and coat ssDNA. A second type of experiment was done using a nanofluidic device to mimic a confined environment. In this experiment, ssDNA coated with Hfq was brought inside a rectangular channel with a cross-sectional diameter of 125 nm using an electric field. Once the complexes are inside the channel, they were allowed to relax for 2 min before imaging. The stretch of the complexes in the longitudinal direction of the channel was measured and is shown in the histogram in Fig. 1*b*. The corresponding histogram pertaining to the combing experiment has also been included. The mean stretch of the nano-confined complexes was found to be 15 ± 2 µm. In a rigid origami structure, ssDNA takes a maximal stretch 0.68 ± 0.02 nm/base (Roth et al, 2018). Accordingly, the stretch per unit contour length (relative stretch) of the complexes inside the channel amounts 0.46 ± 0.06. In the case of naked dsDNA confined to the same channel, the relative stretch was reported to be 0.528 ± 0.005 (Yadav *et al.,* 2020). It must be emphasised that bare ssDNA without protein coating is notoriously difficult to linearise with molecular combing and cannot be stretched inside a nanochannel due to strong intramolecular hybridisation. We conclude that the relative stretches of ssDNA coated with full-length Hfq and naked dsDNA confined to the 125 nm channel are similar, which indicates that the bending rigidity (persistence length) of the coated ssDNA filament is about the same as that of bare dsDNA. In contrast, previous reports with another method allowing imaging of naked ssDNA pointed to lower values with a wide variation for ssDNA extension, that is, from 0.18 nm/base to 0.36 nm/base (Hansma *et al.,* 1992; Woolley and Kelly, 2001), thus ssDNA extension by Hfq and its CTR (0.52 nm/base) is significantly more. Extension of ssDNA by Hfq and/or its CTR also exceeds the extension following coating of ssDNA with a cationic-neutral polypeptide copolymer (0.32 nm/base; Basak *et al.,* 2019). Note that in these experiments, the coated ssDNA molecules are aligned through the application of flow (combing) or confinement to a long and narrow channel. Although some intermolecular aggregation was observed, these aggregates generally break up due to the alignment procedure. Quantitative information regarding intermolecular bridging could, hence, not be obtained from these essentially single-molecule stretching experiments.

The effect of Hfq-CTR was then confirmed with Transmission electron microscopy (TEM). This experiment was done with circular viral DNA (single-stranded) and not linear molecules (Fig. 1*c*). Circular ssDNA molecules were deposited on a carbon surface previously functionalised with positive charges and positively stained. TEM clearly confirms the capability of CTR to spread some regions of the viral DNA in conjunction with folding of other regions by intra- or intermolecular bridging interaction (Fig. 1*c*, sub-panels *b*1 and *b*2). Note that the relative alignment, parallel or

https://doi.org/10.1017/qrd.2022.15 Published online by Cambridge University Press

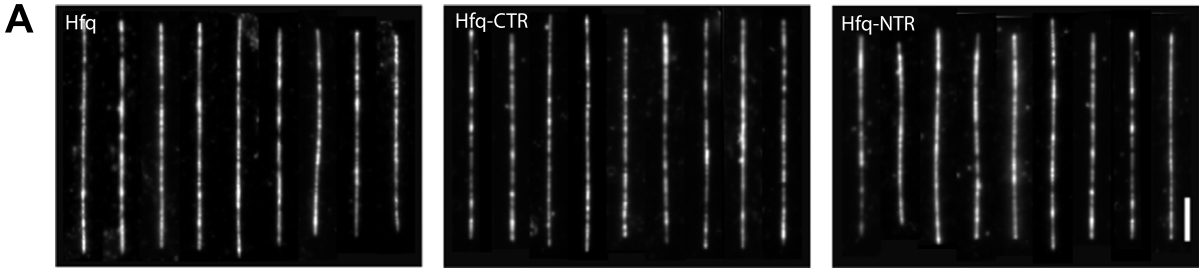

complex	Stretch (μm)	Number of molecules
Hfq (hexamer):base 1:200	25 ± 2	28
Hfq-CTR:base 6:200	25 ± 2	28
Hfq-NTR (hexamer):base 1:200	24 ± 2	24

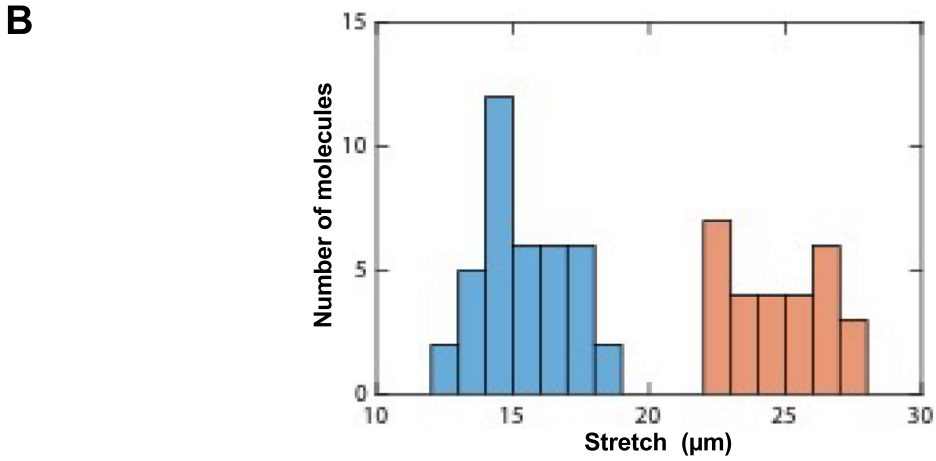

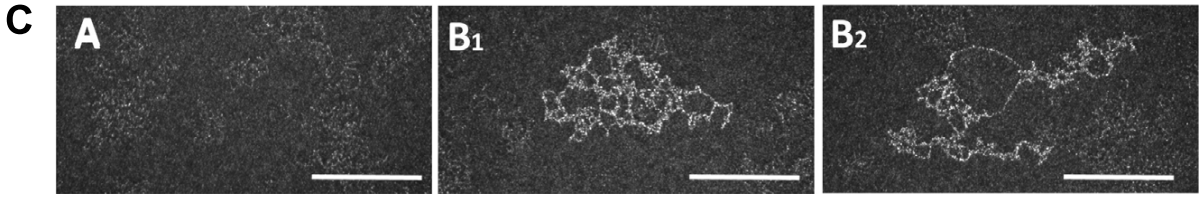

Fig. 1. ssDNA coating by Hfq. (*a*) Montages of ssDNA coated with Hfq or its truncated forms. Molecules are stained with YOYO-1 and stretched on the flat surface by molecular combing. *Scale bar* 5 μm. The corresponding measured extension for combed molecules is also given. Note that the molar concentration of CTR is kept six times higher than hexameric-HFq to maintain the stoichiometric ratio. (*b*) Histogram of ssDNA molecules imaged in combing (orange, 28 molecules) and inside nanofluidic channel (blue, 39 molecules). The average extension for the combing experiment is 25 $\pm$ 2 μm and in the nanofluidic channel is 15 $\pm$ 2 μm. (*c*) TEM evidence of Hfq-ssDNA binding. ΦX174 ssDNA virions were incubated in the presence of CTR. Before incubation, virions ssDNA is difficult to visualise (sub-panel *a*1). CTR binding to ssDNA ΦX174 allows the spreading of some region of the DNA, while others are strongly bridged (sub-panels *b*1 and *b*2). In this case, the CTR causes the association of several ΦX174 that cannot be differentiated and the length of the viral DNA cannot be measured. *Scale bars:* 200 nm.

antiparallel, of ssDNA portions in the bridged regions cannot be determined.

Hfq changes ssDNA structure and allows DNA alignment

Next, the effect of Hfq-CTR on ssDNA has been investigated using SRCD. We identified significant spectral changes over the whole spectrum (Fig. 2). Assuming that the protein is restructuring (amyloid formation) upon DNA binding (Malabirade *et al.*, 2018), we also identified that the ssDNA structure changes. We note a positive band at 180 nm and a negative band at 190 nm both indicative of left-handed NA (Wien *et al.*, 2021). In contrast, a positive band around 185 nm and a negative one between 200 and 210 nm are indicative of right-handed NAs (Wien *et al.*, 2021). The spectral change identified could be correlated with base-tilting of A-rich sequences (Edmondson and Johnson, 1985; Wien *et al.*, 2019). Furthermore, the influence of Hfq on the positive CD signal around 270 nm may be influenced by base pairing and stacking (Holm *et al.*, 2010; Wien *et al.*, 2021).

One possible explanation for the spectral inversion observed could be due to a change in helical parameters. To test this possibility, we used FTIR spectroscopy to analyse sugar puckering. When only C3'-endo sugars are present, characteristic absorption bands located at 865 and 820 cm^{-1} are observed, corresponding to the A-form. A contribution around 840 cm^{-1} is indicative of a C2'-endo conformation (B-form) (Wien *et al.*, 2021). The formation of a Z-like form is excluded as it would give a triplet at 970, 951 and 925 cm^{-1} (Banyay *et al.*, 2003). The A-form would give a triplet

https://doi.org/10.1017/qrd.2022.15 Published online by Cambridge University Press

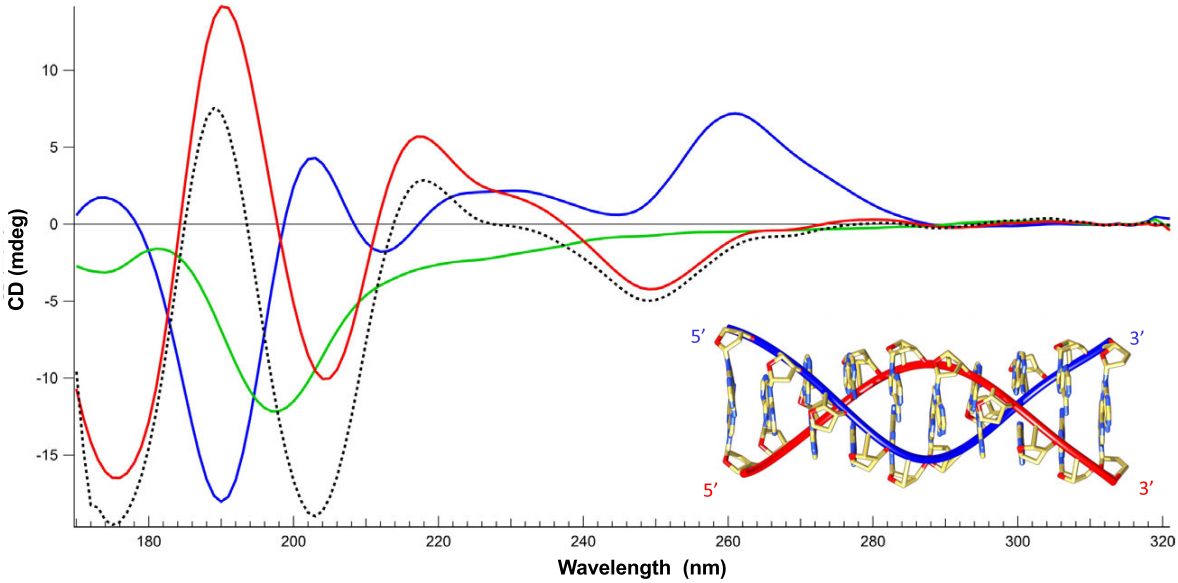

Fig. 2. Structure characterisation of ssDNA complexed to Hfq-CTR by SRCD spectroscopy. Spectra of DNA in the absence (red) and presence of CTR (blue). CTR alone (green). The dotted spectrum represents the theoretical sum of individual spectra of the DNA and CTR. The measured spectrum of the complex is significantly different compared to the DNA + peptide theoretical spectra, indicating an conformational change of the complexed ssDNA. Note that the same analysis with the full-length protein was impractical due to the low solubility of the protein. Inset: model of parallel DNA (Gleghorn *et al.,* 2016).

at 977, 968 and 952 cm^{-1} and the B-form would give a singlet at 970 cm^{-1}. As shown in Fig. 3*a*, we clearly see that the d-ribose stays in C2'-endo since we observe the typical bands near 840 and 970 cm^{-1}. We thus conclude that ssDNA complexed to Hfq remains in B-form.

A possibility could be that the pH 5 used in our conditions could result in the formation of A^+ adenine and subsequently in a parallel helix (Gleghorn *et al.,* 2016). FTIR analysis of our complex confirms this hypothesis: the band at 1658 cm^{-1} is absent in dA_{59} alone, but the shift from 932 to 947 cm^{-1} and the net decrease of the band intensity at 1080 cm^{-1} show that a parallel helix is formed by dA_{59} when bound to CTR (Fig. 3*b*) (Taillandier and Liquier, 2002). This result is confirmed using SRCD as dA_{59} complexed to CTR exhibits a spectrum similar to that of poly(dA) parallel helix (Holm *et al.,* 2012). We thus conclude the CTR induces the formation of ds parallel helix from ss dA_{59}. This is not the case for ssDNA alone; thus, the CTR promotes the formation of this parallel helix.

Next, as the formation of such a parallel helix could result in the alignment of ssDNA, we analysed the possible alignment of the ssDNA molecule by CTR. Indeed, we previously observed that the CTR amyloid region has a propensity to align DNA (Wien *et al.,* 2019). As shown in Fig. 4, a clear alignment by the CTR:ssDNA complex can also be observed under Couette flow conditions. The alignment without rotation in a flow cell was also confirmed by SRLD using a CD cell and a CD cell rotation chamber (Fig. 4*c*). Alignment of the complex in the CD sample may occur upon loading between short path lengths; hence, linear dichroism (LD) signals emerge. These signals, if strong enough, spill into the CD signal via LD-CD cross talk (Sutherland, 2009) and distort the CD spectrum. In order to eliminate the LD contribution acquisition of CD spectra at four angles (0°-90°-180°-270°) were averaged.

Shown in Fig. 4*a* are the SRLD spectra of CTR, ssDNA and finally of the complex CTR:dA_{59}. The LD signal is effectively zero for both Hfq-CTR and ssDNA compared to the very strong LD signal of the complex. This shows that although the two components do not align under flow conditions, the complex readily aligns. In contrast to the LD signal observed for dsDNA complexes with Hfq-CTR (Wien *et al.,* 2019), we observe that the LD signal is positive for all wavelengths including the wavelength range from 240 to 300 nm where the DNA signal dominates. This leads to a surprising conclusion: where long DNA normally aligns along the flow direction giving rise to negative LD signals (Dicko *et al.,* 2008), the parallel dsDNA formed by dA_{59} are incorporated into the polymers of the complex in such a way that they are aligned perpendicular to the length of the amyloid strand. The positive signal at 195 nm is in agreement with the β-sheet secondary structure aligned perpendicular to the amyloid fibrils and thus the flow (Wien *et al.,* 2019) since β-strands have a transition dipole moment near 195 nm aligned perpendicular to the direction of the strand (Nordén *et al.,* 2010).

In conclusion, our results clearly show that *in vitro* the Hfq protein and in particular its CTR amyloid region are able to bind to ssDNA, cover, spread and bridge it, and to allow the alignment of ssDNA molecules. Because ssDNA is an essential intermediate in many DNA metabolic processes, we then analysed the effect of Hfq *in vivo* for two processes where ssDNA is formed. Hfq could indeed be part of the ssDNA-binding SSB protein family in prokaryotic cells, which bind to ssDNA, stabilising and protecting intermediate states of DNA recombination and replication.

This could particularly be the case for A-rich sequences found throughout the *E. coli* genome and when pH decreases during host infection (Tolstorukov *et al.,* 2005; Kenney, 2019). Furthermore, it could prevent ssDNA chemical attack or be involved in removal of

https://doi.org/10.1017/qrd.2022.15 Published online by Cambridge University Press

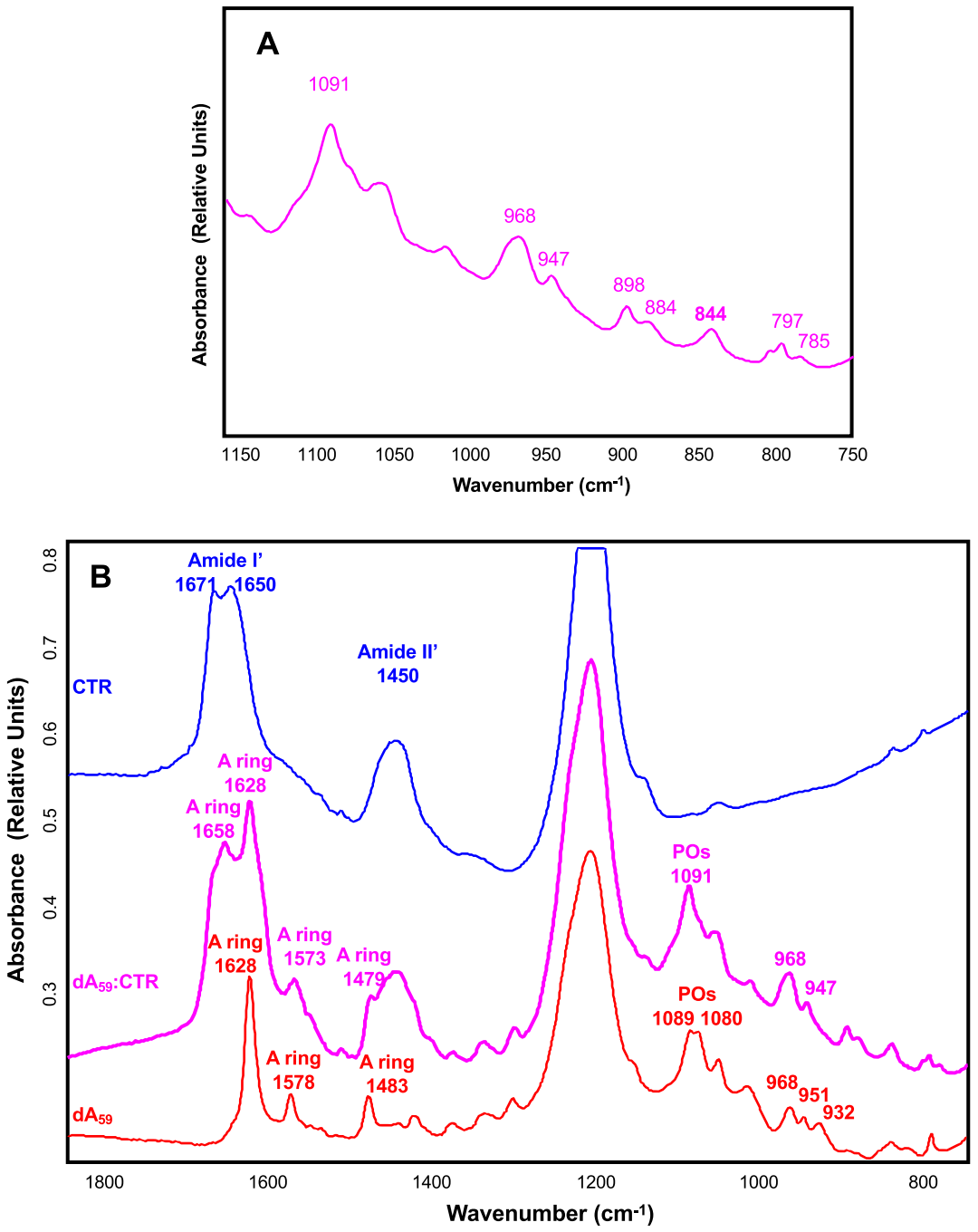

Fig. 3. (*a*) FTIR transmission spectrum of ssDNA in the presence of Hfq-CTR. The ribose stays in C2'-endo since we observe the typical bands at 840 and 970 cm^{-1}. (*b*) FTIR transmission spectrum of ssDNA in the presence of CTR. The band observed at 1658 cm^{-1}, absent in dA_{59} alone, the shift from 932 to 947 cm^{-1} and the net decrease of the band intensity at 1089 cm^{-1} indicates that a parallel helix is formed by dA_{59} when bound to CTR.

secondary structures that could impair ssDNA-related processes (Molan and Zgur Bertok, 2022).

Hfq influences replication of bacteriophage M13 and genetic recombination

To evaluate if Hfq influences biological processes in which ssDNA regions are involved, we have tested efficiencies of M13-bacteriophage replication which has an ssDNA genome and genetic recombination between genomes of λ bacteriophage (Red-recombination system).

When testing development of the M13 bacteriophage, we found that its efficiency is significantly more effective in the Δ*hfq* mutant relative to WT control (Fig. 5*a*). Since effects observed in mutants completely devoid of Hfq might be caused by the absence of various activities of this protein, we repeated these experiments using a

https://doi.org/10.1017/qrd.2022.15 Published online by Cambridge University Press

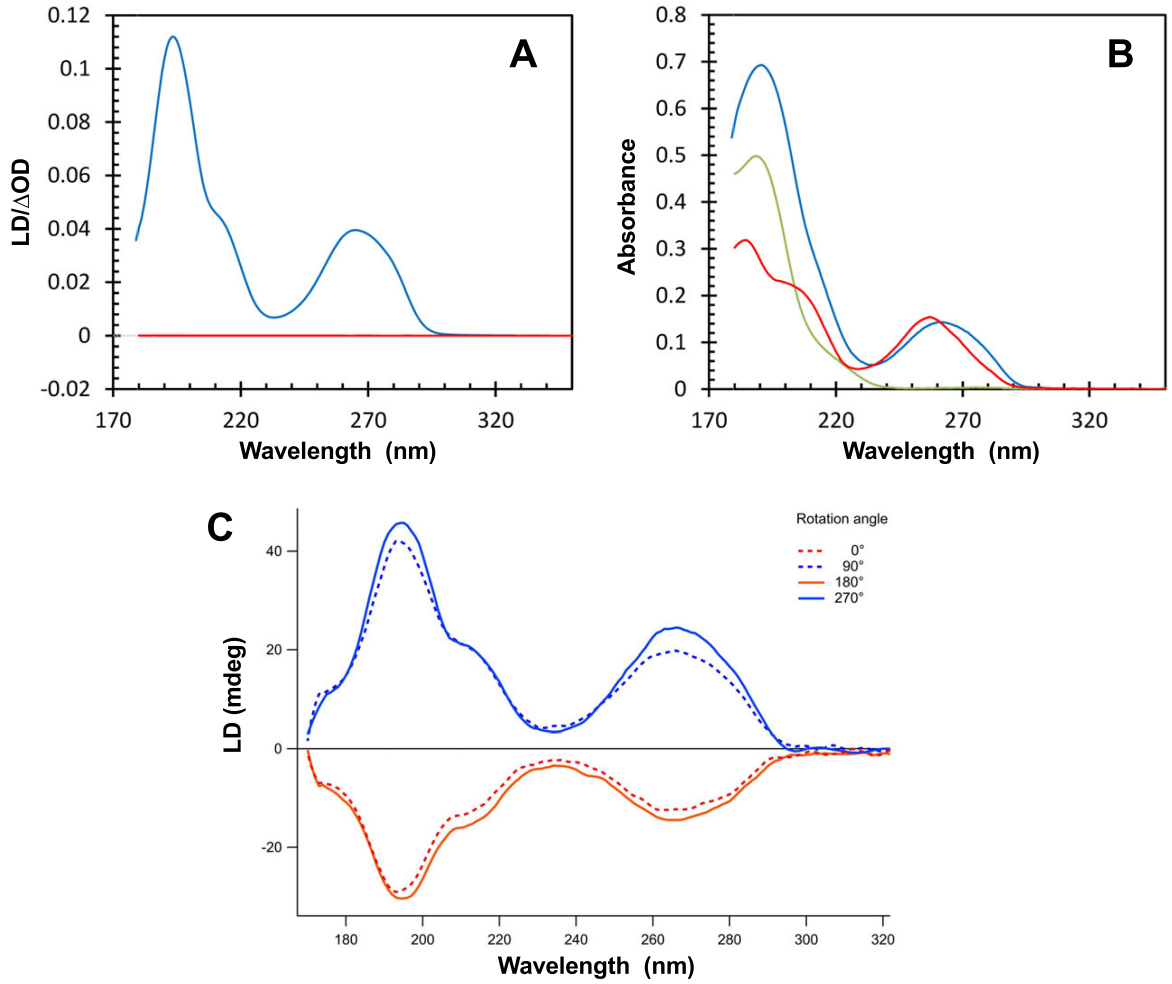

Fig.4. LD signal (*a*) and absorbance spectra (*b*) of the complex dA_{59}:CTR (blue), dA_{59} (red) and Hfq-CTR (green). Spectra were measured with a sample path length of 0.5 mm and rotation speed of the Couette flow cell of 3000 rpm. (*c*) SRLD analysis of the same complex measured in a classic 0.024 mm path length cell, rotating the cell holder every 90°. The overall shape of the spectra is conserved with maxima and minima in the same positions compared to (*a*). Amplitude differences are most likely due to differences of the experiments, with a less perfect alignment of the sample in the classic cell.

mutant with deletion of the Hfq CTR while leaving intact the NTR. In such a mutant, replication of the M13 phage was significantly less efficient relative to the WT counterpart, as shown by slower phage development and lower burst size (Fig. 5*a*).

To test the efficiency of genetic recombination, we have employed λ bacteriophage mutants. Nonsense (amber, or shortly am) λ mutants in genes *P* or *S* can propagate only in suppressor *E. coli* hosts (*supE* or *supF*, respectively) but not in WT bacteria. When WT, Δ*hfq* or ΔCTR cells were infected simultaneously with both phage mutants, Red-recombination could occur. Culture growth was timely stopped and phage lysates were prepared after one single lytic development cycle was reached. Thus, phage progeny contained parental phages and recombinants, including λ*P*(am)*S*(am) and λP^+S^+ variants. The latter phages could be easily distinguished from parental viruses because of their ability to form plaques on the WT host. By comparing phage titers on *WT* and *supE supF* strains, we found that the fraction of recombinant λP^+S^+ phages after propagation in control (hfq^+) cells was equal to 0.17 ± 0.04%, which was significantly higher than fractions of revertants (spontaneous P^+ and S^+ reverse mutants, which appear among mutant phages), achieving a frequency of 0.001% and < 0.0001% for λ*P*(am) and λ*S*(am), respectively. When testing efficiency of recombination in Δ*hfq* and ΔCTR hosts, evident influence of the absence of either whole Hfq or its CTR could be observed. Interestingly, the fraction of λP^+S^+ recombinants was about 2-fold lower after propagation of phages in the Δ*hfq* host than in WT bacteria, while estimated efficiency of recombination was over two times higher in the ΔCTR host relative to the WT counterpart (Fig. 5*b*). Therefore, a lack of Hfq results in λ phage recombination inhibition, while in the presence of only Hfq-NTR, this process is more efficient in *E. coli.*

As the absence of the CTR could influence Hfq stability and its abundance (Arluison *et al.*, 2004), quantification of Hfq and its CTR-truncated form was performed; no significant differences were observed (Gaffke *et al.*, 2021). Therefore, we conclude that differences in efficiencies of phage M13 replication and phage λ genetic recombination between WT bacteria and *hfq* mutants arise from dysfunctions of Hfq in the mutant cells.

https://doi.org/10.1017/qrd.2022.15 Published online by Cambridge University Press

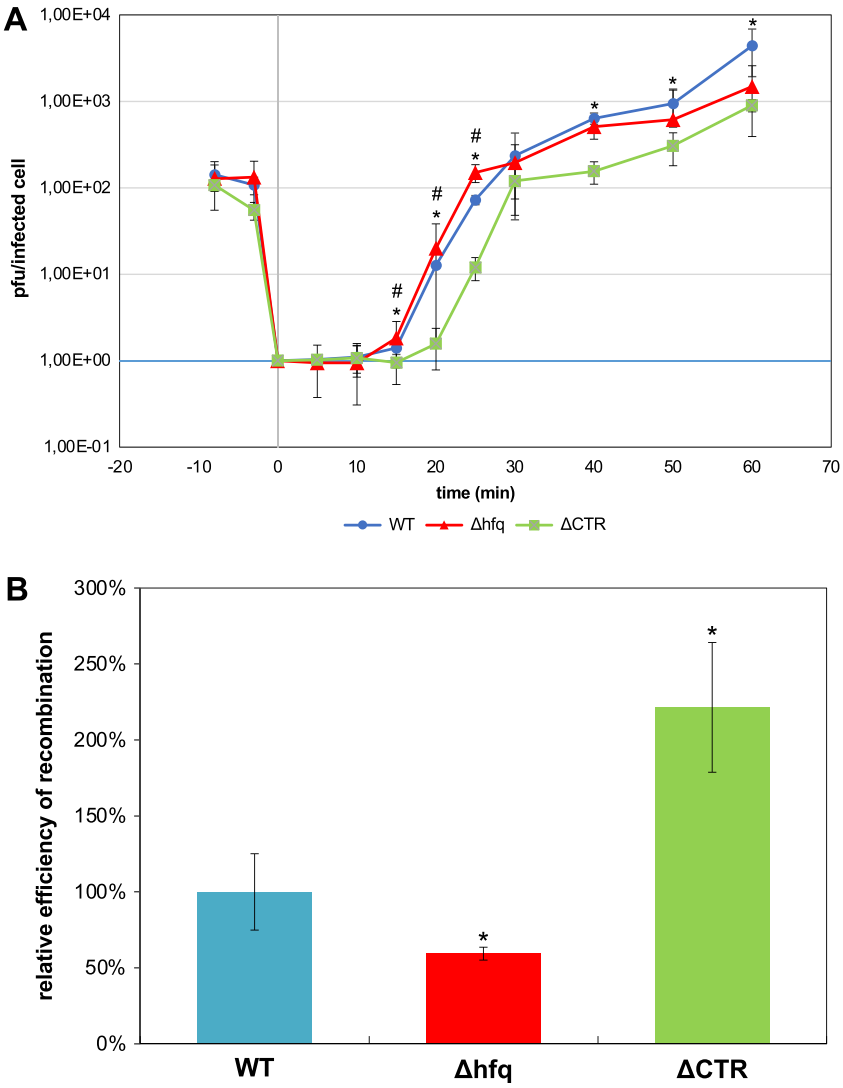

Fig. 5. (*a*) Development of bacteriophage M13 in *E. coli.* The presented results indicate mean values from three experiments with error bars indicating SD. Symbols (#) and (*) indicate statistically significant differences ($p < 0.05$ in the *t*-test) between results obtained for hfq^+ and Δ*hfq*, and hfq^+ and ΔCTR, respectively. (*b*) Efficiency of recombination between λ bacteriophage genomes in *E. coli.* The presented results show mean values from three experiments with error bars indicating SD. Value of 100% represents fraction of λP^+S^+ recombinants appearing after infection of the hfq^+ host cells with λ*cI857S7*(am) and λ*b519imm21susP* phages which was equal to 0.17 ± 0.04%. Symbols (*) indicate statistically significant differences ($p < 0.05$ in the *t*-test) between results obtained for hfq^+ and either Δ*hfq* or ΔCTR hosts.

Discussion

The results presented in this paper show that, in addition to its role in RNA metabolism, Hfq binds to ssDNA and may therefore play an important role in genetic processes involving ssDNA, including recombination and replication. *In vivo*, the Hfq protein has been discovered as a host factor for bacteriophage replication (Franze de Fernandez *et al.*, 1972). Further studies indicated then that this protein mediates various RNA transactions (Vogel and Luisi, 2011; Sobrero and Valverde, 2012).

Although early studies suggested that Hfq interacts with ssRNA, subsequent experiments indicated that this protein can interact with DNA (Cech *et al.*, 2016). In this report, we demonstrate that Hfq interacts also with ssDNA. Note that the role of Hfq in ssDNA binding and remodelling strengthens the general role of bacterial NAPs in similar processes, such as for HU and H-NS/StpA family (Shiraishi *et al.*, 2007; Kamashev *et al.*, 2008; Yang *et al.*, 2019).

We show here that the ssDNA-binding properties of Hfq are mainly due to its CTR. We observe that CTR binding to ssDNA allows its alignment by forming a parallel helix. This is not the case for ssDNA alone; thus, the CTR promotes the formation of this parallel helix probably by changing the pK_A of adenines.

Interestingly, Hfq-CTR has also a propensity to juxtapose two DNA molecules and this is highly suggestive of a role in modulation of efficiency of recombination and/or transformation, as it was formerly shown for another "dsDNA bridging/ssDNA binding" protein, DprA (Mortier-Barriere *et al.*, 2007). To test if such interaction can play a physiological role we have performed efficiency assays for processes that require ssDNA. Our finding that two processes are affected, either positively (M13 replication) or negatively (λ recombination) in the Δ*hfq* mutant might suggest that this is the case. However, any secondary effects of Hfq-mediated changes in regulatory RNA functions could not be excluded in such

https://doi.org/10.1017/qrd.2022.15 Published online by Cambridge University Press

experimental systems. Therefore, we have also used the ΔCTR mutant in which only the NTR of Hfq is present. Surprisingly, we found that effects of the ΔCTR mutation on both M13 replication and λ recombination are more pronounced than in the case of Δ*hfq*, and opposite to those observed in cells completely lacking Hfq. These results corroborate the conclusion that ssDNA binding by Hfq has a physiological relevance. We have also demonstrated that *in vivo* Hfq-CTR stimulates replication of bacteriophage M13 genome, while inhibiting Red recombination. We propose that Hfq-mediated stimulation of M13-replication might relate to changes in ssDNA conformation facilitating alignment of ssDNA in parallel helices, and then the formation of the replication complex, similarly to the mechanism occurring in the Qβ bacteriophage replication. On the other hand, covering ssDNA regions by Hfq during genetic recombination may impair this process due to lower availability of recombining sequences during the exchange process of strands between two DNA molecules.

Recombination efficiency is also controlled by Hfq-CTR which inhibits recombination. Mutant Δ*hfq* cells lacking both the NTR and CTR regions recombine less efficiently in contrast to only CTR deficient cells. WT cells containing Hfq are not substantially more efficient in recombination than Δ*hfq*. Therefore, we hypothesise that effects of the absence of CTR in Δ*hfq* cells might be hidden due to the inability of the NTR to perform its functions. This includes interactions with sRNA and ultimately regulation of gene expression. This definitely makes Hfq an important player to consider in bacterial chromosome structure and gene expression control.

Open Peer Review. To view the open peer review materials for this article, please visit http://doi.org/10.1017/qrd.2022.15.

Acknowledgements. We are very grateful to C. Lavelle (MNHN, Paris), P. Dupaigne (IGR, Villejuif, France) and O. Pietrement (U. of Dijon, France) for their contribution to TEM measurements at an early stage of this work and for many fruitful discussions.

Authors' contributions. K.K. constructed plasmids and *E. coli* mutant strains and performed *in vivo* experiments (replication and recombination assessment). J.v.d.M. and I.Y. did optical microscopy of ssDNA complexes. F.W., V.A., N.C.J. and S.V.H. did SRCD, SRLD and OCD measurement and analysis. A.C. and E.L.C. did TEM measurements. F.G. did FTIR measurements. G.W. and V.A. concepted the study and supervised the work. All authors participated in the design, interpretation of the studies and analysis of the data and review of the manuscript.

Supplementary Materials. To view supplementary material for this article, please visit http://doi.org/10.1017/qrd.2022.15.

Financial support. This research was supported by Singapore Ministry of Education Academic Research Fund (Tier 1 R-144-000-451-114 and Tier 2 MOE-T2EP50121–0003 grants), National Science Center (Poland) (2016/21/N/NZ1/02850 to KK) and University of Gdansk (531-D020-D242–21 to GW). SRCD measurements on DISCO beamline at the SOLEIL Synchrotron were performed under proposal 20200007. SRLD measurements on ASTRID2 synchrotron radiation facility (Aarhus University, Denmark) were performed under proposal ISA-21-102. Campus France is gratefully acknowledged for their financial support of this work through PHC Polonium with Poland 27701VG. This study contributes to the IdEx Université de Paris ANR-18-IDEX-0001. This work was supported by a public grant overseen by the French National research Agency (ANR) as part of the 'Investissement d'Avenir' program, through the 'ADI 2019' project funded by the IDEX Paris-Saclay, ANR-11-IDEX-0003-02.

Conflict of interest. The authors declare no potential conflicts of interest with respect to the research, authorship and/or publication of this article.

References

Allemand JF, Bensimon D, Jullien L, Bensimon A and Croquette V (1997) pH-dependent specific binding and combing of DNA. *Biophysical Journal* **73** (4), 2064–2070.

Arluison V, Folichon M, Marco S, Derreumaux P, Pellegrini O, Seguin J, Hajnsdorf E and Regnier P (2004) The C-terminal domain of Escherichia coli Hfq increases the stability of the hexamer. *European Journal of Biochemistry* **271**(7), 1258–1265.

Bachmann BJ (1972) Pedigrees of some mutant strains of Escherichia coli K-12. *Bacteriological Reviews* **36**(4), 525–557.

Banyay M, Sarkar M and Graslund A (2003) A library of IR bands of nucleic acids in solution. *Biophysical Chemistry* **104**(2), 477–488.

Basak R, Liu F, Qureshi S, Gupta N, Zhang C, De Vries R, Van Kan JA, Dheen ST and Van Der Maarel JRC (2019) Linearization and Labeling of single-stranded DNA for optical sequence analysis. *Journal of Physical Chemistry Letters* **10**(3), 316–321.

Beloin C, Jeusset J, Revet B, Mirambeau G, Le Hegarat F and Le Cam E (2003) Contribution of DNA conformation and topology in right-handed DNA wrapping by the Bacillus subtilis LrpC protein. *The Journal of Biological Chemistry* **278**(7), 5333–5342.

Brennan RG and Link TM (2007) Hfq structure, function and ligand binding. *Current Opinion in Microbiology* **10**(2), 125–133.

Cech GM, Szalewska-Palasz A, Kubiak K, Malabirade A, Grange W, Arluison V and Wegrzyn G (2016) The Escherichia Coli Hfq protein: An unattended DNA-transactions regulator. *Frontiers in Molecular Biosciences* **3**, 36.

Dicko C, Hicks MR, Dafforn TR, Vollrath F, Rodger A and Hoffmann SV (2008) Breaking the 200 nm limit for routine flow linear dichroism measurements using UV synchrotron radiation. *Biophysical Journal* **95**(12), 5974–5977.

Diestra E, Cayrol B, Arluison V and Risco C (2009) Cellular electron microscopy imaging reveals the localization of the Hfq protein close to the bacterial membrane. *PLoS One* **4**(12), e8301.

Edmondson SP and Johnson WC (1985) Base tilt of poly[d(a)]-poly[d(T)] and poly[d(AT)]-poly[d(AT)] in solution determined by linear dichroism. *Biopolymers* **24**(5), 825–841.

El Hamoui O, Yadav I, Radiom M, Wien F, Berret J-F, Van Der Maarel JRC and Arluison V (2020) Interactions between DNA and the Hfq amyloid-like region trigger a viscoelastic response. *Biomacromolecules* **21**(9), 3668–3677.

Folichon M, Arluison V, Pellegrini O, Huntzinger E, Regnier P and Hajnsdorf E (2003) The poly(a) binding protein Hfq protects RNA from RNase E and exoribonucleolytic degradation. *Nucleic Acids Research* **31**(24), 7302–7310.

Fortas E, Piccirilli F, Malabirade A, Militello V, Trepout S, Marco S, Taghbalout A and Arluison V (2015) New insight into the structure and function of Hfq C-terminus. *Bioscience Reports* **35**(2).

Franze De Fernandez MT, Hayward WS. and August JT (1972) Bacterial proteins required for replication of phage Qb ribonucleic acid. *The Journal of Biological Chemistry* **247**, 824–821.

Gaffke L, Kubiak K, Cyske Z and Wegrzyn G (2021) Differential chromosome- and plasmid-borne resistance of Escherichia coli hfq mutants to high concentrations of various antibiotics. *International Journal of Molecular Sciences* **22**(16), 8886.

Geinguenaud F, Calandrini V, Teixeira J, Mayer C, Liquier J, Lavelle C and Arluison V (2011) Conformational transition of DNA bound to Hfq probed by infrared spectroscopy. *Physical Chemistry Chemical Physics* **13**(3), 1222–1229.

Gleghorn ML, Zhao J, Turner DH and Maquat LE (2016) Crystal structure of a poly(rA) staggered zipper at acidic pH: Evidence that adenine N1 protonation mediates parallel double helix formation. *Nucleic Acids Research* **44**(17), 8417–8424.

Goldberg AR and Howe M (1969) New mutations in the S cistron of bacteriophage lambda affecting host cell lysis. *Virology* **38**(1), 200–202.

Gottesman S (2019) Trouble is coming: Signaling pathways that regulate general stress responses in bacteria. *The Journal of Biological Chemistry* **294**(31), 11685–11700.

Hansma HG, Sinsheimer RL, Li MQ and Hansma PK (1992) Atomic force microscopy of single- and double-stranded DNA. *Nucleic Acids Research* **20**(14), 3585–3590.

Holm AI, Munksgaard Nielsen L, Vronning Hoffmann S and Brondsted Nielsen S (2012) On the formation of the double helix between adenine single strands at acidic pH from synchrotron radiation circular dichroism experiments. *Biopolymers* **97**(7), 550–557.

Holm AIS, Nielsen LM, Hoffmann SV and Nielsen SB (2010) Vacuum-ultraviolet circular dichroism spectroscopy of DNA: A valuable tool to elucidate topology and electronic coupling in DNA. *Physical Chemistry Chemical Physics: PCCP* **12**(33), 9581–9596.

Jensen KF (1993) The Escherichia coli K-12 "wild types" W3110 and MG1655 have an RPH frameshift mutation that leads to pyrimidine starvation due to low pyrE expression levels. *Journal of Bacteriology* **175**(11), 3401–3407.

Jiang K, Zhang C, Guttula D, Liu F, Van Kan JA, Lavelle C, Kubiak K, Malabirade A, Lapp A, Arluison V and Van Der Maarel JR (2015) Effects of Hfq on the conformation and compaction of DNA. *Nucleic Acids Research* **43**(8), 4332–4341.

Kamashev D, Balandina A, Mazur AK, Arimondo PB and Rouviere-Yaniv J (2008) HU binds and folds single-stranded DNA. *Nucleic Acids Research* **36** (3), 1026–1036.

Kavita K, Zhang A, Tai CH, Majdalani N, Storz G and Gottesman S (2022) Multiple in vivo Roles for the C-Terminal Domain of the RNA Chaperone Hfq. *Nucleic Acids Research*.

Kenney LJ (2019) The role of acid stress in salmonella pathogenesis. *Current Opinion in Microbiology* **47**, 45–51.

Link TM, Valentin-Hansen P and Brennan RG (2009) Structure of Escherichia coli Hfq bound to polyriboadenylate RNA. *Proceedings of the National Academy of Sciences of the United States of America* **106**(46), 19292–19297.

Majdalani N, Cunning C, Sledjeski D, Elliott T and Gottesman S (1998) DsrA RNA regulates translation of RpoS message by an anti-antisense mechanism, independent of its action as an antisilencer of transcription. *Proceedings of the National Academy of Sciences of the United States of America* **95**(21), 12462–12467.

Malabirade A, Jiang K, Kubiak K, Diaz-Mendoza A, Liu F, Van Kan JA, Berret JF, Arluison V and Van Der Maarel JRC (2017a) Compaction and condensation of DNA mediated by the C-terminal domain of Hfq. *Nucleic Acids Research* **45**(12), 7299–7308.

Malabirade A, Morgado-Brajones J, Trepout S, Wien F, Marquez I, Seguin J, Marco S, Velez M and Arluison V (2017b) Membrane association of the bacterial riboregulator Hfq and functional perspectives. *Scientific Reports* **7**(1), 10724.

Malabirade A, Partouche D, El Hamoui O, Turbant F, Geinguenaud F, Recouvreux P, Bizien T, Busi F, Wien F and Arluison V (2018) Revised role for Hfq bacterial regulator on DNA topology. *Scientific Reports* **8**(1), 16792.

Molan K and Zgur Bertok D (2022) Small prokaryotic DNA-binding proteins protect genome integrity throughout the life cycle. *International Journal of Molecular Sciences* **23** (7).

Mortier-Barriere I, Velten M, Dupaigne P, Mirouze N, Pietrement O, Mcgovern S, Fichant G, Martin B, Noirot P, Le Cam E, Polard P and Claverys JP (2007) A key presynaptic role in transformation for a widespread bacterial protein: DprA conveys incoming ssDNA to RecA. *Cell* **130**(5), 824–836.

Mosberg JA, Lajoie MJ and Church GM (2010) Lambda red recombineering in Escherichia coli occurs through a fully single-stranded intermediate. *Genetics* **186**(3), 791–799.

Nordén B, Rodger A and Daffron T (2010) *Linear Dichroism and Circular Dichroism a Textbook on Polarized-Light Spectroscopy*. Cambridge: RCS Publishing, pp. 317–370.

Oakley AJ (2019) A structural view of bacterial DNA replication. *Protein Science* **28**(6), 990–1004.

Orans J, Kovach AR, Hoff KE, Horstmann NM and Brennan RG (2020) Crystal structure of an Escherichia coli Hfq core (residues 2-69)-DNA complex reveals multifunctional nucleic acid binding sites. *Nucleic Acids Research* **48**(7), 3987–3997.

Patterson TA and Dean M (1987) Preparation of high titer lambda phage lysates. *Nucleic Acids Research* **15**(15), 6298.

Piazza A and Heyer W-D (2019) Moving forward one step back at a time: Reversibility during homologous recombination. *Current Genetics* **65**(6), 1333–1340.

Rajkowitsch L and Schroeder R (2007) Dissecting RNA chaperone activity. *RNA* **13**(12), 2053–2060.

Roth, E., Glick Azaria, A., Girshevitz, O., Bitler, A. & Garini, Y. (2018). Measuring The Conformation And Persistence Length Of Single-Stranded Dna Using A Dna Origami Structure. *Nano Lett*, **18**(11), 6703–6709.

Salivar WO, Tzagoloff H and Pratt D (1964) Some physical-chemical and biological properties of the rod-shaped coliphage M13. *Virology* **24**, 359–371.

Sharan SK, Thomason LC, Kuznetsov SG and Court DL (2009) Recombineering: A homologous recombination-based method of genetic engineering. *Nature Protocols* **4**(2), 206–223.

Shiraishi K, Ogata Y, Hanada K, Kano Y and Ikeda H (2007) Roles of the DNA binding proteins H-NS and StpA in homologous recombination and repair of bleomycin-induced damage in Escherichia coli. *Genes & Genetic Systems* **82**(5), 433–439.

Shulman LM and Davidson I (2017) Viruses with circular single-stranded DNA genomes are everywhere! *Annual Review of Virology* **4**(1), 159–180.

Sobrero P and Valverde C (2012) The bacterial protein Hfq: Much more than a mere RNA-binding factor. *Critical Reviews in Microbiology* **38**(4), 276–299.

Su X-C, Wang Y, Yagi H, Shishmarev D, Mason CE, Smith PJ, Vandevenne M, Dixon NE and Otting G (2014) Bound or free: Interaction of the C-terminal domain of Escherichia coli single-stranded DNA-binding protein (SSB) with the tetrameric core of SSB. *Biochemistry* **53**(12), 1925–1934.

Sutherland JC (2009) Measurement of circular dichroism and related spectroscopies with conventional and synchrotron light sources: Theory and instrumentation. In Wallace BA and Janes RW (eds), *Modern Techniques for Circular Dichroism and Synchrotron Radiation Circular Dichroism Spectroscopy*, IOS press, Amsterdam, The Netherlands. pp. 19–72.

Taghbalout A, Yang Q and Arluison V (2014) The Escherichia coli RNA processing and degradation machinery is compartmentalized within an organized cellular network. *The Biochemical Journal* **458**(1), 11–22.

Taillandier E and Liquier J (2002) *Vibrationnal Spectroscopy of Nucleic Acids*. Willey, NJ, USA.

Takada A, Wachi M, Kaidow A, Takamura M and Nagai K (1997) DNA binding properties of the hfq gene product of Escherichia coli. *Biochem. Biophys. Res. Com.* **236**, 576–579.

Tolstorukov MY, Virnik KM, Adhya S and Zhurkin VB (2005) A-tract clusters may facilitate DNA packaging in bacterial nucleoid. *Nucleic Acids Research* **33**(12), 3907–3918.

Vogel J and Luisi BF (2011) Hfq and its constellation of RNA. *Nature Reviews. Microbiology* **9**(8), 578–589.

Wegrzyn G, Wegrzyn A, Konieczny I, Bielawski K, Konopa G, Obuchowski M, Helinski DR and Taylor K (1995) Involvement of the host initiator function dnaA in the replication of coliphage lambda. *Genetics* **139**(4), 1469–1481.

Wien F, Geinguenaud F, Grange W and Arluison V (2021). SRCD and FTIR Spectroscopies to Monitor Protein-Induced Nucleic Acid Remodeling. Methods in molecular biology, RNA Remodeling Proteins (2209), 87–108.

Wien F, Martinez D, Le Brun E, Jones NC, Vronning Hoffmann S, Waeytens J, Berbon M, Habenstein B and Arluison V (2019) The bacterial amyloid-like Hfq promotes in vitro DNA alignment. *Microorganisms* **7**(12).

Wiggins PA, Dame RT, Noom MC and Wuite GJ (2009) Protein-mediated molecular bridging: A key mechanism in biopolymer organization. *Biophysical Journal* **97**(7), 1997–2003.

Wilusz CJ and Wilusz J (2013) Lsm proteins and Hfq: Life at the 3′ end. *RNA Biology* **10**(4), 592–601.

Woolley AT and Kelly RY (2001) Deposition and characterization of extended single strand DNA molecules on surface. *Nano Letters* **7**, 345–348.

Yadav I, Rosencrans W, Basak R, Van Kan JA and Van Der Maarel JRC (2020) Intramolecular dynamics of dsDNA confined to a quasi-one-dimensional nanochanne. *Phys. Rev. Research* **2**, 013294.

Yang D, Kong Y, Sun W, Kong W and Shi Y (2019) A dopamine-responsive signal transduction controls transcription of salmonella enterica Serovar Typhimurium virulence genes. *MBio* **10**(2).

Zawilak-Pawlik A, Nowaczyk M and Zakrzewska-Czerwinska J (2017) The role of the N-terminal domains of bacterial initiator DnaA in the assembly and regulation of the bacterial replication initiation complex. *Genes* **8** (5).

https://doi.org/10.1017/qrd.2022.15 Published online by Cambridge University Press

3.3. Conclusion and perspectives of this work

In this publication, we demonstrated that Hfq interacts with ssDNA, not only dsDNA. Note that the role of Hfq in ssDNA binding and remodelling strengthens the general role of bacterial NAPs in similar processes, such as for the HU and H-NS family (Kamashev et al. 2007; Shiraishi et al. 2007; Yang et al. 2019). Precisely, we show that the ssDNA binding properties of Hfq are mainly due to its CTR. We observe that CTR binding to ssDNA allows its alignment by forming a parallel helix. The CTR promotes the formation of this parallel helix probably by changing the pK_A of adenines. Interestingly, we also show using synchrotron radiation linear dichroism that Hfq-CTR has a propensity to juxtapose two DNA molecules, and this is highly suggestive of a role in modulation of efficiency of recombination and/or transformation. To test if such interaction can play a physiological role, we have performed assays for processes that require ssDNA. Our finding that two processes (M13 phage replication or recombination) are affected *in vivo*, either positively or negatively. We propose that Hfq-mediated stimulation of M13-replication might relate to changes in ssDNA conformation facilitating alignment of ssDNA in parallel helices and promoting the formation of the replication complex. On the other hand, covering ssDNA regions by Hfq during genetic recombination may impair this process due to lower availability of recombining sequences during the exchange process of strands between two DNA molecules. Note that effects seen for Hfq-mediated changes in regulatory RNA functions could not be excluded *in vivo*.

Chapter IV. *In vivo* analysis of the effect of Hfq on nucleoid structure

4.1. Principles of cryo-soft X-ray tomography (cryo-SXT)

Electron microscopes were invented and developed, using electrons as radiation, because visible light microscopies were limited by the use of wavelength above 400 nm (Knoll and Ruska 1932). Smaller wavelength photons such as the ones in the so-called "water-window" (X-rays at 520 eV have a corresponding wavelength of 2.38 nm) were not usable because of their refraction index preventing them from being focusable with traditional glass lenses. Later, Fresnel zone plates diffractive lenses were developed thus enabling the focusing of X-ray beams (see Figure 24).

This advancement led to the development of the first transmission X-ray microscopes (TXM), using Fresnel zone plates as objective lenses, by the group of Schmahl et al. at the University of Göttingen (Germany) (Niemann, Rudolph, and Schmahl 1976).

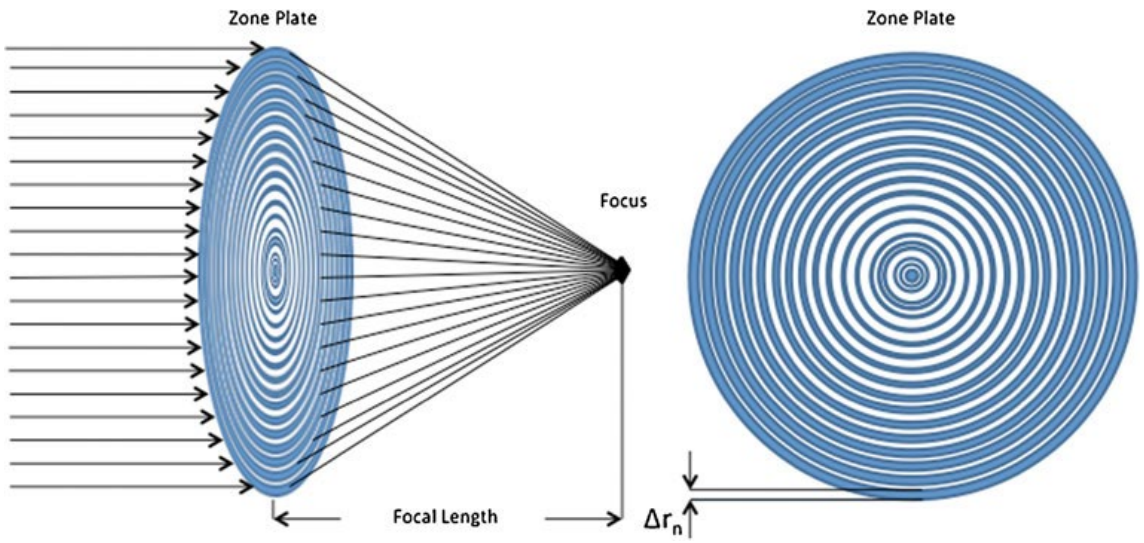

Figure 24. Representation of a Fresnel zone plate used in SXT to focalize X-rays. It is composed of concentric opaque rings that diffract X-rays. The maximum reachable resolution is defined by the width of the outermost ring (Δr_n). (Carzaniga et al. 2014)

Coupled with cryo-preservations methods, soft X-ray tomography can image entire close-to-native cells due to its large field of view and at high-resolution (tens of nanometres),

thus bridging the resolution gap between light and electron microscopies (see Figure 25). As can be seen above, the limiting factor for resolution in cryo-SXT is not imposed by the wavelength of X-rays but by the outermost ring of the Fresnel zone plate used. In addition, in the water-window, water (oxygen) is transparent to X-ray while organic matter (carbon-rich structures) has a high absorption. This makes it the method of choice for unstained biological samples and in our case for the observation of the bacterial nucleoid (J. Groen et al. 2019; Johannes Groen et al. 2021; Hammel et al. 2016) cannot otherwise be differentiated from the cytoplasm (no contrast) with electrons and is thus unsuitable for cryo-TEM.

Note that the observation of the bacterial nucleoid *in cellulo* remains challenging because of the lack of a membrane separating the nucleoid genomic content from the cytoplasm.

In cryo-SXT, X-rays are absorbed by the sample depending on its elemental composition. This generates an absorption contrast which relates to the Beer-Lambert law allowing to recover linear absorption coefficients (LAC) values in the tomographic reconstructions, thus making cryo-SXT a 3D quantitative imaging technique (J. Groen et al. 2019; Johannes Groen et al. 2021). Such analysis is possible at ALBA synchrotron on the MISTRAL beamline (Pereiro et al. 2009; Sorrentino et al. 2015) at a resolution of about 30 nm half pitch (Otón et al. 2016).

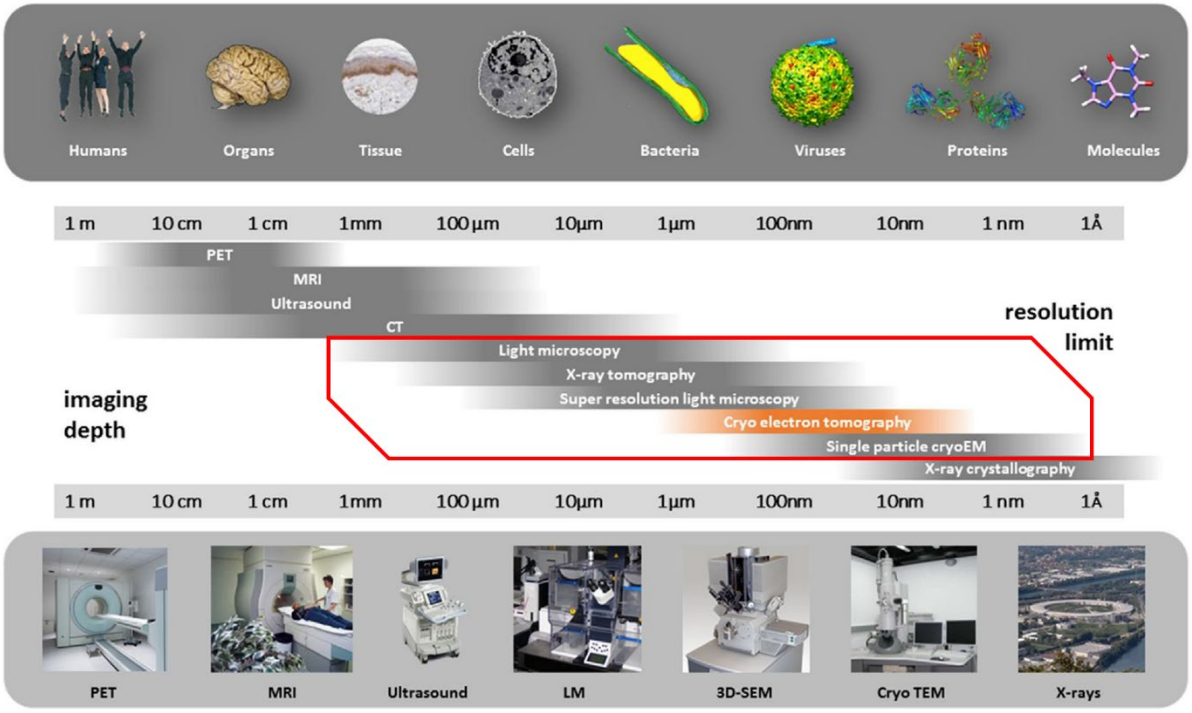

Figure 25. Comparison of the imaging depth and maximum resolution of the different imaging methods. In the red box, the methods which are of interest to study bacteria (i.e., VLM, cryo-SXT, Super-resolution VLM, TET and single particle cryoEM). Adapted from (Koning, Koster, and Sharp 2018).

The preparation of bacterial cell samples and analysis using cryo-SXT is described in detail in the Publication 3 (Cossa, Wien, et al. 2022).

PUBLICATION 3

"Evaluation of the Role of Bacterial Amyloid on Nucleoid Structure Using Cryo-Soft X-Ray Tomography."

In *Bacterial Amyloids*, 2538:319–33. Methods in Molecular Biology. New York, NY: Springer US. 2022. https://doi.org/10.1007/978-1-0716-2529-3_21.

Cossa Antoine, Frank Wien, Florian Turbant, Tadeusz Kaczorowski, Grzegorz Węgrzyn, Véronique Arluison, Ana J. Pérez-Berná, Sylvain Trépout, and Eva Pereiro.

Chapter 21

Evaluation of the Role of Bacterial Amyloid on Nucleoid Structure Using Cryo-Soft X-Ray Tomography

Antoine Cossa, Frank Wien, Florian Turbant, Tadeusz Kaczorowski, Grzegorz Węgrzyn, Véronique Arluison, Ana J. Pérez-Berná, Sylvain Trépout, and Eva Pereiro

Abstract

Bacterial chromosomal DNA is packed within a non-membranous structure, the nucleoid, thanks to nucleoid associated proteins (NAPs). The role of bacterial amyloid has recently emerged among these NAPs, particularly with the nucleoid-associated protein Hfq that plays a direct role in DNA compaction. In this chapter, we present a 3D imaging technique, cryo-soft X-ray tomography (cryo-SXT) to obtain a detailed 3D visualization of subcellular bacterial structures, especially the nucleoid. Cryo-SXT imaging of native unlabeled cells enables observation of the nucleoid in 3D with a high resolution, allowing to evidence in vivo the role of amyloids on DNA compaction. The precise experimental methods to obtain 3D tomograms will be presented.

Key words Bacterial amyloid, Nucleoid, Cryo-tomography, X-ray imaging

1 Introduction

Most bacterial amyloids are extracellular proteins involved in various processes such as the formation of biofilms, contribution to bacterial virulence, and antibiotic resistance [1]. Nevertheless, there are also examples of intracellular amyloids occurring in bacterial cells and taking part in DNA shaping and DNA-related processes.

One example of an amyloid-like protein involved in DNA transactions is RepA, encoded by the *Pseudomonas savastanoi* plasmid pPS10, and especially its N-terminal amyloid-like domains called "winged-helix" (WH) – WH1 [2]. RepA is the principal regulator of plasmid DNA replication. It is necessary for initiating replication and it stimulates this process by binding to specific sequences and promoting conformational changes crucial for the starting of DNA synthesis [3]. Nevertheless, this protein also

Véronique Arluison et al. (eds.), *Bacterial Amyloids: Methods and Protocols*,
Methods in Molecular Biology, vol. 2538, https://doi.org/10.1007/978-1-0716-2529-3_21,

ensures negative regulation of plasmid replication through the so-called "handcuffing" mechanism, operating by coupling two origin regions of sister plasmid molecules, mediated by the WH1 domains, thus preventing over-initiating plasmid DNA synthesis [4]. Furthermore, conformational changes within RepA appear to play crucial roles in switching between stimulatory and inhibitory functions of this protein. The amyloid-like WH1 domains are major players in these processes [5].

Another example is that of the master regulator Hfq, which occurs in many bacterial species, including *Escherichia coli*, in which the functions of this protein are studied most intensively. Hfq C-terminal region (CTR) forms an amyloid-like structure [6]. This feature of Hfq-CTR has been discovered only recently [7, 8], while having an important influence on understating its previously unknown functions like interactions with DNA and making the structure of this molecule more compact and condensed [9, 10]. Indeed, nucleoid-associated proteins (NAPs) such as Hfq bind to DNA, thereby modifying their mechanical properties and structural reorganization. In the case of Hfq, this occurs by bridging interactions between different segments of the same or different portions of DNA [11, 12].

Interestingly, the supercoiling of plasmid DNA is affected by mutations in the *hfq* gene [13, 14], which might partially explain the previously observed effects on the replication process [15]. The global structure of DNA can also be modified by this amyloid-like protein, mainly due to the local alignment of nucleoprotein fibers [16]. Untypical DNA structures like G-quadruplex may also be bound by Hfq, which stabilizes them [17, 18], by playing a potential role in modulating the features of the nucleoid. Considering these facts, it is likely that genomic instability might be partially dependent on Hfq-CTR functions [17–19]. These Hfq-DNA complexes may finally also induce DNA cross-linking and entanglements, and eventually increase the density and viscoelasticity within the nucleoid [20].

This chapter presents cryo-soft X-ray tomography (cryo-SXT) as a powerful method to assess how bacterial amyloids may influence nucleoid structure in vivo, measuring nucleoid volume and density. Furthermore, this chapter shows how it can be used to study the effects of amyloids on bacterial physiology without the need for DNA or protein labeling.

2 Materials

The protocol presented here has been optimized for analyzing *E. coli* cells, although it can be adopted for any bacterial species, with modification of growing conditions and culture media depending on the bacteria of interest.

2.1 Common Material, Chemicals, and Bacterial Media

2.1.1 Bacterial Culture Media

1. LB-rich medium for bacterial growth [21].
2. To observe the effect of starvation, use supplemented M9 minimal medium (for instance, glycerol 0.2%, vitamins, and casamino acids 50 μg/mL) [21].
3. Cold non-supplemented M9 minimal medium for rinsing bacteria.

2.1.2 Laboratory Equipment

The standard laboratory equipment required includes the following:

1. Micropipettes.
2. Eppendorf tubes.
3. Culture tubes allowing correct oxygenation of cells.
4. Incubator for bacterial growth.
5. Spectrophotometer (to follow bacterial growth at OD_{600}).
6. Parafilm.
7. Glass slides.

2.1.3 Chemicals

1. Sterile water.

2.2 Bacterial Strains

Any *E. coli* genetic background (such as MG1655) can be used for this analysis.

To observe the effect of a mutation in a gene encoding a bacterial amyloid, a strain deleted for the gene of interest (such as *Δbfq* [14]) can be constructed using the λ Red system [22].

Alternatively, transduction of the mutated gene of interest can be performed using a strain from the Keio collection if available [23].

Selected transductants must be subjected to chromosomal DNA sequencing of the gene of interest region to confirm the presence of wild-type (WT) or deleted/mutated alleles.

2.3 Preparation of Samples for Cryo-imaging

1. Cryo-EM grids (Fig. 1c): holey carbon-coated gold or copper Quantifoil® Finder grids R2/2 (Quantifoil Micro Tools GmbH, Jena, Germany). Finder grids are recommended for an easier area of interest recovery and correlative studies.
2. A glow-discharger to make the carbon layer of the cryo-EM grids hydrophilic, which is an essential prerequisite step for good sample adsorption on the grids.
3. Manual or automated plunge-freezer for the fast cryo-fixation of the sample on the grid. Note that an automated plunge-freezer can be preferred for additional temperature and humidity control.

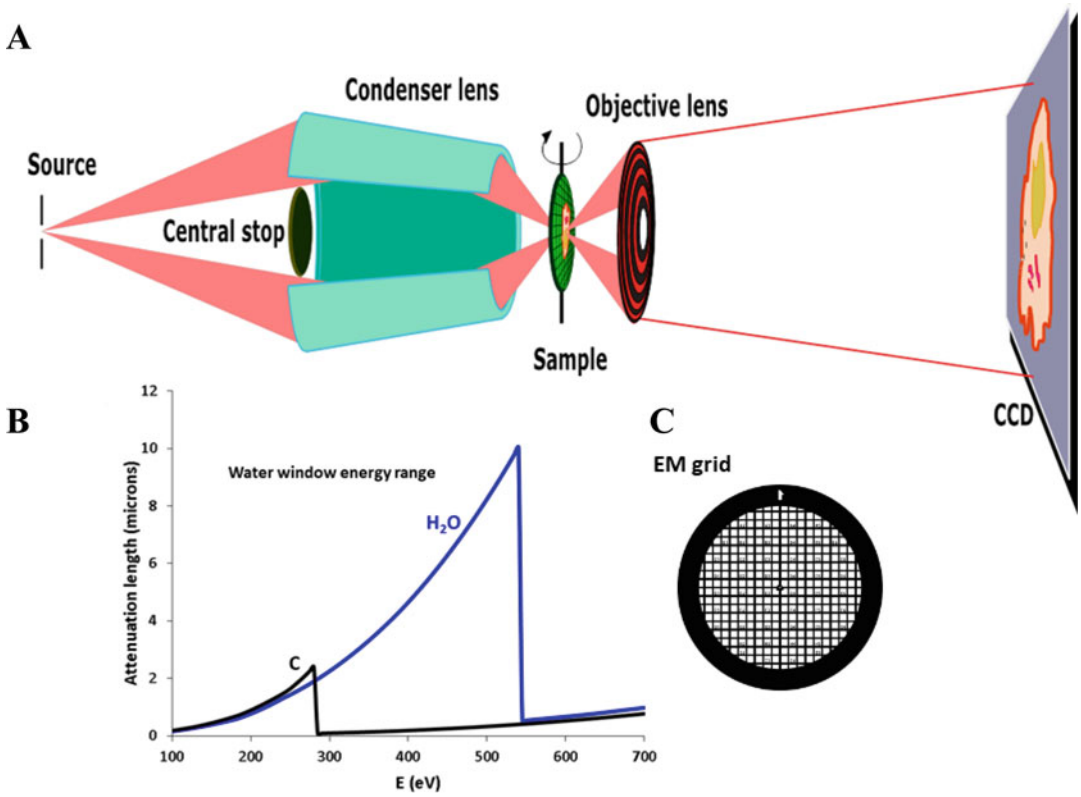

Fig. 1 Overview of the transmission X-ray microscope and its operation principle. (**a**) Schematic representation of the transmission X-ray microscope (TXM). (**b**) Attenuation coefficients of carbon and water – the water window is situated between the absorption K-edges of carbon and oxygen. (**c**) Electron microscopy grid

4. 60 nm or 100 nm gold beads used as fiducial markers (or a mix of both, *see* **Note 1**).
5. Precision and anti-capillary tweezers.
6. Whatman filter paper.

2.4 Cryo-SXT Beamline

Cryo-SXT beamlines are available in different synchrotron facilities: e.g., ALBA/MISTRAL beamline (Barcelona, Spain) [24], Diamond/B24 (Didcot, UK) [25], ALS (Berkeley, USA) [26], HZB (Berlin, Germany) [27], and TPS/24A under construction (Hsinchu, Taiwan).

Beamtime can be obtained through peer-reviewed applications twice a year in most of the above-mentioned beamlines.

2.5 Cryo-TEM

Before the cryo-SXT analysis, we strongly suggest checking vitreous ice quality (*see* **Note 2**) and gold beads and bacteria distribution using a transmission electron microscope with cryo-capabilities (cryo-TEM). To do this, a field emission gun cryo-TEM operating at 200 or 300 kV and equipped with an energy filter (in-column or post-column filter), and a CCD camera or preferentially a direct electron detector camera are recommended.

2.6 Hardware and Software

1. A powerful workstation preferentially equipped with a CUDA-capable GPU and at least 32GB of RAM.
2. IMOD eTomo software [28].
3. Tomo3D software [29].
4. MATLAB (Mathworks Inc).
5. R (https://www.R-project.org/) [30].
6. ChimeraX for data visualization [31].

3 Methods

3.1 Culture Conditions

For the studies presented in this chapter, we used *E. coli* MG1655 (WT, reference strain) and its *Δhfq* amyloid-devoid mutant [14].

For exponential phase cells, bacteria are grown in LB-rich media until they reach an OD_{600} of 0.4. For the (mid)stationary phase, an overnight culture at OD_{600} of 1.5 is analyzed (*see* **Note 3**).

The late stationary phase (OD_{600} depends on the genetic background) can also be analyzed even if bacterial cell morphology and survival may be strongly affected (*see* **Notes 4–6**).

A total of 1.5 mL of culture is centrifuged and washed twice with non-supplemented M9 minimal medium. Then the cells are resuspended in a non-supplemented M9 medium and stored at 4 °C to stop the growth. Finally, dilutions (still in non-supplemented M9) are performed to reach a final OD_{600} of 0.7 for all strains and conditions of growth. The bacteria are then processed for cryo-SXT experiments.

3.2 Sample Preparation for Cryo-Soft X-Ray Tomography

1. Au or Cu carbon-coated Quantifoil® Finder grids are first glow-discharged using plasma.
2. Prior deposition on the grids, 10 μL of each sample condition at 0.7 OD_{600} is mixed with 15 μL of 100 nm gold beads and 5 μL of M9 minimal medium (*see* **Note 7**).

   Fiducial markers enable projections alignment to the common axis of rotation prior to tomographic reconstruction.
3. 5 μL of the sample is deposited on the carbon side of the grid.
4. The excess of the solution is manually blotted using a Whatman filter paper.
5. The grid is plunge-frozen into liquid ethane and cooled down at −174 °C by liquid nitrogen in a cryo-plunger. (If using an automated plunge-freezer, **steps 4 and 5** need to be set in the machine parameters in addition to specific chamber humidity and temperature values).
6. We strongly recommend preparing at least three or four grids per condition.

7. Before SXT analysis, a few grids are screened with a cryo-transmission electron microscope to assess the bacterial concentration and the fiducial distribution on the grid, verify the absence of ice crystals, and evaluate the ice thickness. As cryo-TEM is rather destructive, it is not recommended to use the same grid for cryo-SXT analysis, and we suggest preparing several grids in the same condition.
8. Alternatively the grids can be screened at Mistral using a cryo-visible light microscope (Linkam cryo-stage CMS196 coupled to an Axioscope from Zeiss).

3.3 Cryo-Soft X-Ray Tomography

Cryo-SXT datasets shown here were acquired at the ALBA synchrotron Light Source (Barcelona, Spain) on the transmission X-ray microscopy beamline Mistral (Fig. 1a). Cryo-SXT allows to image cells in near-native conditions within the water window energy range (between the carbon and the oxygen K-absorption edges) (Fig. 1b) as water layers of up to 10 μm can be penetrated, while carbon-rich structures can be imaged with high absorption contrast.

It is a quantitative imaging technique that allows the reconstruction of the linear absorption coefficients (LAC) of the sample's material following the Beer-Lambert law (Eq. 1):

$$\text{Transmission} = I_{\text{norm}} = \frac{I}{I_0} = e^{-\int \mu_l(x,y,z)dz} \tag{1}$$

where I_0 is the intensity impinging on the sample.

The linear absorption coefficient μ_l (μm^{-1}), which is the reconstructed value in the tomograms (*see* **Note 8**), relates to the mass absorption coefficient μ ($\mu m^2/g$) of the material and its density ρ ($g/\mu m^3$).

$$\text{Voxel} = \mu_l = \mu\rho = -\ln\left(\frac{I}{I_0}\right) \tag{2}$$

1. Four samples are mounted in specific holders on a shuttle in a liquid nitrogen workstation. The holders are then covered to prevent ice contamination, transferred to a low vacuum transfer chamber, and finally to the cryo-transmission X-ray microscope (cryo-TXM) (Fig. 1a) experimental vacuum chamber (10^{-7} mbar), preserving cryo-conditions throughout the transfer.
2. Once inside the cryo-cooled TXM vacuum chamber, one of the holders is positioned at the sample stage from the shuttle with a specific robot arm after removing the cover, protecting the grid. Once at the sample stage, the grid is positioned on the rotation axis and the focal plane.

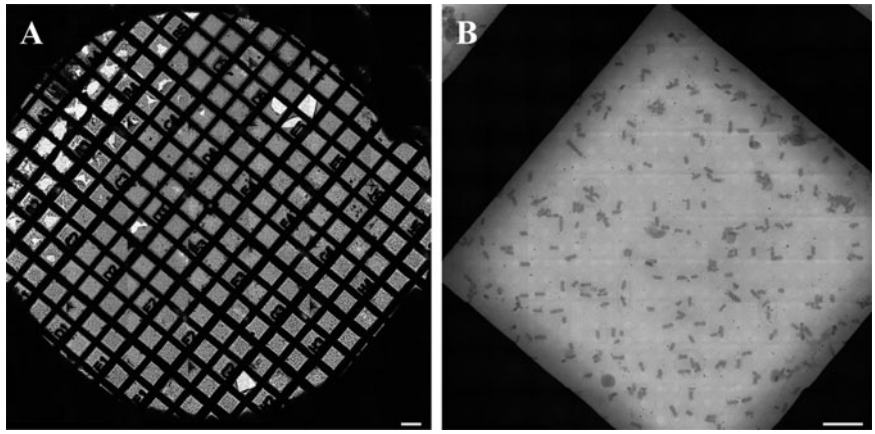

Fig. 2 Pre-acquisition mosaics. (**a**) Full grid mosaic using the online visible light microscope in bright field mode. (**b**) Zero-degree soft X-ray transmission mosaic to select areas of interest (grid square in (**a**)). Scale bars represent 100 μm (**a**) and 10 μm (**b**)

3. Areas of interest on the grids (i.e., thin non-broken and non-crystalline ice) are selected using a visible light microscope online with the transmission X-ray microscope (Fig. 2a).
4. Then, those areas are individually screened by acquiring zero-degree soft X-ray projection mosaics to find the best regions for individual bacteria acquisitions (Fig. 2b).
5. The data presented here was collected using a 25 nm objective Fresnel zone-plate (ZP) to image the transmission signal on a direct illuminated CCD camera (1024 × 1024 pixels, camera pixel size = 13 μm). Note that a 40 nm objective Fresnel ZP is also available on the Mistral beamline and is used for thicker cells.
6. Tilt series are usually collected with an increment of 1° between two projections. The minimal and maximal achievable tilt angles will depend on the position of the region of interest within the grid (i.e., far from the square borders is best) and can range from ±65° (or ± 70° using the 40 nm ZP). Generally, a ± 60° tilt range delivers good results.
7. Magnifications of 1300× and 1650× can be used, with corresponding image pixel sizes of 10 nm and 8 nm, respectively.
8. Usually, a total of around 10 tomographic tilt-series corresponding to 10 cells are acquired for each sample condition.
9. At the end of each tilt-series acquisition, 10 images without sample (a hole in the grid is chosen or the sample holder is removed when no holes are available) are collected for normalization purposes. This is commonly called a flat field

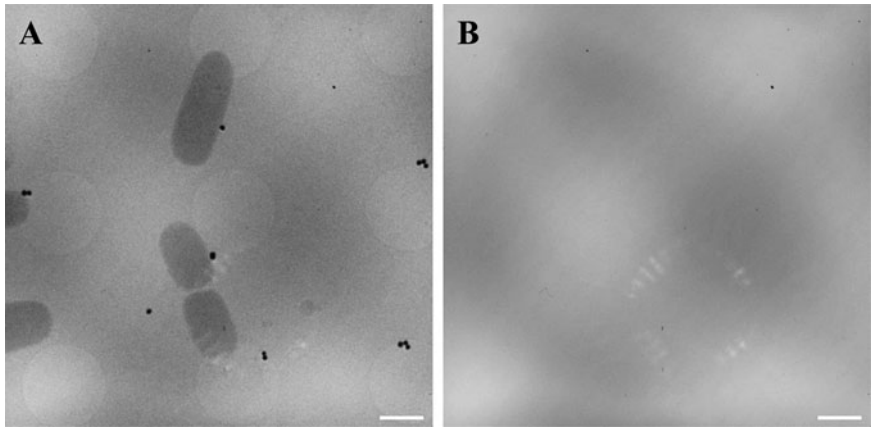

Fig. 3 X-ray projection images. (**a**) Zero-degree projection image from a tilt series. (**b**) Average of 10 flat field images. Scale bars represent 1 μm

(FF) acquisition, which is an image of the incoming beam I_0 in Eq. 1 (Fig. 3b). The FF is dependent on the electron beam intensity of the synchrotron storage ring running in top-up mode and thus fluctuates slightly over time between re-injections occurring every 20 min.

3.4 Cryo-SXT Tilt-Series Processing, Alignment, and Reconstruction

1. First, each tilt series is normalized to correct for the exposure time (when different exposures are used during the tilt series, for instance, longer exposures can be used at high tilt angle) and the non-uniformity of the incident X-ray beam using an average of 10 flat field images.
2. The normalization from Eq. 1 considers the averaged FF, electron beam currents (of the synchrotron storage ring, which is in top-up mode with electron refill every 20 min), and exposure times as denoted in the following equations:

$$I_0 = \frac{1}{N^{\mathrm{FF}}} \sum_{i}^{N} \frac{\mathrm{FF}_i - \mathrm{DF}^{\mathrm{avg}}}{t_{\mathrm{exp}}^{\mathrm{FF}} \times I_{e^-_{\mathrm{beam}}}} \tag{3}$$

$$I = \frac{I_{\mathrm{img}} - \mathrm{DF}^{\mathrm{avg}}}{t_{\mathrm{exp}} \times I_{e^-_{\mathrm{beam}}}} \tag{4}$$

where i is the i^{th} flat field image and I_0 is the normalized averaged flat field image (in our case, equal to 10 images for each tilt series (N^{FF})). Each sample images and flat field images are corrected with the CCD background (Dark Field, DF), which is automatically subtracted by the TXM software and normalized by the exposure times (t_{exp}) and the electron beam currents ($I_{e^-_{\mathrm{beam}}}$).

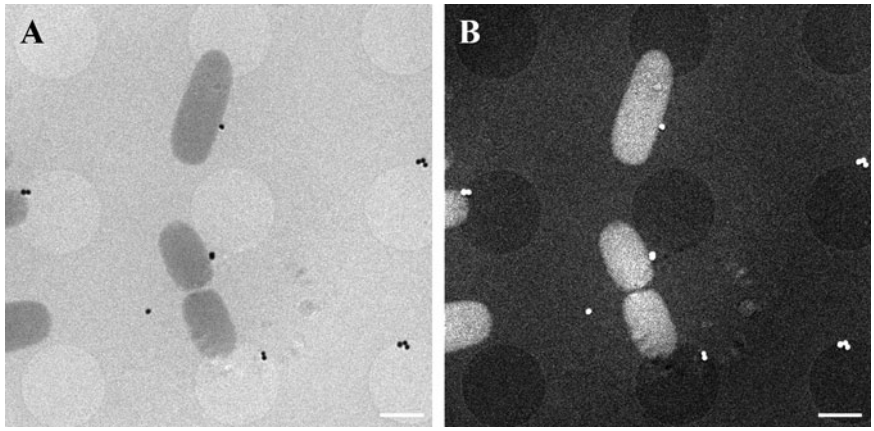

Fig. 4 Normalized transmission and absorbance images. (**a**) Normalized zero-degree transmission image. (**b**) The absorption image computed from (**a**). Scale bars represent 1 μm

3. The absorption signal is then computed by applying a negative Napierian logarithm to all the normalized tilt series (Fig. 4b) before 3D reconstruction.
4. Tilt-series preprocessing can be done onsite using available scripts to convert raw data from the TXM into hdf5 normalized tilt-series files.

Note that a complete description of the online acquisition process and data processing has been described in Groen et al. 2021 [32].

A homemade bash script (based on Mistral's GitHub code) is used to extract the tilt series from the hdf5 files automatically (into MRC file format), compute the absorption signal, and generate aligned tilt series using IMOD command lines [28] to automatically perform the detection, tracking, and alignment of gold fiducials. Finally, the 3D volumes are reconstructed using SIRT (Simultaneous Iterative Reconstruction Technique) from Tomo3D without long object compensation [29] (in our case, 30 iterations were used). This method has the advantage of a relatively fast computation.

5. The 3D volumes are then inspected to assert the alignment quality. If the result is not satisfying, a manual refinement is performed in IMOD (*see* **Note 9**).
6. The absorption tilt-series are reconstructed using ART (Algebraic Reconstruction Technique) or SIRT for recovering LAC values [32, 33].
7. After 3D reconstruction, the voxel values are divided by the pixel size of the original projections to get the LAC values in μm^{-1}.

3.5 Data Processing and Segmentation

Two conjoint MATLAB and R scripts are used to compute the semi-automatic segmentation of the nucleoids, which is distinguishable, thanks to the differential absorption.

1. The first MATLAB script lets the user click the poles of each bacterium of interest on the central Z-section of each reconstructed tomogram (Fig. 5a) to generate pairs of [X, Y] coordinates (red crosses).

Then each selected bacterium is automatically cropped into a subvolume (Fig. 5b) and rotated in-plane along the horizontal axis (Fig. 5c). Following that, each subvolume is rotated to the YZ axis, and the average of the five central slices is displayed for the user to draw an ellipse representing the bacterium (Fig. 5d). This step allows the script to automatically center the bacterium in the subvolume using the center of mass of the ellipse. A sphero-cylinder (i.e., rod shape) is fitted to each bacterium using the bacterium center, width and length metrics computed from the previous step. Voxel values outside the bacterium are set to NaN (Not a Number)

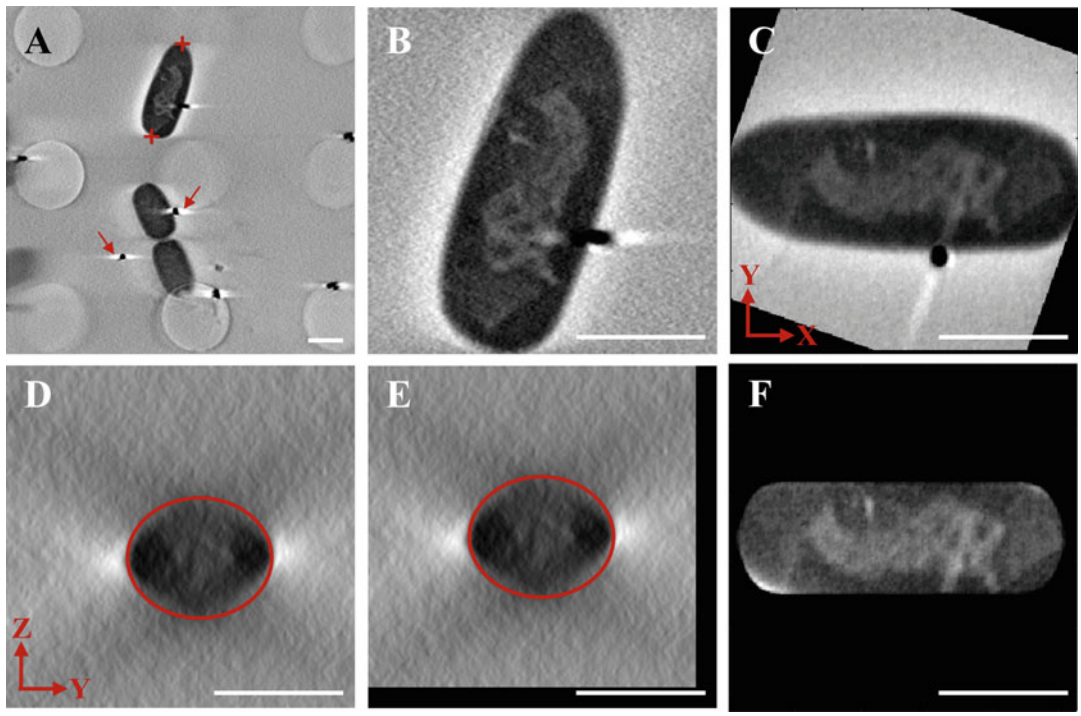

Fig. 5 Semi-automated nucleoid segmentation workflow. (**a**) Bacteria poles clicking (red crosses). Gold beads reconstruction artifacts due to the missing wedge (red arrows). (**b**) Each bacterium is cropped into a subvolume using the coordinates of (**a**). (**c**) The bacterium is automatically placed along the horizontal axis of the subvolume. (**d**) Five slices of the central YZ plane are averaged and displayed to let the user trace an ellipse representing the bacterium. (**e**) The bacterium is automatically centered in the subvolume using the center of mass of the ellipse. (**f**) A sphero-cylinder mask is fitted on the bacterium. Scale bars represent 1 μm

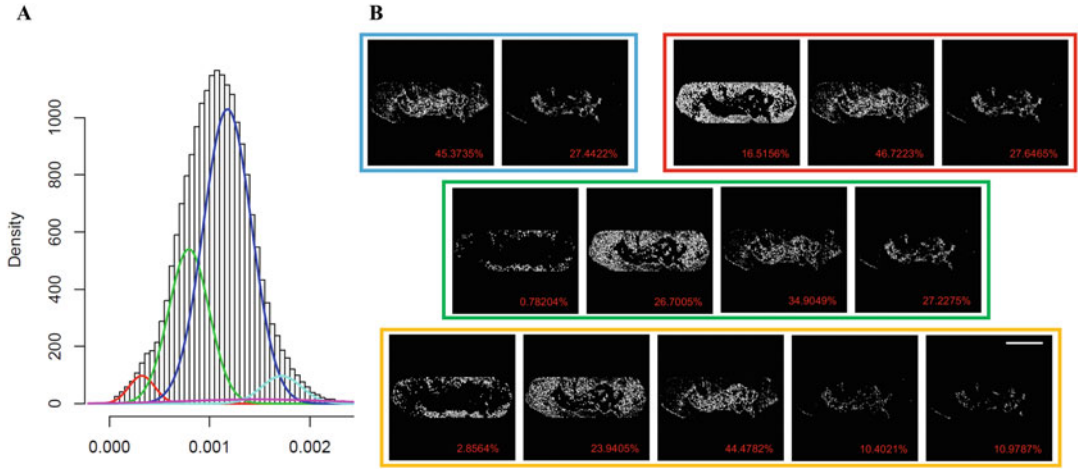

Fig. 6 Semi-automatic segmentation of the nucleoid voxels. (**a**) Gaussian mixture fitting of 5 Gaussians on the cropped bacteria histogram from Fig. 5. (**b**) Segmentation results of the Gaussian fittings. Fitting of two Gaussians in blue, three in red, four in green, and five in orange. Scale bar represents 1 μm

to ease further computations. Finally, a 3D median filter (using a [3,3,3] kernel) is applied to smooth the voxel values before exporting them as a text file.

2. Then masked voxel values are imported in R where a Gaussian mixture model (GMM) fitting is computed to separate the different voxels populations of each masked bacterium (i.e., nucleoid, cytoplasm, membranes, or gold beads) on the histogram (Fig. 6a) using the Mixtools package [34]. Four GMMs are fitted to each bacterium histogram (i.e., 2, 3, 4, and 5 Gaussians) (Fig. 6b). Then the different populations of voxels from the GMM segmentations are exported.
3. A visual inspection is now required to assess which population of the different models represents the nucleoid as best as possible (Fig. 6b). If no population is satisfying enough, the bacterium is discarded from the analysis. The reasons for this are often that the focus tracking was not good enough during data collection (bacteria far from the rotation axis are out of focus at high tilt angles due to the depth of field of the lens) or that too many gold beads are present close to the bacteria, which generate artifacts (white halo, see Fig. 5a) due to the Au high absorption and the missing wedge in the 3D volume reconstruction.
4. A final step of several erosions and dilations is performed to discard the wrongly attributed voxels, lonesome cytoplasm voxels are eliminated, and tiny holes in the nucleoid are recovered. The final volume is exported and statistical analysis on the volume and LAC values is now possible.
5. Visualization is done using ChimeraX.

3.6 LACs Visual Representation

1. To bring out the global tendency of the LAC values of the nucleoids between different strains and conditions, it is possible to compute the averaged LAC histograms per condition using R. LAC values of interest are found between 0.15 and 0.30 μm^{-1} (this might not be the case for other types of bacteria). This range is then divided into intervals of 0.001 (*see* **Note 10**). For each condition, the voxels of each bacterium fitting into an interval are counted and converted into the corresponding volume value using the pixel size of the original images. For each interval, the counts are normalized using the formula $\frac{(x-x_{min})}{(x_{max}-x_{min})}$ to have (artificial) volume values between 0 and 1. And then the average and standard deviation of each interval are computed (*see* **Note 11**).

4 Notes

1. While 100 nm gold fiducials are commonly used for cryo-SXT, a mix of 60 nm and 100 nm can be used as the 60 nm beads provide a more precise tracking position for tilt-series alignment but usually not seen in all projections (because not in focus), whereas 100 nm beads can be tracked on all projections but with a little less precision.
2. Bacteria distribution and ice quality can be checked with a cryo-visible light microscope. Nevertheless, beads cannot be visualized using light microscopy.
3. Note that WT and mutant strains may not grow similarly; mutant strains may grow slower than their WT counterpart.
4. Be sure to verify the presence of the desired mutation in the tested strain by DNA sequencing after constructing the mutant by transduction. The recombination processes in bacterial cells may sometimes lead to the presence of the genetic marker in an unexpected genome region while leaving the gene of interest intact or only partially inactivated.
5. It is a good practice to confirm the effects of the tested mutation by conducting complementation experiments, i.e., to provide the WT form of the gene of interest *in trans* (for example, expressed from a plasmid) in the mutant. Restoration of the WT phenotype in such a complementation experiment excludes any possible polar effects of the mutation, i.e., the influence of the mutation on the neighbor (usually downstream-located) genes that might give specific phenotypic effects. However, be careful to interpret the data (including analysis of the images) due to the presence of plasmids in cells that can modulate interactions of amyloids with the chromosome by competing for amyloid binding.

6. The analysis of the late stationary phase may be difficult for some mutants; for instance, the case for the MG1655-*Δhfq* strain due to the effect of Hfq on σ^S (the stationary phase sigma factor) expression [35].
7. The gold beads may tend to stick to the Gram(−) bacteria's outer membrane, generating reconstruction artifacts in the final volumes. To avoid this, it may be preferable to deposit the gold beads on the grid before depositing the bacterial sample. In total, 5 μL of the 100 nm gold beads solution can be deposited on each grid after being glow-discharged and set to dry overnight in a dry and dust-free environment. Then the grids are glow-discharged a second time prior to the deposition of the bacterial sample. The situation might be different for Gram(+) bacteria.
8. When using flat sample supports, tomographies of 180 degrees projections cannot be acquired. This is the well-known problem of the missing wedge (similarly as in electron tomography) which will affect the resolution of the final volume and the LAC reconstructed values. Note that absolute LAC recovery is affected not only by the missing wedge, if any, but also by the resolution achieved with the instrument, the algorithm used (e.g., ART and SIRT), and even its implementation in the different software available. Studies will therefore focus on the discussion of LAC differences among cell conditions.
9. If gold bead fiducials or high contrast ice contaminations are present close to bacteria, they might produce reconstruction artifacts, thus creating a bias in the interpretation of the LAC values. It is possible to attenuate (or even remove) those artifacts by masking the fiducials from the aligned tilt series using IMOD goldbead removal tool, or inpainting methods such as discrete cosine transform (DCT) [36], or iterative artifacts removing using MaskTomRec [37].
10. It is possible to use other interval steps such as 0.01 but, in our experience, interval steps of 0.001 between LAC values seem to give more accurate results.
11. Note that this type of representation does not enable the direct comparison of the nucleoid volumes because of the normalization but is rather a way to better see the shifts in absorption between conditions.

Acknowledgments

This work was supported by CNRS, CEA, Synchrotron SOLEIL. This study contributes to the IDEX Université de Paris ANR-18-IDEX-0001. SXT measurements at the ALBA Synchrotron were performed under proposal 2018082926. This work was supported by a public grant overseen by the French National Research Agency (ANR) as part of the « Investissements d'Avenir » program, through the "ADI 2019" and "ADI 2021" project funded by the IDEX Paris-Saclay, ANR-11-IDEX-0003-02 (AC & FT). We are grateful to Etienne Lebrun (LLB, CEA Saclay) for his help at an early stage of this work.

References

1. Giraldo R (2020) SynBio and the boundaries between functional and pathogenic RepA-WH1 bacterial amyloids. mSystems 5(3): e00553
2. Torreira E, Moreno-Del Alamo M, Fuentes-Perez ME, Fernandez C, Martin-Benito J, Moreno-Herrero F, Giraldo R, Llorca O (2015) Amyloidogenesis of bacterial prionoid RepA-WH1 recapitulates dimer to monomer transitions of RepA in DNA replication initiation. Structure 23(1):183–189
3. Giraldo R, Fernandez-Tresguerres ME (2004) Twenty years of the pPS10 replicon: insights on the molecular mechanism for the activation of DNA replication in iteron-containing bacterial plasmids. Plasmid 52(2):69–83
4. Gasset-Rosa F, Diaz-Lopez T, Lurz R, Prieto A, Fernandez-Tresguerres ME, Giraldo R (2008) Negative regulation of pPS10 plasmid replication: origin pairing by zipping-up DNA-bound RepA monomers. Mol Microbiol 68(3):560–572
5. Giraldo R, Fernandez C, Moreno-del Alamo M, Molina-Garcia L, Revilla-Garcia A, Sanchez-Martinez MC, Gimenez-Abian JF, Moreno-Diaz de la Espina S (2016) RepA-WH1 prionoid: clues from bacteria on factors governing phase transitions in amyloidogenesis. Prion 10(1):41–49
6. Cech GM, Szalewska-Palasz A, Kubiak K, Malabirade A, Grange W, Arluison V, Wegrzyn G (2016) The Escherichia Coli Hfq protein: an unattended DNA-transactions regulator. Front Mol Biosci 3:36
7. Fortas E, Piccirilli F, Malabirade A, Militello V, Trepout S, Marco S, Taghbalout A, Arluison V (2015) New insight into the structure and function of Hfq C-terminus. Biosci Rep 35(2):e00190
8. Partouche D, Militello V, Gomez-Zavaglia A, Wien F, Sandt C, Arluison V (2019) In situ characterization of Hfq bacterial amyloid: a Fourier-transform infrared spectroscopy study. Pathogens 8(1):36
9. Malabirade A, Jiang K, Kubiak K, Diaz-Mendoza A, Liu F, van Kan JA, Berret JF, Arluison V, van der Maarel JRC (2017) Compaction and condensation of DNA mediated by the C-terminal domain of Hfq. Nucleic Acids Res 45(12):7299–7308
10. Beaufay F, Amemiya HM, Guan J, Basalla J, Meinen BA, Chen Z, Mitra R, Bardwell JCA, Biteen JS, Vecchiarelli AG, Freddolino PL, Jakob U (2021) Polyphosphate drives bacterial heterochromatin formation. Sci Adv 7(52): eabk0233
11. Jiang K, Zhang C, Guttula D, Liu F, van Kan JA, Lavelle C, Kubiak K, Malabirade A, Lapp A, Arluison V, van der Maarel JR (2015) Effects of Hfq on the conformation and compaction of DNA. Nucleic Acids Res 43(8):4332–4341
12. Wiggins PA, Dame RT, Noom MC, Wuite GJ (2009) Protein-mediated molecular bridging: a key mechanism in biopolymer organization. Biophys J 97(7):1997–2003
13. Tsui HC, Leung HC, Winkler ME (1994) Characterization of broadly pleiotropic phenotypes caused by an *hfq* insertion mutation in *Escherichia coli* K-12. Mol Microbiol 13:35–49
14. Malabirade A, Partouche D, El Hamoui O, Turbant F, Geinguenaud F, Recouvreux P, Bizien T, Busi F, Wien F, Arluison V (2018) Revised role for Hfq bacterial regulator on DNA topology. Sci Rep 8(1):16792

15. Cech GM, Pakula B, Kamrowska D, Wegrzyn G, Arluison V, Szalewska-Palasz A (2014) Hfq protein deficiency in Escherichia coli affects ColE1-like but not lambda plasmid DNA replication. Plasmid 73:10–15
16. Wien F, Martinez D, Le Brun E, Jones NC, Vronning Hoffmann S, Waeytens J, Berbon M, Habenstein B, Arluison V (2019) The bacterial amyloid-like Hfq promotes in vitro DNA alignment. Microorganisms 7(12):639
17. Parekh VJ, Wien F, Grange W, De Long TA, Arluison V, Sinden RR (2020) Crucial role of the C-terminal domain of Hfq protein in genomic instability. Microorganisms 8(10):1598
18. Parekh VJ, Niccum BA, Shah R, Rivera MA, Novak MJ, Geinguenaud F, Wien F, Arluison V, Sinden RR (2019) Role of Hfq in genome evolution: instability of G-Quadruplex sequences in E. coli. Microorganisms 8(1):28
19. Chen J, Gottesman S (2017) Hfq links translation repression to stress-induced mutagenesis in E. coli. Genes Dev 31(13):1382–1395
20. El Hamoui O, Yadav I, Radiom M, Wien F, Berret J-F, van der Maarel JRC, Arluison V (2020) Interactions between DNA and the Hfq amyloid-like region trigger a viscoelastic response. Biomacromolecules 21(9): 3668–3677
21. Sambrook J, Fritsch EF, Maniatis T (1989) Molecular cloning: a laboratory manual, 2nd edn. CSHL Press
22. Datsenko KA, Wanner BL (2000) One-step inactivation of chromosomal genes in Escherichia coli K-12 using PCR products. Proc Natl Acad Sci U S A 97(12):6640–6645
23. Baba T, Ara T, Hasegawa M, Takai Y, Okumura Y, Baba M, Datsenko KA, Tomita M, Wanner BL, Mori H (2006) Construction of Escherichia coli K-12 in-frame, single-gene knockout mutants: the Keio collection. Mol Syst Biol 2(2006):0008
24. Sorrentino A, Nicolas J, Valcarcel R, Chichon FJ, Rosanes M, Avila J, Tkachuk A, Irwin J, Ferrer S, Pereiro E (2015) MISTRAL: a transmission soft X-ray microscopy beamline for cryo nano-tomography of biological samples and magnetic domains imaging. J Synchrotron Radiat 22(4):1112–1117
25. Harkiolaki M, Darrow MC, Spink MC, Kosior E, Dent K, Duke E (2018) Cryo-soft X-ray tomography: using soft X-rays to explore the ultrastructure of whole cells. Emerg Top Life Sci 2(1):81–92
26. Le Gros MA, McDermott G, Larabell CA (2005) X-ray tomography of whole cells. Curr Opin Struct Biol 15(5):593–600
27. Schneider G, Guttmann P, Rehbein S, Werner S, Follath R (2012) Cryo X-ray microscope with flat sample geometry for correlative fluorescence and nanoscale tomographic imaging. J Struct Biol 177(2):212–223
28. Kremer JR, Mastronarde DN, McIntosh JR (1996) Computer visualization of three-dimensional image data using IMOD. J Struct Biol 116(1):71–76
29. Agulleiro JI, Fernandez JJ (2011) Fast tomographic reconstruction on multicore computers. Bioinformatics 27(4):582–583
30. R core team (2020) R: a language and environment for statistical computing. R Foundation for Statistical Computing, Vienna Austria
31. Goddard TD, Huang CC, Meng EC, Pettersen EF, Couch GS, Morris JH, Ferrin TE (2018) UCSF ChimeraX: meeting modern challenges in visualization and analysis. Protein Sci 27(1): 14–25
32. Groen J, Sorrentino A, Aballe L, Oliete R, Valcarcel R, Okolo C, Kounatidis I, Harkiolaki M, Perez-Berna AJ, Pereiro E (2021) A 3D cartographic description of the cell by cryo soft X-ray tomography. J Vis Exp (169), e62190:1–17
33. Messaoudi C, Aschman N, Cunha M, Oikawa T, Sorzano CO, Marco S (2013) Three-dimensional chemical mapping by EFTEM-TomoJ including improvement of SNR by PCA and ART reconstruction of volume by noise suppression. Microsc Microanal 19(6):1669–1677
34. Benaglia T, Chauveau D, Hunter DR, Young D (2009) Mixtools: an R package for analyzing finite mixture models. J Stat Softw 32(6):1–29
35. Battesti A, Majdalani N, Gottesman S (2011) The RpoS-mediated general stress response in Escherichia coli. Annu Rev Microbiol 65: 189–213
36. Garcia D (2010) Robust smoothing of gridded data in one and higher dimensions with missing values. Comput Stat Data Anal 54(4): 1167–1178
37. Fernandez JJ, Laugks U, Schaffer M, Bauerlein FJ, Khoshouei M, Baumeister W, Lucic V (2016) Removing contamination-induced reconstruction artifacts from cryo-electron tomograms. Biophys J 110(4):850–859

4.2. Cryo-SXT applied to the analysis of Hfq mutant cells

As previously discussed in Chapter II, Hfq shapes and compacts DNA, nevertheless, this role has not been established *in vivo*. For this goal we compared the morphology of cells affected in Hfq expression. Precisely the bacterial strains used were MG1655 WT (Wild Type, reference strain), MG1655-Δ*hfq* and MG1655-Δ*ctr* (truncated protein with only the first 72 amino-acids) (Malabirade et al. 2018). The later strain was used because Hfq plays both direct and indirect roles on DNA structure. Indeed, Hfq mediates post-transcriptional regulation of NAP expression using small noncoding RNA (sRNA). Using this CTR-deleted form of the protein that should not be affected in riboregulation should help to discriminate direct and indirect effects on DNA structure (the NTR only should allow riboregulation). In Publication 4 below, using cryo-soft X-ray tomography imaging of native unlabelled cells and using a semi-automatic analysis and segmentation procedure, we show that Hfq significantly remodels the *E. coli* nucleoid.

PUBLICATION 4

"Cryo-Soft X-Ray Tomography to Explore Escherichia Coli Nucleoid Remodelling by Hfq Master Regulator."

In *Journal of Structural Biology*, 214 (4): 107912.

https://doi.org/10.1016/j.jsb.2022.107912 .

Cossa Antoine, Sylvain Trépout, Frank Wien, Johannes Groen, Etienne Le Brun, Florian Turbant, Laetitia Besse, Eva Pereiro, and Véronique Arluison.

Cryo soft X-ray tomography to explore *Escherichia coli* nucleoid remodeling by Hfq master regulator

Antoine Cossa[1,2]†, Sylvain Trépout[1,3]†*, Frank Wien[4], Johannes Groen[5], Etienne Le Brun[2], Florian Turbant[2,6], Eva Pereiro[5], Véronique Arluison[2,7]*

[1] Institut Curie, Université PSL, CNRS UAR2016, Inserm US43, Université Paris-Saclay, Multimodal Imaging Center, 91400 Orsay, France

[2] Laboratoire Léon Brillouin LLB, CEA, CNRS UMR12, Université Paris-Saclay, CEA Saclay, 91191 Gif-sur-Yvette, France

[3] Ramaciotti Centre for Cryo-Electron Microscopy, Monash University, Clayton, Victoria, 3800 Australia

[4] Synchrotron SOLEIL, L'Orme des Merisiers, Saint Aubin BP48, 91192, Gif-sur-Yvette, France

[5] Mistral Beamline, Alba Light Source, Cerdanyola del Valles, 08290 Barcelona, Spain

[6] Department of Molecular Biology, University of Gdansk, Wita Stwosza 59, 80-308 Gdansk, Poland

[7] Université Paris Cité, UFR Sciences du vivant, 75006 Paris cedex, France

† These authors contributed equally to this work

* To whom correspondence should be addressed. Tel: +33(0)169083282; Fax: +33(0)169089536; Email: veronique.arluison@u-paris.fr / veronique.arluison@cea.fr

Correspondence may also be addressed to sylvain.trepout@monash.edu

ABSTRACT

The bacterial chromosomic DNA is packed within a membrane-less structure, the nucleoid, due to the association of DNA with proteins called Nucleoid Associated Proteins (NAPs). Among these NAPs, Hfq is one of the most intriguing as it plays both direct and indirect roles on DNA structure. Indeed, Hfq is best known to mediate post-transcriptional regulation by using small noncoding RNA (sRNA). Although Hfq presence in the nucleoid has been demonstrated for years, its precise role is still unclear. Recently, it has been shown *in vitro* that Hfq forms amyloid-like structures through its C-terminal region, hence belonging to the bridging family of NAPs. Here, using cryo soft X-ray tomography imaging of native unlabeled cells and using a semi-automatic analysis and segmentation procedure, we show that Hfq significantly remodels the *Escherichia coli* nucleoid. More specifically, Hfq influences nucleoid density especially during the stationary growth phase when it is more abundant. Our results indicate that Hfq could regulate nucleoid compaction directly *via* its interaction with DNA, but also at the post-transcriptional level *via* its interaction with RNAs. Taken together, our findings reveal a new role for this protein in nucleoid remodeling *in vivo*, that may serve in response to stress conditions and in adapting to changing environments.

KEYWORDS: Nucleoid associated protein (NAP); functional amyloid; bacterial heterochromatin; DNA Bridging; X-ray high-resolution imaging; post-transcriptional regulation, noncoding RNA.

INTRODUCTION

Hfq is a pleiotropic regulator found in about 50% of sequenced Gram-positive and Gram-negative bacteria (Sun et al., 2002). While its function in Gram(+) is still unclear (Bouloc and Repoila, 2016), it was initially discovered as an *Escherichia coli* host factor required for bacteriophage Qβ RNA replication (Franze de Fernandez et al., 1968). Even if *hfq* is not an essential gene, its importance in RNA metabolism and in many related cellular functions was demonstrated by the observation of numerous adverse phenotypes in *hfq*$^-$ cells (Tsui et al., 1994). These unfavorable effects of *hfq* mutation are linked to the role of Hfq in the stimulation of RNA annealing, an activity called "RNA chaperone" (Arluison et al., 2007; Rajkowitsch et al., 2007). In particular, Hfq interacts with small non-coding RNAs (sRNAs) and facilitates base-pairing of sRNAs with their target mRNAs (Vogel and Luisi, 2011). The sRNA:mRNA complex formed typically inhibits mRNA translation and often lead to subsequent RNAs degradation (Aiba, 2007). Less frequently, sRNAs also activate RNA translation (McCullen et al., 2010). A well-known example of sRNA-based regulation consists of the annealing of MicA, a small noncoding RNA of *E. coli*, to *ompA* mRNA, which encodes an outer membrane porin (Udekwu et al., 2005). The roles of Hfq and sRNA are particularly important for bacterial stress resistance, when bacteria must survive in changing conditions (Gottesman, 2019; Gottesman et al., 2006). Indeed, Hfq is involved in bacterial virulence as it helps respond to new conditions encountered in the host during infection (Kendall et al., 2011; Porcheron and Dozois, 2015). This role of Hfq in virulence is illustrated with a *Vibrio cholerae* Δ*hfq* mutant that is highly attenuated in a mouse model infection (Ding et al., 2004). In turn, Hfq and sRNA are also involved in antibiotic resistance (Gaffke et al., 2021; Wang et al., 2021), bacterial communication and quorum sensing (Rutherford et al., 2015), two processes that could influence bacterial pathogenicity.

The RNA chaperone function of Hfq is primarily due to its N-terminal region (NTR). Indeed, this region of the protein adopts a typical fold, the Sm-fold (Wilusz and Wilusz, 2005). Structurally this fold is characterized by a secondary structure consisting of an α-helix followed by a twisted five-stranded β-sheet. This β-sheet allows the self-assembly of Hfq into its functional form, a ring-shaped homohexamer (Brennan and Link, 2007). The surface of the Sm ring comprising the N-terminal α-helices is designated as the proximal face; the opposite face is referred to as the distal face. Both surfaces of the NTR have been shown to bind RNAs with different specificities and affinities (Brennan and Link, 2007; Robinson et al., 2014; Sauer et al., 2012; Updegrove et al., 2016). In *E. coli*, each Hfq monomer consists of 102 amino acid residues in which the Sm/NTR region contains about 65 residues. But in addition to this NTR, Hfq also comprises a C-terminal region (CTR) of about 35 residues. The CTR region extends outside the NTR, at the periphery of the torus (Arluison et al., 2004) and is preferentially located at the proximal side of the torus (Wen et al., 2017). Structurally, this region has been described for years as intrinsically disordered and indeed, to date, its precise 3D structure is still unknown (Dimastrogiovanni et al., 2014; Orans et al., 2020; Vogel and Luisi, 2011). Recently, a new property has been discovered for this region as the CTR has been shown to be able to convert to an amyloid structure under certain conditions (Fortas et al., 2015; Partouche et al., 2019). Notably, the presence of a nucleic acid promotes this conversion from an intrinsically disordered region into an amyloid domain (Malabirade et al., 2018). This transition strengthens the hexameric structure (Arluison et al., 2004). The role of the CTR on RNA annealing is controversial. Nevertheless, it seems to be dispensable for most sRNA-based regulations (Arluison et al., 2004; Olsen et al., 2010), even if the lack of this CTR could affect a few sRNA-mediated regulations (Salim et al., 2012; Turbant et al., 2021a; Vecerek et al., 2008; Vincent et al., 2012).

Besides these RNA-related functions, Hfq has also been shown to interact with DNA (Takada et al., 1997) and is found in the nucleoid, i.e., the membrane-less compact structure where the bacterial chromosome is compacted by proteins (Dorman, 2014). Hfq thus belongs to the family of Nucleoid-Associated Proteins (NAPs), jointly with a dozen of other DNA-binding proteins (Azam and Ishihama, 1999; Dame et al., 2020; Dillon and Dorman, 2010; Dorman et al., 2020). Hfq's role in DNA structuring is unclear but it is the third most prevalent protein in the nucleoid during the exponential growth phase (Azam and Ishihama, 1999) and its concentration increases by a factor of two during the stationary phase (Diestra et al., 2009). While other NAPs such as H-NS (histone-like nucleoid structuring protein), HU (heat-unstable nucleoid protein), Dps (DNA-binding protein from starved cells) or IHF (integration host factor) seem to be uniformly distributed in the nucleoid, Hfq seems to have a heterogeneous localization pattern (Azam et al., 2000). Densely occupied regions have recently been evidenced in *E. coli* genome (referred as Extended Protein Occupancy Domains, EPOD) and may contain higher concentration of Hfq (Amemiya et al., 2021). As Hfq average concentration in the nucleoid is about 10-20% of total Hfq (~10-15 µM) (Azam and Ishihama, 1999; Diestra et al., 2009), its local concentration could thus locally reach tens to hundreds of µM. This high concentration could in turn favor the amyloid self-assembly of Hfq via its CTR (Milles et al., 2013).

Usually, NAPs have three DNA-binding modes which are: (*i*) bending (examples are HU, IHF, Dps), (*ii*) wrapping (i.e., leucine-responsive regulatory protein, Lrp) or (*iii*) bridging (H-NS). Hfq belongs to the third family of bridging NAPs and significantly compacts DNA (El Hamoui et al., 2020; Geinguenaud et al., 2011; Jiang et al., 2015; Malabirade et al., 2018; Verma et al., 2019; Wiggins et al., 2009). The Hfq bridging property presumably helps the bacterial chromosome (4.6 Mb, 1.5 mm long) to fit *in vivo* within the small bacterial nucleoid volume (~0.2 μm^3) (Skoko et al., 2006). While Hfq-NTR interacts non-specifically with the DNA

backbone (Orans et al., 2020), the compacting potential relies mainly on the CTR region of Hfq, independently of the Sm/NTR region (Jiang et al., 2015; Kubiak et al., 2022; Malabirade et al., 2017). Hfq-CTR may indeed drive bacterial heterochromatin formation (Beaufay et al., 2021). Hfq has a preference for A-tract repeats (Geinguenaud et al., 2011; Link et al., 2009; Updegrove et al., 2010), that are found regularly throughout bacterial DNA and may influence promoter efficiency (Aiyar et al., 1998; Tolstorukov et al., 2005). Hfq is thus presumably important for DNA packing in EPOD that are transcriptionally silent (Amemiya et al., 2021; Beaufay et al., 2021). Indeed, some phenotypic effects due to the lack of Hfq initially attributed to RNA regulation (Tsui et al., 1994) may be directly linked to defects in DNA-related processes (Cech et al., 2014; Chen and Gottesman, 2017; Gaffke et al., 2021; Haniford and Ellis, 2015; Kubiak et al., 2022; Le Derout et al., 2010; Parekh et al., 2019; Tsui et al., 1994). While numerous experiments point to an important role for Hfq and in particular of its CTR in DNA packaging (Beaufay et al., 2021), its precise influence on this process *in vivo* still remains poorly understood. To address this question, we used cryo Soft X-ray Tomography (cryo-SXT). This technique allows DNA imaging in 3D at high resolution (~ 30 nm half pitch) while preserving bacterial cells in a near-native state (Oton et al., 2016). Indeed, in contrast to eukaryotic cells, the lack of membrane surrounding the bacterial DNA makes its observation *in vivo* challenging without staining (for instance by using diamidino-phenylindole DAPI, (Hoff, 1988)). One major advantage of this technique, compared to super-resolution fluorescence techniques working below the diffraction limit (PALM/STORM, (Wang et al., 2011)) is to be able to analyze label-free DNA as DNA staining may influence its structure and compaction (Bettridge et al., 2021; Hammel et al., 2016; Remesh et al., 2020). Our cryo-SXT analysis demonstrates the influence of Hfq on nucleoid compaction in particular during the stationary growth phase of *E. coli*, and to illustrate the role of Hfq-CTR in this process. These results confirm a new mechanism of DNA bridging by a NAP using an amyloid structure in

vivo and unveil a novel function for Hfq in nucleoid remodeling that may help to adapt to changing environments.

MATERIALS AND METHODS

All chemicals, unless otherwise stated, were purchased from Sigma-Aldrich.

Bacteria strains and culture conditions

The bacterial strains used were MG1655 WT (Wild Type, reference strain), MG1655-Δ*hfq* and MG1655-Δ*ctr* (truncated protein with only the first 72 amino-acids) (Malabirade et al., 2018). The *hfq* gene region of these strains have been sequenced to confirm the presence of various *hfq* alleles (*hfq*$^+$, Δ*hfq* or Δ*ctr*). For exponential phase cells, bacteria were grown in LB rich media until they reached an OD_{600} of 0.4. For mid-stationary phase, an overnight culture with an OD_{600} 1.5 was analyzed. Note that strains do not grow similarly, especially MG1655-Δ*hfq* strain that grows more slowly. In addition, the analysis of late stationary phase is difficult in the case of Δ*hfq* strain, due to the effect of Hfq on σ^S. 1.5 mL of culture were centrifuged, washed in non-supplemented M9 minimal medium and then cells were resuspended in non-supplemented M9 medium and stored at 4°C to stop the growth. Dilutions were performed to reach a final OD_{600} of 0.7 for all strains and conditions of growth. The bacteria were then subsequently processed for cryo-SXT experiments.

Sample preparation for cryo soft X-ray tomography

Holey carbon-coated gold Quantifoil® Finder grids (Quantifoil Micro Tools, Großlöbichau, Germany) R2/2 (reference: Au G200F1) were glow-discharged using a PELCO EasiGlow™ (Ted Pella, Inc., Redding, CA, USA). Prior deposition on the grids, 10 µL of each sample condition at 0.7 OD_{600} were mixed with 15 µL of 100 nm gold beads (reference: GC100 from

BBI solutions) used as fiducial markers for enabling projections alignment to common axis for rotation prior to tomographic reconstruction and 5 µL of M9 media. 5 µL of sample were deposited on the carbon side of the grid, the excess of solution was manually blotted using a Whatman filter paper and then the grid was plunge-frozen into liquid ethane cooled down at −174°C by liquid nitrogen in a Leica EM CPC cryo-plunger (Leica Microsystems, Wetzlar, Germany). Three grids were prepared per condition, for a total of 18 grids. A few grids were screened with a cryo-transmission electron microscope (JEOL 2200FS) to assess the bacteria concentration and the fiducial distribution on the grid, as well as to verify the absence of ice crystals and evaluate the ice thickness prior to cryo-SXT analysis.

Cryo soft X-ray tomography

Cryo-SXT datasets were acquired at the ALBA synchrotron Light Source (Barcelona, Spain), on the transmission X-ray microscopy (TXM) beamline (MISTRAL BL09, proposal 2018082926) (Sorrentino et al., 2015).

Samples were mounted in specific holders and transferred to the cryo-TXM experimental vacuum chamber, preserving cryo-conditions throughout the transfer. Once inside the cryo-cooled vacuum chamber the grids were positioned in the focal point and at the axis of rotation of the TXM chamber. Using a visible light microscope on-line with the X-ray microscope, areas of interest were selected. Prior to individual bacteria screening, zero-degree soft X-ray projection mosaics were acquired to evaluate sample quality and to identify best regions on the grids. For our data collection a 25 nm objective Fresnel zone-plate was used to project the transmission signal on a direct illuminated CCD camera (1024 × 1024 pixels, camera pixel size = 13 µm). Acquisitions were performed using X-ray photons in the so-called water-window energy range at 520 eV (corresponding wavelength is 2.38 nm). At this energy, water (oxygen) is “transparent” (i.e., very low absorption) to X-rays while proteins and DNA (carbon

and nitrogen) have a strong absorption, thus creating contrast (Wolter, 1952). Tilt-series were collected with an increment of 1° between two projections. The number of projections per tilt-series ranged between 120 and 128 depending on the minimal and maximal tilt-angles that were achieved, which were about ±60° (Loconte et al., 2022). Magnifications of 1,300X and 1,650X were used, with corresponding image pixel-sizes of 10 nm and 8 nm, respectively. A total of 64 tomographic tilt-series were acquired and distributed as follows: exponential phase WT (12 tomograms), exponential phase Δ*hfq* (14 tomograms), exponential phase Δ*ctr* (10 tomograms), stationary phase WT (9 tomograms), stationary phase Δ*hfq* (9 tomograms) and stationary phase Δ*ctr* (10 tomograms).

Cryo-SXT tilt-series processing, alignment and reconstruction

To correct the non-uniformity of the X-ray beam, each tilt-series image was normalized using an average of 10 images taken without sample, commonly called a flat field (FF). Because the flat field varies over time (it is dependent on the beam intensity of the synchrotron storage ring), it was measured after each tilt-series collection. The normalization considered the averaged FF, beam currents and exposure times as denoted in the following equation from (Oton et al., 2015):

$$Img^{i}_{nomalized} = \frac{\frac{Img^{i}}{T^{i}_{exposure} I^{i}_{beam}}}{\sum_{f=1}^{N_{FF}} \frac{I^{f}_{flatfield}}{T^{f}_{exposure} I^{f}_{beam}}}$$

Where i is the i-th image in the tilt-series, f is the f-th flat field image and N_{FF} is the number of FF images used to estimate the average FF, which in our case equal 10 (for each tilt-series). I denotes the incident X-ray beam current.

The mass absorption coefficient μ is related to the transmitted intensity I through a material of density ρ and total thickness d by:

$$I = I_0 e^{-\mu \rho d}$$

Where I_0 is the intensity impinging on the sample.

The linear absorption coefficient (LAC) μ_l (μm^{-1}), which is the reconstructed value in the tomograms, relates to the mass absorption coefficient μ ($\mu m^2/g$) of the material and its density ρ ($g/\mu m^3$).

$$\mu_l = \mu\rho$$

$$Voxel = \mu_l = \mu\rho = -ln\left(\frac{I}{I_0}\right)$$

To compute the absorption signal, a negative Napierian logarithm was applied to each normalized tilt-series prior to reconstruction. All tilt-series were processed using a homemade bash script to automate the extraction of the tilt-series from the hdf5 files, absorption tilt-series computation, automated fiducial detection/tracking/alignment using IMOD command lines (Kremer et al., 1996) and reconstruction of the 3D volumes using simultaneous iterative reconstruction technique (SIRT) algorithm from Tomo3D software (z = 300 pixels, 20 iterations) (Agulleiro and Fernandez, 2011; Agulleiro and Fernandez, 2015) to have a first look at the reconstructed volumes before further processing.

Data processing and segmentation

Selected transmission tilt-series were manually aligned using fiducials (gold beads were automatically detected and tracked, then their position was manually refined) in Etomo from IMOD software (Kremer et al., 1996). The resulting alignment was then applied to corresponding absorption tilt-series. Because the gold beads used for the alignment tend to stick to the bacteria outer membrane and to further improve the reconstruction quality, these fiducials were removed from the images. To do so, the fiducials close to bacteria of interest in the absorption tilt-series were manually masked using Napari (Sofroniew, 2022). This mask was then applied to the tilt-series to replace the fiducial pixels by NaNs (Not a Number) before applying inpainting to generate new pixel values (500 iterations of an iterative discrete cosine

transform-based inpainting algorithm implemented in MATLAB) (Garcia, 2010). The resulting tilt-series were then reconstructed using SIRT without long object compensation, implemented in Tomo3D (Z = full height, 30 iterations). Volumes were then YZ-flipped to have the missing-wedge along the Z axis, cropped to Z = 300 px, and the voxel values divided by 0.01 or 0.008 depending on the pixel size (respectively 10 and 8 nm) to recover the LAC values (in μm^{-1}). Supplementary figure S1 shows the differences between normal versus inpainted volume slices. Individual bacteria were then cropped into subvolumes for which the segmentation of their nucleoid was performed iteratively using LabKit (Arzt et al., 2022). Each resulting probability map was exported and thresholded to values above 0.5. The nucleoid part of the resulting binary volume was separated from other parts (i.e., mostly artefacts or bacteria membrane) using the "Find connected regions" tool from Fiji (Schindelin et al., 2012). In case the nucleoid would still be connected to other artefacts, the result was manually refined. Finally, the 3D mask was applied to the original bacteria subvolume and the nucleoid voxels exported for further analysis using R (https://www.R-project.org/) (R Team, 2020). Note that the missing-wedge, which is equivalent for all datasets, underestimates the values of the LAC for all strains similarly; therefore, a comparison of reconstructed LACs across strains can be performed.

Visualization of segmented data

The different volumes generated in MATLAB (low-absorbance nucleoid, high-absorbance nucleoid and bacteria volumes) were exported in a format compatible with ChimeraX, which was used for data visualization (Goddard et al., 2018). The core domains (Figure 5), corresponding to hollow pocket-like regions inside the nucleoid, are represented using a Gaussian sphere which was designed using the MO 3 command in SPIDER (Frank et al., 1996). The size of the sphere was manually adapted to fit the inner diameter of the hollow region.

Statistical analysis

LAC histograms were computed in R. Histogram counts (i.e., number of voxels) of each bacterium nucleoid were computed using LAC bins (i.e., intervals) of 0.005. Then for each bin, the counts of each bacterium were converted into the corresponding volume using the voxel size. The bin counts of each bacterium were normalized using $\frac{(x - x_{min})}{(x_{max} - x_{min})}$ to have a range of volume values in the interval [0, 1]. Finally, the mean and standard deviation of each bin were computed.

For each condition, the mean LAC value of each segmented nucleoid was plotted as a box plot (Figure 2B). To evaluate the statistical significance of the distribution per condition, we first performed Shapiro normality tests on each condition, all of which could not reject the normal distribution hypothesis. Then, because each condition contained less than 30 individuals, Mann-Whitney non-parametric tests were done. A total of nine tests were performed, comparing the two growth phases of each strain (3 tests) and the strains at each growth phase (6 tests) with a desired $\alpha = 0.05$. The same statistical analysis protocol was used to compare the mean nucleoid volumes.

Full length and truncated Hfq relative quantification

Relative quantification of full-length Hfq and CTR-truncated Hfq forms was performed using Western Blot and Dot blot. Briefly, crude extracts at the same OD were diluted serially for both strains. The Δ*hfq* strain was used as control to subtract background. Membranes of blots were successively incubated with anti-Hfq polyclonal antibody from Goat (Origene, Germany), with anti-goat secondary antibody coupled to alkaline phosphatase (Sigma) and revealed with the NBT/BCIP Reagent Kit (Sigma). Intensities of bands were evaluated using ImageJ (Schneider et al., 2012). Note that the polyclonal anti-Hfq antibodies may recognize slightly less the truncated form of the protein and thus explaining the small differences observed.

RESULTS AND DISCUSSION

As Hfq effects on DNA structure may be direct or indirect (see our previous work about the effect of Hfq on DNA topology (Malabirade et al., 2018)), we analyzed three bacterial strains: (*i*) MG1655 WT (Wild Type, reference strain), (*ii*) MG1655-Δ*hfq* (totally devoid of Hfq protein) and (*iii*) MG1655-Δ*ctr*, expressing a truncated form of the protein with only the first 72 amino-acids corresponding to the NTR (Malabirade et al., 2018). Each strain was studied during exponential and stationary growth phases, generating a total of 6 different conditions. Bacteria were plunge-frozen on electron microscopy grids. Cryo-SXT tilt-series were collected to study the 3D structure of bacteria. A set of representative bacteria (usually 3 bacteria per condition) out of 30 were selected and are described throughout the whole analysis workflow for the sake of clarity and transparency. Note that each voxel in the SXT reconstructed volume corresponds to the linear absorption coefficient (LAC) (referred to as the absorbance in the text) of the material comprised within it (Groen et al., 2019). The absorbance, which translates into the density, of the various analyzed nucleoids can then be compared. A collection of reconstructed tomogram slices is presented to appreciate the morphological differences between the different strains (Figure 1).

Nucleoids (Figure 1, Nu) can clearly be observed inside the cells as clear zones (lower absorption) inside the darker cytoplasm (higher absorption) (Figure 1, Cy). Depending on the cell growth phase, this nucleoid can be oval-shaped (B3), dumbbell-shaped (A1) or round-shaped just after replication (C1). Note that from these various shapes arise heterogeneities in the statistics discussed below. Some nucleoids have an apparent hollow structure (Figure 1, NuCo) that is particularly visible on some bacteria (Figure 1, bacteria A1, A3, C1, D1 and F3). These hollow structures are made of higher absorbance matter as the corresponding pixels are darker (i.e., lower pixel value) than that of the nucleoid and similar to those of the cytoplasm. Membranes can also be observed (Figure 1, Me in bacteria B2 and F2). The resolution of the

method is estimated ~ 26 nm based on the Fresnel zone plate used (Oton et al., 2016) and allows to observe inner and outer membranes (Supplementary Figure S2). Nevertheless, due to the absence of staining and low contrast, the double membrane characteristic of Gram-negative bacteria cannot be observed in all the cells. In stationary phase cells, granules, possibly polyphosphate granules based on their shape, size and contrast (Mandala et al., 2020; Pallerla et al., 2005; Racki et al., 2017), can also be observed (Figure 1, Gr in bacteria B2 and D3). Indeed, polyphosphate granules are expected to appear as low-density material (i.e., white pixels) because they possess a high oxygen content, which generates almost no contrast in the water window in cryo-SXT. Non-inpainted reconstructed tomogram slices of more bacteria are available in supplementary Figures 3-8.

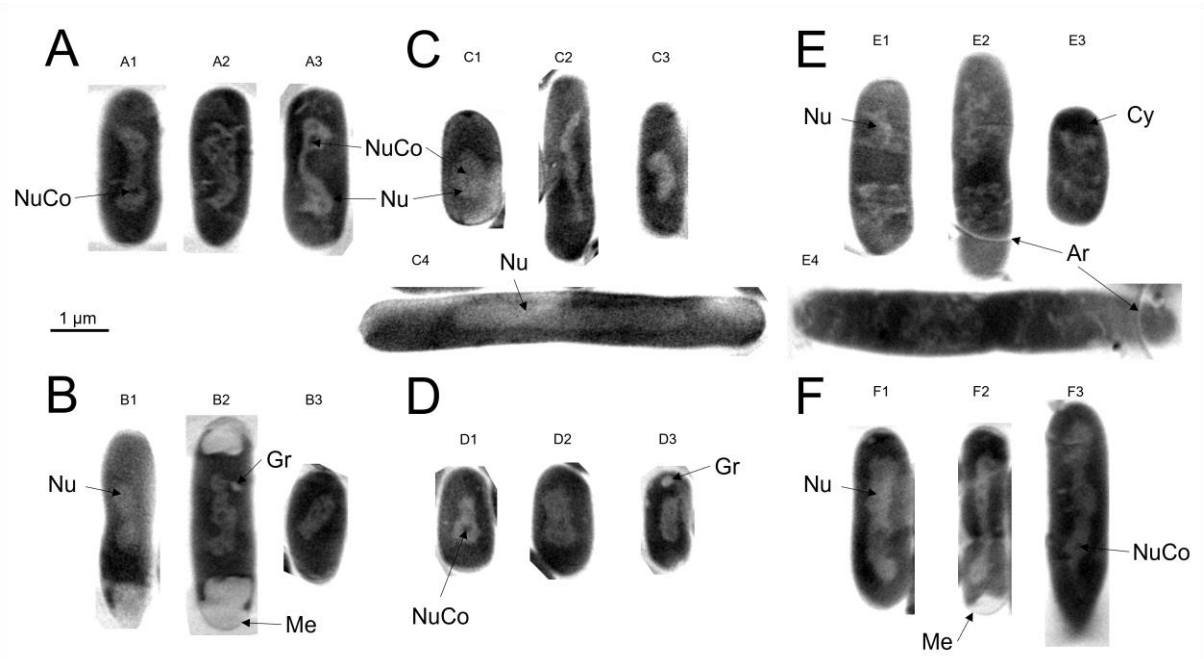

Figure 1. Tomographic reconstructed slices of representative bacteria for the different strains and growth phases. The slices have been extracted from absorbance reconstructed volumes which contrast has been inverted to resemble that of electron microscopy transmission images. A) Exponential phase WT cells. B) Mid-stationary phase WT cells. C) Exponential phase Δ*hfq* cells. D) Stationary phase Δ*hfq* cells. E) Exponential phase Δ*ctr* cells. F) Stationary phase Δ*ctr* cells. Scale bar is 1 µm. Several cellular structures have been highlighted: the nucleoid (Nu), the nucleoid core (NuCo), the cytoplasm (Cy), the membrane (Me) and the granules (Gr), artifacts (Ar) due to the presence of holes in the grids.

The nucleoid volume, absorbance and shape of the different strains were then analyzed and compared. The choice of these three strains allowed us to discriminate indirect effects due to

sRNA-based regulations, mainly due to Hfq-NTR, from those directly due to DNA compaction by Hfq-CTR (Jiang et al., 2015; Malabirade et al., 2017).

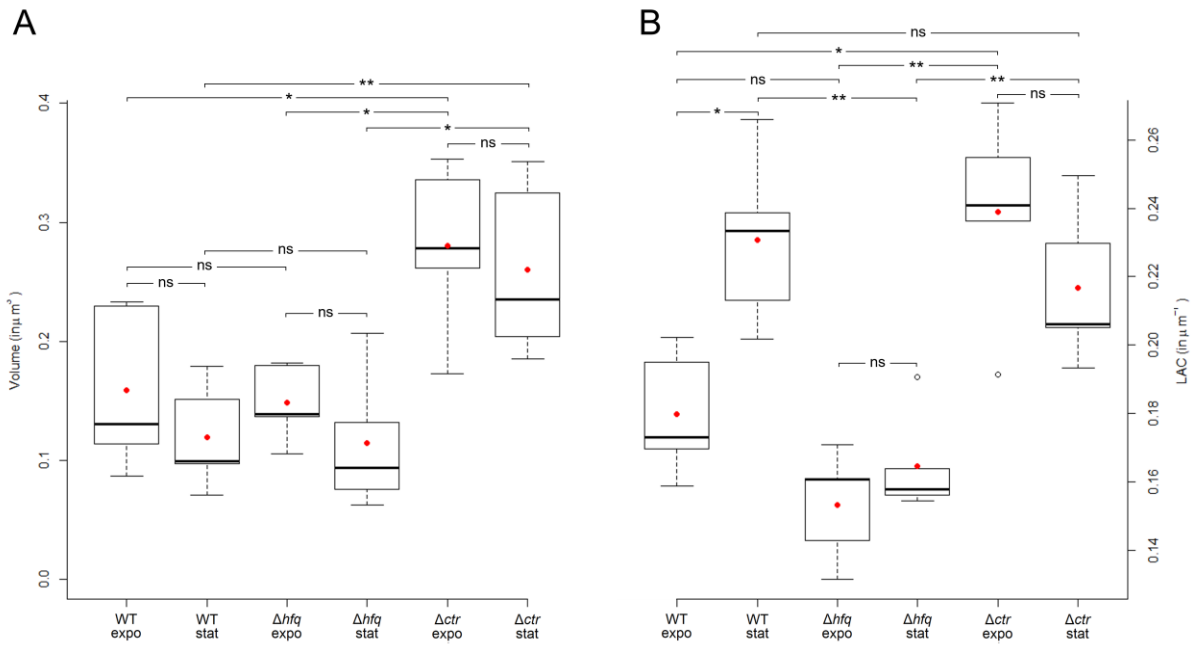

Figure 2. Summary of the nucleoid volumes and optical densities. A) Box plot representation of the nucleoid volume of the different bacteria strains. B) Box plot representation of the mean nucleoid absorbance (LAC) of each bacterium per strain type. The mean and median values are indicated by a red dot and a bold black horizontal line, respectively.

Evolution of nucleoid volume and absorbance between exponential and stationary phases in WT cells

The analysis presented in Figure 2 shows that the averaged nucleoid volume ($\bar{V}$) is higher in exponential phase cells ($\bar{V} = 0.159\ \mu m^3$) compared to mid-stationary phase ones ($\bar{V} = 0.120\ \mu m^3$). Note that the WT cells actively divide during exponential phase, giving either short bacteria that just divided ($\bar{V} \approx 0.10\ \mu m^3$), or long bacteria that will divide soon ($\bar{V} \approx 0.22\ \mu m^3$). For this reason, it is difficult to calculate a p-value to ensure volumes are significantly different (see also below). The absorbance of the nucleoid also evolves as it is significantly less dense in exponential phase ($\overline{LAC} = 0.180\ \mu m^{-1}$) compared to stationary phase ($\overline{LAC} = 0.231\ \mu m^{-1}$, p-value = 0.015) (Figure 2B and Figure 3A, left panel, red and

blues curves respectively). The mean, median and standard deviation values of the different populations are summarized in Table 1.

	Volumes (µm^3)		
	Mean	Median	Std
WT expo	0.159	0.131	0.0680
WT stat	0.120	0.099	0.0441
Δ*hfq* expo	0.149	0.139	0.0322
Δ*hfq* stat	0.114	0.094	0.0579
Δ*ctr* expo	0.280	0.278	0.0711
Δ*ctr* stat	0.260	0.235	0.0737

	LACs (µm^{-1})		
	Mean	Median	Std
WT expo	0.180	0.173	0.0182
WT stat	0.231	0.234	0.0248
Δ*hfq* expo	0.153	0.161	0.0159
Δ*hfq* stat	0.165	0.158	0.0150
Δ*ctr* expo	0.239	0.241	0.0298
Δ*ctr* stat	0.217	0.206	0.0227

Table 1. Summary of the nucleoid volumes and LAC, mean, median and standard deviation values. These values are associated with the box plots of Figure 2.

Overall, in WT cells, the LAC is shifted to higher values during stationary growth phase, which therefore indicates higher nucleoid absorbance. More precisely, the distribution of the LAC values is bimodal. There is a first sub-population centered around 0.16 µm^{-1} and a second sub-population centered around 0.19 µm^{-1} in the exponential phase, which are shifted towards 0.22 and 0.27 µm^{-1} in the stationary phase. This bimodal distribution could reflect the coexistence of bacteria sub-populations, as they are not synchronized for their division. These results agree with previous studies as the nucleoid absorbance has already been described to be higher for stationary-phase cells compared to exponential phase growing ones (Hammel et al., 2016; Zhu et al., 2020). Note that the results presented here do not show a strong reduction of the nucleoid volume as that observed in previous studies. This observation may be explained by the fact that the analysis was carried out on mid-stationary phase cells, due to the difficulty of reaching late stationary phase for the Δ*hfq* strain because of the positive effect of Hfq on σ^S expression, the stress and stationary phase sigma factor (Battesti et al., 2011). As described later in this work, WT cells were compared to *hfq* mutants grown in the same conditions, focusing on mid-stationary phase was mandatory for our analysis. One would have expected a more important nucleoid volume reduction in late stationary phase, as described previously with the same

reference strain MG1655 (Hammel et al., 2016). To summarize, in the presence of Hfq the transition from exponential to mid-stationary phase slightly reduces the nucleoid volume while significantly increasing its absorbance.

Effect of Hfq deletion on nucleoid volume and absorbance in Δhfq cells

In the Δ*hfq* strain, the nucleoid volumes in exponential phase cells ($\bar{V} = 0.149\ \mu m^3$) and in stationary phase cells ($\bar{V} = 0.114\ \mu m^3$) are not statistically different (p-value = 0.222, Figure 2A). Moreover, in the Δ*hfq* strain, the nucleoid absorbance does not change significatively between exponential and stationary phases (p-value = 0.691). The LAC values of both growth phases are centered between 0.153 and 0.165 μm^{-1} (Figures 2B and 3A, middle panel). Thus, in the absence of Hfq, neither the volume nor the absorbance of the nucleoid are significantly modified when the cells shift from exponential to stationary phase.

The comparison with WT cells reinforces this analysis. The nucleoid volumes of exponential WT cells (0.159 μm^3) and exponential Δ*hfq* cells (0.149 μm^3) are not statistically different (p-value = 1.00, Figure 2) and the distributions of their LAC values, again related to nucleoid density, are not significantly different either (LAC centered around 0.180 and 0.153 μm^{-1} respectively, p-value = 0.095; Figures 2B and 3B, left panel, orange and purple curves respectively). Thus, in exponential phase, the absence of Hfq does not seem to influence the volume of the nucleoid, nor its absorbance and density.

Oppositely, during the stationary phase, although the nucleoid volume is not significantly different (p-value = 0.691) (Figure 2), the absorbance is significantly lower in Δ*hfq* cells compared to WT cells (Figures 2B and 3B, right panel, orange and purple curves respectively) (p-value = 0.008). The LAC value distribution of the stationary Δ*hfq* cells are centered at 0.165 μm^{-1}. Considering previous *in vitro* analysis, these results were partially expected, as the absence of Hfq should result in less compaction and thus in an increase of the volume and/or a

decrease in absorbance (Jiang et al., 2015; Malabirade et al., 2017). Here we observe only an effect on the absorbance. Hence, these results suggest a positive role for the Hfq protein on DNA compaction and in nucleoid during the stationary phase, when Hfq is the most abundant (Diestra et al., 2009). Note that the reorganization of *E. coli* nucleoid upon entering the stationary phase was previously attributed to Dps and IHF NAPs (Lee et al., 2015). Here we show that Hfq may also play an additional role on nucleoid density (direct or indirect, see below) during the stationary growth phase.

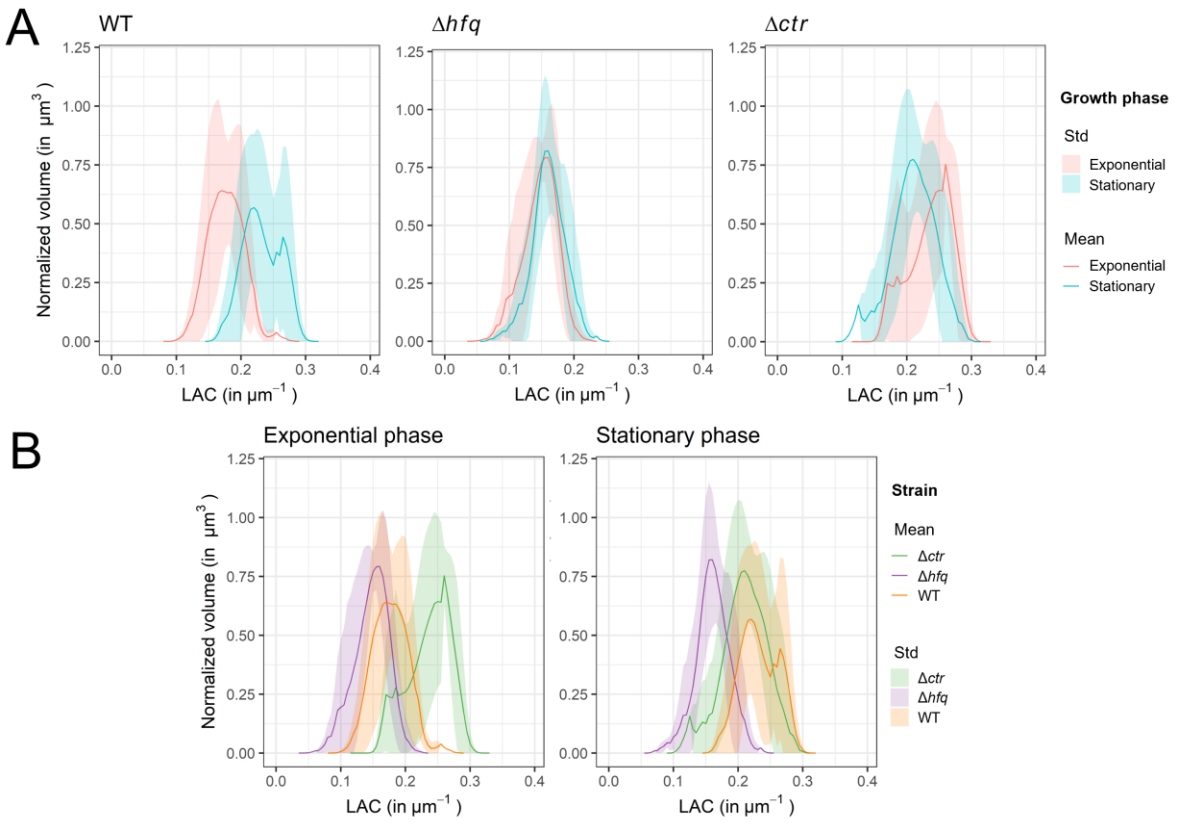

Figure 3. Histograms of nucleoid volumes as a function of LAC for each *E. coli* strain. Results are displayed to highlight both the effects of the growth phase for each strain (A) and the effects of the different *hfq* mutations during each growth phase (B). A) LAC histograms per strain with exponential phases in red and stationary phases in cyan. B) LAC histograms per growth phase with the WT strain in orange, the Δ*hfq* strain in purple and the Δ*ctr* one in green. Histograms represent the mean value (intense line) and the standard deviation (transparent), (see Methods).

Effect of Hfq-CTR deletion on nucleoid volume and absorbance in Δctr cells

As Hfq effects could be indirect *via* sRNA-based regulations (Malabirade et al., 2018), the outcome of CTR deletion was then tested by using Δ*ctr* cells. Indeed, Hfq-CTR is dispensable

for most sRNA-based regulations, even if few exceptions exist (Olsen et al., 2010; Turbant et al., 2021a; Vecerek et al., 2008). In short, deletion of the CTR should abolish the direct effect of Hfq on DNA compaction (Malabirade et al., 2017), while most sRNA-regulations controlled by Hfq-NTR should remain (Brennan and Link, 2007). Our analysis shows that the nucleoid volume is not significantly different between exponential phase Δ*ctr* cells ($\bar{V} = 0.280\ \mu m^3$) compared to stationary phase cells ($\bar{V} = 0.260\ \mu m^3$) (p-value = 0.691, Figure 2A). The absorbance of the nucleoid is not significantly less dense in exponential phase compared to the stationary phase even though the mean LAC changes from 0.239 to 0.217 μm^{-1} (p-value = 0.309, Figures 2B and 3A, right panel, red and blue curves respectively). Thus, in absence of the Hfq-CTR, the transition from exponential to stationary phase, both the absorbance and the volume do not seem to change much.

Compared to WT condition values, we also observe that the deletion of the CTR significantly induces an increase of the volume (from 0.159 to 0.280 μm^3, p-value = 0.032) and of the absorbance (from 0.180 to 0.239 μm^{-1}, p-value = 0.032) during the exponential phase of growth. During the stationary phase, the deletion of the CTR also induces a significant increase of the volume (from 0.120 to 0.260 μm^3, p-value = 0.008) and no significant change of the absorbance (LAC decreases from 0.231 to 0.217 μm^{-1}, p-value = 0.421). Thus, the absence of the CTR domain is associated with an increase of the volume during both the exponential and stationary phases of growth, and an increase of the absorbance only during exponential phase compared to WT conditions. As the CTR is expected to compact DNA, its absence should result in a less dense nucleoid occupying a larger volume. This is what is observed for the volume. Conversely, the absorbance/density of the nucleoid is either increased (during the exponential phase) or remains unchanged (during the stationary phase).

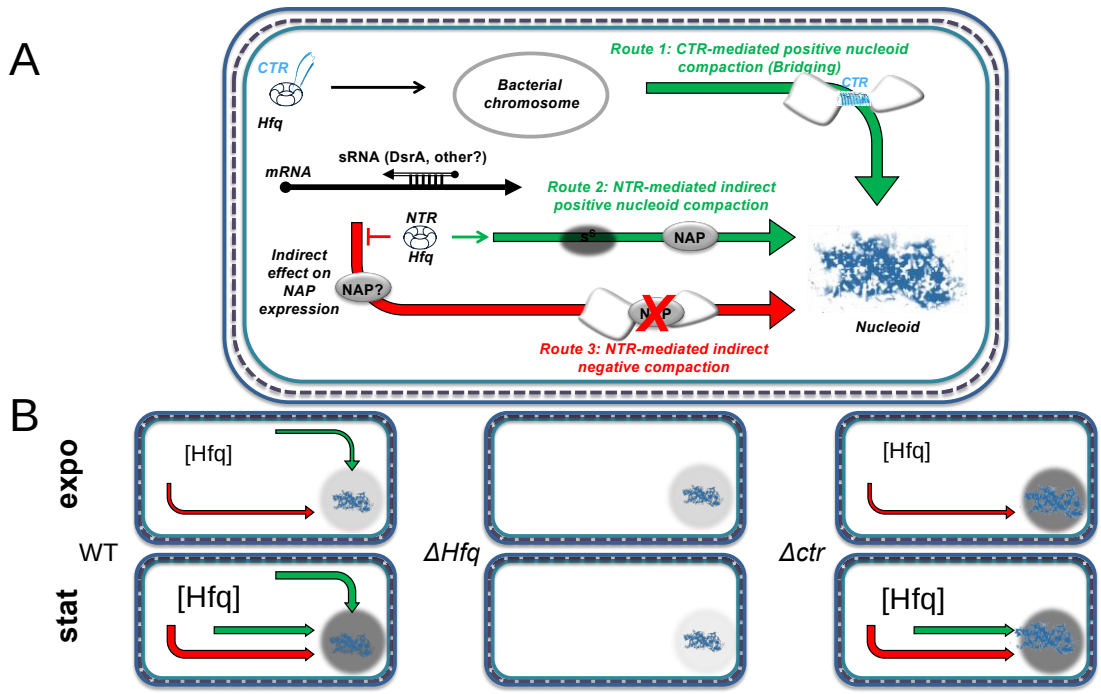

Figure 4. Model of Hfq-dependent regulations controlling DNA volume and compaction. A) Network of the Hfq-related pathways regulating the DNA compaction. The route 1 represents the CTR-mediated DNA compaction as previously shown *in vitro* (Malabirade et al., 2017). Route 2 is a NTR-mediated compaction pathway, representing the NAPs under the control of promoters driven by σ^S factor, its expression being itself dependent on sRNAs post-transcriptional regulation (Battesti et al., 2011). As it is driven by σ^S factor, route 2 is primarily active during the stationary growth phase. Route 3 is a NTR-mediated pathway too, it represents the translation of NAPs such as H-NS which are dependent on sRNAs, and which can be indirectly regulated by Hfq. Yet, route 3 is most likely negatively regulated (Lalaouna et al., 2015; Majdalani et al., 1998). sRNA regulators controlling mRNAs are depicted as open arrows; mRNAs as thick black lines; 5' and 3' of RNAs are depicted by a "ball and arrow head", respectively; Hfq-NTR is depicted as a blue toroidal hexamer; Hfq-CTR as a blue amyloid β-strand; σ^S as yellow ellipse; NAPs as grey ellipses; chromosomic DNA is represented as a grey line; nucleoid is represented with a blue picture; positive and negative regulations by Hfq are indicated by arrows and T-shape lines, and colored in green and red, respectively; the dotted line symbolizes the peptidoglycan between the outer and inner membranes. B) Schemes showing the activated pathways for all studied conditions. The size of the nucleoid picture symbolizes the volume of the nucleoid. The level of grey in the disc behind the nucleoid picture symbolizes the absorbance value of the nucleoid (i.e., the darker, the higher the absorbance).

Compared to the Δ*hfq* cells, the results show that the nucleoid volume and absorbance in Δ*ctr* cells are significantly increased in both growth phases. The volume changes from 0.149 to 0.280 μm^3 (p-value = 0.032) and the LAC increases from 0.153 to 0.239 μm^{-1} in exponential phase (p-value = 0.008). The volume changes from 0.114 to 0.260 μm^3 (p-value = 0.032) and the LAC increases from 0.165 to 0.217 μm^{-1} (p-value = 0.032) in stationary phase. Thus, the

deletion of Hfq-CTR in Δ*ctr* cells generates a new phenotype, different from that of the complete deletion of Hfq in Δ*hfq* cells. Several hypotheses could explain these observations (see model in Figure 4):

(*i*) The presence of the Hfq-CTR domain could influence Hfq stability, as shown previously *in vitro* (Arluison et al., 2004) and thus its abundance *in vivo*. The effect observed could thus be due to different concentrations of full-length Hfq or truncated Hfq. We can rule out this hypothesis as, in agreement with previous reports (Gaffke et al., 2021; Turbant et al., 2021b), the relative amounts of Hfq and its CTR-truncated form were similar (Supplementary Figure S9). The differences observed thus rely on the regulation mode exerted by Hfq when its CTR is present or not, not on its abundance in the cell.

(*ii*) As previously demonstrated, the CTR of Hfq, which binds DNA, is capable of forming an amyloid structure (Fortas et al., 2015; Malabirade et al., 2018; Partouche et al., 2019) and drives bacterial heterochromatin formation (Beaufay et al., 2021). In these conditions, an amyloid aggregation of Hfq through its CTR, could play an important role in the compaction of DNA (Figure 4A, Route 1). This hypothesis explains why the nucleoid volume is smaller when the CTR is present (wild-type control) as opposed to when it is absent (Δ*ctr*) Figure 4B).

To reinforce this conclusion, we intended to perform a complementation test of the Δ*ctr* strain with a CTR-expressing plasmid *in trans* to try to restore the wild type phenotype. Nevertheless, this was not possible as this part of the protein cannot be expressed independently of the NTR in the bacteria as it is unstable when translated alone (Kubiak et al., 2022; Taghbalout et al., 2014).

(*iii*) Then, the NTR part of the protein may also have a role as it allows sRNA-regulations that influence nucleoid compaction. This can be seen with the different phenotypes observed for Δ*hfq* and Δ*ctr* strains that both lack the CTR region. A well-known example of sRNA-based regulation by Hfq is DsrA, a small noncoding RNA of *E. coli* that targets different mRNA.

These include *rpoS* and *hns* mRNA, which encodes σ^S, the stress and stationary phase sigma factor (Battesti et al., 2011; Majdalani et al., 1998) and the nucleoid-structuring protein H-NS (Lease and Belfort, 2000), respectively. While DsrA sRNAs positively regulates the expression of *rpoS* in particular during the stationary phase, it negatively regulates *hns* mRNAs translation (Lalaouna and Masse, 2016). It was recently shown that H-NS does not significantly affect nucleoid volume and compaction (Gao et al., 2017). Nevertheless, Hfq may positively (Figure 4A, Route 2) or negatively (Figure 4A, Route 3) regulate other NAPs *via* its NTR.

(*iv*) Finally, we cannot overlook the indirect effects of the amyloid-like aggregation of Hfq CTR, which could impact the availability of the NTR, preventing interactions with other proteins and/or RNAs. Since the Hfq concentration in the nucleoid during the stationary phase is twice that during exponential phase (Diestra et al., 2009), the protein could be more prone to form amyloid-like structures in these conditions (Fortas et al., 2015; Partouche et al., 2019). Hfq could thus be differently available for potential interactions with other partners, a mechanism which would be more important during the stationary phase because of the higher protein concentration. In the WT condition, the aggregation of the CTR could prevent the NTR interacting with other proteins. In Δ*ctr* cells, this CTR-mediated control is absent and may result in uncontrolled interactions *via* the NTR, which we suspect to explain the abnormally high nucleoid absorbance in these CTR-deprived cells (Figure 4B).

Nucleoid shape in WT cells

In parallel, we also analyzed the spatial distribution of the nucleoid domains as a function of their absorbance. In exponential phase WT cells, high-absorbance nucleoid regions (Figure 5A, red isosurface), probably EPOD domains (Amemiya et al., 2021), surround low-absorbance nucleoid regions (Figure 5A, yellow isosurface). Moreover, hollow regions located deep inside the nucleoid, as already observed in Figure 1, have an absorbance different from that of the

nucleoid, similar to that of the cytoplasm, and as such, were not detected as part of the nucleoid during the semi-automatic segmentation analysis. Blue spheres have been manually placed to locate the hollow regions in the 3D isosurfaces (Figure 6A). These regions have been described and designated as "cores" in previous works (Remesh et al., 2020; Wang et al., 2011). In stationary phase WT cells, the situation is similar at the exception of bacteria B1 in which low-absorbance regions are exposed to the surface of the nucleoid (Figure 5B) and has no "core". The presence of nucleoid high- and low-absorbance domains as well as the nucleoid cores can also be visualised in animations which are available as supplementary data (Supplementary Movies 1-6).

These domains may presumably be Ori, Ter, Left, and Right arms (Valens et al., 2004), but cannot be formally identified with cryo-SXT. Correlative SXT imaging in combination with fluorescence and/or cryo-transmission electron microscopy using labelled marker proteins (Diestra et al., 2009; Espeli and Boccard, 2006) could help to answer this question in the future.

Effect of Hfq and its CTR on nucleoid shape

In Δ*hfq* cells the high-absorbance nucleoid (Figure 5C-D, red isosurfaces) still surrounds the low-absorbance one (Figure 5C-D, yellow isosurfaces), both in exponential phase and stationary phase. In Δ*ctr* cells, the high- and low-absorbance nucleoid regions coexist side by side at the surface of nucleoid as if the nucleoid regions are laterally distributed (Figure 5E-F). This is different from what we observed in other cell types where high- and low-absorbance regions were organized in different shells (Figure 5A-D). Moreover, the presence of cores is still detected in these strains (i.e., Δ*hfq* and Δ*ctr* cells), except for the Δ*hfq* exponential phase strain (Figure 6). Even though this analysis cannot describe the nature of core domains, it unveils the general absence of core domains in exponential phase Δhfq cells is directly or

indirectly linked to the presence of Hfq-CTR. Thus, it turns out that Hfq and its CTR does not only influence the absorbance and the volume of the nucleoid but also its shape.

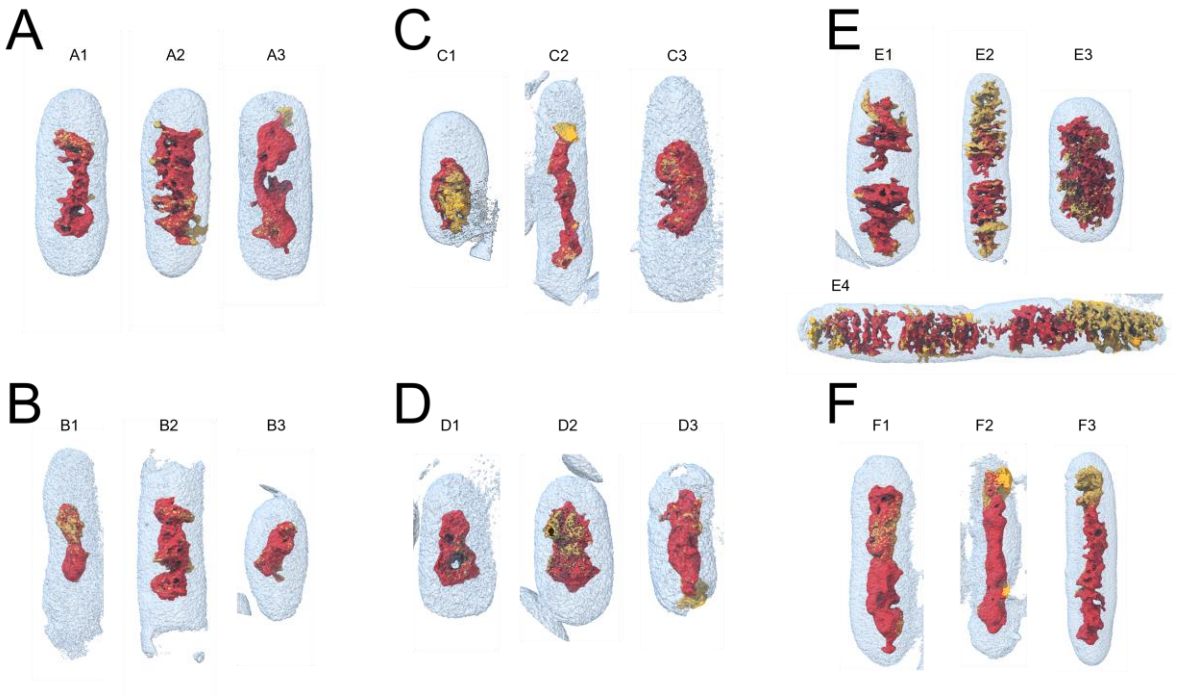

Figure 5. Visualization of the nucleoid volume and absorbance for each bacteria strain. The different segmentations have been automatically generated using a unique algorithm which was equally applied to all bacteria. A) Exponential phase WT cells. B) Mid-stationary phase WT cells. C) Exponential phase Δ*hfq* cells. D) Stationary phase Δ*hfq* cells. E) Exponential phase Δ*ctr* cells. F) Stationary phase Δ*ctr* cells. The bacteria are displayed with different scales to better visualize the nucleoids, hence the absence of scale bar. The blue isosurfaces are segmentations of the bacteria membranes. The red and yellow isosurfaces are segmentations of the high-absorbance and low-absorbance regions of the nucleoid, respectively. The densely occupied regions are likely EPOD domains that have been recently evidenced in *E. coli* (Amemiya et al., 2021).

Effect of Hfq and its CTR on cell shape

Finally, elongated cells were observed in the Δ*hfq* strain (Figure 1, bacteria C4). Such elongated cells were not observed in the WT strain. We thus confirm that the absence of Hfq results in the formation of some elongated cells, as previously described (Tsui et al., 1994). Interestingly, we also observed this phenotype for the strain expressing Hfq devoid of its C-terminal region (Δ*ctr*) (Figure 1, bacteria E4). We then performed the first analysis of volume, absorbance and shape of nucleoids in *hfq* mutant elongated cells. The volume and absorbance of the elongated nucleoids were 0.712 μm^3 and 0.594 μm^3 and 0.139 μm^{-1} and 0.204 μm^{-1} for these Δ*hfq* and

Δ*ctr* cells, respectively. Based on the nucleoid semi-automatic segmentation, these elongated cells also have interdigitated low-absorbance and high-absorbance nucleoid domains (Figure 5, E4, bottom bacteria), as in regular-size bacteria.

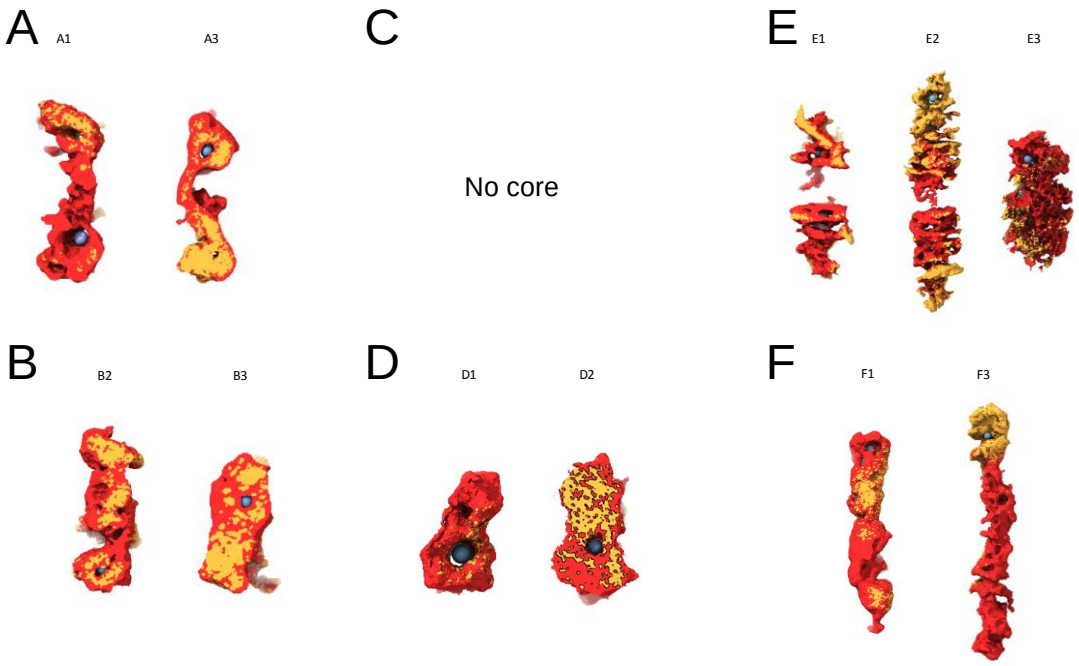

Figure 6. Visualization of the nucleoid cores. A) Exponential phase WT cells. B) Mid-stationary phase WT cells. C) Exponential phase Δ*hfq* cells. D) Stationary phase Δ*hfq* cells. E) Exponential phase Δ*ctr* cells. F) Stationary phase Δ*ctr* cells. The red and yellow isosurfaces are segmentations of the high-absorbance and low-absorbance regions of the nucleoid, respectively. In some of the bacteria, the nucleoid is characterized by the presence of one (or more) hollow region(s) which are known as nucleoid cores, previously observed in tomographic slices of the bacteria (Figure 1). These cores are highlighted using blue spheres which have been manually placed at the center of the hollow regions. The bacteria are displayed with different scales to better visualize the nucleoid cores, hence the absence of scale bar.

CONCLUSION

Taken together our analysis confirms (*i*) that the role of Hfq on DNA structuring exists not only *in vitro* but is confirmed *in vivo*, particularly during the stationary phase when Hfq is the most abundant; (*ii*) that Hfq interaction with DNA *via* its CTR induces nucleoid remodeling that may serve for DNA-related regulations to adapt to changing environments; (*iii*) that additional effects due to Hfq-NTR related to sRNA-based regulation also exist. Thus, our analysis reinforces the role of NAP for this master regulator that may help to answer to stresses encountered by bacteria. Similarly to H-NS, Hfq may be a transcriptional regulator affecting

the expression of genes involved in stress protection, such as σ^S (*rpoS*) or two-component systems (PhoP) (Holowka and Zakrzewska-Czerwinska, 2020).

SUPPLEMENTARY DATA

Supplementary data is available in a separate attached file.

ACKNOWLEDGEMENTS

We acknowledge J.M. Carazo and C.O. Sorzano (CNB, Madrid, Spain) for many fruitful discussions. We acknowledge F. Busi (UMR8251, Paris, France) and M. Buckle (ENS, Paris-Saclay, France) for critical reading of the manuscript. We acknowledge G. Wegrzyn and T. Kaczorowski (University of Gdansk, Poland) for their helpful advice on naming bacteria cytoplasmic structures and reading of the manuscript. We acknowledge ALBA synchrotron (Barcelona, Spain) for provision of synchrotron radiation facilities (proposal 2018082926) and would like to thank A. Sorrentino for assistance during data collection at the MISTRAL beamline. We acknowledge the Multimodal Imaging Centre at Institut Curie (Orsay, France) for providing access to the cryo-transmission electron microscopy facility.

FUNDING

This research was supported in part by CNRS and CEA (VA), synchrotron SOLEIL (FW), Institut Curie (ST). Cryo-SXT measurements on MISTRAL BL09 beamline at ALBA Synchrotron were performed under proposal 2018082926. This study contributes to the IdEx Université de Paris ANR-18-IDEX-0001 (VA). This work was supported by a public grant overseen by the French National research Agency (ANR) as part of the "Investissement d'Avenir" program, through the "ADI 2019" and "ADI 2021" projects funded by the IDEX Paris-Saclay, ANR-11-IDEX-0003-02 (AC & FT).

CONFLICTS OF INTEREST

The authors declare no conflict of interest.

AUTHOR CONTRIBUTIONS

Data curation: AC, ST, JG, EP; Formal analysis: AC, ST, FW, FT, EP, VA; Funding acquisition: ST, VA; Investigation: AC, ST, FW, ELB, FT, EP, VA; Methodology: AC, ST, FW, ELB, FT, EP, VA; Project administration: ST, VA; Resources; ST, VA; Software: AC, ST, JG, FW, EP; Supervision: ST, VA; Validation AC, ST, EP, VA; Visualization AC, ST, EP; Roles/Writing - original draft AC, ST, VA; Writing - review & editing: AC, ST, FW, EP, VA.

REFERENCES

Agulleiro, J.I., Fernandez, J.J., 2011. Fast tomographic reconstruction on multicore computers. Bioinformatics 27, 582-583.

Agulleiro, J.I., Fernandez, J.J., 2015. Tomo3D 2.0--exploitation of advanced vector extensions (AVX) for 3D reconstruction. J Struct Biol 189, 147-152.

Aiba, H., 2007. Mechanism of RNA silencing by Hfq-binding small RNAs. Curr Opin Microbiol 10, 134-139.

Aiyar, S.E., Gourse, R.L., Ross, W., 1998. Upstream A-tracts increase bacterial promoter activity through interactions with the RNA polymerase alpha subunit. Proc Natl Acad Sci U S A 95, 14652-14657.

Amemiya, H.M., Goss, T.J., Nye, T.M., Hurto, R.L., Simmons, L.A., Freddolino, P.L., 2021. Distinct heterochromatin-like domains promote transcriptional memory and silence parasitic genetic elements in bacteria. EMBO J, e108708.

Arluison, V., Hohng, S., Roy, R., Pellegrini, O., Regnier, P., Ha, T., 2007. Spectroscopic observation of RNA chaperone activities of Hfq in post-transcriptional regulation by a small non-coding RNA. Nucleic Acids Res 35, 999-1006.

Arluison, V., Folichon, M., Marco, S., Derreumaux, P., Pellegrini, O., Seguin, J., Hajnsdorf, E., Regnier, P., 2004. The C-terminal domain of Escherichia coli Hfq increases the stability of the hexamer. Eur J Biochem 271, 1258-1265.

Arzt, M., Deschamps, J., Schmied, C., Pietzsch, T., Schmidt, D., Tomancak, P., Haase, R., Jug, F., 2022. LABKIT: Labeling and Segmentation Toolkit for Big Image Data. Front. Comput. Sci. 4, 777728.

Azam, T.A., Ishihama, A., 1999. Twelve species of the nucleoid-associated protein from Escherichia coli. Sequence recognition specificity and DNA binding affinity. J Biol Chem 274, 33105-33113.

Azam, T.A., Hiraga, S., Ishihama, A., 2000. Two types of localization of the DNA-binding proteins within the Escherichia coli nucleoid. Genes Cells 5, 613-626.

Battesti, A., Majdalani, N., Gottesman, S., 2011. The RpoS-Mediated General Stress Response in Escherichia coli (*). Annu Rev Microbiol 65, 189-213.

Beaufay, F., Amemiya, H.M., Guan, J., Basalla, J., Meinen, B.A., Chen, Z., Mitra, R., Bardwell, J.C.A., Biteen, J.S., Vecchiarelli, A.G., Freddolino, P.L., Jakob, U., 2021. Polyphosphate drives bacterial heterochromatin formation. Sci Adv 7, eabk0233.

Bettridge, K., Verma, S., Weng, X., Adhya, S., Xiao, J., 2021. Single-molecule tracking reveals that the nucleoid-associated protein HU plays a dual role in maintaining proper nucleoid volume through differential interactions with chromosomal DNA. Mol Microbiol 115, 12-27.

Bouloc, P., Repoila, F., 2016. Fresh layers of RNA-mediated regulation in Gram-positive bacteria. Curr Opin Microbiol 30, 30-35.

Brennan, R.G., Link, T.M., 2007. Hfq structure, function and ligand binding. Curr Opin Microbiol 10, 125-133.

Cech, G.M., Pakula, B., Kamrowska, D., Wegrzyn, G., Arluison, V., Szalewska-Palasz, A., 2014. Hfq protein deficiency in Escherichia coli affects ColE1-like but not lambda plasmid DNA replication. Plasmid 73, 10-15.

Chen, J., Gottesman, S., 2017. Hfq links translation repression to stress-induced mutagenesis in E. coli. Genes & development 31, 1382-1395.

Dame, R.T., Rashid, F.-Z.M., Grainger, D.C., 2020. Chromosome organization in bacteria: mechanistic insights into genome structure and function. Nature reviews Genetics 21, 227-242.

Diestra, E., Cayrol, B., Arluison, V., Risco, C., 2009. Cellular electron microscopy imaging reveals the localization of the Hfq protein close to the bacterial membrane. PLoS One 4, e8301.

Dillon, S.C., Dorman, C.J., 2010. Bacterial nucleoid-associated proteins, nucleoid structure and gene expression. Nature reviews Microbiology 8, 185-195.

Dimastrogiovanni, D., Frohlich, K.S., Bandyra, K.J., Bruce, H.A., Hohensee, S., Vogel, J., Luisi, B.F., 2014. Recognition of the small regulatory RNA RydC by the bacterial Hfq protein. Elife 3.

Ding, Y., Davis, B.M., Waldor, M.K., 2004. Hfq is essential for Vibrio cholerae virulence and downregulates sigma expression. Mol Microbiol 53, 345-354.

Dorman, C.J., 2014. Function of nucleoid-associated proteins in chromosome structuring and transcriptional regulation. J Mol Microbiol Biotechnol 24, 316-331.

Dorman, C.J., Schumacher, M.A., Bush, M.J., Brennan, R.G., Buttner, M.J., 2020. When is a transcription factor a NAP? Curr Opin Microbiol 55, 26-33.

El Hamoui, O., Yadav, I., Radiom, M., Wien, F., Berret, J.-F., van der Maarel, J.R.C., Arluison, V., 2020. Interactions between DNA and the Hfq Amyloid-like Region Trigger a Viscoelastic Response. Biomacromolecules 21, 3668-3677.

Espeli, O., Boccard, F., 2006. Organization of the Escherichia coli chromosome into macrodomains and its possible functional implications. J Struct Biol 156, 304-310.

Fortas, E., Piccirilli, F., Malabirade, A., Militello, V., Trepout, S., Marco, S., Taghbalout, A., Arluison, V., 2015. New insight into the structure and function of Hfq C-terminus. Biosci Rep 35.

Frank, J., Radermacher, M., Penczek, P., Zhu, J., Li, Y., Ladjadj, M., Leith, A., 1996. SPIDER and WEB: processing and visualization of images in 3D electron microscopy and related fields. J Struct Biol 116, 190-199.

Franze de Fernandez, M.T., Eoyang, L., August, J.T., 1968. Factor fraction required for the synthesis of bacteriophage Qbeta-RNA. Nature 219, 588-590.

Gaffke, L., Kubiak, K., Cyske, Z., Wegrzyn, G., 2021. Differential Chromosome- and Plasmid-Borne Resistance of Escherichia coli hfq Mutants to High Concentrations of Various Antibiotics. Int J Mol Sci 22, 8886.

Gao, Y., Foo, Y.H., Winardhi, R.S., Tang, Q., Yan, J., Kenney, L.J., 2017. Charged residues in the H-NS linker drive DNA binding and gene silencing in single cells. Proc Natl Acad Sci U S A 114, 12560-12565.

Garcia, D., 2010. Robust smoothing of gridded data in one and higher dimensions with missing values. Comput Stat Data Anal 54, 1167-1178.

Geinguenaud, F., Calandrini, V., Teixeira, J., Mayer, C., Liquier, J., Lavelle, C., Arluison, V., 2011. Conformational transition of DNA bound to Hfq probed by infrared spectroscopy. Phys Chem Chem Phys 13, 1222-1229.

Goddard, T.D., Huang, C.C., Meng, E.C., Pettersen, E.F., Couch, G.S., Morris, J.H., Ferrin, T.E., 2018. UCSF ChimeraX: Meeting modern challenges in visualization and analysis. Protein Sci 27, 14-25.

Gottesman, S., 2019. Trouble is coming: Signaling pathways that regulate general stress responses in bacteria. The Journal of biological chemistry 294, 11685-11700.

Gottesman, S., McCullen, C.A., Guillier, M., Vanderpool, C.K., Majdalani, N., Benhammou, J., Thompson, K.M., FitzGerald, P.C., Sowa, N.A., FitzGerald, D.J., 2006. Small RNA regulators and the bacterial response to stress. Cold Spring Harb Symp Quant Biol 71, 1-11.

Groen, J., Conesa, J.J., Valcarcel, R., Pereiro, E., 2019. The cellular landscape by cryo soft X-ray tomography. Biophys Rev, 611-619.

Hammel, M., Amlanjyoti, D., Reyes, F.E., Chen, J.H., Parpana, R., Tang, H.Y., Larabell, C.A., Tainer, J.A., Adhya, S., 2016. HU multimerization shift controls nucleoid compaction. Sci Adv 2, e1600650.

Haniford, D.B., Ellis, M.J., 2015. Transposons Tn10 and Tn5. Microbiol Spectr 3, MDNA3-0002-2014.

Hoff, K.A., 1988. Rapid and simple method for double staining of bacteria with 4',6-diamidino-2-phenylindole and fluorescein isothiocyanate-labeled antibodies. Appl Environ Microbiol 54, 2949-2952.

Holowka, J., Zakrzewska-Czerwinska, J., 2020. Nucleoid Associated Proteins: The Small Organizers That Help to Cope With Stress. Front Microbiol 11, 590.

Jiang, K., Zhang, C., Guttula, D., Liu, F., van Kan, J.A., Lavelle, C., Kubiak, K., Malabirade, A., Lapp, A., Arluison, V., van der Maarel, J.R., 2015. Effects of Hfq on the conformation and compaction of DNA. Nucleic Acids Res 43, 4332-4341.

Kendall, M.M., Gruber, C.C., Rasko, D.A., Hughes, D.T., Sperandio, V., 2011. Hfq virulence regulation in enterohemorrhagic Escherichia coli O157:H7 strain 86-24. J Bacteriol 193, 6843-6851.

Kremer, J.R., Mastronarde, D.N., McIntosh, J.R., 1996. Computer visualization of three-dimensional image data using IMOD. J Struct Biol 116, 71-76.

Kubiak, K., Wien, F., Yadav, I., Jones, N.C., Vrønning Hoffmann, S., Le Cam, E., Cossa, A., Geinguenaud, F., van der Maarel , J.R.C., Węgrzyn, G., Arluison, V., 2022. Amyloid-like Hfq interaction with single-stranded DNA: involvement in recombination and replication in Escherichia coli. . QRB Discovery in press, https://doi.org/10.1017/qrd.2022.1015.

Lalaouna, D., Masse, E., 2016. The spectrum of activity of the small RNA DsrA: not so narrow after all. Curr Genet 62, 261-264.

Lalaouna, D., Morissette, A., Carrier, M.C., Masse, E., 2015. DsrA regulatory RNA represses both hns and rbsD mRNAs through distinct mechanisms in Escherichia coli. Mol Microbiol 98, 357-369.

Le Derout, J., Boni, I.V., Regnier, P., Hajnsdorf, E., 2010. Hfq affects mRNA levels independently of degradation. BMC Mol Biol 11, 17.

Lease, R.A., Belfort, M., 2000. Riboregulation by DsrA RNA: trans-actions for global economy. Mol Microbiol 38, 667-672.

Lee, S.Y., Lim, C.J., Droge, P., Yan, J., 2015. Regulation of Bacterial DNA Packaging in Early Stationary Phase by Competitive DNA Binding of Dps and IHF. Sci Rep 5, 18146.

Link, T.M., Valentin-Hansen, P., Brennan, R.G., 2009. Structure of Escherichia coli Hfq bound to polyriboadenylate RNA. Proc Natl Acad Sci U S A 106, 19292-19297.

Loconte, V., Singla, J., Li, A., Chen, J.H., Ekman, A., McDermott, G., Sali, A., Le Gros, M., White, K.L., Larabell, C.A., 2022. Soft X-ray tomography to map and quantify organelle interactions at the mesoscale. Structure 30, 510-521 e513.

Majdalani, N., Cunning, C., Sledjeski, D., Elliott, T., Gottesman, S., 1998. DsrA RNA regulates translation of RpoS message by an anti-antisense mechanism, independent of its action as an antisilencer of transcription. Proc Natl Acad Sci U S A 95, 12462-12467.

Malabirade, A., Jiang, K., Kubiak, K., Diaz-Mendoza, A., Liu, F., van Kan, J.A., Berret, J.F., Arluison, V., van der Maarel, J.R.C., 2017. Compaction and condensation of DNA mediated by the C-terminal domain of Hfq. Nucleic Acids Res 45, 7299-7308.

Malabirade, A., Partouche, D., El Hamoui, O., Turbant, F., Geinguenaud, F., Recouvreux, P., Bizien, T., Busi, F., Wien, F., Arluison, V., 2018. Revised role for Hfq bacterial regulator on DNA topology. Sci Rep 8, 16792.

Mandala, V.S., Loh, D.M., Shepard, S.M., Geeson, M.B., Sergeyev, I.V., Nocera, D.G., Cummins, C.C., Hong, M., 2020. Bacterial Phosphate Granules Contain Cyclic Polyphosphates: Evidence from (31)P Solid-State NMR. J Am Chem Soc 142, 18407-18421.

McCullen, C.A., Benhammou, J.N., Majdalani, N., Gottesman, S., 2010. Mechanism of positive regulation by DsrA and RprA small noncoding RNAs: pairing increases translation and protects rpoS mRNA from degradation. J Bacteriol 192, 5559-5571.

Milles, S., Huy Bui, K., Koehler, C., Eltsov, M., Beck, M., Lemke, E.A., 2013. Facilitated aggregation of FG nucleoporins under molecular crowding conditions. EMBO Rep 14, 178-183.

Olsen, A.S., Moller-Jensen, J., Brennan, R.G., Valentin-Hansen, P., 2010. C-Terminally truncated derivatives of Escherichia coli Hfq are proficient in riboregulation. J Mol Biol 404, 173-182.

Orans, J., Kovach, A.R., Hoff, K.E., Horstmann, N.M., Brennan, R.G., 2020. Crystal structure of an Escherichia coli Hfq Core (residues 2-69)-DNA complex reveals multifunctional nucleic acid binding sites. Nucleic acids res 48, 3987-3997.

Oton, J., Sorzano, C.O., Marabini, R., Pereiro, E., Carazo, J.M., 2015. Measurement of the modulation transfer function of an X-ray microscope based on multiple Fourier orders analysis of a Siemens star. Opt Express 23, 9567-9572.

Oton, J., Pereiro, E., Perez-Berna, A.J., Millach, L., Sorzano, C.O., Marabini, R., Carazo, J.M., 2016. Characterization of transfer function, resolution and depth of field of a soft X-ray microscope applied to tomography enhancement by Wiener deconvolution. Biomed Opt Express 7, 5092-5103.

Pallerla, S.R., Knebel, S., Polen, T., Klauth, P., Hollender, J., Wendisch, V.F., Schoberth, S.M., 2005. Formation of volutin granules in Corynebacterium glutamicum. FEMS Microbiol Lett 243, 133-140.

Parekh, V.J., Niccum, B.A., Shah, R., Rivera, M.A., Novak, M.J., Geinguenaud, F., Wien, F., Arluison, V., Sinden, R.R., 2019. Role of Hfq in Genome Evolution: Instability of G-Quadruplex Sequences in E. coli. Microorganisms 8.

Partouche, D., Militello, V., Gomez-Zavaglia, A., Wien, F., Sandt, C., Arluison, V., 2019. In Situ Characterization of Hfq Bacterial Amyloid: A Fourier-Transform Infrared Spectroscopy Study. Pathogens 8.

Porcheron, G., Dozois, C.M., 2015. Interplay between iron homeostasis and virulence: Fur and RyhB as major regulators of bacterial pathogenicity. Vet Microbiol 179, 2-14.

Racki, L.R., Tocheva, E.I., Dieterle, M.G., Sullivan, M.C., Jensen, G.J., Newman, D.K., 2017. Polyphosphate granule biogenesis is temporally and functionally tied to cell cycle exit during starvation in Pseudomonas aeruginosa. Proc Natl Acad Sci U S A 114, E2440-E2449.

Rajkowitsch, L., Chen, D., Stampfl, S., Semrad, K., Waldsich, C., Mayer, O., Jantsch, M.F., Konrat, R., Blasi, U., Schroeder, R., 2007. RNA chaperones, RNA annealers and RNA helicases. RNA Biol 4, 118-130.

Remesh, S.G., Verma, S.C., Chen, J.H., Ekman, A.A., Larabell, C.A., Adhya, S., Hammel, M., 2020. Nucleoid remodeling during environmental adaptation is regulated by HU-dependent DNA bundling. Nat Commun 11, 2905.

Robinson, K.E., Orans, J., Kovach, A.R., Link, T.M., Brennan, R.G., 2014. Mapping Hfq-RNA interaction surfaces using tryptophan fluorescence quenching. Nucleic Acids Res 42, 2736-2749.

Rutherford, S.T., Valastyan, J.S., Taillefumier, T., Wingreen, N.S., Bassler, B.L., 2015. Comprehensive analysis reveals how single nucleotides contribute to noncoding RNA function in bacterial quorum sensing. Proc Natl Acad Sci U S A 112, E6038-6047.

Salim, N.N., Faner, M.A., Philip, J.A., Feig, A.L., 2012. Requirement of upstream Hfq-binding (ARN)x elements in glmS and the Hfq C-terminal region for GlmS upregulation by sRNAs GlmZ and GlmY. Nucleic Acids Res 40, 8021-8032.

Sauer, E., Schmidt, S., Weichenrieder, O., 2012. Small RNA binding to the lateral surface of Hfq hexamers and structural rearrangements upon mRNA target recognition. Proc Natl Acad Sci U S A 109, 9396-9401.

Schindelin, J., Arganda-Carreras, I., Frise, E., Kaynig, V., Longair, M., Pietzsch, T., Preibisch, S., Rueden, C., Saalfeld, S., Schmid, B., Tinevez, J.Y., White, D.J., Hartenstein, V., Eliceiri, K., Tomancak, P., Cardona, A., 2012. Fiji: an open-source platform for biological-image analysis. Nat Methods 9, 676-682.

Schneider, C.A., Rasband, W.S., Eliceiri, K.W., 2012. NIH Image to ImageJ: 25 years of image analysis. Nat Methods 9, 671-675.

Skoko, D., Yoo, D., Bai, H., Schnurr, B., Yan, J., McLeod, S.M., Marko, J.F., Johnson, R.C., 2006. Mechanism of chromosome compaction and looping by the Escherichia coli nucleoid protein Fis. Journal of molecular biology 364, 777-798.

Sofroniew, N.e.a. 2022. napari: a multi-dimensional image viewer for Python, https://zenodo.org/record/6598542#.YvitGS-FA6U.

Sorrentino, A., Nicolas, J., Valcarcel, R., Chichon, F.J., Rosanes, M., Avila, J., Tkachuk, A., Irwin, J., Ferrer, S., Pereiro, E., 2015. MISTRAL: a transmission soft X-ray microscopy beamline for cryo nano-tomography of biological samples and magnetic domains imaging. J Synchrotron Radiat 22, 1112-1117.

Sun, X., Zhulin, I., Wartell, R.M., 2002. Predicted structure and phyletic distribution of the RNA-binding protein Hfq. Nucleic Acids Res 30, 3662-3671.

Taghbalout, A., Yang, Q., Arluison, V., 2014. The Escherichia coli RNA processing and degradation machinery is compartmentalized within an organized cellular network. Biochem J 458, 11-22.

Takada, A., Wachi, M., Kaidow, A., Takamura, M., Nagai, K., 1997. DNA binding properties of the *hfq* gene product of *Escherichia coli*. Biochem. Biophys. Res. Com. 236, 576-579.

R Team, 2020. R: A language and environment for statistical computing R Foundation for Statistical Computing.

Tolstorukov, M.Y., Virnik, K.M., Adhya, S., Zhurkin, V.B., 2005. A-tract clusters may facilitate DNA packaging in bacterial nucleoid. Nucleic Acids Res 33, 3907-3918.

Tsui, H.C., Leung, H.C., Winkler, M.E., 1994. Characterization of broadly pleiotropic phenotypes caused by an *hfq* insertion mutation in *Escherichia coli* K-12. Mol. Microbiol. 13, 35-49.

Turbant, F., Wu, P., Wien, F., Arluison, V., 2021a. The Amyloid Region of Hfq Riboregulator Promotes DsrA:rpoS RNAs Annealing. Biology (Basel) 10.

Turbant, F., Waeytens, J., Campidelli, C., Bombled, M., Martinez, D., M., G., B., H., Raussens, V., Wien, F., Velez, M., Arluison, V., 2021b. Membrane perturbations caused by the bacterial riboregulator Hfq. in preparation.

Udekwu, K.I., Darfeuille, F., Vogel, J., Reimegard, J., Holmqvist, E., Wagner, E.G., 2005. Hfq-dependent regulation of OmpA synthesis is mediated by an antisense RNA. Genes Dev 19, 2355-2366.

Updegrove, T.B., Zhang, A., Storz, G., 2016. Hfq: the flexible RNA matchmaker. Curr Opin Microbiol 30, 133-138.

Updegrove, T.B., Correia, J.J., Galletto, R., Bujalowski, W., Wartell, R.M., 2010. E. coli DNA associated with isolated Hfq interacts with Hfq's distal surface and C-terminal domain. Biochim Biophys Acta 1799, 588-596.

Valens, M., Penaud, S., Rossignol, M., Cornet, F., Boccard, F., 2004. Macrodomain organization of the Escherichia coli chromosome. EMBO J 23, 4330-4341.

Vecerek, B., Rajkowitsch, L., Sonnleitner, E., Schroeder, R., Blasi, U., 2008. The C-terminal domain of Escherichia coli Hfq is required for regulation. Nucleic Acids Res 36, 133-143.

Verma, S.C., Qian, Z., Adhya, S.L., 2019. Architecture of the Escherichia coli nucleoid. PLoS Genet 15, e1008456.

Vincent, H.A., Henderson, C.A., Stone, C.M., Cary, P.D., Gowers, D.M., Sobott, F., Taylor, J.E., Callaghan, A.J., 2012. The low-resolution solution structure of Vibrio cholerae Hfq in complex with Qrr1 sRNA. Nucleic Acids Res 40, 8698-8710.

Vogel, J., Luisi, B.F., 2011. Hfq and its constellation of RNA. Nat Rev Microbiol 9, 578-589.

Wang, D., Li, H., Ma, X., Tang, Y., Tang, H., Huang, D., Lin, M., Liu, Z., 2021. Hfq Regulates Efflux Pump Expression and Purine Metabolic Pathway to Increase Trimethoprim Resistance in Aeromonas veronii. Front Microbiol 12, 742114.

Wang, W., Li, G.W., Chen, C., Xie, X.S., Zhuang, X., 2011. Chromosome organization by a nucleoid-associated protein in live bacteria. Science 333, 1445-1449.

Wen, B., Wang, W., Zhang, J., Gong, Q., Shi, Y., Wu, J., Zhang, Z., 2017. Structural and dynamic properties of the C-terminal region of the Escherichia coli RNA chaperone Hfq: integrative experimental and computational studies. Phys Chem Chem Phys 19, 21152-21164.

Wiggins, P.A., Dame, R.T., Noom, M.C., Wuite, G.J., 2009. Protein-mediated molecular bridging: a key mechanism in biopolymer organization. Biophys J 97, 1997-2003.

Wilusz, C.J., Wilusz, J., 2005. Eukaryotic Lsm proteins: lessons from bacteria. Nat Struct Mol Biol 12, 1031-1036.

Wolter, H., 1952. Spiegelsysteme streifenden Einfalls als abbildende Optiken für Röntgenstrahlen Wiley.

Zhu, Y., Mustafi, M., Weisshaar, J.C., 2020. Biophysical Properties of Escherichia coli Cytoplasm in Stationary Phase by Superresolution Fluorescence Microscopy. mBio 11.

4.3. New developments of the cryo-SXT analysis protocol

Compared to the protocol described in Publication 3 (Cossa, Wien, et al. 2022), we improved our analysis in Publication 4. These improvements should be part of a new chapter of Methods in Molecular Biology series in 2023 to update the method specifically applied to Gram-negative bacterial analysis.

First, the gold bead fiducials were creating reconstruction streak artefacts inside of the bacteria and were affecting the corresponding linear absorption coefficients (LAC) values thus biasing our analysis. We have therefore conceived a new protocol to eliminate those artefacts by masking the gold beads fiducials and re-analysed all the cell conditions. The step-by-step procedure is described below and in the Methods of Publication 4.

It should be noted that this problem is particularly important in Gram *(-)* bacteria that have an electrostatically charged outer membrane that attracts gold beads (which are positively charged). We have now established that this problem can be counteracted during the sample preparation step by applying the gold bead fiducials on the grids and letting them dry in a dust-free environment prior to the deposition of the bacterial samples (see Notes, in Publication 3 (Cossa, Wien, et al. 2022)). While not completely solving this problem, as the addition of the bacterial cells releases a portion of the beads from the grid, we noticed that it significantly reduces it.

Protocol for fiducial masking

The fiducials close to bacteria of interest in the absorption tilt-series were manually masked using Napari (Sofroniew, Nicholas et al. 2022) and a Wacom Cintiq graphic pen display. The resulting mask was then applied to the tilt-series to remove the fiducial pixels by replacing them with the NaN (Not a Number) value (i.e., can be assimilated to empty pixels). Next, the inpainting fill in those NaNs by estimating their pixel values. Note that because of this, it is crucial that the masks cover all the pixels of the beads in order for the inpainting algorithm not to artificially recreate the beads. Therefore, the masking should be a little wider than the actual size of the beads. We used 500 iterations of an iterative discrete cosine transform-based (DCT) inpainting algorithm implemented in MATLAB (Garcia 2010).

Second, while repeating all the processing pipeline after masking the beads, we have noticed that we originally used, by mistake, a default parameter in the reconstruction step which

is the long object compensation that is commonly used in electron tomography and should not be applied here. This parameter was affecting the absolute LAC values obtained which were being rescaled.

Therefore, resulting inpainted tilt-series were reconstructed using 30 iterations of Simultaneous Iterative Reconstruction Technique (SIRT) (Gilbert 1972), at full Z-height and without long object compensation, implemented in Tomo3D.

We verified that the new reconstructed LAC values with SIRT using Tomo3D software without long object compensation are equivalent to those obtained with TomoPy using SIRT or ART and with TomoJ using ART.

Volumes were then cropped to Z = 300 px, YZ-flipped to have the missing-wedge along the Z-axis, and the voxel values divided by 0.01 or 0.008 depending on the pixel size (respectively 10 and 8 nm) to recover the linear absorption coefficient (LAC) values (in μm^{-1}). Figure 26 shows the differences between normal versus inpainted volume slices.

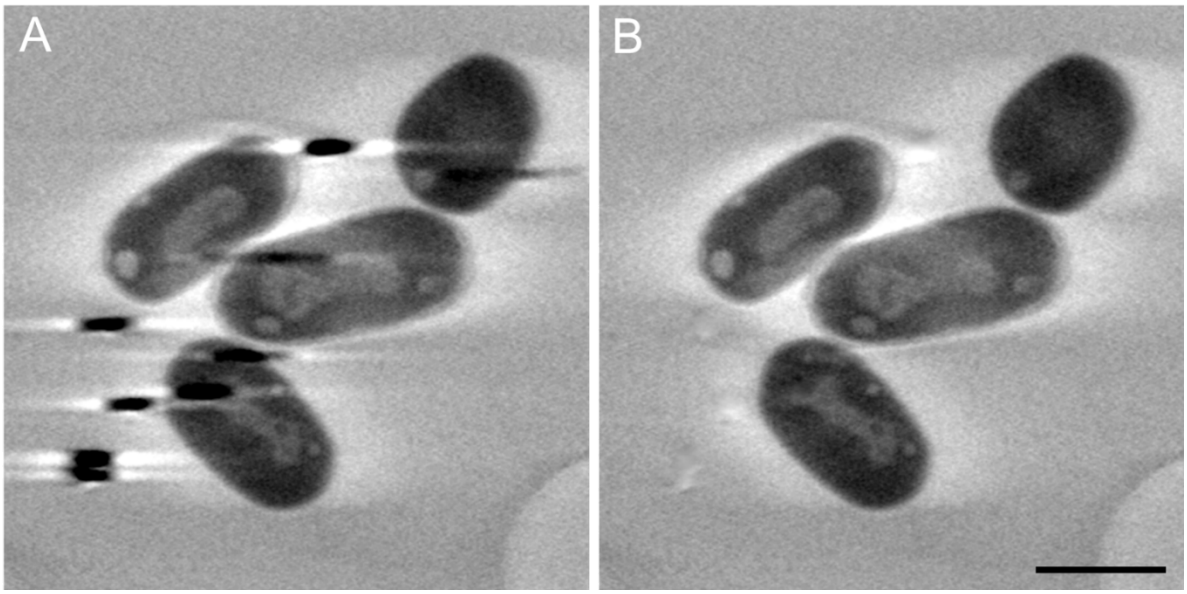

Figure 26. Comparison of the same 3D reconstruction slices without (A) and with (B) masking and inpainting of the gold bead fiducials on the aligned tilt-series. While some artefacts are still visible at the position of the fiducials, the streak artefacts completely disappeared. This example was done on *Δhfq* stationary phase cells. Note that both volumes were reconstructed using the same parameters in Tomo3D (30 iterations of SIRT, full Z length, without long object compensation). Scale bar represents 1 µm.

The next critical point is the limitations of missing wedge due to tilt-angle limitation. To image bacteria using cryo-SXT on the MISTRAL beamline at ALBA synchrotron, the 40 nm Fresnel zone plate (40ZP) might give overall better tomograms than the 25 nm ZP (25ZP) because of their depth of field (DoF), respectively 3.3 and 1.6 µm (Otón et al. 2016). The 25ZP has a better resolution but at the cost of a lower DoF compared to the 40ZP. This lower DoF induces a fiducial tracking of lower quality at high tilt-angles because the gold bead fiducials become blurry and thus harder to track precisely. This effect is stronger the farther the fiducials are from the tilt-axis. Note that to partly alleviate this limitation, it is possible to mix 100 nm and 60 nm gold beads as the 100 nm ones are trackable on most tilt-images but with a lower accuracy than the 60 nm ones which permit a better alignment at the cost of not being trackable on all views. Furthermore, combining the 40ZP with dual-axes tilt-series acquisition has the potential to give better results/resolution than the 25ZP because of a reduction of the missing wedge to a missing pyramid. Then, this could lead to a better 3D segmentation.

As for the effect due to the missing wedge, it is known that it impacts the LAC values of the reconstructed tomograms by underestimating values by about 10 to 20%. This aspect is currently being investigated at MISTRAL using phantoms to determine which reconstruction algorithm gives the most accurate LAC values.

In addition, the reconstructed nucleoid volumes also suffer from this missing wedge issue as it is well known that it provokes an elongation along the Z-axis. But, as all cell conditions discussed here suffer from the same bias in LAC under-estimation and from the same reconstructed volume elongation and considering that we are discussing relative values among cell conditions and not absolute ones, we believe this not to be a limiting factor when interpreting the data.

Finally, we are aware that other problems still need to be corrected in the future to improve accuracy of the results. Among these problems Quantifoil Au grids for instance have carbon holes that induce artefacts in 3D reconstruction. We can also mention the difficulty specific to bacteria to segment the nucleoid because of the lack of membrane separating it from the rest of the cell. Finally future analyses should extend the number of individuals to have stronger statistics.

4.4. Correlative imaging

Initially, one of the goals of my PhD project was to carefully retrieve the cryo-grids after cryo-SXT imaging to correlatively analyze the exact same bacteria using cryo-TEM in our lab at Institut Curie. This procedure necessitates great care as handling the cryo-grids needs to be done in a cryo-environment (i.e., with liquid nitrogen). While a first batch of grids was successfully retrieved and sent back to our lab, the cryo-TEM imaging did not yield exploitable results because of the presence of a lot of ice contamination and too thick ice.

These observations led us to pivot to analyze the next batch of grids using cryo-STEM. Unfortunately, due to a problem during transportation, the cells were lost, and this analysis has not been possible. We hoped to redo the experiment but due to COVID crisis, we could unfortunately not plan a new series of experiments before the end of my PhD.

4.5. Conclusions and perspectives

From our analysis, we can conclude that Hfq influences nucleoid density especially during the stationary growth phase when it is more abundant. Our results indicate that Hfq could regulate nucleoid compaction directly *via* its interaction with DNA, but also at the post-transcriptional level via its interaction with sRNA. Taken together, our findings reveal a new role for this protein in nucleoid remodelling *in vivo*, that may serve in response to stress conditions and in adapting to changing environments.

As a general remark about the method, we must indicate that LAC values reported can be significantly different than those previously reported for X-ray tomography of *E. coli,* for instance by Hammel et al. or Remesh et al. (Hammel et al. 2016; Remesh et al. 2020). This can be explained. There is indeed no reference to absolute LAC values and differences in LAC values are common in the literature. The nucleoid LAC values reported in the two publications mentioned above in the same group using the same set up and method indeed are significantly different: while Hammel *et al.* reported a WT MG1655 nucleoid LAC of 0.22 μm^{-1}, Remesh et al. reported LAC of 0.41 μm^{-1} for the same experimental conditions. As these differences and the exact type of reconstruction used are not discussed in the mentioned papers, it is difficult to understand where the difference could originate. Our thought is that the different algorithm implementation in the respective reconstruction software used might explain this.

Note that these data were collected with the same instrument using full tilt projection series (spanning over 180 degrees evenly).

Results from WT MG1655 are the only we can use for comparison of data in (Hammel et al. 2016; Remesh et al. 2020) with our data, which are closer to the values reported by Hammel et al. (Hammel et al. 2016). In our discussion, we have focused on the relative differences between reconstructed LAC values for the different cell conditions and not on the absolute LAC values of each of them, exactly as this was done in Hammel et al. and in Remesh et al (Hammel et al. 2016; Remesh et al. 2020). As indicated previously, the most important point is that all our data have been collected with the same instrument and have been processed in the same way, thus relative differences are biologically meaningful.

The last point we can mention is that we have obtained nucleoid structures presenting low and high absorbance domains, as well as the nucleoid cores. Unfortunately, the domains cannot be further identified and compared with previous data about *E. coli* nucleoid macrodomains (Espéli and Boccard 2006). Indeed, fluorescence microscopy analyses have revealed the non-random organization of chromosomic DNA in bacteria. Precisely, in *E. coli*, four large regions centred on the replication origin domain (Ori), the replication termination domain (Ter) and two additional macrodomains flanking the Ter domain have been evidenced. It has made possible to label these domains due to protein tag available for light microscopy. Unfortunately, to date an approach for labelling specifically the proteins using cryo-SXT is not available but should bring many useful information if it can be developed (see Chapter VI).

Chapter V. Sparse cryo-STEM tomography for biological samples

5.1. Introduction to cryo-scanning transmission electron microscopy (cryo-STEM)

In scanning mode, the electron beam is condensed into a (sub)nanometric probe (contrasting with the parallel beam in TEM mode) which is focused on the sample plane and raster scans it using a set of two scanning coils. Unlike in TEM, the signal is not acquired as a direct image but rather pixel by pixel and line by line.

In STEM, the objective lens is located before the sample (contrary to TEM) and the signal is collected on the bright field (BF) detector, annular dark field (ADF) (Figure 27) and eventually on a high-angular ADF (HAADF).

In STEM the contrast is not based on phase contrast like in TEM but on electron scattering (Sharon G. Wolf and Elbaum 2019). It is thus an amplitude contrast depending on the atomic Z-number and the sample thickness. In bright field (BF) imaging, the signal is produced by transmitted and inelastically scattered electrons attaining the BF detector versus elastically scattered electrons creating darker contrast (see Figure 13).

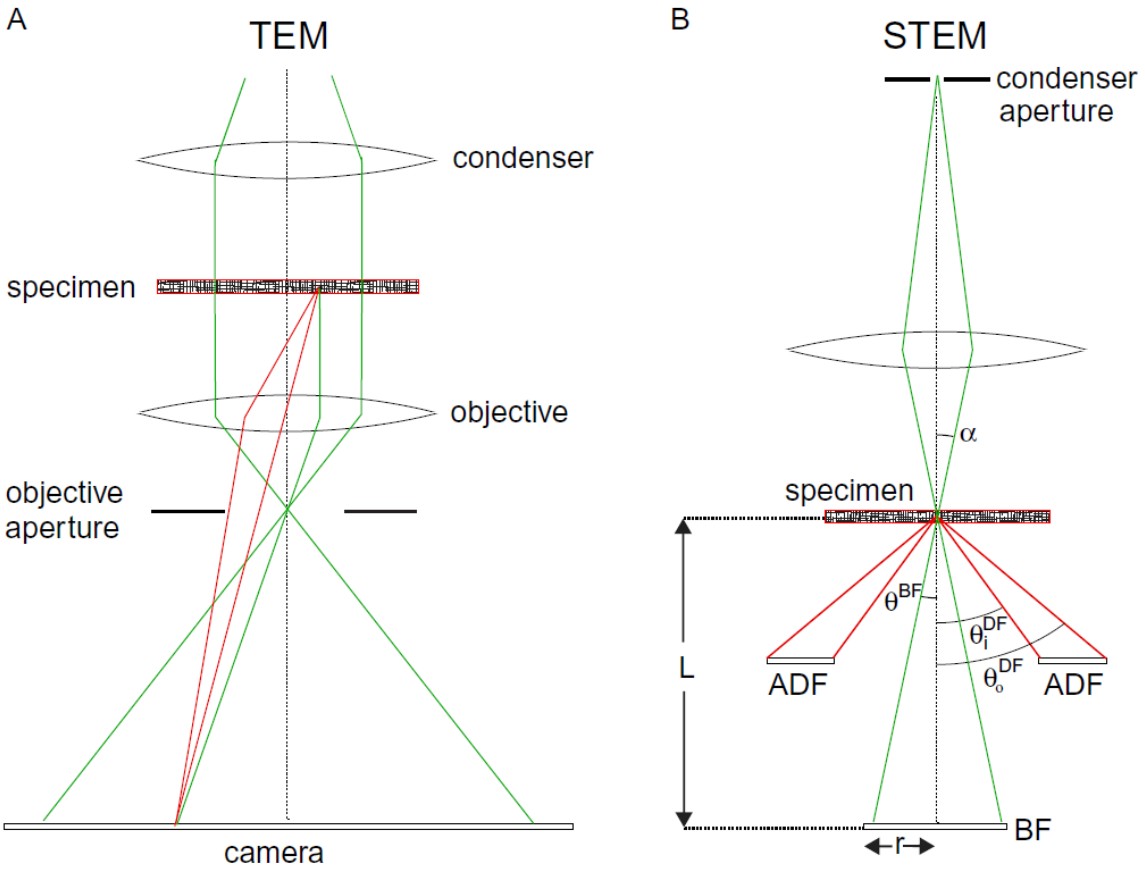

Figure 27. Schematics of the optical differences between TEM (A) and STEM (B) imaging modes. ADF, Annular Dark Field; BF, Bright Field; α, semi-convergence angle; θ_o, outer acceptance angle; θ_i, inner acceptance angle; r, detector segment radius; L, camera length **(Sharon G. Wolf and Elbaum 2019)**.

Due to the differences in the way the electron dose is administered to the sample, cryo-STEM induces less electron radiation damages at equal electron dose than cryo-TEM (Sharon Grayer Wolf, Houben, and Elbaum 2014) and provides a greater electron mean free path, meaning that cryo-STEM can image through thicker specimens even exceeding the micrometre barrier (Rez, Larsen, and Elbaum 2016; Trépout 2020). Those two characteristics make cryo-STEM most suitable for the study of whole cell biological samples. Even though this method was historically widely used in material science it is gaining more and more popularity among the biological field.

In cryo-STEM, there are several microscope parameters that can adjusted to our needs to reduce electron radiation. One is the dwell time, which is defined by the time the scanning electron beam takes to scan a single pixel. The faster the dwell time, the less radiation damage is applied to the sample. Depending on the sample thickness, the convergence of the beam can

be adjusted by the condenser aperture. A more convergent beam, resulting in a smaller probe, thus provides better resolution, but with a decreased depth of focus. On the opposite, less convergent beams up to almost parallel beams generate increased depth of focus but at the expense of a diminished resolution because the probe size is greater than 1 nm.

The electron dose remains the main limitation for tomography as the number of projection images increases. To overcome this restraint, different acquisition methods have been developed.

We are interested in bright field (BF) signals because of the light elements (low atomic Z-number) constituent of unstained biological cryo-samples.

5.1.1. Sparcity and inpainting

Inpainting techniques are mathematical methods that permit recovery of a signal close to the fully sampled one starting from an undersampled signal. It can be applied to recover missing information in a dataset, such as missing pixels in a sparse image. In our lab, at Institut Curie, we usually use an inpainting algorithm based on the discrete cosine transform (Garcia 2010) implemented in MATLAB. This algorithm has the advantage of considering all data of a sparse image to estimate the value of missing pixels while classical interpolation methods only consider the surrounding pixels.

The Institut Curie lab where I worked for a part of my PhD is pioneering in the collection of sparse images in STEM and STET (Trépout 2019). Using a similar approach, we propose a sparse sampling method based on the acquisition of regularly spaced lines in cryo-STEM tomography (cryo-STET). The acquisition of lines allows better control of the electron-dose deposition, especially when the EM is not equipped with a faster shutter at the level of the condenser. Our results show that this method, complemented with inpainting, enables the acquisition of good results while decreasing the total electron dose received by the sample, and/or doing tomographic acquisition at higher magnification (Cossa, Cren, et al. 2022; Cossa, Arluison, and Trépout 2021).

Details of the method are presented in the Publication 5.

PUBLICATION 5

“Sparse Cryo-STEM Tomography for Biological Samples.”

In *Microscopy and Analysis*, (36)4:16 – 19 (EU), August 2022.

Cossa Antoine, Christel Cren, Thomas Mouveaux, Philippe Bastin, Mathieu Gissot, and Sylvain Trépout.

Sparse cryo-STEM tomography for biological samples

A. Cossa[1,2,3], C. Cren[4], T. Mouveaux[5], P. Bastin[4], M. Gissot[5], S. Trépout[2,6]

[1] Laboratoire Léon Brillouin LLB, CEA, CNRS UMR12, Université Paris-Saclay, CEA Saclay, F-91191 Gif-sur-Yvette, France
[2] Institut Curie, Université PSL, CNRS UAR2016, Inserm US43, Université Paris-Saclay, Multimodal Imaging Center, 91400 Orsay, France
[3] National Center of Biotechnology, CSIC, Campus Univ. Autónoma de Madrid, 28049 Cantoblanco, Madrid, Spain
[4] Trypanosome Cell Biology Unit, Inserm U1201, Institut Pasteur, 25 Rue du Docteur Roux, 75015 Paris, France
[5] Univ. Lille, CNRS, Inserm, CHU Lille, Institut Pasteur de Lille, U1019 - UMR 9017 - CIIL - Centre d'Infection et d'Immunité de Lille, 59000 Lille, France
[6] Monash Ramaciotti Centre for Cryo Electron Microscopy, Monash University, Melbourne, Victoria, 3800 Australia

Abstract

Cryo-STEM tomography is a unique and unrivalled method capable of imaging micrometre-thick samples at the nanometre scale. Yet, the electron dose received by the sample during cryo-STEM tomography experiments is high, thus preventing i) the observation of thicker samples and ii) the use of higher magnifications, which would both require even higher electron doses. Here, we describe a new low-dose method which consists in collecting a fraction of the image pixels. The limitations of the method are discussed and an actual sparse cryo-STEM tomography dataset is presented as a proof of principle.

Acknowledgements

This work was supported by the "ADI 2019" project funded by the IDEX Paris-Saclay, ANR-11-IDEX-0003-02.

Corresponding Author Details

Sylvain Trépout, Monash University, Ramaciotti Centre for Cryo-EM, G92, 15 Innovation Walk, Clayton Campus, Victoria, 3800 Australia. Email: sylvain.trepout@monash.edu

Citation

Cossa, Antoine, Christel Cren, Thomas Mouveaux, Philippe Bastin, Mathieu Gissot, and Sylvain Trépout. 2022. "Sparse Cryo-STEM Tomography for Biological Samples." Microscopy and Analysis, August 2022.

Introduction

Structural biology plays an important role in the understanding of cellular processes. By resolving the structure of a cellular molecular complex or a protein, it is possible to partly understand how it functions. Transmission electron microscopy (TEM) has the potential to resolve the structure of biological objects thanks to its high-resolution capabilities. Cryo-TEM is a method combining TEM and cryo-methods which is able to study vitrified samples in a near-native state at very high resolution. Moreover, tomographic acquisition (cryo-TET) can be performed to study the 3D structure of objects, consisting in collecting several tilted views of the same sample (typically in the tilt range ±65°), which are used to computationally reconstruct the 3D volume of the object of interest. Cryo-TET is mainly limited by the maximum sample thickness which is ~250nm [1], depending on the accelerating voltage (i.e., 200 or 300kV) and the absence or presence of a post-sample energy filter which can increase the signal-to-noise ratio (SNR) of the collected images by discarding inelastically scattered electrons. Hence, cryo-TET cannot be used on thick samples such as prokaryotes or eukaryotes unless it is combined with thinning approaches such as focused ion beam. If used below the thickness limit, cryo-TET can achieve nanometric resolution of cellular content and even sub-nanometric resolution when combined with sub-tomogram averaging.

Scanning TEM (STEM) is an alternative to standard TEM mainly used in material sciences. STEM uses a convergent electron beam focused at the sample plane which is moved in a raster scanning fashion, enabling point by point imaging of the sample [2-3]. STEM is gradually being used in biological sciences. Indeed, STEM tomography (STET) has been used to explore the structure of biological samples embedded inside thick resin sections. Compared to TET, STET has the potential to image thicker samples (up to 1µm), yet at the expense of resolution since imaging of thick samples requires the use of 1 to 2nm probe sizes, which drastically limits the resolution. Cryo-STEM tomography (cryo-STET) has been developed in 2014 [4]. In cryo-STET, the sample is deposited on the grid (alternatively it can also be grown directly on the grid) and there is no need for further thinning, making the sample preparation step quick and easy. It can be applied to study entire thick samples such as prokaryotes and eukaryotes. Since cryo-STET does not involve the use of the polymers which are found in resins but rather H_2O, the mean free path of the incident electrons is increased and then samples of at least 1.5µm can be observed [5] as more electrons reach the detector.

The main limitation of cryo-STET of thick biological samples is the electron dose that it requires, making high magnification (hence high-resolution) studies difficult or near impossible. First, very thick samples (>1µm) need an increase of the electron dose to have sufficient SNR because of the higher percentage of electrons scattering occurring while passing through the sample. This is materialized by an increase of the pixel dwell time. Second, reaching high magnifications requires the beam to scan the sample surface more slowly, meaning that higher sample irradiation occurs. Since cryo-fixed biological samples are very sensitive to radiation damage caused by the electron beam, it becomes obvious that imaging thick biological samples at high magnification is particularly tricky. It is estimated that the maximum total electron dose received by the sample should not be over $100e^-/Å^2$. Though, cryo-STET has been shown to be a less damaging method compared to cryo-TET and that higher doses can be used without seeing the sample burn [4]. Then, a solution must be found to reduce the electron dose.

In electron microscopy, the reduction of the electron dose can be performed using different strategies. In the particular case of ET, this can be performed at the level of the tilt-series (i.e., tilt down-sampling) or at the level of the image (i.e., image down-sampling). On one hand, tilt down-sampling is trivial and simply consists in reducing the number of collected

tilt images. On the other hand, image down-sampling is much more challenging and consists in collecting a limited number of pixels per acquired image (i.e., producing sparse images). Image down-sampling is superior to tilt down-sampling because it produces more homogeneous collection of the information, hence improving the reconstruction quality [6]. Currently, sparse image collection is mastered by a handful of laboratories worldwide that exploit the point-to-point imaging pattern of STEM [7-11].

In the present work, we propose a new method to collect sparse images, using parallel line scans. Instead of collecting all the lines that an image is composed of, we propose to acquire only a fraction of them, dramatically reducing the total electron dose received by the sample and thus allowing us to increase magnification or increase dwell time. This sparse scheme requires an additional pre-processing step after acquisition to recover the missing information. This process is called image inpainting, this term was introduced by Bertalmio *et al*. 2000 [12] and consists in using mathematical methods to recover the missing information in an image based on the surrounding information (i.e., pixels). Several methods can be used such as discrete cosine transform (DCT) [13] or shearlet transform [14].

Materials and Methods

Cell culture

T. brucei AnTat 1.1E bloodstream forms were cultivated in HMI-11 medium supplemented with 10% foetal calf serum at 37°C in 5% CO_2. Exponential growth-phase cells (~$2x10^6$ parasites/mL) were used for this study.

T. gondii tachyzoites of the RH strain were propagated *in vitro* in human foreskin fibroblasts using Dulbecco's Modified Eagle Medium supplemented with 10% foetal calf serum, 2mM glutamine and 1% penicillin-streptomycin. Tachyzoites were grown in ventilated tissue culture flasks at 37°C and 5% CO_2. Tachyzoite at a concentration of 10^7 parasites/mL were used for this study.

Sample preparation

After cell culture, the two cell types (i.e., *T. brucei* and *T. gondii*) were fixed with formaldehyde (paraformaldehyde 4% w/w final concentration) directly in the culture medium to preserve the cell integrity. The sample (5µl drop) was deposited on a glow-discharged Quantifoil 200 mesh R2/2 grid (Quantifoil, Großlöbichau, Germany). The grids were pre-coated with gold beads of different sizes that were used for tracking and focusing purposes during the automated data collection. The pre-coating was made with a gold bead solution which was composed of commercial 15nm gold beads (Aurion) and lab-made gold nanorods of various dimensions (synthesised at Li's laboratory, Ecole Normale Supérieure Chimie Paris-Tech, Paris, France) mixed in equivalent proportions. After depositing the sample, the grids were manually blotted from the back side using a Whatman filter paper and plunge-frozen into liquid ethane at −174°C using a Leica EM-CPC equipment (Leica, Wetzlar, Germany). After freezing, the grids were stored in a liquid nitrogen tank until observation by cryo-electron tomography.

Cryo-STEM tomography data collection, alignment and reconstruction

Before data collection, cryo-plunged electron microscopy grids were mounted on a Gatan 914 high-tilt cryo-holder (Gatan, Pleasanton, CA, USA). Cryo-STET datasets were collected on a JEOL 2200FS 200kV field emission gun hybrid TEM/STEM electron microscope (JEOL, Tokyo, Japan). 3k by 3k images were collected in bright-field mode using

Electron dose reduction for cryo-STEM tomography

a 20µm condenser aperture and an on-axis JEOL STEM detector placed at 40cm camera length (the signal was digitised to 16-bit values using a Digiscan II ADC). The dwell time was set between 1 and 3µs/pixel and the magnifications used was 60,000x (corresponding pixel size is 1nm).

Images and tilt-series were collected in Digital Micrograph. Fully-automatic cryo-STET tilt-series were collected using a home-made script developed in Digital Micrograph. The STET acquisition software used here has previously been presented in detail [7]. Tilt-series were collected between −65° and + 65° using 2° tilt increments. The total electron dose received by the sample was $80e^-/Å^2$ for the full images collected on the *T. gondii* sample and $24e^-/Å^2$ for the sparse images collected on the *T. brucei* sample.

Fiducial-based alignment of the tilt-series was performed in Etomo (v.4.9.10) [15-16]. 3D volume reconstructions were computed using 30 iterations of simultaneous iterative reconstruction technique (SIRT) as implemented in Tomo3D (v2.0) [17-18]. Data exploration and analysis was performed using ImageJ [19], MATLAB (The MathWorks Inc., Natick, MA, USA), Python (3.9) and manual segmentation was performed in PhotoFiltre.

In silico sparse image generation and inpainting

A conventional tilt-series was first binned by a factor two and normalized using the whole tilt-series histogram. Then, a Python script was used to generate *in silico* sparse images. Briefly, a fraction of the frame lines was removed from each tilt-angle image of the tilt-series, leaving regularly spaced pixel lines. The missing values were set to NaN (Not a Number) for further inpainting process. Bicubic interpolation inpainting was processed via a homemade Python script. DCT inpainting (250 iterations) was performed in MATLAB.

Performance evaluation metrics

Commonly used evaluation metrics were computed to assess the performance of each inpainting algorithm, i.e., the mean squared error (MSE), the peak signal to noise ratio (PSNR), which both measure the fidelity of the inpainted image compared to the original one, and the structural similarity index measure (SSIM) [20]. The latter measures the perceptive quality of the inpainting rather than absolute error of the individual pixels as MSE or PSNR. In order to have a representative metrics evaluation on the inpainted tilt-series as well as on the reconstructed volumes, a rescale of the tilt-series images intensities was performed in the interval [-1, +1] using the whole tilt-series histogram. For the volumes, the rescale was done on the whole volumes and the metrics were evaluated on each Z-slice.

$$MSE = \frac{1}{m\,n}\sum_{i=0}^{m-1}\sum_{j=0}^{n-1}[I(i,j) - K(i,j)]^2$$

$$PSNR = 10.\log_{10}\left(\frac{MAX_I^2}{MSE}\right)$$

$$SSIM(x,y) = \frac{(2\mu_x\mu_y + c_1)(2\sigma_{xy} + c_2)}{(\mu_x^2 + \mu_y^2 + c_1)(\sigma_x^2 + \sigma_y^2 + c_2)}$$

Where m and n are the number of rows and columns in the image respectively, I is the reference image, K is the reconstructed image, μ_x is the average x, μ_y is the average of y, σ_{xy}

is the covariance of x and y, σ_x^2 is the variance x, σ_y^2 is the variance y and c_1 and c_2 are two variables to avoid divisions by close-to-zero denominators.

Results / Discussion

In silico sparsity simulation on *T. gondii* images

First, we evaluated the reconstruction quality of two different inpainting strategies, the bicubic reconstruction and the DCT reconstruction. For that purpose, we generated several differently-downsampled sparse images *in silico* using fully-framed images from a cryo-STEM tomographic tilt-series acquired on *T. gondii*. Images were collected at the apical end of the cell. After data collection, only a certain fraction of each tilt-image lines was kept to mimic a sparse acquisition (e.g., 10%, 20%, and 50%). Note that this scheme enables to use full-framed images as reference to compute the metrics. Each image of each tilt-series went through this process. After removing a certain fraction of the lines, inpainting was performed using either bicubic interpolation or DCT. The following table presents the evaluation metrics values for each tested condition.

	Scanned lines (%)	MSE (10^{-4})	PSNR (dB)	SSIM (%)
Reference	100	0.00	100.00	100.00
Bicubic inpainting	50	1.46	44.67	62.90
	20	2.55	42.26	36.67
	10	4.45	39.62	27.08
DCT inpainting	50	**1.24**	**45.38**	**66.62**
	20	1.88	43.57	43.66
	10	2.07	43.17	35.28

Table 1. Inpainting reconstruction quality of the tilt-series assessed using evaluation metrics (MSE, PSNR and SSIM). Each value reported in this table corresponds to the average value for the whole tilt-series.

As can be observed from the results reported in Table 1, the lower the number of simulated scanned lines, the lower the quality of the reconstruction for all metrics. This was expected. With 50% of the lines scanned, the bicubic interpolation generates pixels which values are not so different from the original ones, as can be seen by the MSE value which is 1.46×10^{-4} and preserves well the perceived structural observation (SSIM value is 62.90%). With 20% and 10% of the lines scanned, the bicubic interpolation fails at reconstructing accurate pixel values as the metrics crash. The quality decreases as measured with the metric values is particularly rapid for the bicubic interpolation. This is not the case for the DCT reconstruction which always performs better and appears to be more robust when the number of lines scanned decreases. This can be observed as the MSE and PSNR values for the DCT reconstruction of the images containing only 10% of the lines are better (i.e., better reconstruction quality) compared to the same metrics for the bicubic reconstruction of the images containing 20% of the lines. For the SSIM metric, the two types of reconstruction (i.e., 10% DCT and 20% bicubic) have similar quality. The results show that DCT performs better than bicubic with two times fewer pixels. DCT is robust as MSE and PSNR only change slightly when the number of lines scanned is diminished from 20% to 10% (from 1.88×10^{-4} to 2.07×10^{-4} and from 43.57dB to 43.17dB, respectively). On the other hand, the SSIM shows that a significant part of the structure is lost and cannot be recovered even with DCT.

Electron dose reduction for cryo-STEM tomography

During the tomographic reconstruction process, the values of the 2D projection images are projected in a 3D volume. This process could potentially lead to a low-quality 3D volume (if the pixel value differences are being added) or a regular quality 3D volume (if the pixel value differences are averaged out). Since DCT performed much better than the bicubic reconstruction on the tilt-series images, only DCT-reconstructed volumes were analysed. Before assessing this question, it was important to perform a fair comparison of the 3D volumes. Indeed, since the sparse tilt-series do not contain as original and accurate structural information as the reference tilt-series, their alignment could be of inferior quality. For this reason, the alignment of the reference tilt-series was applied on the other tilt-series. This has the advantage of enabling pixel-by-pixel comparison of the 3D volumes as it was done for the tilt-series. The results can be found in the Table 2.

	Scanned lines (%)	MSE (10^{-3})	PSNR (dB)	SSIM (%)
Reference	100	0.00	100.00	100.00
DCT inpainting	50	0.32	40.92	71.15
	20	2.44	32.14	47.77
	10	4.88	29.16	44.79

Table 2. **Inpainting reconstruction quality of the 3D volumes assessed using evaluation metrics (MSE, PSNR and SSIM).** Each value corresponds to the average for the whole 3D volume (1000 Z-slices).

Similarly to what was observed for the reconstruction of the missing pixels in the tilt-series, the lower the number of simulated scanned lines, the lower the quality of the reconstruction for all tested metrics. This was expected too. Yet, compared to the values computed on the tilt-series, the MSE and PSNR values display rapid deterioration of the reconstruction quality while the SSIM value shows a much slower degradation. This can be explained by the fact that the values of the voxels constituting the 3D reconstructions originate from the values of the pixels constituting the 2D images. Meaning that in the sparse dataset, the voxel values are defined by original pixel values and inpainted pixel values. Then when the proportion of inpainted pixels becomes much higher than that of the original pixels, the computed voxel values deviate significantly from the reference values, which is what is measured by MSE and PSNR. From the SSIM point of view, the reconstruction from the dataset containing 50% of the original lines has a high structural similarity with the reference. Interestingly, this difference is higher than what was computed for the tilt-series (71.15% versus 66.62%). The SSIM of the two other reconstructions are not very different.

To better appreciate the structural information contained in the different reconstructions, images (Z-slices) from the 3D volumes have been extracted (Figure 1). Several structural elements of *T. gondii* can be observed in the reference reconstruction (Figure 1A). Recently, several of these structures have been characterised at higher resolution [21]. When only 50% of the original pixels are present, the structural elements are still visible, yet the reconstruction appears noisier. When only 20% and 10% of the original pixels are present, the reconstruction quality is visually deteriorated and almost no structural elements can be spotted, except for the ones found at the periphery of the cell (i.e., the conoid, the plasma membrane and the inner membrane complex). Note that this *T. gondii* cell is ~2.5µm thick and that only few electrons can pass through such a thick sample explaining the weak contrast in the 3D reconstruction.

Electron dose reduction for cryo-STEM tomography

Actual cryo-STET sparse acquisition on *T. brucei*

After investigating the quality reduction of a sparse cryo-STET dataset generated *in silico* compared to a conventional cryo-STET one, the next step was to actually collect a sparse cryo-STET dataset at the microscope. This was performed on *T. brucei*, a parasite thinner than *T. gondii*. In this dataset, only 10% of the pixels were collected using the previously described scheme, performing very low-dose conditions. DCT was applied to reconstruct the missing pixels. Images were collected at the middle of the cell were the cell is ~1µm thick. The studied cell possessed two flagella, an old one and new one which we could discriminate because the growing end of the new one was visible (Figure 2). Even though only 10% of the pixels were collected, the observable structural details are important. Several elements can be distinguished in the cytoplasm and the lumen of the microtubules can be observed in some parts of the old flagellum (Figure 2D, arrow-heads). The organisation of the structural elements observed in this sparse cryo-STET dataset is similar to that found in conventional cryo-STET dataset [5].

Summary and conclusions

In this pioneering work we present the potential of sparse cryo-STET on thick biological samples. Images containing only 10% of the pixels can be collected and reconstructed to generate 3D volumes containing the structural elements found using conventional imaging methods. The quality of the 3D volume is necessary of inferior quality and resolution but considering the reduction of the electron dose applied to the sample, there is currently no other method with a better resolution/dose ratio on whole cells. Sparse cryo-STET has many potential applications for thick specimens such as large prokaryotes and eukaryotes which for the moment cannot be observed at the nanometre scale without enduring a thinning process. There is also room for improvement of the method, at the level of the data acquisition (e.g., different smarter sparse schemes) but also at the level of the pixel reconstruction and the overall 3D volume reconstruction quality.

References

[1] K. Aoyama, T. Takagi, A. Hirase, A. Miyazawa, STEM tomography for thick biological specimens, Ultramicroscopy, 109 (2008), pp. 70-80, 10.1016/j.ultramic.2008.08.005

[2] P.A. Midgley, M. Weyland, 3D electron microscopy in the physical sciences: the development of Z-contrast and EFTEM tomography, Ultramicroscopy, 96 (2003), pp. 413-431, 10.1016/S0304-3991(03)00105-0

[3] S.J. Pennycook, P.D. Nellist, Scanning Transmission Electron Microscopy, Springer, New York, New York, NY (2011)

[4] S.G. Wolf, L. Houben, M. Elbaum, Cryo-scanning transmission electron tomography of vitrified cells, Nat Methods, 11 (2014), pp. 423-428, 10.1038/nmeth.2842

[5] S. Trépout, In situ structural analysis of the flagellum attachment zone in Trypanosoma brucei using cryo-scanning transmission electron tomography, Journal of Structural Biology: X, Volume 4, 2020, 100033, 10.1016/j.yjsbx.2020.100033

[6] L. Donati, M. Nilchian, S. Trépout, C. Messaoudi, S. Marco, M. Unser, Compressed sensing for STEM tomography, Ultramicroscopy, 179 (2017), pp. 47-56, 10.1016/j.ultramic.2017.04.003

[7] S. Trépout, Tomographic Collection of Block-Based Sparse STEM Images: Practical Implementation and Impact on the Quality of the 3D Reconstructed Volume, Materials, 12 (2019), pp. 2281, 10.3390/ma12142281

[8] X. Li, O. Dyck, S.V. Kalinin, S. Jesse, Compressed Sensing of Scanning Transmission Electron Microscopy (STEM) With Nonrectangular Scans, Microsc Microanal, 24 (2018), pp. 623-633, 10.1017/S143192761801543X

[9] H.S. Anderson, J. Ilic-Helms, B. Rohrer, J. Wheeler, K. Larson, Sparse imaging for fast electron microscopy, Proc. SPIE-IS&T Electron. Imaging 8657, 86570C (2013), 10.1117/12.2008313

[10] A. Béché, B. Goris, B. Freitag, J. Verbeeck, Development of a fast electromagnetic beam blanker for compressed sensing in scanning transmission electron microscopy, Appl. Phys. Lett. 108, 093103 (2016), 10.1063/1.4943086

[11] H. Vanrompay, A. Béché, J. Verbeeck, S. Bals, Experimental Evaluation of Undersampling Schemes for Electron Tomography of Nanoparticles, Part. Part. Syst. Charact., 36 (2019), pp. 1900096, 10.1002/ppsc.201900096

[12] M. Bertalmio, G. Sapiro, V. Caselles, C. Ballester, Image Inpainting, SIGGRAPH '00: Proceedings of the 27th annual conference on Computer graphics and interactive techniques (2000) pp. 417–424, 10.1145/344779.344972

[13] D. Garcia, Robust smoothing of gridded data in one and higher dimensions with missing values. Comput. Stat. Data Anal. 2010;54:1167–1178. doi: 10.1016/j.csda.2009.09.020.

[14] G. Kutyniok, W.-Q. Lim, R Reisenhofer, ShearLab 3D: faithful digital shearlet transforms based on compactly supported shearlets. ACM Trans. Math. Softw. 42 (2016) 5:1–5:42, 10.1145/2740960

[15] J.R. Kremer, D.N. Mastronarde, J.R. McIntosh, Computer visualization of three-dimensional image data using IMOD, J Struct Biol, 116 (1996), pp. 71-76, 10.1006/jsbi.1996.0013

[16] D.N. Mastronarde, S.R. Held, Automated tilt series alignment and tomographic reconstruction in IMOD, J Struct Biol, 197 (2017), pp. 102-113, 10.1016/j.jsb.2016.07.011

[17] J.I. Agulleiro, J.J. Fernandez, Fast tomographic reconstruction on multicore computers,

Bioinformatics 27 (2011), pp. 582-583, 10.1093/bioinformatics/btq692

[18] J.I. Agulleiro, J.J. Fernandez, Tomo3D 2.0 - Exploitation of Advanced Vector eXtensions (AVX) for 3D reconstruction, Journal of Structural Biology 189 (2015), pp. 147-152, 10.1016/j.jsb.2014.11.009

[19] C.A. Schneider, W.S. Rasband, K.W. Eliceiri, NIH Image to ImageJ: 25 years of image analysis, Nat Methods, 9 (2012), pp. 671-675, 10.1038/nmeth.2089

[20] Z. Wang; A.C. Bovik; H.R. Sheikh; E.P. Simoncelli, Image quality assessment: from error visibility to structural similarity, IEEE Transactions on Image Processing, 13:4 (2004), pp. 600-612, 10.1109/TIP.2003.819861.

[21] S.Y. Sun, L. Segev-Zarko, M. Chen, G.D. Pintilie, M.F. Schmid, S.J. Ludtke, J.C. Boothroyd, W. Chiu, Cryo-ET of Toxoplasma parasites gives subnanometer insight into tubulin-based structures, PNAS 119(6) (2022), e2111661119, 10.1073/pnas.2111661119

Figures

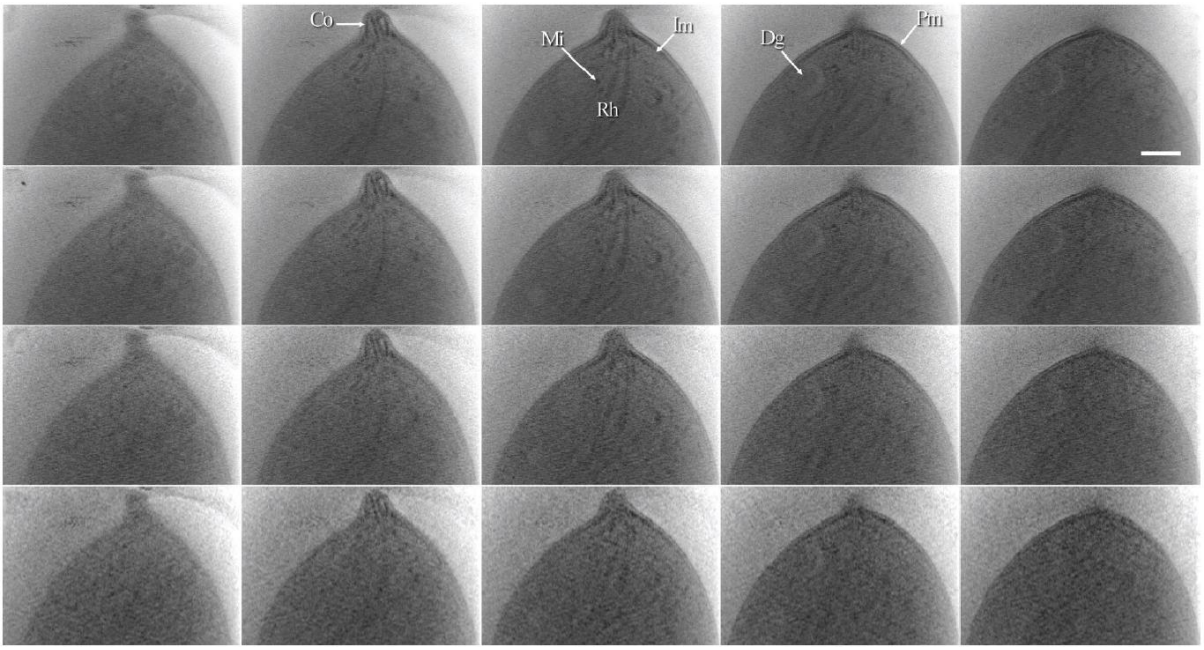

Figure 1. Comparison of conventional and sparse cryo-STET reconstructions of *T. gondii*. The Z-slices are 20 nm-thick and are spaced by 200 nm. A) Z-slices of the reconstruction from the reference fully-collected images. B) Z-slices of the reconstruction from the sparse images containing 50% of the original pixels. C) Z-slices of the reconstruction from the sparse images containing 20% of the original pixels. D) Z-slices of the reconstruction from the sparse images containing 10% of the original pixels. Some structural elements have been highlighted: the plasma membrane (Pm), the pellicle with the internal membrane complex (Im), the conoid (Co), micronemes (Mi), rhoptries (Rh) and a dense granule (Dg). The scale bar is 400 nm.

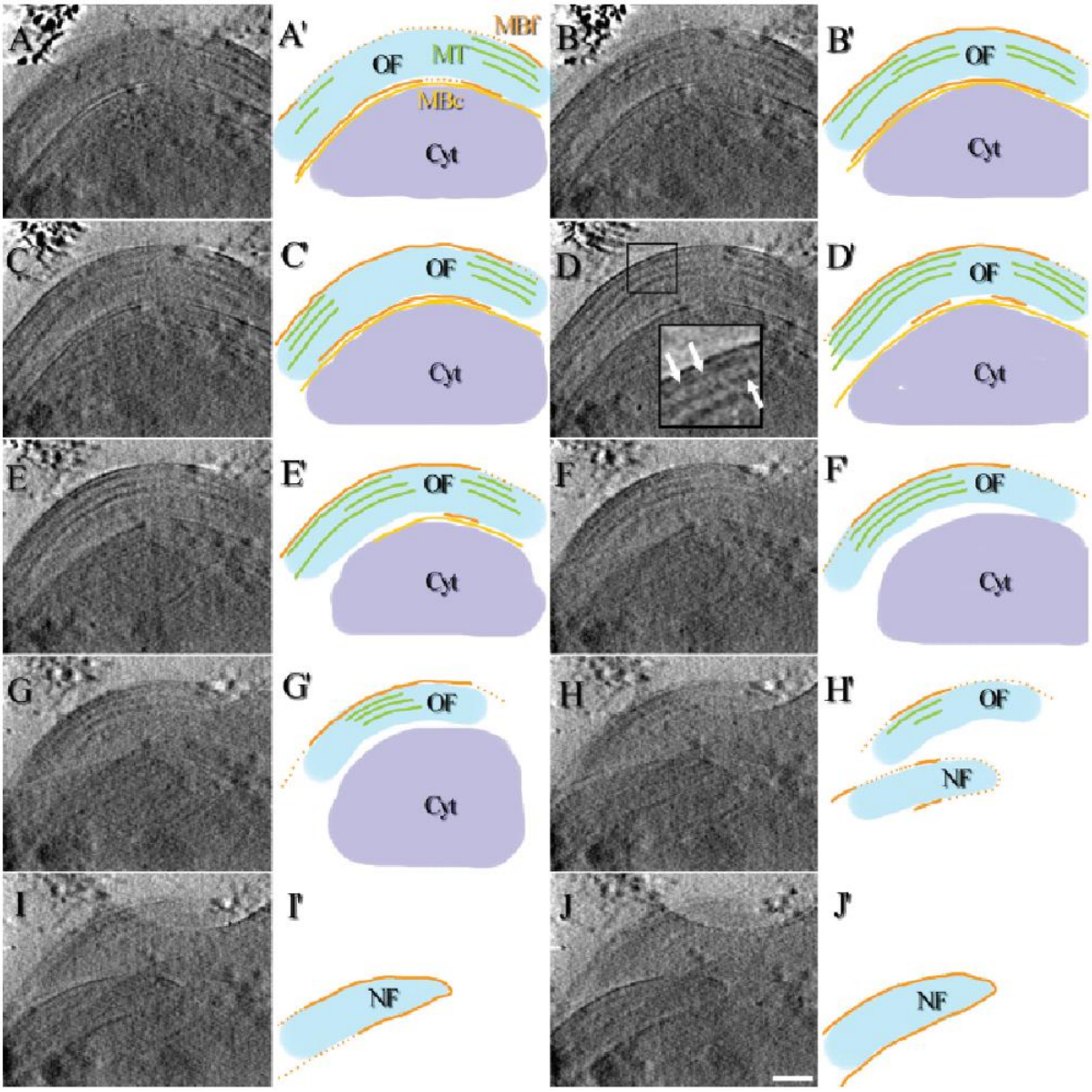

Figure 2. Observation of a *T. brucei* cell using sparse cryo-STET where only 10% of the pixels have been collected. A-J) Z-slices (2 nm-thick) spaced by 40 nm. A'-J') Manual segmentation of the cell showing the location of the cytoplasm (Cyt), the old (OF) and new (NF) flagella, the cytoplasmic membrane (MBc), the flagellar membrane (MBf) and the microtubule doublets and central pair inside the flagellum (MT). The lumen of the microtubule can be resolved in some parts of the reconstruction (white arrow-heads in the zoom-in image). The scale bar is 400 nm.

5.1.2. Unpublished results

After validating that the sparse cryo-STET can perform dose reduction compared to cryo-STET, we performed other experiments to further explore the potential of sparse cryo-STET on whole bacterial cells that are usually too thick to be observed using conventional cryo-TEM. Using *E. coli* as test sample, we collected various sparse cryo-STET dataset to evaluate i) the effect of electron dose distribution (few high SNR pixels versus numerous low SNR pixels) and ii) the possibility to reach high magnifications using sparse images.

Shearlet inpainting is another kind of inpainting based on wavelets theory (i.e., a time-frequency representation) (Kutyniok, Lim, and Steidl 2014). We have reasons to believe it can outperform discrete cosine transforms-based inpainting. One of the bottlenecks of shearlets inpainting is that it is very computer intensive.

The goal is to evaluate to what degree downsampling cryo-STEM images while maintaining the same total electron dose affects the resulting SNR after inpainting compared to fully sampled images at lower electron dose (i.e., lower dwell time) per pixel. And secondly, evaluating if undersampling strategies enables the acquisition of tomographic tilt-series at higher magnifications.

The sparse cryo-STET and shearlets inpainting results are still being processed and will be part of a future manuscript in the next months.

5.2. Discussion of the results and perspectives

We presented a method that successfully enables the acquisition of sparse cryo-STEM tomography dataset on thick biological samples. This method can be used to acquire cryo-STEM datasets and enables a satisfying recovery of the missing data.

Yet, this method requires improvements to evaluate the best sampling rate (which might depend on the type of sample observed) and in the choice of inpainting method. Indeed, the latest developments on inpainting methods include deep-learning ones which could give even better results provided a representative dataset of cryo-STEM images is given to the algorithm.

As all methods, deep-learning ones need to be taken with great care as they are likely to introduce plausible artefacts. This comment is especially important since, many times, we

lack a clear understanding of the type of information these neural methods are really extracting from the data.

The performance of these methods should be evaluated in future works.

To fulfil the requirements of compressed sensing (CS) theory, the image sampling should be incoherent in order not to create artefacts. However, the acquisition scheme we evaluated acquire regularly spaced lines of pixels. Indeed, this sampling method enabled us to obtain good visual results, but it is not ideal according to CS theory. Because the lines are all oriented in the same direction, this creates anisotropic images as acquired lines possess the full sampling resolution along their axis while perpendicularly to them, pixels are extrapolated which inevitably reduces the attainable resolution in this direction. From this point of view, we note that the term “compressed sensing” is used here in a broad manner, since the experimental conditions are not precisely those that would match the mathematical needs.

Finally, provided some refinement in the acquisition sampling scheme and eventually in the inpainting method, sparse cryo-STEM would be a method of choice to perform correlative analysis with cryo-SXT of sensitive biological samples such as bacteria. Indeed, even though cryo-SXT is less damaging than cryo-electron tomography, the need of dose reduction for correlative analysis is of prime importance. Using sparse cryo-STEM on the same bacteria previously imaged by cryo-SXT could enable us to take advantage of the contrast between the cytoplasm and the bacterial nucleoid brought by the water-window (cryo-SXT) and the ability to clearly resolve the membranes of bacteria (cryo-STEM).

Chapter VI. Specific labelling of Hfq: development of a tag for cryo-SXT and cryo-STEM

As indicated in Chapter IV, using cryo-SXT, we observed nucleoid structures presenting low and high absorbance domains, as well as nucleoid cores. Unfortunately, the domains cannot be further compared to that identified using fluorescence microscopy and referred as nucleoid macrodomains (Espéli and Boccard 2006). The main reason is that currently a label to specifically tag a protein using cryo-SXT is not available.

With a new synchrotron proposal allocated in 2021, we thus intended to image Hfq location specifically within the nucleoid by using a recently developed protein tag for X-ray imaging called LBT, standing for Lanthanide Binding Tag (Victor et al. 2020). In the near future, this would allow the mapping of specific proteins of interest by X-ray fluorescence, cryo-SXT and cryo-(S)TEM.

Our reason for choosing Hfq as a first model was guided by two main reasons. First, its property to form hexamers (at least) that would give six times more signal than a monomer (Link, Valentin-Hansen, and Brennan 2009). This should be even more pronounced when Hfq polymerizes and forms an amyloid structure (Fortas et al. 2015). The second reason is that no tag is currently available to label Hfq allowing its proper folding and correct localization. Actually, most of the fluorescently tagged Hfq protein formed inclusion bodies that do not allow an accurate analysis. Finally, we have a tunable expression system available for this protein (Diestra et al. 2009).

Precisely we constructed an *E. coli* strain allowing the expression of Hfq-LBT fusion proteins. The expression of Hfq-LBT is induced by Arabinose (the *hfq-lbt* gene was placed under the control of an inducible promoter called P_{BAD}). This allows a moderate expression of the protein, comparable to the physiological expression. For this goal, cells are grown in minimal medium supplemented with glycerol 0.2% (glucose would repress the expression of the protein from the promoter). Subsequently, L-arabinose is added to induce the expression of the promoter and thus the protein. The advantages of this system are: *(i)* the absence of L-arabinose produces very low levels of transcription from P_{BAD} (low leakiness of the promotor);

(ii) the system has a good titratability and the amount of protein expressed is correlated with the amount of inducer added. We can use L-arabinose concentration ranging from 0.001% to 0.1% from few minutes (the P_{BAD} promoter has a very fast induction rate) to overnight induction time. The concentration of arabinose may vary to adapt to the level of protein expression needed (see Diestra et al. as an example for Hfq expression (Diestra et al. 2009)).

For our cryo-SXT analysis, cells were cryofixed after protein expression and Lanthanide incubation. Samples were prepared in our lab and data collection was performed in remote access due to the SARS-CoV-2 pandemic. For statistics, a minimum of 8 tomograms for each strain and in each growth-phase were acquired. We collected about 50 good tomographic tilt-series (each with at least 1-3 cells). Reconstructed tomograms have started to be analyzed in our lab.

In conclusion, even if this analysis is still ongoing, our results already suggest visual differences between labelled cells and controls (Figure 22). We hope our group can go ahead with this analysis after my PhD with colleagues at the CNB-CSIC in Madrid and at ALBA synchrotron.

Note that because this tag was initially developed for X-ray fluorescence microscopy and given that the two lanthanides used in this study (as in (Victor et al. 2020)) are Europium and Erbium which have L_α and L_β X-ray emission peaks between 5-8 keV. Their study was performed using hard X-rays above 10 keV using samples at room temperature which is quite different from cryo-SXT conditions.

While our preliminary results seem to indicate local concentrations which would correlate with previously demonstrated localization of Hfq in *E. coli*, we still need to confirm that the lanthanides have a specific affinity for the tag compared to non-tagged organic material. In that sense, it would be interesting to perform cryo-XRF in correlation with cryo-SXT to confirm the presence of the lanthanides at the specific locations identified using cryo-SXT.

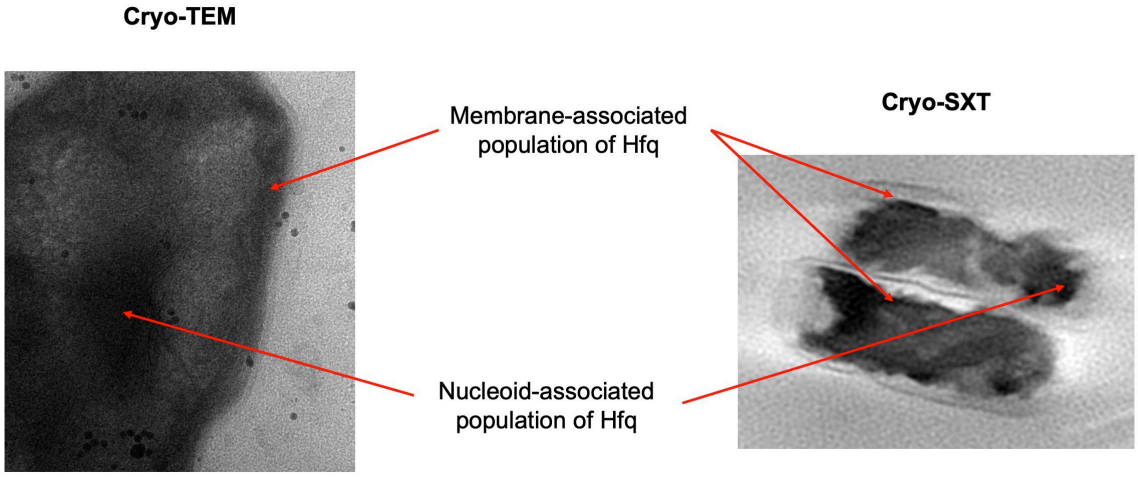

Figure 28. Cryo-TEM (left) and Cryo-SXT (right) analysis of *E. coli* cells with europium-labelled LBT-Hfq. This agrees with the previously known location of Hfq in the nucleoid and near the bacteria inner membrane (Diestra et al. 2009).

As for the use of the LBT in cryo-STEM tomography, the preliminary results show an increase in contrast inside the cytoplasm of the bacteria cells which appear darker. This also seems to improve contrast between the cytoplasm and the nucleoid which appear brighter than the cytoplasm (see Figure 29).

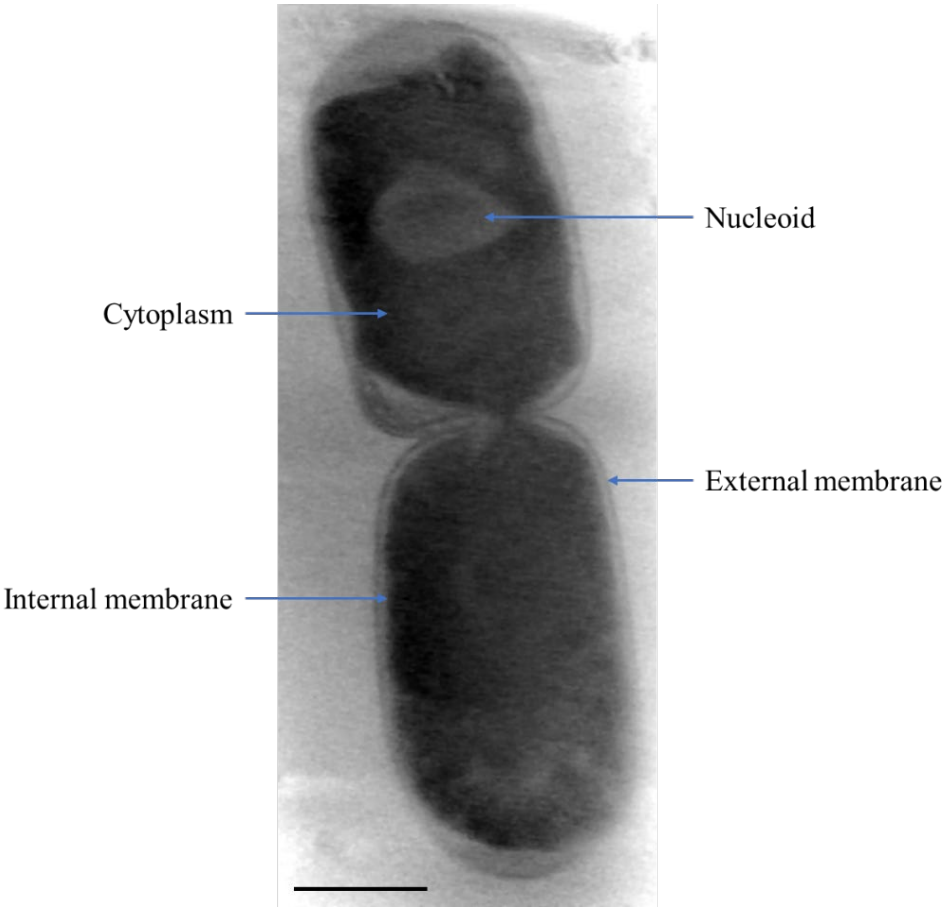

Figure 29. Average of five slices of the reconstructed volume of a dividing *E. coli* bacterium containing the Hfq-LBT and incubated 10 minutes with Europium, acquired in cryo-STEM. Scale bar represents 300 nm.

Using this label for Hfq and sparse cryo-STEM tomography (as explained in Chapter V) will hopefully enable acquisitions at higher magnification to obtain the precise localizations of Hfq in its cellular context.

Chapter VII. General conclusions

My goal during this PhD thesis research consisted of developing methods to analyse how compounds will affect cells by targeting an important factor for bacterial adaptation, the Hfq protein. While this bacterial protein is mainly known to act on noncoding RNA regulation in order for the bacteria to adapt to various stresses, including those encountered during host infection, it also binds DNA and affects different DNA-related processes such as replication or recombination. To target Hfq cellular functions and in particular its function related to DNA-based regulation we will specifically focus on one of its structural properties, the formation of an amyloid structure. Precisely our goal is to target this bacterial amyloid to develop new antimicrobials. Such a structure that gives new functions to this protein is referred to as a functional amyloid, and it helps in maintaining the normal physiological state of the bacterial cell (Otzen and Riek 2019). They are called functional in contrast with the better known and more studied pathological amyloids implicated in over 30 human disorders, such as neurodegenerative Alzheimer's or Parkinson's diseases (Knowles, Vendruscolo, and Dobson 2014). During this amyloid assembly, the protein undergoes a structural rearrangement leading to the assembly of β-sheets and subsequent formation of a cross β-sheet quaternary structure. This conformation is the fingerprint of amyloids.

Using various *in vitro* and *in vivo* approaches, my work analysed the ability of Hfq to assemble into amyloid fibres on DNA, which allows it to compact DNA (Malabirade et al. 2018). The characterization of the amyloid structure formed on DNA is based on a multidisciplinary approach exploring various structural and biophysical techniques (Malabirade, Jiang, et al. 2017). My contribution to this work includes cryo-TEM imaging, complementary to X-ray and neutron scattering (Matsuo and Peters 2022; Matsuo et al. 2022; Malabirade, Jiang, et al. 2017). We also intend to develop new methods for *in cellulo* imaging of the nucleoid (Cossa, Trépout, et al. 2022; Victor et al. 2020). Using these techniques, we have new tools to observe the phenotype of Hfq depleted cells, which will be used in the near future to observe the effect of new antibacterial compounds. Precisely, we will use cryo-SXT or cryo-(S)TEM tomography for our analyses. We have already used these methods to investigate unlabelled *E. coli* cells and intend to combine them with a new protein tag dense to electrons and X-rays, which could furthermore be used for X-ray fluorescence imaging (Victor et al. 2020).

The following summarizes the salient results and conclusions of this Thesis:

- Chapter II presents how Hfq-CTR interacts with double stranded DNA and allows its compaction. 3D models are in construction to explain how the peptide shapes the DNA. Different models based on SANS experiments have been proposed and our analysis using cryo-TEM should allow refinement of the analysis. Even if this work is not completely finished it should lead to a new publication in 2023.
- Chapter III shows how Hfq and its CTR interact with single stranded DNA. The main conclusion of this part of the work is that Hfq CTR folds and align ssDNA, with consequences on genetic expression *in vivo*.
- Chapter IV allows conclusions about the effect of Hfq and its CTR *in situ* in the cell. This chapters constitute the main part of my PhD work and brings important elements to prove that Hfq (due to its CTR) allows the compaction of DNA directly, but also indirectly by using sRNA- based regulations.
- Chapter V shows perspectives of cryo-STEM for the analysis of bacteria. This chapter also discussed how correlative imaging using cryo-SXT/cryo-STEM could be done. This was a subject I should have developed during my PhD, especially to develop new algorithms during my stay in Spain. But due to sanitary crisis, it was unfortunately not possible to do this development.
- Chapter VI finally shows the development of a protein Tag called LBT that could be used for correlative imaging (cryo-SXT, cryo-(S)TEM and X-ray fluorescence). First tests are very promising, and I hope our groups will be able to develop this new tool in the future.

Chapter VIII. Perspectives

The problem of antibacterial resistance is particularly complex due to the absence of new drug development over the last thirty years. Much effort has been undertaken during last years to modify and improve existing antibiotics. However, the main problem with this approach is the development of new bacterial resistance, which usually requires little or no modification of existing mechanisms. Therefore, the search for novel antibacterial targets in cells is of utmost importance.

The objective of our group is thus to develop compounds that can inhibit or interfere with the self-assembly of Hfq and Hfq/DNA interaction. Our group already observed that some compounds, known to prevent the self-assembly of amyloids formed during neurodegenerative pathologies, are capable of affecting bacterial amyloid fibrillation and the survival of the bacterium (Partouche et al. 2018; Turbant, Partouche, et al. 2021). The main advantage of this approach known as "therapeutic repositioning" is the use of compounds already known and used against human diseases. Toxicity, pharmacokinetic and tolerance studies of such compounds are generally well documented. Therapeutic repositioning thus makes it possible to avoid preclinical trials as well as phase 1 clinical trials (tolerance), thus significantly reducing the duration and cost to allow the development and formulation of new antibiotics in an accelerated manner. We believe that this approach may allow the development of a new class of antibiotics that can block Hfq self-assembly and with important consequences on bacterial physiology and virulence. If we already identified two promising compounds, although these compounds need to be improved to be more efficient. Replica-Exchange Molecular Dynamics (REMD) simulation approaches will be applied to accomplish this improvement. This *in silico* technique has the advantage of allowing an exhaustive sampling of the different conformations of amyloid regions. Analysis of the dynamics of assembly will help drive the optimization of compounds. *In silico* and *in vitro* assays will then be applied to screen for inhibitors and evaluate their efficacy (IC_{50} measurements of inhibitory compounds). Then, *in vivo* tests will be performed to see the effect of compounds on bacterial survival, including Minimum Inhibitory Concentration (MIC) measurements and imaging.

Expected breakthroughs and benefits of my PhD project are thus twofold: 1) develop methods for the investigation of the bacterial nucleoid and NAP function *in cellulo*, and 2)

provide the opportunity to analyse results for the development of novel antibiotics of the future that could be patentable.

Bibliography

Abe, H., A. Miyahara, T. Oshima, K. Tashiro, Y. Ogura, S. Kuhara, N. Ogasawara, T. Hayashi, and T. Tobe. 2008. “Global Regulation by Horizontally Transferred Regulators Establishes the Pathogenicity of Escherichia Coli.” *DNA Research* 15 (1): 25–38. https://doi.org/10.1093/dnares/dsm033.

Agrawal, Nikhil, and Adam A. Skelton. 2019. “Structure and Function of Alzheimer’s Amyloid Beta Proteins from Monomer to Fibrils: A Mini Review.” *The Protein Journal* 38 (4): 425–34. https://doi.org/10.1007/s10930-019-09854-3.

Agulleiro, J. I., and J. J. Fernandez. 2011. “Fast Tomographic Reconstruction on Multicore Computers.” *Bioinformatics* 27 (4): 582–83. https://doi.org/10.1093/bioinformatics/btq692.

Agulleiro, Jose-Ignacio, and Jose-Jesus Fernandez. 2015. “Tomo3D 2.0 – Exploitation of Advanced Vector EXtensions (AVX) for 3D Reconstruction.” *Journal of Structural Biology* 189 (2): 147–52. https://doi.org/10.1016/j.jsb.2014.11.009.

Aiba, H. 2007. “Mechanism of RNA Silencing by Hfq-Binding Small RNAs.” *Curr Opin Microbiol* 10: 134–39.

Ait-Bara, S., and A. J. Carpousis. 2015. “RNA Degradosomes in Bacteria and Chloroplasts: Classification, Distribution and Evolution of RNase E Homologs.” *Mol Microbiol* 97: 1021–1135.

Amemiya, H. M., T. J. Goss, T. M. Nye, R. L. Hurto, L. A. Simmons, and P. L. Freddolino. 2021. “Distinct Heterochromatin-like Domains Promote Transcriptional Memory and Silence Parasitic Genetic Elements in Bacteria.” *EMBO J*, e108708.

Andersen, A. 1984. “Simultaneous Algebraic Reconstruction Technique (SART): A Superior Implementation of the ART Algorithm.” *Ultrasonic Imaging* 6 (1): 81–94. https://doi.org/10.1016/0161-7346(84)90008-7.

Arluison, Véronique, Sungchul Hohng, Rahul Roy, Olivier Pellegrini, Philippe Régnier, and Taekjip Ha. 2007. "Spectroscopic Observation of RNA Chaperone Activities of Hfq in Post-Transcriptional Regulation by a Small Non-Coding RNA." *Nucleic Acids Research* 35 (3): 999–1006. https://doi.org/10.1093/nar/gkl1124.

Arluison, Véronique, and Aziz Taghbalout. 2015. "Cellular Localization of RNA Degradation and Processing Components in Escherichia Coli." In *RNA Remodeling Proteins*, edited by Marc Boudvillain, 1259:87–101. Methods in Molecular Biology. New York, NY: Springer New York. https://doi.org/10.1007/978-1-4939-2214-7_6.

Azam, Talukder Ali, Sota Hiraga, and Akira Ishihama. 2000. "Two Types of Localization of the DNA-Binding Proteins within the Escherichia Coli Nucleoid: Intracellular Localization of E. Coli DNA-Binding Proteins." *Genes to Cells* 5 (8): 613–26. https://doi.org/10.1046/j.1365-2443.2000.00350.x.

Azam, Talukder Ali, and Akira Ishihama. 1999. "Twelve Species of the Nucleoid-Associated Protein from Escherichia Coli." *Journal of Biological Chemistry* 274 (46): 33105–13. https://doi.org/10.1074/jbc.274.46.33105.

Azam, Talukder Ali, Akira Iwata, Akiko Nishimura, Susumu Ueda, and Akira Ishihama. 1999. "Growth Phase-Dependent Variation in Protein Composition of the *Escherichia Coli* Nucleoid." *Journal of Bacteriology* 181 (20): 6361–70. https://doi.org/10.1128/JB.181.20.6361-6370.1999.

Badaut, Cyril, Roy Williams, Véronique Arluison, Emeline Bouffartigues, Bruno Robert, Henri Buc, and Sylvie Rimsky. 2002. "The Degree of Oligomerization of the H-NS Nucleoid Structuring Protein Is Related to Specific Binding to DNA." *Journal of Biological Chemistry* 277 (44): 41657–66. https://doi.org/10.1074/jbc.M206037200.

Bardill, J. Patrick, Xiaonan Zhao, and Brian K. Hammer. 2011. "The Vibrio Cholerae Quorum Sensing Response Is Mediated by Hfq-Dependent SRNA/MRNA Base Pairing Interactions: SRNA/MRNA Pairing Controls V. Cholerae Quorum Sensing." *Molecular Microbiology* 80 (5): 1381–94. https://doi.org/10.1111/j.1365-2958.2011.07655.x.

Barucker, Christian, Anja Harmeier, Joerg Weiske, Beatrix Fauler, Kai Frederik Albring, Stefan Prokop, Peter Hildebrand, et al. 2014. "Nuclear Translocation Uncovers the Amyloid Peptide Aβ42 as a Regulator of Gene Transcription*." *Journal of Biological Chemistry* 289 (29): 20182–91. https://doi.org/10.1074/jbc.M114.564690.

Battesti, Aurelia, Nadim Majdalani, and Susan Gottesman. 2011. "The RpoS-Mediated General Stress Response in *Escherichia Coli*." *Annual Review of Microbiology* 65 (1): 189–213. https://doi.org/10.1146/annurev-micro-090110-102946.

Bennett, P M. 2008. "Plasmid Encoded Antibiotic Resistance: Acquisition and Transfer of Antibiotic Resistance Genes in Bacteria: Plasmid-Encoded Antibiotic Resistance." *British Journal of Pharmacology* 153 (S1): S347–57. https://doi.org/10.1038/sj.bjp.0707607.

Benureau, Yann, Eliana Moreira Tavares, Ali-Akbar Muhammad, Sonia Baconnais, Eric Le Cam, and Pauline Dupaigne. 2020. "Method Combining BAC Film and Positive Staining for the Characterization of DNA Intermediates by Dark-Field Electron Microscopy." *Biology Methods and Protocols* 5 (1): bpaa012. https://doi.org/10.1093/biomethods/bpaa012.

Bepler, Tristan, William S Noble, and Bonnie Berger. 2019. "Topaz-Denoise: General Deep Denoising Models for CryoEM." *Bioinformatics*.

Betzig, Eric, George H. Patterson, Rachid Sougrat, O. Wolf Lindwasser, Scott Olenych, Juan S. Bonifacino, Michael W. Davidson, Jennifer Lippincott-Schwartz, and Harald F. Hess. 2006. "Imaging Intracellular Fluorescent Proteins at Nanometer Resolution." *Science* 313 (5793): 1642–45. https://doi.org/10.1126/science.1127344.

Blount, Zachary D. 2015. "The Unexhausted Potential of E. Coli." *ELife* 4 (March): e05826. https://doi.org/10.7554/eLife.05826.

Bohn, C'eline, C'edric Rigoulay, and Philippe Bouloc. 2007. "No Detectable Effect of RNA-Binding Protein Hfq Absence in Staphylococcus Aureus." *BMC Microbiology* 7 (1): 10.

Bonar, L., A. S. Cohen, and M. M. Skinner. 1969. "Characterization of the Amyloid Fibril as a Cross- Protein." *Experimental Biology and Medicine* 131 (4): 1373–75. https://doi.org/10.3181/00379727-131-34110.

Bouloc, Philippe, and Francis Repoila. 2016. “Fresh Layers of RNA-Mediated Regulation in Gram-Positive Bacteria.” *Current Opinion in Microbiology* 30 (April): 30–35. https://doi.org/10.1016/j.mib.2015.12.008.

Brennan, Richard G, and Todd M Link. 2007. “Hfq Structure, Function and Ligand Binding.” *Current Opinion in Microbiology* 10 (2): 125–33. https://doi.org/10.1016/j.mib.2007.03.015.

Camero, Sergio, Jose M. Ayuso, Alejandro Barrantes, María J. Benítez, and Juan S. Jiménez. 2013. “Specific Binding of DNA to Aggregated Forms of Alzheimer’s Disease Amyloid Peptides.” *International Journal of Biological Macromolecules* 55 (April): 201–6. https://doi.org/10.1016/j.ijbiomac.2013.01.007.

Carpousis, Agamemnon J., Nathalie Campo, Lydia Hadjeras, and Lina Hamouche. 2022. “Compartmentalization of RNA Degradosomes in Bacteria Controls Accessibility to Substrates and Ensures Concerted Degradation of MRNA to Nucleotides.” *Annual Review of Microbiology* 76 (1): 533–52. https://doi.org/10.1146/annurev-micro-041020-113308.

Carzaniga, Raffaella, Marie-Charlotte Domart, Lucy M. Collinson, and Elizabeth Duke. 2014. “Cryo-Soft X-Ray Tomography: A Journey into the World of the Native-State Cell.” *Protoplasma* 251 (2): 449–58. https://doi.org/10.1007/s00709-013-0583-y.

Cech, Grzegorz M., Bartosz Pakuła, Dominika Kamrowska, Grzegorz Węgrzyn, Véronique Arluison, and Agnieszka Szalewska-Pałasz. 2014. “Hfq Protein Deficiency in Escherichia Coli Affects ColE1-like but Not λ Plasmid DNA Replication.” *Plasmid* 73 (May): 10–15. https://doi.org/10.1016/j.plasmid.2014.04.005.

Cech, Grzegorz M., Agnieszka Szalewska-Pałasz, Krzysztof Kubiak, Antoine Malabirade, Wilfried Grange, Veronique Arluison, and Grzegorz Węgrzyn. 2016. “The Escherichia Coli Hfq Protein: An Unattended DNA-Transactions Regulator.” *Frontiers in Molecular Biosciences* 3 (July). https://doi.org/10.3389/fmolb.2016.00036.

Chao, Yanjie, and Jörg Vogel. 2010. “The Role of Hfq in Bacterial Pathogens.” *Current Opinion in Microbiology* 13 (1): 24–33. https://doi.org/10.1016/j.mib.2010.01.001.

Chen, Jiandong, and Susan Gottesman. 2017. “Hfq Links Translation Repression to Stress-Induced Mutagenesis in *E. Coli*.” *Genes & Development* 31 (13): 1382–95. https://doi.org/10.1101/gad.302547.117.

Chiti, Fabrizio, and Christopher M. Dobson. 2017. “Protein Misfolding, Amyloid Formation, and Human Disease: A Summary of Progress Over the Last Decade.” *Annual Review of Biochemistry* 86 (1): 27–68. https://doi.org/10.1146/annurev-biochem-061516-045115.

Christopoulou, Niki, and Sander Granneman. 2022. “The Role of RNA-binding Proteins in Mediating Adaptive Responses in Gram-positive Bacteria.” *The FEBS Journal* 289 (7): 1746–64. https://doi.org/10.1111/febs.15810.

Cossa, Antoine, Véronique Arluison, and Sylvain Trépout. 2021. “Sparse Cryo-STEM Tomography for Biological Samples.” *Microscopy and Microanalysis* 27 (S1): 3028–30. https://doi.org/10.1017/S1431927621010515.

Cossa, Antoine, Christel Cren, Thomas Mouveaux, Philippe Bastin, Mathieu Gissot, and Sylvain Trépout. 2022. “Sparse Cryo-STEM Tomography for Biological Samples.” *Microscopy and Analysis*, August 2022.

Cossa, Antoine, and Sylvain Trépout. 2022. “Cryo-Electron Microscopy to Analyze the Structure of Bacterial Amyloids In Vitro.” In *Bacterial Amyloids*, edited by Véronique Arluison, Frank Wien, and Andrés Marcoleta, 2538:13–23. Methods in Molecular Biology. New York, NY: Springer US. https://doi.org/10.1007/978-1-0716-2529-3_2.

Cossa, Antoine, Sylvain Trépout, Frank Wien, Johannes Groen, Etienne Le Brun, Florian Turbant, Laetitia Besse, Eva Pereiro, and Véronique Arluison. 2022. “Cryo Soft X-Ray Tomography to Explore Escherichia Coli Nucleoid Remodeling by Hfq Master Regulator.” *Journal of Structural Biology* 214 (4): 107912. https://doi.org/10.1016/j.jsb.2022.107912.

Cossa, Antoine, Frank Wien, Florian Turbant, Tadeusz Kaczorowski, Grzegorz Węgrzyn, Véronique Arluison, Ana J. Pérez-Berná, Sylvain Trépout, and Eva Pereiro. 2022. “Evaluation of the Role of Bacterial Amyloid on Nucleoid Structure Using Cryo-Soft X-Ray Tomography.” In *Bacterial Amyloids*, edited by Véronique Arluison, Frank Wien, and Andrés Marcoleta, 2538:319–33. Methods in Molecular Biology. New York, NY: Springer US. https://doi.org/10.1007/978-1-0716-2529-3_21.

Cutter, Amber R., and Jeffrey J. Hayes. 2015. “A Brief Review of Nucleosome Structure.” *FEBS Letters* 589 (20PartA): 2914–22. https://doi.org/10.1016/j.febslet.2015.05.016.

Dame, Remus Thei, Claire Wyman, and Nora Goosen. 2000. “H-NS Mediated Compaction of DNA Visualised by Atomic Force Microscopy.” *Nucleic Acids Research* 28 (18): 3504–10. https://doi.org/10.1093/nar/28.18.3504.

Di Scala, Coralie, Nouara Yahi, Sonia Boutemeur, Alessandra Flores, Léa Rodriguez, Henri Chahinian, and Jacques Fantini. 2016. “Common Molecular Mechanism of Amyloid Pore Formation by Alzheimer’s β-Amyloid Peptide and α-Synuclein.” *Scientific Reports* 6 (1): 28781. https://doi.org/10.1038/srep28781.

Diestra, Elia, Bastien Cayrol, Véronique Arluison, and Cristina Risco. 2009. “Cellular Electron Microscopy Imaging Reveals the Localization of the Hfq Protein Close to the Bacterial Membrane.” Edited by Claudine Mayer. *PLoS ONE* 4 (12): e8301. https://doi.org/10.1371/journal.pone.0008301.

Dimastrogiovanni, Daniela, Kathrin S Fröhlich, Katarzyna J Bandyra, Heather A Bruce, Susann Hohensee, Jörg Vogel, and Ben F Luisi. 2014. “Recognition of the Small Regulatory RNA RydC by the Bacterial Hfq Protein.” *ELife* 3 (December): e05375. https://doi.org/10.7554/eLife.05375.

Dorman, Charles J. 2009. “Chapter 2 Nucleoid-Associated Proteins and Bacterial Physiology.” In *Advances in Applied Microbiology*, 67:47–64. Elsevier. https://doi.org/10.1016/S0065-2164(08)01002-2.

Dorman, Charles J, Maria A Schumacher, Matthew J Bush, Richard G Brennan, and Mark J Buttner. 2020. “When Is a Transcription Factor a NAP?” *Current Opinion in Microbiology* 55 (June): 26–33. https://doi.org/10.1016/j.mib.2020.01.019.

Drolle, Elizabeth, Alexander Negoda, Keely Hammond, Evgeny Pavlov, and Zoya Leonenko. 2017. “Changes in Lipid Membranes May Trigger Amyloid Toxicity in Alzheimer’s Disease.” Edited by Igor Sokolov. *PLOS ONE* 12 (8): e0182194. https://doi.org/10.1371/journal.pone.0182194.

Eisenberg, David S., and Michael R. Sawaya. 2017. “Structural Studies of Amyloid Proteins at the Molecular Level.” *Annual Review of Biochemistry* 86 (1): 69–95. https://doi.org/10.1146/annurev-biochem-061516-045104.

El Hamoui, Omar, Indresh Yadav, Milad Radiom, Frank Wien, Jean-Francois Berret, Johan R. C. van der Maarel, and Véronique Arluison. 2020. “Interactions between DNA and the Hfq Amyloid-like Region Trigger a Viscoelastic Response.” *Biomacromolecules* 21 (9): 3668–77. https://doi.org/10.1021/acs.biomac.0c00747.

El-Agnaf, Omar M. A., Katerina E. Paleologou, Brett Greer, Abdulmawala M. Abogrein, Jenny E. King, Sultan A. Salem, Nigel J. Fullwood, et al. 2004. “A Strategy for Designing Inhibitors of α -synuclein Aggregation and Toxicity as a Novel Treatment for Parkinson’s Disease and Related Disorders.” *The FASEB Journal* 18 (11): 1315–17. https://doi.org/10.1096/fj.03-1346fje.

El-Mowafi, Shaima A., John N. Alumasa, Sarah E. Ades, and Kenneth C. Keiler. 2014. “Cell-Based Assay To Identify Inhibitors of the Hfq-SRNA Regulatory Pathway.” *Antimicrobial Agents and Chemotherapy* 58 (9): 5500–5509. https://doi.org/10.1128/AAC.03311-14.

Espéli, Olivier, and Frédéric Boccard. 2006. “Organization of the Escherichia Coli Chromosome into Macrodomains and Its Possible Functional Implications.” *Journal of Structural Biology* 156 (2): 304–10. https://doi.org/10.1016/j.jsb.2006.07.010.

Fang, Ferric C, and Sylvie Rimsky. 2008. “New Insights into Transcriptional Regulation by H-NS.” *Current Opinion in Microbiology* 11 (2): 113–20. https://doi.org/10.1016/j.mib.2008.02.011.

Fender, Aurélie, Johan Elf, Kornelia Hampel, Bastian Zimmermann, and E. Gerhart H. Wagner. 2010. “RNAs Actively Cycle on the Sm-like Protein Hfq.” *Genes & Development* 24 (23): 2621–26. https://doi.org/10.1101/gad.591310.

Fernandez, Maria Theresa Franze de, William S. Hayward, and J. Thomas August. 1972. “Bacterial Proteins Required for Replication of Phage Qβ Ribonucleic Acid.” *Journal of Biological Chemistry* 247 (3): 824–31. https://doi.org/10.1016/S0021-9258(19)45681-0.

Fitzpatrick, Anthony W. P., Galia T. Debelouchina, Marvin J. Bayro, Daniel K. Clare, Marc A. Caporini, Vikram S. Bajaj, Christopher P. Jaroniec, et al. 2013. "Atomic Structure and Hierarchical Assembly of a Cross-β Amyloid Fibril." *Proceedings of the National Academy of Sciences* 110 (14): 5468–73. https://doi.org/10.1073/pnas.1219476110.

Fortas, Emilie, Federica Piccirilli, Antoine Malabirade, Valeria Militello, Sylvain Trépout, Sergio Marco, Aziz Taghbalout, and Véronique Arluison. 2015. "New Insight into the Structure and Function of Hfq C-Terminus." *Bioscience Reports* 35 (2): e00190. https://doi.org/10.1042/BSR20140128.

Franze de Fernandez, M. T., Lilian Eoyang, and J. T. August. 1968. "Factor Fraction Required for the Synthesis of Bacteriophage Qβ-RNA." *Nature* 219 (5154): 588–90. https://doi.org/10.1038/219588a0.

Gaffke, Lidia, Krzysztof Kubiak, Zuzanna Cyske, and Grzegorz Węgrzyn. 2021. "Differential Chromosome- and Plasmid-Borne Resistance of Escherichia Coli Hfq Mutants to High Concentrations of Various Antibiotics." *International Journal of Molecular Sciences* 22 (16): 8886. https://doi.org/10.3390/ijms22168886.

Garcia, Damien. 2010. "Robust Smoothing of Gridded Data in One and Higher Dimensions with Missing Values." *Computational Statistics & Data Analysis* 54 (4): 1167–78. https://doi.org/10.1016/j.csda.2009.09.020.

Geinguenaud, Frédéric, Vania Calandrini, José Teixeira, Claudine Mayer, Jean Liquier, Christophe Lavelle, and Véronique Arluison. 2011. "Conformational Transition of DNA Bound to Hfq Probed by Infrared Spectroscopy." *Phys. Chem. Chem. Phys.* 13 (3): 1222–29. https://doi.org/10.1039/C0CP01084G.

Gilbert, Peter. 1972. "Iterative Methods for the Three-Dimensional Reconstruction of an Object from Projections." *Journal of Theoretical Biology* 36 (1): 105–17. https://doi.org/10.1016/0022-5193(72)90180-4.

Gordon, Richard, Robert Bender, and Gabor T. Herman. 1970. "Algebraic Reconstruction Techniques (ART) for Three-Dimensional Electron Microscopy and X-Ray Photography." *Journal of Theoretical Biology* 29 (3): 471–81. https://doi.org/10.1016/0022-5193(70)90109-8.

Gottesman, S., and G. Storz. 2011. “Bacterial Small RNA Regulators: Versatile Roles and Rapidly Evolving Variations.” *Cold Spring Harbor Perspectives in Biology* 3 (12): a003798–a003798. https://doi.org/10.1101/cshperspect.a003798.

Gottesman, Susan. 2004. “The Small RNA Regulators of *Escherichia Coli* : Roles and Mechanisms.” *Annual Review of Microbiology* 58 (1): 303–28. https://doi.org/10.1146/annurev.micro.58.030603.123841.

Groen, J., J. J. Conesa, R. Valcárcel, and E. Pereiro. 2019. “The Cellular Landscape by Cryo Soft X-Ray Tomography.” *Biophysical Reviews* 11 (4): 611–19. https://doi.org/10.1007/s12551-019-00567-6.

Groen, Johannes, Andrea Sorrentino, Lucía Aballe, Robert Oliete, Ricardo Valcárcel, Chidinma Okolo, Ilias Kounatidis, Maria Harkiolaki, Ana Joaquina Pérez-Berná, and Eva Pereiro. 2021. “A 3D Cartographic Description of the Cell by Cryo Soft X-Ray Tomography.” *Journal of Visualized Experiments*, no. 169 (March): 62190. https://doi.org/10.3791/62190.

Gürsoy, Dogˇa, Francesco De Carlo, Xianghui Xiao, and Chris Jacobsen. 2014. “TomoPy: A Framework for the Analysis of Synchrotron Tomographic Data.” *Journal of Synchrotron Radiation* 21 (5): 1188–93. https://doi.org/10.1107/S1600577514013939.

Hammel, Michal, Dhar Amlanjyoti, Francis E. Reyes, Jian-Hua Chen, Rochelle Parpana, Henry Y. H. Tang, Carolyn A. Larabell, John A. Tainer, and Sankar Adhya. 2016. “HU Multimerization Shift Controls Nucleoid Compaction.” *Science Advances* 2 (7): e1600650. https://doi.org/10.1126/sciadv.1600650.

Haniford, David B., and Michael J. Ellis. 2015. “Transposons Tn *10* and Tn *5*.” Edited by Mick Chandler and Nancy Craig. *Microbiology Spectrum* 3 (1): 3.1.06. https://doi.org/10.1128/microbiolspec.MDNA3-0002-2014.

Harrison, Julia A., Derek Pickard, Christopher F. Higgins, Anjam Khan, Stephen N. Chatfield, Tahir Ali, Charles J. Dorman, Carlos E. Hormaeche, and Gordon Dougan. 1994. “Role of Hns in the Virulence Phenotype of Pathogenic Salmonellae.” *Molecular Microbiology* 13 (1): 133–40. https://doi.org/10.1111/j.1365-2958.1994.tb00408.x.

Hołówka, Joanna, and Jolanta Zakrzewska-Czerwińska. 2020. “Nucleoid Associated Proteins: The Small Organizers That Help to Cope With Stress.” *Frontiers in Microbiology* 11 (April): 590. https://doi.org/10.3389/fmicb.2020.00590.

Howells, Malcolm, Christopher Jacobsen, Tony Warwick, and A. Van den Bos. 2007. “Principles and Applications of Zone Plate X-Ray Microscopes.” In *Science of Microscopy*, edited by Peter W. Hawkes and John C. H. Spence, 835–926. New York, NY: Springer New York. https://doi.org/10.1007/978-0-387-49762-4_13.

Hwang, Wonseok, Véronique Arluison, and Sungchul Hohng. 2011. “Dynamic Competition of DsrA and RpoS Fragments for the Proximal Binding Site of Hfq as a Means for Efficient Annealing.” *Nucleic Acids Research* 39 (12): 5131–39. https://doi.org/10.1093/nar/gkr075.

Ikeda, Yoshiki, Mieko Yagi, Teppei Morita, and Hiroji Aiba. 2011. “Hfq Binding at RhlB-Recognition Region of RNase E Is Crucial for the Rapid Degradation of Target MRNAs Mediated by SRNAs in Escherichia Coli: Hfq-Binding Site within RNase E.” *Molecular Microbiology* 79 (2): 419–32. https://doi.org/10.1111/j.1365-2958.2010.07454.x.

Jiang, Kai, Ce Zhang, Durgarao Guttula, Fan Liu, Jeroen A. van Kan, Christophe Lavelle, Krzysztof Kubiak, et al. 2015. “Effects of Hfq on the Conformation and Compaction of DNA.” *Nucleic Acids Research* 43 (8): 4332–41. https://doi.org/10.1093/nar/gkv268.

Kamashev, D., A. Balandina, A. K. Mazur, P. B. Arimondo, and J. Rouviere-Yaniv. 2007. “HU Binds and Folds Single-Stranded DNA.” *Nucleic Acids Research* 36 (3): 1026–36. https://doi.org/10.1093/nar/gkm667.

Kavita, Kumari, Francois de Mets, and Susan Gottesman. 2018. “New Aspects of RNA-Based Regulation by Hfq and Its Partner SRNAs.” *Current Opinion in Microbiology* 42 (April): 53–61. https://doi.org/10.1016/j.mib.2017.10.014.

Ke, Xiaoxing, Carla Bittencourt, and Gustaaf Van Tendeloo. 2015. “Possibilities and Limitations of Advanced Transmission Electron Microscopy for Carbon-Based Nanomaterials.” *Beilstein Journal of Nanotechnology* 6 (July): 1541–57. https://doi.org/10.3762/bjnano.6.158.

Khemici, Vanessa, Leonora Poljak, Ben F. Luisi, and Agamemnon J. Carpousis. 2008. “The RNase E of *Escherichia Coli* Is a Membrane-Binding Protein.” *Molecular Microbiology*, November. https://doi.org/10.1111/j.1365-2958.2008.06454.x.

Kim, Su-Im, Jae Yeong Ha, Song-Yi Choi, Su-Hyung Hong, and Heon-Jin Lee. 2022. “Use of Bacterial Extracellular Vesicles for Gene Delivery to Host Cells.” *Biomolecules* 12 (9): 1171. https://doi.org/10.3390/biom12091171.

Knoll, M., and E. Ruska. 1932. “Das Elektronenmikroskop.” *Zeitschrift f*[illegible]*r Physik* 78 (5–6): 318–39. https://doi.org/10.1007/BF01342199.

Knowles, Tuomas P. J., Michele Vendruscolo, and Christopher M. Dobson. 2014. “The Amyloid State and Its Association with Protein Misfolding Diseases.” *Nature Reviews Molecular Cell Biology* 15 (6): 384–96. https://doi.org/10.1038/nrm3810.

Koning, Roman I., Abraham J. Koster, and Thomas H. Sharp. 2018. “Advances in Cryo-Electron Tomography for Biology and Medicine.” *Annals of Anatomy - Anatomischer Anzeiger* 217 (May): 82–96. https://doi.org/10.1016/j.aanat.2018.02.004.

Kremer, James R., David N. Mastronarde, and J.Richard McIntosh. 1996. “Computer Visualization of Three-Dimensional Image Data Using IMOD.” *Journal of Structural Biology* 116 (1): 71–76. https://doi.org/10.1006/jsbi.1996.0013.

Kubiak, Krzysztof, Frank Wien, Indresh Yadav, Nykola C. Jones, Søren Vrønning Hoffmann, Eric Le Cam, Antoine Cossa, et al. 2022. “Amyloid-like Hfq Interaction with Single-Stranded DNA: Involvement in Recombination and Replication in *Escherichia Coli*.” *QRB Discovery* 3: e15. https://doi.org/10.1017/qrd.2022.15.

Kutyniok, Gitta, Wang-Q Lim, and Gabriele Steidl. 2014. “Shearlets: Theory and Applications: Shearlets: Theory and Applications.” *GAMM-Mitteilungen* 37 (2): 259–80. https://doi.org/10.1002/gamm.201410012.

Lang, Benjamin, Nicolas Blot, Emeline Bouffartigues, Malcolm Buckle, Marcel Geertz, Claudio O. Gualerzi, Ramesh Mavathur, et al. 2007. “High-Affinity DNA Binding Sites for H-NS Provide a Molecular Basis for Selective Silencing within Proteobacterial Genomes.” *Nucleic Acids Research* 35 (18): 6330–37. https://doi.org/10.1093/nar/gkm712.

Le Derout, Jacques, Irina V Boni, Philippe Régnier, and Eliane Hajnsdorf. 2010. “Hfq Affects MRNA Levels Independently of Degradation.” *BMC Molecular Biology* 11 (1): 17. https://doi.org/10.1186/1471-2199-11-17.

Link, Todd M., Poul Valentin-Hansen, and Richard G. Brennan. 2009. “Structure of Escherichia Coli Hfq Bound to Polyriboadenylate RNA.” *Proceedings of the National Academy of Sciences* 106 (46): 19292–97. https://doi.org/10.1073/pnas.0908744106.

López-Laguna, Hèctor, Julieta Sánchez, Ugutz Unzueta, Ramón Mangues, Esther Vázquez, and Antonio Villaverde. 2020. “Divalent Cations: A Molecular Glue for Protein Materials.” *Trends in Biochemical Sciences* 45 (11): 992–1003. https://doi.org/10.1016/j.tibs.2020.08.003.

Lučić, Vladan, Alexander Rigort, and Wolfgang Baumeister. 2013. “Cryo-Electron Tomography: The Challenge of Doing Structural Biology in Situ.” *Journal of Cell Biology* 202 (3): 407–19. https://doi.org/10.1083/jcb.201304193.

Maarel, Johan R. C. van der, Durgarao Guttula, Véronique Arluison, Stefan U. Egelhaaf, Isabelle Grillo, and V. Trevor Forsyth. 2016. “Structure of the H-NS–DNA Nucleoprotein Complex.” *Soft Matter* 12 (15): 3636–42. https://doi.org/10.1039/C5SM03076E.

Mackie, George A. 2013. “RNase E: At the Interface of Bacterial RNA Processing and Decay.” *Nature Reviews Microbiology* 11 (1): 45–57. https://doi.org/10.1038/nrmicro2930.

Majdalani, Nadim, SuAnn Chen, Jonathan Murrow, Kristin St John, and Susan Gottesman. 2004. “Regulation of RpoS by a Novel Small RNA: The Characterization of RprA: RprA, a Small RNA Regulator of RpoS.” *Molecular Microbiology* 39 (5): 1382–94. https://doi.org/10.1111/j.1365-2958.2001.02329.x.

Majdalani, Nadim, Christofer Cunning, Darren Sledjeski, Tom Elliott, and Susan Gottesman. 1998. “DsrA RNA Regulates Translation of RpoS Message by an Anti-Antisense Mechanism, Independent of Its Action as an Antisilencer of Transcription.” *Proceedings of the National Academy of Sciences* 95 (21): 12462–67. https://doi.org/10.1073/pnas.95.21.12462.

Malabirade, Antoine, Kai Jiang, Krzysztof Kubiak, Alvaro Diaz-Mendoza, Fan Liu, Jeroen A. van Kan, Jean-François Berret, Véronique Arluison, and Johan R.C. van der Maarel. 2017. "Compaction and Condensation of DNA Mediated by the C-Terminal Domain of Hfq." *Nucleic Acids Research* 45 (12): 7299–7308. https://doi.org/10.1093/nar/gkx431.

Malabirade, Antoine, Javier Morgado-Brajones, Sylvain Trépout, Frank Wien, Ileana Marquez, Jérôme Seguin, Sergio Marco, Marisela Velez, and Véronique Arluison. 2017. "Membrane Association of the Bacterial Riboregulator Hfq and Functional Perspectives." *Scientific Reports* 7 (1): 10724. https://doi.org/10.1038/s41598-017-11157-5.

Malabirade, Antoine, David Partouche, Omar El Hamoui, Florian Turbant, Frédéric Geinguenaud, Pierre Recouvreux, Thomas Bizien, Florent Busi, Frank Wien, and Véronique Arluison. 2018. "Revised Role for Hfq Bacterial Regulator on DNA Topology." *Scientific Reports* 8 (1): 16792. https://doi.org/10.1038/s41598-018-35060-9.

Mandin, Pierre, and Maude Guillier. 2013. "Expanding Control in Bacteria: Interplay between Small RNAs and Transcriptional Regulators to Control Gene Expression." *Current Opinion in Microbiology* 16 (2): 125–32. https://doi.org/10.1016/j.mib.2012.12.005.

Marcoleta, Andrés, Frank Wien, Véronique Arluison, Rosalba Lagos, and Rafael Giraldo. 2019. "Bacterial Amyloids." In *ELS*, edited by John Wiley & Sons, Ltd, 1st ed., 1–9. Wiley. https://doi.org/10.1002/9780470015902.a0028401.

Massé, Eric, and Susan Gottesman. 2002. "A Small RNA Regulates the Expression of Genes Involved in Iron Metabolism in *Escherichia Coli*." *Proceedings of the National Academy of Sciences* 99 (7): 4620–25. https://doi.org/10.1073/pnas.032066599.

Mastronarde, David N., and Susannah R. Held. 2017. "Automated Tilt Series Alignment and Tomographic Reconstruction in IMOD." *Journal of Structural Biology* 197 (2): 102–13. https://doi.org/10.1016/j.jsb.2016.07.011.

Matsuo, Tatsuhito, Véronique Arluison, Frank Wien, and Judith Peters. 2022. "Structural Information on Bacterial Amyloid and Amyloid-DNA Complex Obtained by Small-Angle Neutron or X-Ray Scattering." In *Bacterial Amyloids*, edited by Véronique Arluison, Frank Wien, and Andrés Marcoleta, 2538:75–93. Methods in Molecular Biology. New York, NY: Springer US. https://doi.org/10.1007/978-1-0716-2529-3_6.

Matsuo, Tatsuhito, and Judith Peters. 2022. “Fiber Diffraction and Small-Angle Scattering for Structural Investigation of Bacterial Amyloids.” In *Bacterial Amyloids*, edited by Véronique Arluison, Frank Wien, and Andrés Marcoleta, 2538:95–107. Methods in Molecular Biology. New York, NY: Springer US. https://doi.org/10.1007/978-1-0716-2529-3_7.

McQuail, Josh, Agamemnon J. Carpousis, and Sivaramesh Wigneshweraraj. 2022. “The Association between Hfq and RNase E in Long-term Nitrogen-starved *Escherichia Coli*.” *Molecular Microbiology* 117 (1): 54–66. https://doi.org/10.1111/mmi.14782.

MessaoudiI, Cédric, Thomas Boudier, Carlos Sorzano, and Sergio Marco. 2007. “TomoJ: Tomography Software for Three-Dimensional Reconstruction in Transmission Electron Microscopy.” *BMC Bioinformatics* 8 (1): 288. https://doi.org/10.1186/1471-2105-8-288.

Milanesi, Lilia, Tania Sheynis, Wei-Feng Xue, Elena V. Orlova, Andrew L. Hellewell, Raz Jelinek, Eric W. Hewitt, Sheena E. Radford, and Helen R. Saibil. 2012. “Direct Three-Dimensional Visualization of Membrane Disruption by Amyloid Fibrils.” *Proceedings of the National Academy of Sciences* 109 (50): 20455–60. https://doi.org/10.1073/pnas.1206325109.

Milles, Sigrid, Khanh Huy Bui, Christine Koehler, Mikhail Eltsov, Martin Beck, and Edward A Lemke. 2013. “Facilitated Aggregation of FG Nucleoporins under Molecular Crowding Conditions.” *EMBO Reports* 14 (2): 178–83. https://doi.org/10.1038/embor.2012.204.

Milojevic, Tetyana, Elisabeth Sonnleitner, Alessandra Romeo, Kristina Djinović-Carugo, and Udo Bläsi. 2013. “False Positive RNA Binding Activities after Ni-Affinity Purification from *Escherichia Coli*.” *RNA Biology* 10 (6): 1066–69. https://doi.org/10.4161/rna.25195.

Morena, J. Jiménez de la, P. Conesa, Y. C. Fonseca, F. P. de Isidro-Gómez, D. Herreros, E. Fernández-Giménez, D. Strelak, et al. 2022. “ScipionTomo: Towards Cryo-Electron Tomography Software Integration, Reproducibility, and Validation.” *Journal of Structural Biology* 214 (3): 107872. https://doi.org/10.1016/j.jsb.2022.107872.

Muffler, Andrea, Daniela Fischer, and Regine Hengge-Aronis. 1996. “The RNA-Bindingprotein HF-I, Known as a Host Factor for Phage RNA Replication, Is Essential-for RpoS Translation in Escherichia Coli,” 10.

Myhrvold, Cameron, Jonathan W. Kotula, Wade M. Hicks, Nicholas J. Conway, and Pamela A. Silver. 2015. "A Distributed Cell Division Counter Reveals Growth Dynamics in the Gut Microbiota." *Nature Communications* 6 (1): 10039. https://doi.org/10.1038/ncomms10039.

Nave, Colin. 2018. "A Comparison of Absorption and Phase Contrast for X-Ray Imaging of Biological Cells." *Journal of Synchrotron Radiation* 25 (5): 1490–1504. https://doi.org/10.1107/S1600577518009566.

Niemann, B., D. Rudolph, and G. Schmahl. 1976. "X-Ray Microscopy with Synchrotron Radiation." *Applied Optics* 15 (8): 1883. https://doi.org/10.1364/AO.15.001883.

Nikulin, Alexey, Elena Stolboushkina, Anna Perederina, Ioulia Vassilieva, Udo Blaesi, Isabella Moll, Galina Kachalova, et al. 2005. "Structure of *Pseudomonas Aeruginosa* Hfq Protein." *Acta Crystallographica Section D Biological Crystallography* 61 (2): 141–46. https://doi.org/10.1107/S0907444904030008.

Nogales, Eva. 2018. "Profile of Joachim Frank, Richard Henderson, and Jacques Dubochet, 2017 Nobel Laureates in Chemistry." *Proceedings of the National Academy of Sciences* 115 (3): 441–44. https://doi.org/10.1073/pnas.1718898114.

Obregon, Karla A., Connor T. Hoch, and Maxim V. Sukhodolets. 2015. "Sm-like Protein Hfq: Composition of the Native Complex, Modifications, and Interactions." *Biochimica et Biophysica Acta (BBA) - Proteins and Proteomics* 1854 (8): 950–66. https://doi.org/10.1016/j.bbapap.2015.03.016.

Olsen, Anders Steno, Jakob Møller-Jensen, Richard G. Brennan, and Poul Valentin-Hansen. 2010. "C-Terminally Truncated Derivatives of Escherichia Coli Hfq Are Proficient in Riboregulation." *Journal of Molecular Biology* 404 (2): 173–82. https://doi.org/10.1016/j.jmb.2010.09.038.

Orans, Jillian, Alexander R Kovach, Kirsten E Hoff, Nicola M Horstmann, and Richard G Brennan. 2020. "Crystal Structure of an Escherichia Coli Hfq Core (Residues 2–69)–DNA Complex Reveals Multifunctional Nucleic Acid Binding Sites." *Nucleic Acids Research* 48 (7): 3987–97. https://doi.org/10.1093/nar/gkaa149.

Otón, Joaquín, Eva Pereiro, Ana J. Pérez-Berná, Laia Millach, Carlos Oscar S. Sorzano, Roberto Marabini, and José M. Carazo. 2016. "Characterization of Transfer Function, Resolution and Depth of Field of a Soft X-Ray Microscope Applied to Tomography Enhancement by Wiener Deconvolution." *Biomedical Optics Express* 7 (12): 5092. https://doi.org/10.1364/BOE.7.005092.

Otzen, Daniel, and Roland Riek. 2019. "Functional Amyloids." *Cold Spring Harbor Perspectives in Biology* 11 (12): a033860. https://doi.org/10.1101/cshperspect.a033860.

Parekh, Virali J., Brittany A. Niccum, Rachna Shah, Marisa A. Rivera, Mark J. Novak, Frederic Geinguenaud, Frank Wien, Véronique Arluison, and Richard R. Sinden. 2019. "Role of Hfq in Genome Evolution: Instability of G-Quadruplex Sequences in E. Coli." *Microorganisms* 8 (1): 28. https://doi.org/10.3390/microorganisms8010028.

Park, Seongjin, Karine Prévost, Emily M Heideman, Marie-Claude Carrier, Muhammad S Azam, Matthew A Reyer, Wei Liu, Eric Massé, and Jingyi Fei. 2021. "Dynamic Interactions between the RNA Chaperone Hfq, Small Regulatory RNAs, and MRNAs in Live Bacterial Cells." *ELife* 10 (February): e64207. https://doi.org/10.7554/eLife.64207.

Partouche, David, Valeria Militello, Andrea Gomez-Zavaglia, Frank Wien, Christophe Sandt, and Véronique Arluison. 2019. "In Situ Characterization of Hfq Bacterial Amyloid: A Fourier-Transform Infrared Spectroscopy Study." *Pathogens* 8 (1): 36. https://doi.org/10.3390/pathogens8010036.

Partouche, David, Florian Turbant, Omar El Hamoui, Camille Campidelli, Marianne Bombled, Sylvain Trépout, Frank Wien, and Véronique Arluison. 2018. "Epigallocatechin Gallate Remodelling of Hfq Amyloid-Like Region Affects Escherichia Coli Survival." *Pathogens* 7 (4): 95. https://doi.org/10.3390/pathogens7040095.

Pehau-Arnaudet, Gérard, Danièle Joseleau-Petit, and Véronique Arluison. 2012. "New Insights into the Final Stage of Bacterial Cell Division." *American Journal of Molecular and Cellular Biology*. https://doi.org/10.7726/ajmcb.2012.1002.

Peleg, Anton Y., and David C. Hooper. 2010. "Hospital-Acquired Infections Due to Gram-Negative Bacteria." *New England Journal of Medicine* 362 (19): 1804–13. https://doi.org/10.1056/NEJMra0904124.

Pereiro, E., J. Nicolás, S. Ferrer, and M. R. Howells. 2009. “A Soft X-Ray Beamline for Transmission X-Ray Microscopy at ALBA.” *Journal of Synchrotron Radiation* 16 (4): 505–12. https://doi.org/10.1107/S0909049509019396.

Płaczek, Marcin, and Magdalena Kosela. 2016. “Microscopic Methods in Analysis of Submicron Phospholipid Dispersions.” *Acta Pharmaceutica* 66 (1): 1–22. https://doi.org/10.1515/acph-2016-0003.

Poole, Keith. 2012. “Stress Responses as Determinants of Antimicrobial Resistance in Gram-Negative Bacteria.” *Trends in Microbiology* 20 (5): 227–34. https://doi.org/10.1016/j.tim.2012.02.004.

Porcheron, Gaëlle, and Charles M. Dozois. 2015. “Interplay between Iron Homeostasis and Virulence: Fur and RyhB as Major Regulators of Bacterial Pathogenicity.” *Veterinary Microbiology* 179 (1–2): 2–14. https://doi.org/10.1016/j.vetmic.2015.03.024.

Rabhi, Makhlouf, Olivier Espéli, Annie Schwartz, Bastien Cayrol, A Rachid Rahmouni, Véronique Arluison, and Marc Boudvillain. 2011. “The Sm-like RNA Chaperone Hfq Mediates Transcription Antitermination at Rho-Dependent Terminators: Hfq-Mediated Transcription Antitermination.” *The EMBO Journal* 30 (14): 2805–16. https://doi.org/10.1038/emboj.2011.192.

Remesh, Soumya G., Subhash C. Verma, Jian-Hua Chen, Axel A. Ekman, Carolyn A. Larabell, Sankar Adhya, and Michal Hammel. 2020. “Nucleoid Remodeling during Environmental Adaptation Is Regulated by HU-Dependent DNA Bundling.” *Nature Communications* 11 (1): 2905. https://doi.org/10.1038/s41467-020-16724-5.

Rez, Peter, Thomas Larsen, and Michael Elbaum. 2016. “Exploring the Theoretical Basis and Limitations of Cryo-STEM Tomography for Thick Biological Specimens.” *Journal of Structural Biology* 196 (3): 466–78. https://doi.org/10.1016/j.jsb.2016.09.014.

Ribet, David, and Pascale Cossart. 2015. “How Bacterial Pathogens Colonize Their Hosts and Invade Deeper Tissues.” *Microbes and Infection* 17 (3): 173–83. https://doi.org/10.1016/j.micinf.2015.01.004.

Rochat, Tatiana, Philippe Bouloc, Qi Yang, Lionello Bossi, and Nara Figueroa-Bossi. 2012. "Lack of Interchangeability of Hfq-like Proteins." *Biochimie* 94 (7): 1554–59. https://doi.org/10.1016/j.biochi.2012.01.016.

Rosa-Trevín, J.M. de la, J. Otón, R. Marabini, A. Zaldívar, J. Vargas, J.M. Carazo, and C.O.S. Sorzano. 2013. "Xmipp 3.0: An Improved Software Suite for Image Processing in Electron Microscopy." *Journal of Structural Biology* 184 (2): 321–28. https://doi.org/10.1016/j.jsb.2013.09.015.

Rosa-Trevín, J.M. de la, A. Quintana, L. del Cano, A. Zaldívar, I. Foche, J. Gutiérrez, J. Gómez-Blanco, et al. 2016. "Scipion: A Software Framework toward Integration, Reproducibility and Validation in 3D Electron Microscopy." *Journal of Structural Biology* 195 (1): 93–99. https://doi.org/10.1016/j.jsb.2016.04.010.

Rust, Michael J, Mark Bates, and Xiaowei Zhuang. 2006. "Sub-Diffraction-Limit Imaging by Stochastic Optical Reconstruction Microscopy (STORM)." *Nature Methods* 3 (10): 793–96. https://doi.org/10.1038/nmeth929.

Ruysschaert, Jean-Marie, and Vincent Raussens. 2018. "ATR-FTIR Analysis of Amyloid Proteins." In *Peptide Self-Assembly*, edited by Bradley L. Nilsson and Todd M. Doran, 1777:69–81. Methods in Molecular Biology. New York, NY: Springer New York. https://doi.org/10.1007/978-1-4939-7811-3_3.

Santiago-Frangos, Andrew, Jeliazko R Jeliazkov, Jeffrey J Gray, and Sarah A Woodson. 2017. "Acidic C-Terminal Domains Autoregulate the RNA Chaperone Hfq." *ELife* 6 (August): e27049. https://doi.org/10.7554/eLife.27049.

Santiago-Frangos, Andrew, Kumari Kavita, Daniel J. Schu, Susan Gottesman, and Sarah A. Woodson. 2016. "C-Terminal Domain of the RNA Chaperone Hfq Drives SRNA Competition and Release of Target RNA." *Proceedings of the National Academy of Sciences* 113 (41). https://doi.org/10.1073/pnas.1613053113.

Santiago-Frangos, Andrew, and Sarah A. Woodson. 2018. "Hfq Chaperone Brings Speed Dating to Bacterial SRNA." *WIREs RNA* 9 (4). https://doi.org/10.1002/wrna.1475.

Sauer, Evelyn. 2013. "Structure and RNA-Binding Properties of the Bacterial LSm Protein Hfq." *RNA Biology* 10 (4): 610–18. https://doi.org/10.4161/rna.24201.

Sauter, Claude, Jérôme Basquin, and Dietrich Suck. 2003. “Sm-like Proteins in Eubacteria: The Crystal Structure of the Hfq Protein from Escherichia Coli.” *Nucleic Acids Research* 31 (14): 4091–98. https://doi.org/10.1093/nar/gkg480.

Schechter, Lisa M., Sumita Jain, Samina Akbar, and Catherine A. Lee. 2003. “The Small Nucleoid-Binding Proteins H-NS, HU, and Fis Affect *HilA* Expression in *Salmonella Enterica* Serovar Typhimurium.” *Infection and Immunity* 71 (9): 5432–35. https://doi.org/10.1128/IAI.71.9.5432-5435.2003.

Schneider, Dominique, Esther Duperchy, Joëlle Depeyrot, Evelyne Coursange, Richard E. Lenski, and Michel Blot. 2002. “Genomic Comparisons among Escherichia Coli Strains B, K-12, and O157:H7 Using IS Elements as Molecular Markers.” *BMC Microbiology* 2 (1): 18. https://doi.org/10.1186/1471-2180-2-18.

Schumacher, Maria A., Robert F. Pearson, Thorleif Møller, Poul Valentin-Hansen, and Richard G Brennan. 2002. “Structures of the Pleiotropic Translational Regulator Hfq and an Hfq–RNA Complex: A Bacterial Sm-like Protein.” *The EMBO Journal* 21 (13): 3546–56. https://doi.org/10.1093/emboj/cdf322.

Sender, Ron, Shai Fuchs, and Ron Milo. 2016. “Revised Estimates for the Number of Human and Bacteria Cells in the Body.” *PLOS Biology* 14 (8): e1002533. https://doi.org/10.1371/journal.pbio.1002533.

Shiraishi, Kouya, Yasuyuki Ogata, Katsuhiro Hanada, Yasunobu Kano, and Hideo Ikeda. 2007. “Roles of the DNA Binding Proteins H-NS and StpA in Homologous Recombination and Repair of Bleomycin-Induced Damage in Escherichia Coli.” *Genes & Genetic Systems* 82 (5): 433–39. https://doi.org/10.1266/ggs.82.433.

Shore, Carolyn K., and Allan Coukell. 2016. “Roadmap for Antibiotic Discovery.” *Nature Microbiology* 1 (6): 16083. https://doi.org/10.1038/nmicrobiol.2016.83.

Sittka, Alexandra, Verena Pfeiffer, Karsten Tedin, and Jörg Vogel. 2007. “The RNA Chaperone Hfq Is Essential for the Virulence of Salmonella Typhimurium.” *Molecular Microbiology* 63 (1): 193–217. https://doi.org/10.1111/j.1365-2958.2006.05489.x.

Söderström, Bill, and Daniel O. Daley. 2017. “The Bacterial Divisome: More than a Ring?” *Current Genetics* 63 (2): 161–64. https://doi.org/10.1007/s00294-016-0630-2.

Sofroniew, Nicholas, Lambert, Talley, Evans, Kira, Nunez-Iglesias, Juan, Bokota, Grzegorz, Winston, Philip, Peña-Castellanos, Gonzalo, et al. 2022. "Napari: A Multi-Dimensional Image Viewer for Python." Zenodo. https://doi.org/10.5281/ZENODO.6598542.

Sonnleitner, Elisabeth, Johanna Napetschnig, Taras Afonyushkin, Karin Ecker, Branislav Večerek, Isabella Moll, Vladimir R. Kaberdin, and Udo Bläsi. 2004. "Functional Effects of Variants of the RNA Chaperone Hfq." *Biochemical and Biophysical Research Communications* 323 (3): 1017–23. https://doi.org/10.1016/j.bbrc.2004.08.190.

Sorrentino, Andrea, Josep Nicolás, Ricardo Valcárcel, Francisco Javier Chichón, Marc Rosanes, Jose Avila, Andrei Tkachuk, Jeff Irwin, Salvador Ferrer, and Eva Pereiro. 2015. "MISTRAL: A Transmission Soft X-Ray Microscopy Beamline for Cryo Nano-Tomography of Biological Samples and Magnetic Domains Imaging." *Journal of Synchrotron Radiation* 22 (4): 1112–17. https://doi.org/10.1107/S1600577515008632.

Sorzano, Carlos Oscar Sanchez, Cédric Messaoudi, Matthias Eibauer, Jr Bilbao-Castro, R Hegerl, S Nickell, S Marco, and Jm Carazo. 2009. "Marker-Free Image Registration of Electron Tomography Tilt-Series." *BMC Bioinformatics* 10 (1): 124. https://doi.org/10.1186/1471-2105-10-124.

Sorzano, C.O.S., F. de Isidro-Gómez, E. Fernández-Giménez, D. Herreros, S. Marco, J.M. Carazo, and C. Messaoudi. 2020. "Improvements on Marker-Free Images Alignment for Electron Tomography." *Journal of Structural Biology: X* 4: 100037. https://doi.org/10.1016/j.yjsbx.2020.100037.

Sorzano, C.O.S., R. Marabini, J. Velázquez-Muriel, J.R. Bilbao-Castro, S.H.W. Scheres, J.M. Carazo, and A. Pascual-Montano. 2004. "XMIPP: A New Generation of an Open-Source Image Processing Package for Electron Microscopy." *Journal of Structural Biology* 148 (2): 194–204. https://doi.org/10.1016/j.jsb.2004.06.006.

Srivastava, Atul K., Jay M. Pittman, Jonathan Zerweck, Bharat S. Venkata, Patrick C. Moore, Joseph R. Sachleben, and Stephen C. Meredith. 2019. "B-Amyloid Aggregation and Heterogeneous Nucleation." *Protein Science*, August, pro.3674. https://doi.org/10.1002/pro.3674.

Storz, Gisela, Jason A Opdyke, and Aixia Zhang. 2004. “Controlling MRNA Stability and Translation with Small, Noncoding RNAs.” *Current Opinion in Microbiology* 7 (2): 140–44. https://doi.org/10.1016/j.mib.2004.02.015.

Strelak, David, Amaya Jiménez-Moreno, José L. Vilas, Erney Ramírez-Aportela, Ruben Sánchez-García, David Maluenda, Javier Vargas, et al. 2021. “Advances in Xmipp for Cryo–Electron Microscopy: From Xmipp to Scipion.” *Molecules* 26 (20): 6224. https://doi.org/10.3390/molecules26206224.

Sukhodolets, Maxim V., and Susan Garges. 2003. “Interaction of *Escherichia Coli* RNA Polymerase with the Ribosomal Protein S1 and the Sm-like ATPase Hfq.” *Biochemistry* 42 (26): 8022–34. https://doi.org/10.1021/bi020638i.

Sun, Xueguang, Igor Zhulin, and Roger M Wartell. 2002. “Predicted Structure and Phyletic Distribution of the RNA-Binding Protein Hfq,” 10.

Taghbalout, Aziz, and Lawrence Rothfield. 2008. “RNaseE and RNA Helicase B Play Central Roles in the Cytoskeletal Organization of the RNA Degradosome.” *Journal of Biological Chemistry* 283 (20): 13850–55. https://doi.org/10.1074/jbc.M709118200.

Taghbalout, Aziz, Qingfen Yang, and Véronique Arluison. 2014. “The *Escherichia Coli* RNA Processing and Degradation Machinery Is Compartmentalized within an Organized Cellular Network.” *Biochemical Journal* 458 (1): 11–22. https://doi.org/10.1042/BJ20131287.

Trépout, Sylvain. 2019. “Tomographic Collection of Block-Based Sparse STEM Images: Practical Implementation and Impact on the Quality of the 3D Reconstructed Volume.” *Materials* 12 (14): 2281. https://doi.org/10.3390/ma12142281.

Trépout, Sylvain. 2020. “In Situ Structural Analysis of the Flagellum Attachment Zone in Trypanosoma Brucei Using Cryo-Scanning Transmission Electron Tomography.” *Journal of Structural Biology: X* 4: 100033. https://doi.org/10.1016/j.yjsbx.2020.100033.

Tsui, H C, G Feng, and M E Winkler. 1997. “Negative Regulation of MutS and MutH Repair Gene Expression by the Hfq and RpoS Global Regulators of Escherichia Coli K-12.” *Journal of Bacteriology* 179 (23): 7476–87. https://doi.org/10.1128/jb.179.23.7476-7487.1997.

Tsui, Ho-Ching Tiffany, Hon-Chiu Eastwood Leung, and Malcolm E. Winkler. 1994. "Characterization of Broadly Pleiotropic Phenotypes Caused by an Hfq Insertion Mutation in Escherichia Coli K-12." *Molecular Microbiology* 13 (1): 35–49. https://doi.org/10.1111/j.1365-2958.1994.tb00400.x.

Turbant, Florian, Omar El Hamoui, David Partouche, Christophe Sandt, Florent Busi, Frank Wien, and Véronique Arluison. 2021. "Identification and Characterization of the Hfq Bacterial Amyloid Region DNA Interactions." *BBA Advances* 1: 100029. https://doi.org/10.1016/j.bbadva.2021.100029.

Turbant, Florian, David Partouche, Omar El Hamoui, Sylvain Trépout, Théa Legoubey, Frank Wien, and Véronique Arluison. 2021. "Apomorphine Targets the Pleiotropic Bacterial Regulator Hfq." *Antibiotics* 10 (3): 257. https://doi.org/10.3390/antibiotics10030257.

Turbant, Florian, Jehan Waeytens, Camille Campidelli, Marianne Bombled, Denis Martinez, Axelle Grélard, Birgit Habenstein, et al. 2022. "Unraveling Membrane Perturbations Caused by the Bacterial Riboregulator Hfq." *International Journal of Molecular Sciences* 23 (15): 8739. https://doi.org/10.3390/ijms23158739.

Turbant, Florian, Pengzhi Wu, Frank Wien, and Véronique Arluison. 2021. "The Amyloid Region of Hfq Riboregulator Promotes DsrA:RpoS RNAs Annealing." *Biology* 10 (9): 900. https://doi.org/10.3390/biology10090900.

Updegrove, Taylor B., John J. Correia, Roberto Galletto, Wlodzimierz Bujalowski, and Roger M. Wartell. 2010. "E. Coli DNA Associated with Isolated Hfq Interacts with Hfq's Distal Surface and C-Terminal Domain." *Biochimica et Biophysica Acta (BBA) - Gene Regulatory Mechanisms* 1799 (8): 588–96. https://doi.org/10.1016/j.bbagrm.2010.06.007.

Večerek, Branislav, Lukas Rajkowitsch, Elisabeth Sonnleitner, Renée Schroeder, and Udo Bläsi. 2008. "The C-Terminal Domain of Escherichia Coli Hfq Is Required for Regulation." *Nucleic Acids Research* 36 (1): 133–43. https://doi.org/10.1093/nar/gkm985.

Verma, Subhash C., Zhong Qian, and Sankar L. Adhya. 2019. "Architecture of the Escherichia Coli Nucleoid." *PLOS Genetics* 15 (12): e1008456. https://doi.org/10.1371/journal.pgen.1008456.

Victor, Tiffany W., Katherine H. O'Toole, Lindsey M. Easthon, Mingyuan Ge, Randy J. Smith, Xiaojing Huang, Hanfei Yan, et al. 2020. "Lanthanide-Binding Tags for 3D X-Ray Imaging of Proteins in Cells at Nanoscale Resolution." *Journal of the American Chemical Society* 142 (5): 2145–49. https://doi.org/10.1021/jacs.9b11571.

Vogel, Jörg, and Ben F. Luisi. 2011. "Hfq and Its Constellation of RNA." *Nature Reviews Microbiology* 9 (8): 578–89. https://doi.org/10.1038/nrmicro2615.

Vreede, Jocelyne, and Remus Th. Dame. 2012. "Predicting the Effect of Ions on the Conformation of the H-NS Dimerization Domain." *Biophysical Journal* 103 (1): 89–98. https://doi.org/10.1016/j.bpj.2012.05.040.

Waeytens, Jehan, Jérémie Mathurin, Ariane Deniset-Besseau, Véronique Arluison, Luc Bousset, Human Rezaei, Vincent Raussens, and Alexandre Dazzi. 2021. "Probing Amyloid Fibril Secondary Structures by Infrared Nanospectroscopy: Experimental and Theoretical Considerations." *The Analyst* 146 (1): 132–45. https://doi.org/10.1039/D0AN01545H.

Wagner, Thorsten, Felipe Merino, Markus Stabrin, Toshio Moriya, Claudia Antoni, Amir Apelbaum, Philine Hagel, et al. 2019. "SPHIRE-CrYOLO Is a Fast and Accurate Fully Automated Particle Picker for Cryo-EM." *Communications Biology* 2 (1): 218. https://doi.org/10.1038/s42003-019-0437-z.

Wang, Siyuan, Jeffrey R. Moffitt, Graham T. Dempsey, X. Sunney Xie, and Xiaowei Zhuang. 2014. "Characterization and Development of Photoactivatable Fluorescent Proteins for Single-Molecule–Based Superresolution Imaging." *Proceedings of the National Academy of Sciences* 111 (23): 8452–57. https://doi.org/10.1073/pnas.1406593111.

Wang, Wei-Lin, Shao-Yan Xu, Zhi-Gang Ren, Liang Tao, Jian-Wen Jiang, and Shu-Sen Zheng. 2015. "Application of Metagenomics in the Human Gut Microbiome." *World Journal of Gastroenterology* 21 (3): 803. https://doi.org/10.3748/wjg.v21.i3.803.

Wilusz, Carol J, and Jeffrey Wilusz. 2005. "Eukaryotic Lsm Proteins: Lessons from Bacteria." *Nature Structural & Molecular Biology* 12 (12): 1031–36. https://doi.org/10.1038/nsmb1037.

Wilusz, Carol J., and Jeffrey Wilusz. 2013. "Lsm Proteins and Hfq: Life at the 3′ End." *RNA Biology* 10 (4): 592–601. https://doi.org/10.4161/rna.23695.

Wolf, Sharon G., and Michael Elbaum. 2019. “CryoSTEM Tomography in Biology.” In *Methods in Cell Biology*, 152:197–215. Elsevier. https://doi.org/10.1016/bs.mcb.2019.04.001.

Wolf, Sharon Grayer, Lothar Houben, and Michael Elbaum. 2014. “Cryo-Scanning Transmission Electron Tomography of Vitrified Cells.” *Nature Methods* 11 (4): 423–28. https://doi.org/10.1038/nmeth.2842.

Wolter, Hans. 1952. “Spiegelsysteme streifenden Einfalls als abbildende Optiken für Röntgenstrahlen.” *Annalen der Physik* 445 (1–2): 94–114. https://doi.org/10.1002/andp.19524450108.

Xia, Xiaoyun, Jessie Larios-Valencia, Zhi Liu, Fu Xiang, Biao Kan, Hui Wang, and Jun Zhu. 2017. “OxyR-Activated Expression of Dps Is Important for Vibrio Cholerae Oxidative Stress Resistance and Pathogenesis.” Edited by Michael R. Volkert. *PLOS ONE* 12 (2): e0171201. https://doi.org/10.1371/journal.pone.0171201.

Yang, Dezhi, Ying Kong, Wei Sun, Wei Kong, and Yixin Shi. 2019. “A Dopamine-Responsive Signal Transduction Controls Transcription of Salmonella Enterica Serovar Typhimurium Virulence Genes.” Edited by Pascale F. Cossart. *MBio* 10 (2): e02772-18. https://doi.org/10.1128/mBio.02772-18.

Youkharibache, Philippe, Stella Veretnik, Qingliang Li, Kimberly A. Stanek, Cameron Mura, and Philip E. Bourne. 2019. “The Small β-Barrel Domain: A Survey-Based Structural Analysis.” *Structure* 27 (1): 6–26. https://doi.org/10.1016/j.str.2018.09.012.

Zhang, Aixia, Karen M. Wassarman, Carsten Rosenow, Brian C. Tjaden, Gisela Storz, and Susan Gottesman. 2003. “Global Analysis of Small RNA and MRNA Targets of Hfq: Global Analysis of Hfq Targets.” *Molecular Microbiology* 50 (4): 1111–24. https://doi.org/10.1046/j.1365-2958.2003.03734.x.

Zhou, Yizhou, Luz P. Blanco, Daniel R. Smith, and Matthew R. Chapman. 2012. “Bacterial Amyloids.” In *Amyloid Proteins*, edited by Einar M. Sigurdsson, Miguel Calero, and María Gasset, 849:303–20. Methods in Molecular Biology. Totowa, NJ: Humana Press. https://doi.org/10.1007/978-1-61779-551-0_21.